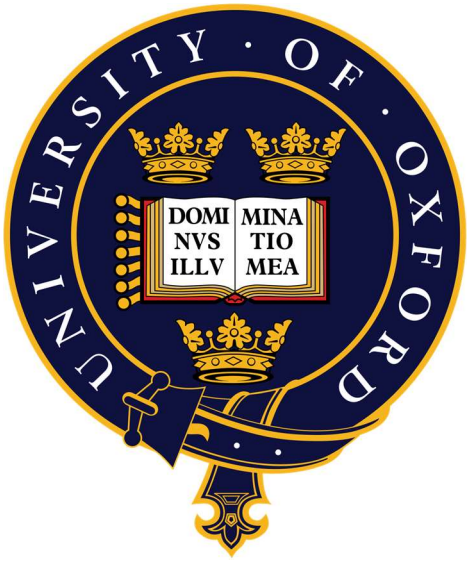
Engineering the electron relay in [FeFe] hydrogenase: Step-wise truncation of the iron-sulfur cluster motifs in the F-domain



Tin Pou Lai

St. Cross College

University of Oxford

Michaelmas term 2025

A thesis submitted to the Board of the Faculty of Physical Sciences, for the degree of

Doctor of Philosophy, University of Oxford

Abstract

Engineering the electron relay in [FeFe] hydrogenase: Step-wise truncation of the iron-sulfur cluster motifs in the F-domain

Tin Pou Lai

St. Cross college, University of Oxford

Iron-sulfur (FeS) clusters play a crucial role in facilitating electron transfer within metalloenzymes, ensuring efficient catalysis by mediating electron flow between the protein surface and buried active sites. This study explores the engineering of electron relays in a highly efficient H_2-producing enzyme, the [FeFe] hydrogenase from *C. acetobutylicum* (*Ca*HydA1), which contains five iron-sulfur clusters, by a systematic truncation of the FeS clusters in the F-cluster domain (i.e., domain containing the FeS redox cofactors), the influence of the FeS clusters on catalytic behavior, oxygen sensitivity, and the electronic characteristics of the active site has been investigated. The findings aim to inform the design of improved biohybrid or synthetic catalysts (e.g., containing electron relays) for biotechnological applications.

A heterologous overexpression system was developed for the apo-form (i.e., the enzyme containing the FeS cluster but lucking the binuclear site) of *Ca*HydA1 [FeFe] hydrogenase to enable *in vitro* reconstitution with synthetic cofactors. This approach allowed higher protein yields and purity compared to the maturase-based system and achieved superior incorporation of the $[2Fe]_H$ cofactor, validated by fourier transform infrared spectrometer (FTIR), electron paramagnetic resonance (EPR) spectroscopy,

and electrochemical analyses. The systematic truncation of accessory FeS clusters domain in *Ca*HydA1 [FeFe] hydrogenase generated three variants (S75, D127, S208) with intact active sites but altered electron relay structures. Spectroscopic and functional characterization revealed that truncations influenced active site electronic properties, catalytic bias, and protein-electrode interactions. In addition, there is still debate regarding the binding site of the biological redox parent for this particular enzyme. Solution assays with the physiological redox partner (*Ca* Ferredoxin, *Ca*Fd) suggested the binding site of the *Ca*Fd is the [2Fe-2S] cluster domain.

Electrochemical studies highlighted the role of the [2Fe-2S] cluster as the primary electron entry point and its influence on the catalytic bias, redox potentials and oxygen sensitivity. The truncated variants retained comparable oxygen sensitivity to the wild-type enzyme, suggesting that the O_2 sensitivity is not governed by the F-clusters but rather by the size of the gas channel. IR spectroelectrochemical studies further revealed long-range effects of truncations on the redox potential of $[4Fe\text{-}4S]_H$ and pH-dependent structural flexibility in the wild-type enzyme.

Overall, this work provides a systematic investigation of the electron relay's long-range influence on *Ca*HydA1 [FeFe] hydrogenase catalysis, offering insights into its electron transfer mechanisms and interactions with redox partners. These findings advance the understanding of FeS cluster engineering, paving the way for tailored hydrogenase variants with optimized properties for future biotechnological applications.

Acknowledgements

I would first like to express my deepest gratitude to my supervisor Professor Kylie Vincent for your invaluable guidance and continuous support. You have been supportive and helpful during the last few years. I am grateful to you for giving me the opportunity to work in the lab on this exciting project.

Second, my heartfelt thanks must go to Dr. Patricia Rodriguez-Macia. You have provided me endless support and guidance ever since you came to Oxford. This project cannot be fulfilled without your kind guidance and valuable ideas. Thank you so much for being such an exceptional teacher but also a lifelong friend. You truly are a super woman, and I wish you every success and happiness in Leicester.

I sincerely thank Dr. Simone Morra. You guided and trained me on molecular biology research skills through the early days of my DPhil, introducing me amazing *Ca*HydA1. Thank you for introducing me the biology world and I wish you all the best in Nottingham.

I would like to express my sincere gratitude to Dr. William Myers for his invaluable assistance and guidance with the Electron Paramagnetic Resonance (EPR) experiments conducted at CAESR. His expertise and support were instrumental in the success of this work.

I would like to extend my heartfelt gratitude to my friends and colleagues (Wangzhe Li, Xu Zhao and many others) in the lab for their unwavering support, encouragement, and camaraderie throughout this Journey.

I am deeply grateful to my parents for their unconditional love, encouragement, and sacrifices that have enabled me to pursue my dreams. To my sister, thank you for always believing in me, cheering me on, and being my constant source of support and inspiration. A special thanks to my cousin, CJ, for always being there with words of encouragement and helping me navigate challenges along the way. Finally, a piece of comfort comes from my girlfriend, April. Thank you for your constant encouragement, patience and support. Your belief in me, even during the most challenging moments, has been my greatest source of strength. Thank you for always standing by my side. I believe our journey will continue forever.

Abbreviations

A	Ampere
Å	Angstrom(10^{-10} m)
CA	Chronoamperograms
CV	Cyclic voltammogram
*Ca*HydA1	*Clostridium acetobutylicum* HydA1
*Ca*Fd	*Clostridium acetobutylicum* Ferredoxin
*Cr*HydA1	*Chlamydomonas reinhardtii* HydA1
*Cb*HydA1	*Clostridium beijerinckii* HydA1
*C*pHydA1	*Clostridium pasteurianum* HydA1
^{o}C	Degrees centigrade
CE	Counter electrode
Da	Dalton
*Dd*HydAB	*Desulfovibrio desulfuricans* HydAB
E	Electrode potential
E^{o}	Standard reduction potential
IR	Infrared
I	Current
K_M	Michaelis constant
MV	Methyl Viologen
O.D.	Optical density
PCR	Polymerase chain reaction
PFE	Protein film electrochemistry
SCE	Standard hydrogen electrode
SEC	Spectroelectrochemistry
SHE	Standard hydrogen electrode
t	Time
T	Temperature
UV-Vis	Ultraviolet-Visable
V	Volts
WE	Working eletrode
WT	Wild type

Table of contents

Chapter 1: Introduction 2

1.1 Hydrogenases 2

1.1.1 Hydrogenases 2

1.1.2 The physiological role of hydrogenases 3

1.2 Classification of hydrogenases 5

1.2.1 [NiFe] hydrogenases 5

1.2.2 [Fe] only hydrogenases 7

1.3 The structure and classification of [FeFe] Hydrogenases 9

1.3.1 The structure of [FeFe] Hydrogenases 9

1.3.2 Classification of [FeFe] Hydrogenases 13

1.4 Synthesis of [FeFe] hydrogenases 15

1.4.1 *In vivo* maturation of [FeFe] hydrogenases 15

1.4.2 *In vitro* maturation of [FeFe] hydrogenases 16

1.5 The catalytic cycle of [FeFe] Hydrogenase 18

1.6 The catalytic activity of [FeFe] hydrogenases 24

1.7 The aim and scope of this thesis 27

Chapter 2: Theory and Experimental Methods 31

2.1 Molecular biology 31

2.1.1 Strains and plasmids 31

2.1.2 Cell growth and culture 32

2.1.3 Expression and purification of Protein 35

2.1.4 Hydrogenases solution activity assays 41

2.2 Electrochemistry 42

2.2.1 Proton-Coupled Electron transfer 42

2.2.2 The three-electrode system 44

2.2.3 Protein film electrochemistry 48

2.3 Infrared spectroscopy 51

2.3.1 Theory of infrared spectroscopy 51

2.3.2 Infrared spectroscopy applied to hydrogenases 52

2.3.2 IR spectroeletrochemistry 54

2.4 Electronic paramagnetic resonance (EPR) 56

2.4.1 Theory of electron paramagnetic resonance (EPR) spectroscopy 56

2.4.2 EPR spectroscopy of metalloproteins 58

2.5 UV-Vis spectroscopy 60

Chapter 3: Development of a heterologous overexpression system for apo-CaHydA1 [FeFe] hydrogenase and in vitro maturation with synthetic cofactors 63

3.1 Introduction and aim of this chapter 63

3.1.1 Classification of [FeFe] hydrogenases 63

3.1.2 *In vivo* maturation of [FeFe] hydrogenase 64

3.1.3 *In vitro* maturation of [FeFe] hydrogenase 67

3.1.4 The aim of the chapter 69

3.2 Recombinant expression of holo-*Ca*hydA1 [FeFe] hydrogenase - *In vivo* maturation ... 70

3.3 Overexpression of apo-*Ca*HydA1 [FeFe] hydrogenase and *in vitro* maturation with synthetic cofactors 72

3.3.1 Overexpression of apo-*Ca*HydA1 using codon optimised gene 72

3.3.2 Overexpression of apo-*Ca*HydA1 using native gene 76

3.3.3 *in vitro* maturation of apo-*Ca*HydA1 with synthetic cofactors 79

3.4 Functional characterization of wild-type *Ca*HydA1 [FeFe] hydrogenase: Comparison between *in vivo* and *in vitro* maturated enzyme 80

3.5 Discussion and Conclusion 85

Chapter 4: Functional and spectroscopic characterization of the truncated variants and comparison with the wild-type enzyme 89

4.1 Introduction and aim of this chapter 89

4.1.1 The role of FeS clusters in the metalloenzymes 89

4.1.2 The role of FeS clusters in [FeFe] hydrogenases 91

4.1.3 The aim of the chapter 96

4.2 Systematic truncation of the F-domain in *Ca*HydA1 [FeFe] hydrogenases 98

4.2.1 Overexpression of *Ca*HydA1- S75 [FeFe] hydrogenase 98

4.2.2 Overexpression of M2 type like *Ca*HydA1- D127 [FeFe] hydrogenase 101

4.2.3 Overexpression of M1 type like *Ca*HydA1- S208 [FeFe] hydrogenase 106

4.3 Functional characterisation of truncated *Ca*HydA1 [FeFe] hydrogenases 109

4.3.1 Solution activity assay with artificial redox partner 109

4.3.2 Solution activity assays with the physiological redox partner 112

4.3.3 Electrochemistry 115

4.4 Spectroscopic characterisation of truncated *Ca*HydA1 [FeFe] hydrogenases 116

4.4.1 IR spectroscopic assignment for truncated *Ca*HydA1 [FeFe] hydrogenases 116

4.4.2 EPR spectroscopic assignment of truncated *Ca*HydA1 [FeFe] hydrogenases 124

4.5 Discussion and conclusion 130

4.5.1 Systematic truncation of the F-domain in CaHydA1 [FeFe] hydrogenases 130

4.5.2 Functional characterizations of truncated *Ca*HydA1 [FeFe] hydrogenases 132

4.5.3 Spectroscopic characterisation of truncated *Ca*HydA1 [FeFe] hydrogenases 133

4.5.4 Conclusion 135

Chapter 5: Comparing the Catalytic Activity of Truncated Variants and WT Enzyme, and Their Tolerance Towards Competitive Inhibitors 138

5.1 Introduction and aim of the chapter 138

5.1.1 Electrocatalytic mechanism and Catalytic activity of [FeFe] hydrogenases 138

5.1.2 Tolerance of [FeFe] hydrogenases towards competitive inhibitors 141

5.1.3 Aim of the chapter 142

5.2 Electrocatalytic characterisation of WT enzyme and truncated variants 143

5.2.1 Electrocatalytic characterisation of WT enzyme and truncated variants under different pH values 143

5.2.2 Electrocatalytic characterisation of WT enzyme and truncated variants: high-potential inactivation 149

5.3 Comparing tolerance towards competitive inhibitors in WT enzyme and its truncated variants 152

5.3.1 O_2 inhibition during H_2 oxidation 152

5.3.2 CO inhibition during H_2 oxidation 155

5.4 Discussion and conclusion 157

5.4.1 Electrocatalytic characterisation of WT enzyme and truncated variants 157

5.4.2 Comparing tolerance towards competitive inhibitors in WT enzyme and its truncated variants 158

5.4.3 Conclusion 159

Chapter 6: IR Spectroelectrochemical Studies on the redox behavior of $[4Fe\text{-}4S]_H$ in *Ca*HydA1 [FeFe] Hydrogenase and its Truncated Variants, and New Active-site States 162

6.1 Introduction and aim of the chapter 162

6.1.1 Redox potential of FeS cluster in [FeFe] hydrogenases 162

6.1.2 Two active-site states observed in *Cb*HydA1 [FeFe] hydrogenase 164

6.1.3 Aim of the chapter 164

6.2 Redox behaviours of $[4Fe\text{-}4S]_H$ in *Ca*HydA1 [FeFe] hydrogenase and truncated variants 166

6.2.1 Redox behaviour of $[4Fe\text{-}4S]_H$ in *Ca*HydA1 [FeFe] hydrogenase 166

6.2.2 Comparison of the redox behavior of $[4Fe\text{-}4S]_H$ in WT *Ca*HydA1 [FeFe] hydrogenase and its truncated variants 169

6.3 New active-site States 172

6.3.1 Two active-site states observed in the 'as is' state in D127 truncated variants ... 172

6.3.2 pH dependent interconversion of the two active-site states in the 'as is' state of the WT enzyme 173

6.4 Discussion and conclusions 180

6.4.1 Redox behaviors of $[4Fe\text{-}4S]_H$ in*Ca*HydA1 [FeFe] hydrogenases and its truncated variants 180

6.4.2 New Active-site State in WT Enzyme 181

6.4.3 Conclusion 182

Chapter 7: Conclusion and Outlook 184

7.1 Conclusion 184

7.1.1 Development of a heterologous overexpression system for apo-*Ca*HydA1 [FeFe] hydrogenase and *in vitro* maturation with synthetic cofactor 184

7.1.2 Functional and spectroscopic characterization of the truncated variants and comparison with the wild-type enzyme 185

7.1.3 Comparing the catalytic activity of truncated variants and WT enzyme, and their tolerance towards competitive inhibitors 186

7.1.4 IR spectroelectrochemical studies of the redox behavior of $[4Fe\text{-}4S]_H$ in *Ca*HydA1 [FeFe] hydrogenase and its truncated variants, new active-site statess 187

7.2 Outlook 188

References 190

Chapter 1

Introduction

Chapter 1: Introduction

1.1 Hydrogenases

1.1.1 Hydrogenases

Hydrogen is the simplest green energy fuel in the post-fossil fuel era. Commercially available catalysts for fuel cells or electrolysers at present are based on precious metals like palladium (Pd) and platinum (Pt). In nature, for billions of years, H_2 has been used as an energy source for microbial energy metabolism by a class of metalloenzyme called hydrogenases. Hydrogenases can catalyse the interconversion of protons and electrons to molecular hydrogen ($2H^+ + 2\ e^- \rightleftharpoons H_2$) at very high rates (catalytic turnover up to $\sim 10^4$ μmol / min / mg) and very efficiently (i.e. negligible energy waste, low overpotential).[1]

Depending on the demand of the host organism, and to which biological redox partner they are linked, hydrogenases are biased towards either H_2 oxidation or H_2 production. On the basis of their metal content in the active site, hydrogenases can be categorised into three different classes: [NiFe] hydrogenases, [FeFe] hydrogenases and [Fe] hydrogenases. [NiFe] hydrogenases are broadly studied because they are found to be more O_2 tolerant than [FeFe] hydrogenases, and recently they have been applied in H_2-driven biotechnology.[2] Examples include heterogeneous biocataytic NADH recycling, [3] application of hydrogenases in flavin recycling to support catalysis by ene reductases[4] and nitro reductases;[5] nitro reductions catalysed by hydrogenase on carbon.[6]

However, [FeFe] hydrogenases are very O_2 sensitive which makes it difficult to employ them

in biotechnological applications even though they are 100 times more efficient than the [NiFe] hydrogenases.[7] Recent research highlighted the potential application of [FeFe] hydrogenases in biofuel cell,[8] and used for efficient solar hydrogen production.[9]

1.1.2 The physiological role of hydrogenases

The interconversion of protons and electrons to molecular hydrogen ($2H^+ + 2\ e^- \rightleftharpoons H_2$) is an essential reaction in nature. Hydrogenases are utilised in many microorganisms to either produce H_2 as an energy source or consume H_2 for numerous useful metabolic activities.[10] For the metabolic activities such as fermentation, hydrogen photoproduction and anaerobic CO oxidation, H_2 is produced as energy source. On the other hand, hydrogenases consume H_2 for metabolic activities such as sulfate reducing, chemolithoautotrophic and aerobic H_2 oxidation, methanogenesis, acetogenesis. [10] Table 1 summarises the physiological roles of hydrogenases.

Table 1: Summary of physiological roles of hydrogenases in nature

Metabolic activity	Chemical reaction	Class of Hydrogenase
Fermentation	$CH_3CH_2CH_2COOH + 2H_2O \rightarrow 2CH_3COOH + 2H_2$ $CH_3CH_2COOH + 2H_2O \rightarrow 2CH_3COOH + CO_2 + 2H_2$	[FeFe] hydrognease [11] [12] [13]
Hydrogen photoproduction	$2H_2O + light \rightarrow O_2 + 4H^+ + 4e^-$; $2H^+ + 2e^- \rightarrow H_2$	[FeFe] hydrognease [14] [15]
Sulfate reducing	$4H_2 + H_2SO_4 \rightarrow H_2S + 4H_2O$ $2H_2 + S \rightarrow + H_2S$	[NiFe] and [FeFe] hydrogenases [10] [16] [17] [18]
Anaerobic CO oxidation	$CO + H_2O \rightarrow CO_2 + H_2$	[NiFe] hydrogenase[19] [20] [21]
Chemolithoautotrophic and aerobic H_2 oxidation	$2H_2 + O_2 \rightarrow 2H_2O$	[NiFe] hydrogenase[22]
Methanogenesis	$4H_2 + CO_2 \rightarrow CH_4 + 2H_2O$	[NiFe] hydrogenase[19] [23]

	$CH_3OH + H_2 \rightarrow \quad + CH_4 + H_2O$	
Acetogenesis	$CO_2 + 4H_2 \rightarrow CH_3COOH + 2H_2O$	[NiFe] and [FeFe] hydrogenases[10] [24] [25]

Fermentation process

The anaerobic fermentation of sugar such as glucose is undertaken by gram positive *Clostridium* bacteria (such as *Clostridium pasteurianum* or *Clostridium acetobutylicum*), with sugar being converted to H_2 and organic acids (predominantly acetic acid and butyric acid) to produce ATP (Adenosine diphosphate) as energy source. The simplified fermentation process in *Clostridium* bacteria is shown in figure 1. Firstly, glucose is converted to pyruvate via glycolysis, in which ATP is synthesised from the phosphorylation of ADP (Adenosine diphosphate).[26] Pyruvate-ferredoxin oxidoreductase oxidises pyruvate yielding acetyl CoA, CO_2 and reduced ferredoxin.[13] The electrons are transferred from reduced ferredoxin (as physiological redox partner) to [FeFe] hydrogenases to reduce H^+ to H_2. Finally, further ATP synthesis is achieved by converting acetyl-CoA to acetic acid and butyric acid. The physiological role of [FeFe] hydrogenases in the fermentation process is vital for the survival of the microorganism as it recycles the reduced ferredoxin using protons in the bulk solvent as ultimate electron acceptor. The interaction between ferredoxin as physiological redox partner and [FeFe] hydrogenases will be discussed further in chapter 4.

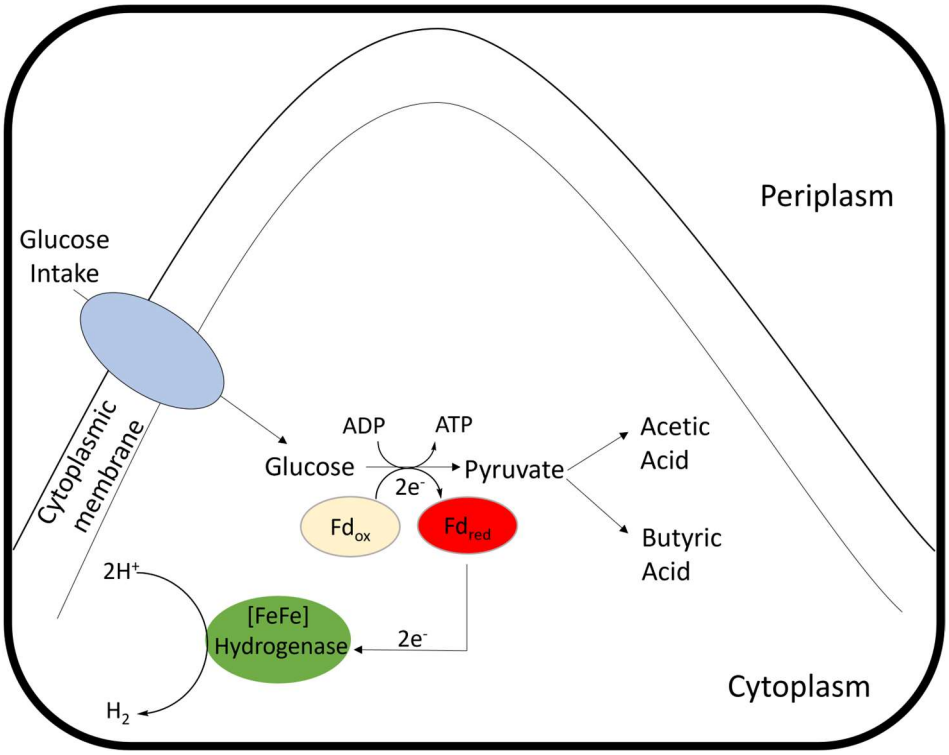


Figure 1: Simplified scheme of the fermentation process in *Clostridium* bacteria highlighting the physiological role of [FeFe] hydrogenases. Oxidised ferredoxin is shown in simplified form (Fd_{ox}); reduced ferredoxin is shown in Fd_{red}. 2 equivalents of Ferredoxin are needed to take up 2 electrons. The figure is adapted from reference[27] made in PowerPoint.

1.2 Classification of hydrogenases

1.2.1 [NiFe] hydrogenases

[NiFe] hydrogenases typically consist of two subunits, with the unique active centre [NiFe] cluster present in the large subunit and FeS clusters to mediate electrons located in the small subunit. (Figure 1A shows a crystal structure of O_2-sensitive [NiFe] hydrogenase from *D. vulgaris* Miyazaki F (*Dv*MF), the active site is zoomed in). The [NiFe] active site contains 4 cysteine ligands, with two cysteine bridging the Ni and Fe atoms and the other two cysteine being in the terminal positions. One CO and two CN ligands bond to the Fe atom to keep it in a low oxidation state, Fe (II), and low spin state adopting a pseudo-octahedral configuration.

Additionally, a bridging ligand was found in between Ni and Fe atom, which varied based on the redox state of the [NiFe] active site. (Figure 1B shows the NI-R state where a hydrogen is found at the bridging position)

One of the most distinctive features is the iron-sulfur (FeS) clusters in this class of enzyme. In O_2-tolerant [NiFe] hydrogenase, for example *E.* coli [NiFe] hydrogenase-1 (hyd1), there is a [4Fe-3S] cluster as proximal cluster, as well as medial [3Fe-4S] and distal [4Fe-4S] clusters in the small subunit. However, in O_2-sensitive [NiFe] hydrogenases, for example *E.* coli [NiFe] hydrogenase-2 (hyd-2), there is a [4Fe-4S] cluster as proximal cluster. It is thought that the proximal [4Fe-3S] cluster in hyd-1 contributes to the O_2 tolerance of this enzyme as it is able to possess three redox state which allows rapid transfer of electrons to reduce O_2 to water.[28]

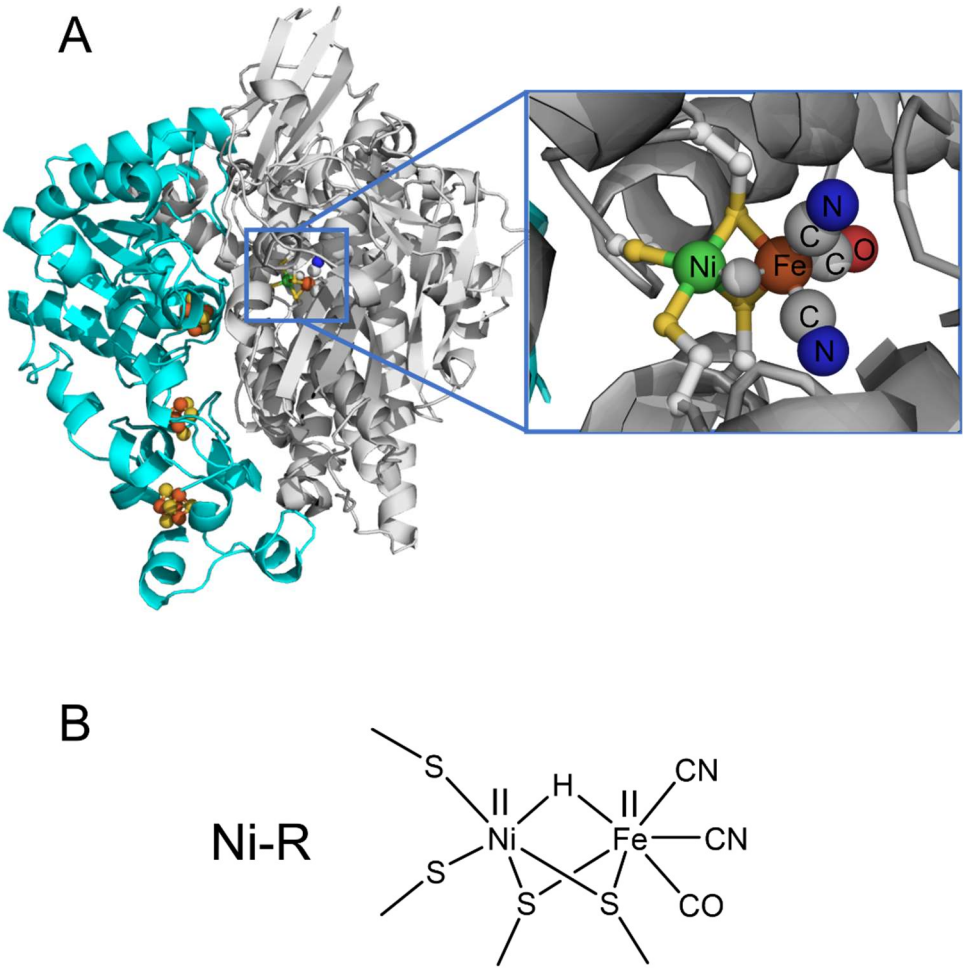


Figure 2: (A) X-ray crystal structure of [NiFe] hydrogenases from *D. vulgaris* Miyazaki F (*Dv*MF), representing the [NiFe] active site, solved by Ogata *et al*,[29] (PDB 4U9H). The active site is zoomed in, the white region shows the large subunit embedding the [NiFe] active site. The blue region represents the small subunit harbouring three FeS clusters. The figure was made using Pymol. (B) Chemical structure of Ni-R state of [NiFe] hydrogenases.

1.2.2 [Fe] only hydrogenases

Unlike [FeFe] hydrogenases and [NiFe] hydrogenases that consist of both active site and FeS clusters to mediate electrons, [Fe] only hydrogenases contain only FeGP (Iron guanilylpyridinol) as active site cofactor. They are also known as FeS cluster free hydrogenases or H_2-forming

methylenetetrahydromethanopterin dehydrogenases (Hmd). [30] This hydrogenase catalyses the reversible reaction of methenyl-MPT^+ and H_2 to methenyl-H_4MPT and H^+ (Figure 3B) and this step is essential for *in vivo* energy metabolism of formation of methane from CO_2 and H_2 in methanogenic archaea. [31]

The active site of [Fe] hydrogenase contains only one iron, adopting an octahedral coordination and low spin. The iron atom bonds to the GP cofactor via a nitrogen atom as well as an acyl bond (Figure 2A shows the crystal structure of [Fe] hydrogenase from *Methanococcus aeilius*, the active site FeGP is zoomed in). Additionally, a cysteine at position 176 from the protein backbone is bound to the iron atom. Two further strong field CO ligands are bound to the iron atom. The remaining coordination site is bound to a water molecule in open forms of [Fe] hydrogenases. The activation of the active site is done by removal of the water ligand by methenyl-H_4MPT^+ substrate binding, [32] And this allows the thermos-neutral binding of H_2 to the unsaturated iron centre in closed forms. The methenyl-H_4MPT^+ acts as a hydride accepter, and together with the iron centre, it forms a frustrated Lewis pair for efficiently splitting a H_2 molecule. [33]

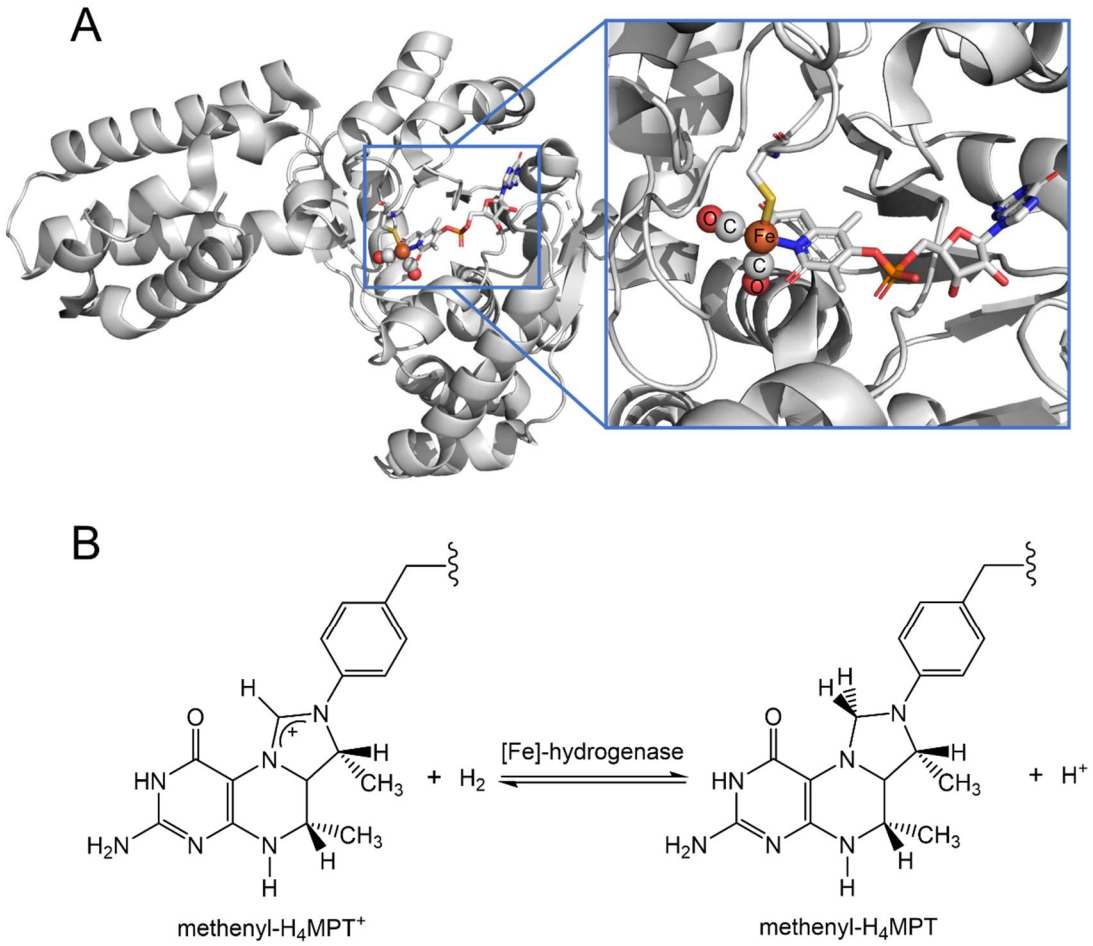


Figure 3: (A) X-ray crystal structure of [Fe] hydrogenases from *Methanococcus aeilius,* representing the active site FeGP. The structure was solved by Huang *et al*, (PDB 6HAV). [32-34]The active site is zoomed in. The figure was made using Pymol. (B) Reversible catalysis of [Fe] hydrogenase interconverts methenyl-MPT$^+$ and H_2 to methenyl-H_4MPT and H^+.

1.3 The structure and classification of [FeFe] Hydrogenases

1.3.1 The structure of [FeFe] Hydrogenases

[FeFe] hydrogenases are the most active amongst the hydrogenases, and catalyse the reversible reaction of protons and electrons to molecular hydrogen ($2H^+ + 2\ e^- \rightleftharpoons H_2$) with a turnover frequency up to $10^4\ s^{-1}$ for H_2 production with negligible overpotential (i.e. no extra or minimal energy to start the catalysis, operating very closed to the thermodynamic

potential). [1] The most commonly investigated [FeFe] hydrogenases are usually found in green algae and bacteria, for example *Chlamydomonas reinhardtii* (*Cr*)HydA1,[35] [36] *Clostridium pasterianum* (*Cp*)I, [37]*Clostridium acetobutylicum* (*Ca*)HydA1[38] *and Desulfovibrio desulfuricans* (*Dd*)HydAB.[39] [40]

Active site

The active site of these enzymes is called the H-cluster, and it is composed of a canonical [4Fe-4S] cluster ($[4Fe\text{-}4S]_H$) and a diiron subcluster ($[2Fe]_H$), as shown in Figure 4. A key feature of the H-cluster structure is the azadithiolate group (ADT) bridging the two Fe ions. The Fe closer to the $[4Fe\text{-}4S]_H$ cluster is called proximal (Fe_p), and the one harbouring the open coordination site is called distal (Fe_d). The two Fe ions are further linked together by a bridging CO ligand, and each Fe contains one terminal CN^- and one terminal CO. These strong-field ligands are good σ-donating and π-accepting ligands, which stabilise the Fe ions in low spin and low oxidation states. The N atom of the ADT group serves as a base to facilitate the heterolytic splitting of H_2 as well as a proton relay to remove protons from the active site to the protein surface. [41] [42]The arrangement of the amine and Fe_d is constrained such that no bonds can form between the two, with the N atom of the ADT acting as a Lewis base, and the low valent Fe_d metal acting as a Lewis acid, both constituting a Frustrated Lewis Pair (FLP) which is crucial for catalysis (Figure 4). In terms of electron transfer, $[4Fe\text{-}4S]_H$ acts as an electron relay. Bacterial [FeFe] hydrogenases also contain an additional domain (F-domain) hosting additional FeS clusters (called F-clusters), that function as electron transfer cofactors located within a tunnelling electron transfer distance (10 - 11 Å), forming the electron transfer chain (i.e. electron relay). [43] (Figure 3A shows the crystal structure of *Cp*I [FeFe] hydrogenase, which

consists of overall 5 FeS clusters.)

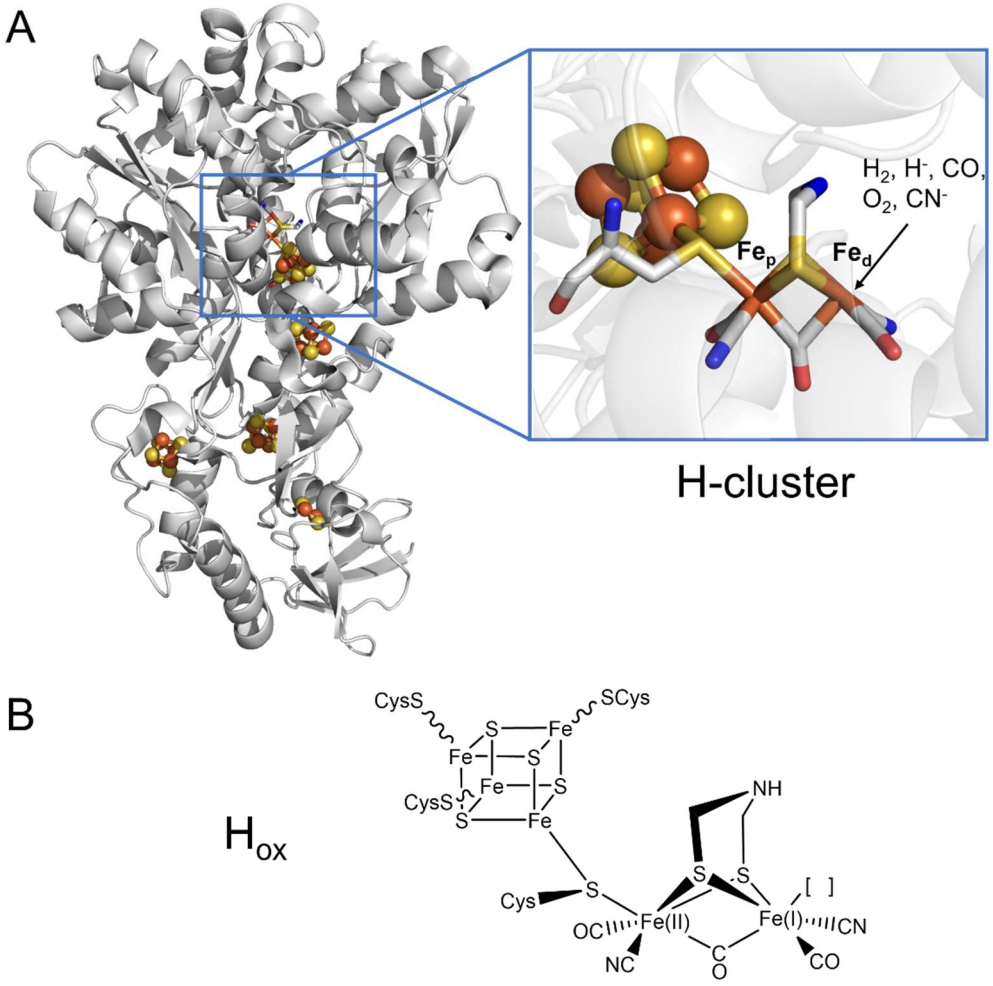


Figure 4: (A) X-ray crystal structure of [FeFe] hydrogenases from *Clostridium pasterianum* (*Cp*I), (PDB 3C8Y). [44]The active site H-cluster is zoomed in. (B) The chemical structure of H_{ox} state of [FeFe] hydrogenases. [ ] exemplifies the open coordination site where H_2 and H^- as well as inhibitor binds. Figure 4A was made using Pymol and Figure 4B was made using ChemDraw.

Proton channel

The proton-transfer pathway is a rather important component for efficient catalysis by [FeFe] hydrogenases as it allows fast transport of protons between bulk solvent and the active site centre. The secondary coordination sphere (i.e. the amino acids residues constructing the

proton transfer pathway) of [FeFe] hydrogenases are highly conserved across the [FeFe] hydrogenase family.[45] Initially, the proton transfer pathway of *Dd*HydAB and *Cp*I was studied by computational methods,[41] resulting in a proposal that the proton is transported via two glutamate, one serine, one water molecule and a cysteine residue. The cysteine residue is the primary proton acceptor lying very close to the N atom of the bridge-head of $[2Fe]_H$. [45] Functional and structural studies have been carried out by Duan *et. al* to investigate the proton transfer pathway of *Cr*HydA1 and *Cp*I.[46] The proton transfer pathway in [FeFe] hydrogenase (see figure 5) was shown, their results showed that by mutating any of C299, E279, S319, E282 or R286 to other amino residues resulted in a drastic decrease of catalytic activity.

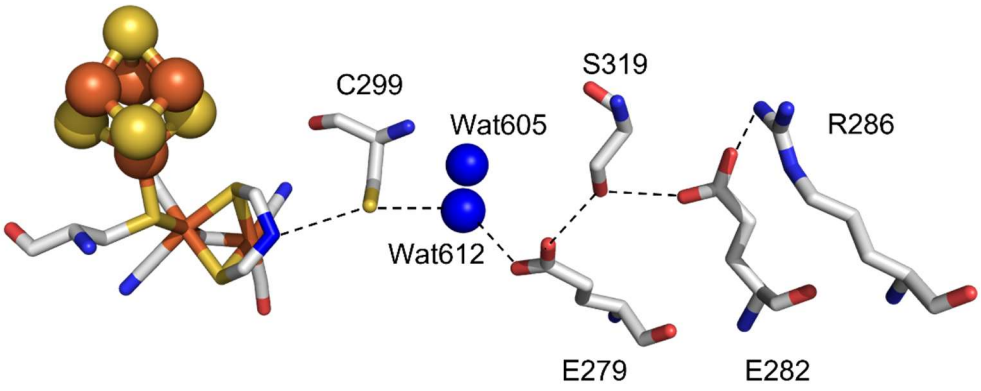


Figure 5: Proton transfer pathway of *Cp*I [FeFe] hydrogenase (PDB: 3C8Y). [46] The figure was made in Pymol.

Gas channel

Like [NiFe] hydrogenase, the active site H-cluster is buried in the centre of the protein, therefore, a hydrophobic gas channel are required for substrate H_2, or inhibitors such as O_2 and CO to access the active site in [FeFe] hydrogenases. From the crystal structures, the gas

channel in [FeFe] hydrogenases are shorter compared to [NiFe] hydrogenases, which could rationalise the fact that [FeFe] hydrogenases in general have greater catalytic activity in contrast to [NiFe] hydrogenases.[1] Previous efforts in mutating the amino acids constructing gas channels to engineer O_2 tolerant or less O_2 sensitive [FeFe] hydrogenases were not successful. Nonetheless, the activity and the stability of the enzyme were altered. [47]

1.3.2 Classification of [FeFe] Hydrogenases

According to Meyer's classification of [FeFe] hydrogenase[48] (see figure 6), prototypical [FeFe] hydrogenases can be classified into five main types, but the most typical are M1-3 types. The simplest [FeFe] hydrogenase is known as M1-type, which only contains the catalytic centre (H-cluster) in the H-domain. M2 type [FeFe] hydrogenases consist of two domains, the H-domain and the F-cluster domain. In the F-cluster domain, they harbour two additional bacterial type ferredoxin [4Fe-4S] clusters to facilitate electron transfer from the buried active site to the protein surface. One example of M2 type hydrogenase is *Dd*HydAB[49]. The M3-type [FeFe] hydrogenases also contain an H-domain and an F-cluster domain, but features two further N-terminal cluster binding motifs in the F-domain. Examples are *Cp*I[50] and *Ca*HydA1[51] [52]. One of these motifs harbours a [4Fe-4S] cluster ligated by one histidine residue and three cysteine residues, and the other contains a plant type ferredoxin [2Fe-2S] cluster. There are M4 and M5 type [FeFe] hydrogenases containing more FeS clusters, but these are less studied generally[53] [54]. These hydrogenases described above are also grouped as [FeFe] hydrogenases (group A), they are found the most active for H_2 production and therefore are the most characterised. Interestingly, electron-bifurcating [FeFe] hydrogenases such as *Thermotoga (T.) maritima* (*Tm*)HydABC contains multiple subunits of M3 and M4-type like

hydrogenase subunit and forms a related sub class to the prototypical [FeFe] hydrogenases[55] [56] [57].

The group B [FeFe] hydrogenases are ancestral and group C: Sensory enzymes are generally less characterised. One example of Group B [FeFe] hydrogenases is *Cp*III, it has been shown that this enzyme is active and exhibits different catalytic bias (a term which was described in the previous section) compared to *Cp*I and *Cp*II. Recently, it was shown that the sensory enzymes *Tm*HydS and *Thermoanaerobacter mathranii* (*Tam*)HydS exhibiting unique features in both spectroscopic and functional characteristics. [58] [59] These enzymes have been categorized into sensory enzymes because they harbour a Per-Arnt-Sim (PAS) domain close to the active site pocket and it is thought that it contributes to transcriptional regulation as it is able to detect the H_2 level of the cellular environment.

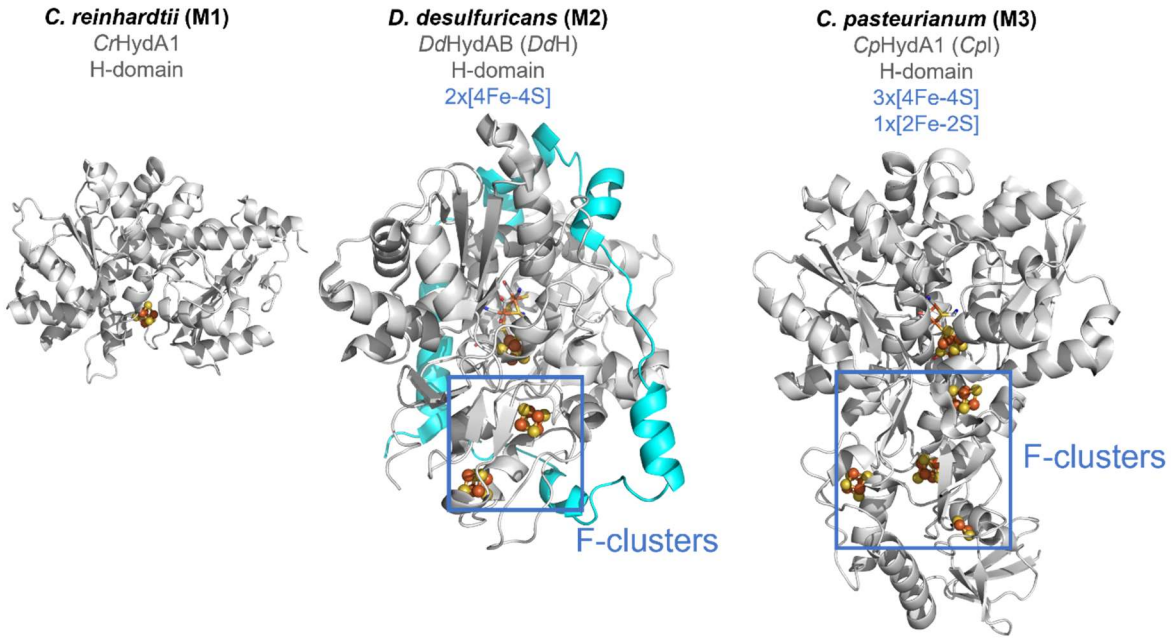


Figure 6: Meyer's classification for [FeFe] hydrogenases: X-ray crystal structures of [FeFe] hydrogenases from M1-type: *Chlamydomonas reinhardtii* (*Cr*HydA1),(PDB 3LX4) [60]; M2 type: *Desulfovibrio desulfuricans* (*Dd*HydAB), (PDB 6SG2)[61]; M3 type: *Clostridium pasterianum* (*Cp*I), (PDB

3C8Y). [44] This figure was made in Pymol.

Apart from prototypical group A [FeFe] hydrogenases, ancestral group B [FeFe] hydrogenases and group C Sensory enzymes mentioned above, [FeFe] hydrogenases from archaea are also found active and can be classified into several types: A_{arc}, B_{arc},E_{arc} and F_{arc}.[62] Minimal enzyme *Micrarchaeota* (denoted *Mu*) from subgroup A1 in group A_{arc} and *Forterrea multitransposorum* (*Fm*) from group E_{arc} are particularly characterized. *Mu* [FeFe] hydrogenases are shown to be the most active exhibiting comparable activity to prototypical *Cr*HydA1 [FeFe] hydrogenase. Multisubunit group B *Prometheoarchaeum syntrophicum (Ps)* and Altarchaeota (denoted *Ia*) from subgroup A3 in group A_{arc} are also characterized, but shown to be less active.[62]

1.4 Synthesis of [FeFe] hydrogenases

1.4.1 *In vivo* maturation of [FeFe] hydrogenases

The [FeFe] hydrogenases can be maturated *in vivo* (biosynthesis) or *in vitro*. In the *in vivo* maturation, three different maturases are involved (HydG, HydE, HydF). The apo-protein containing the [4Fe-4S] cluster or clusters but lacking the binuclear site, is synthesised by the iron-sulfur cluster (ISC) machinery of the cells. Recent research shows that HydG is responsible for synthesis of the $[Fe(CN)(CO)_2(cysteinate)]^-$ synthon; HydE then uses this substrate to synthesise $[Fe_2(\mu\text{-}SH)_2(CN)_2(CO)_4]^{2-}$; HydF completes the synthesis of the adt-dimer and enables the *in vivo* maturation of apo-protein. [63] (Figure 7 shows schematic representations of the individual role of each maturase enzyme and the origin of atoms in the biosynthesis of

H-cluster)

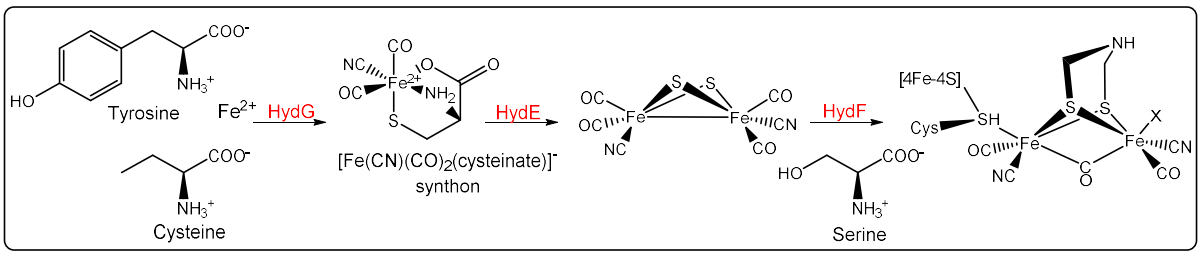


Figure 7: Schematic representation of the individual role of each maturase enzyme and origins of atoms in the biosynthesis of H-cluster. The scheme is adapted from reference[64] and was made using ChemDraw.

1.4.2 *In vitro* maturation of [FeFe] hydrogenases

In 2013, Berggren and co-workers found that [FeFe] hydrogenases can also be maturated *in vitro*, which was a ground-breaking advance for the field. Apo-HydA and HydF could be overexpressed in *E. coli,* and then mixed *in vitro* with artificially synthesised cofactor ($[2Fe]^{ADT}$) and HydF. HydF was able to transfer the artificial cofactor to the apo-hydrogenase to produce a fully assembled active site H-cluster, generating an artificially maturated holo [FeFe] hydrogenase, which was shown to be functional and spectroscopically identical to the native protein. [65]

More surprisingly, a bit later, Esselborn and co-workers showed that apo-HydA could be 100 % maturated by the artificial cofactor without the assistance of HydF[66] (Figure 9 shows a schematic representation of artificial maturation of [FeFe] hydrogenase). This was shown to work for hydrogenases from six different organisms (*Cr*, *Cp*, *Dd*, *Tm*, *Chlorella variabillis, Cv* and *Megasphera elsdenii, Me*).[40] [58] [66] [67] [68] These findings imply that we can, now,

manipulate both the protein scaffold and the active-site cofactor, to produce synthetic variants of [FeFe] hydrogenases. Figure 8 summarises the chemically modified H-clusters, $[Fe_2(SCH_2XCH_2S)(CO)_4(CN)_2]$, where X=O for $[2Fe]^{ODT}$, without X for $[2Fe]^{EDT}$ and X=CH_2 for $[2Fe]^{PDT}$, [69]isotopic labelled H-cluster (such as ^{57}Fe, ^{13}C, and ^{15}N), [70] [71] changing CO to CN^-, change in metals and change in steric bulk in bridge in the H-cluster).[72] This also allows a much simpler mechanism for site-directed mutagenesis (SDM) as the molecular biology box for *E. coli* is very well understood and the apo proteins can be expressed in *E. coli*. The artificial maturation approach generates high yields of very pure protein. Finally, this makes it possible to study the apo-protein separately and to investigate how the artificial maturation works.

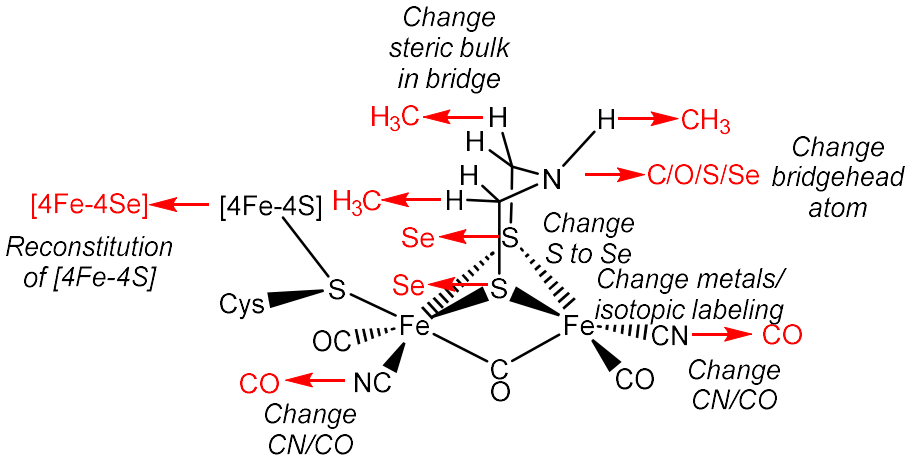


Figure 8: Scheme of the chemical modification of the [2Fe] subsite made up to now. The figure was adapted from reference.[72] The scheme was made in ChemDraw.

During the *in vitro* maturation, when the synthetic cofactor spontaneously binds to the $[4Fe\text{-}4S]_H$ cluster, one CO ligand is lost and another CO ligand moves into a bridging position between the two Fe atoms, opening a vacant site at Fe_d, which is trans to the bridging CO. In addition, the CO/CN^- ligands shift into an octahedral coordination at each Fe atom. Each of the two Fe atoms adopts a perpendicular equatorial plane, which allows the mixed valence

Fe(I)Fe(II) state of H_{ox}. [65]

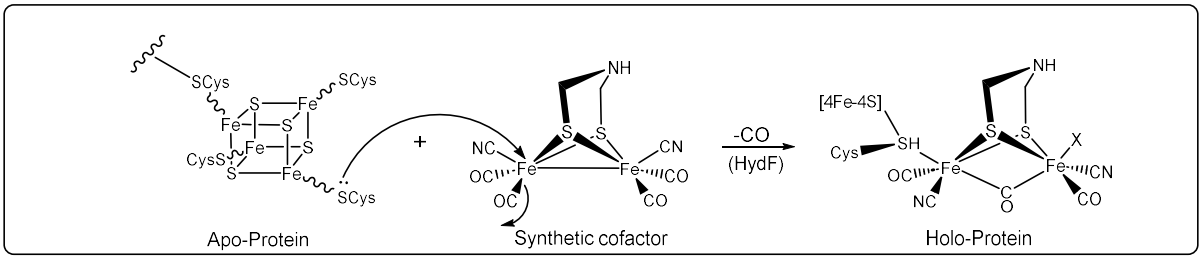


Figure 9: Schematic representation of artificial maturation of [FeFe] hydrogenase. The scheme was made by ChemDraw.

The activation of apo-protein with $[2Fe]^{ADT}$ was studied using protein film electrochemistry under redox control and to study the kinetics of H-cluster assembly. It was shown that the assembly of H-cluster assembly starts with tight binding between the $[2Fe]^{ADT}$ and apo-protein, producing a stable intermediate. The covalent bond formation between the $[2Fe]^{ADT}$ and $[4Fe\text{-}4S]_H$ is potential dependent, indicating that the controlling factor is the oxidation state of $[4Fe\text{-}4S]_H$. Their model proposed that the oxidation state of $[4Fe\text{-}4S]_H$ needs to be 2+ in order to form a μ-S-Cys bond with $[2Fe]^{ADT}$. In the final step, CO releases to complete the H-cluster assembly. This step was found to be a fast process and they suggest the rate-determining step could be the final rearrangement of the [2Fe] component. [73]

1.5 The catalytic cycle of [FeFe] Hydrogenase

The $[4Fe\text{-}4S]_H$ cluster and the $[2Fe]_H$ subcluster are strongly redox coupled, resulting in the H-cluster being a very fast and efficient catalyst for H_2 conversion, comparable with some of the most active precious metals such as platinum or palladium. During the catalytic cycle, the oxidation states of the $[2Fe]_H$ subcluster and the $[4Fe\text{-}4S]_H$ cluster vary, therefore allowing the

use of electron paramagnetic resonance (EPR) spectroscopy to study the catalytic intermediates of [FeFe] hydrogenases. The CN^- and CO ligands at the active site are used as an IR probes, thus allowing the use of Fourier-transform infrared (FTIR) spectroscopy coupled with electrochemical control (spectroelectrochemistry) to investigate the catalytic mechanism of [FeFe] hydrogenases and to identify the electronic structure of each catalytic intermediate, since these ligands are extremely sensitive to changes in the electron density of their environment (i.e. the oxidation state of the Fe ions and the redox state of $[4Fe\text{-}4S]_H$). Up to now, the catalytic cycle has been investigated intensively for *Cr*HydA1 [FeFe] hydrogenase (M1-type) since it is the simplest model amongst [FeFe] hydrogenase,[74-76] but it has been much less explored for F-cluster containing [FeFe] hydrogenases (M2 and M3-types), as they are much more complex enzymes, but much more active and reversible than M1-type hydrogenases.[77-79]

Currently seven catalytically active states have been identified and spectroscopically characterised: H_{ox}, H_{red}, $H_{red}H^+$, $H_{sred}H^+$, $H_{hyd:ox}$, $H_{hyd:red}$ and H_{hyd}. [74], [76], [80-84] (Figure 10 shows he catalytic cycle of [FeFe] hydrogenase.) In general, the catalytic cycle of [FeFe] hydrogenases involves two proton-coupled electron transfer processes. In the resting H_{ox} state, the $[2Fe]_H$ site is in a mixed valence $Fe_p(II)Fe_d(I)$) configuration with the [4Fe-4S] cluster oxidised (2+).[76] The resting state Hox is therefore paramagnetic and EPR-active. One electron reduction of H_{ox} at the [4Fe-4S] cluster yields the H_{red} state, and thus the binuclear site stays in a mixed valence configuration ($Fe_p(II)Fe_d(I)$). [74] Proton-coupled electron transfer from the $[4Fe\text{-}4S]_H$ cluster to the binuclear part $[2Fe]_H$ yields the $H_{red}H^+$ state. (In a mixed valence configuration ($Fe_p(I)Fe_d(I)$))

H_{red} and $H_{red}H^+$ states are both diamagnetic and therefore EPR silent.) The $[4Fe\text{-}4S]_H$ cluster can then be further reduced by one electron to form the most reduced $H_{sred}H^+$ state. [80] It was shown in cryogenic temperatures that the bridging CO was observed in $H_{red}H^+$ state and $H_{sred}H^+$ state indicating a semi-bridging CO structure in these states.[85] Finally, H_{hyd} is obtained from $H_{sred}H^+$ by transferring the proton from the protonated ADT (NH_2^+) to the open coordination at Fe_d, forming a terminal hydride with a homovalent $Fe_p(II)Fe_d(II)$ configuration and a reduced (1+) $[4Fe\text{-}4S]_H$ cluster. [81-83] Both $H_{sred}H^+$ and H_{hyd} are paramagnetic and therefore EPR-active. H_{ox} can be regenerated by protonation of the amine to form H_2 via proton-coupled electron transfer from the $[4Fe\text{-}4S]_H$ cluster to $[2Fe]_H$, and this completes the catalytic cycle. However, recent study shows that under illumination with blue light (120 min, 455 nm), $H_{red}H^+$ and $H_{sred}H^+$ in *Cr*HydA1 reversibly convert to a hydride containing isomer $H_{hyd:ox}$ and $H_{hyd:red}$ respectively. [84] Additionally, the H_{ox} state can bind to exogeneous CO generating the inactive H_{ox}-CO state. This H_{ox}-CO state can be reduced on the $[4Fe\text{-}4S]_H$ cluster by one electron to obtain the H_{red}-CO.[75] If the H_{red}-CO state is further reduced by one electron, it results in the release of CO generating the $H_{sred}H^+$ state. [75] The degradation of the $[2Fe]_H$ subcluster by O_2 liberates CO that in turn ('cannibalisation'), binds to the remaining intact H-cluster leading to the formation of the inactive H_{ox}-CO state, thus, the CO-bound forms can also be seen upon exposure to O_2 without addition of exogenous CO. [39] Figure 10 summarises the catalytic cycle as it is currently understood.

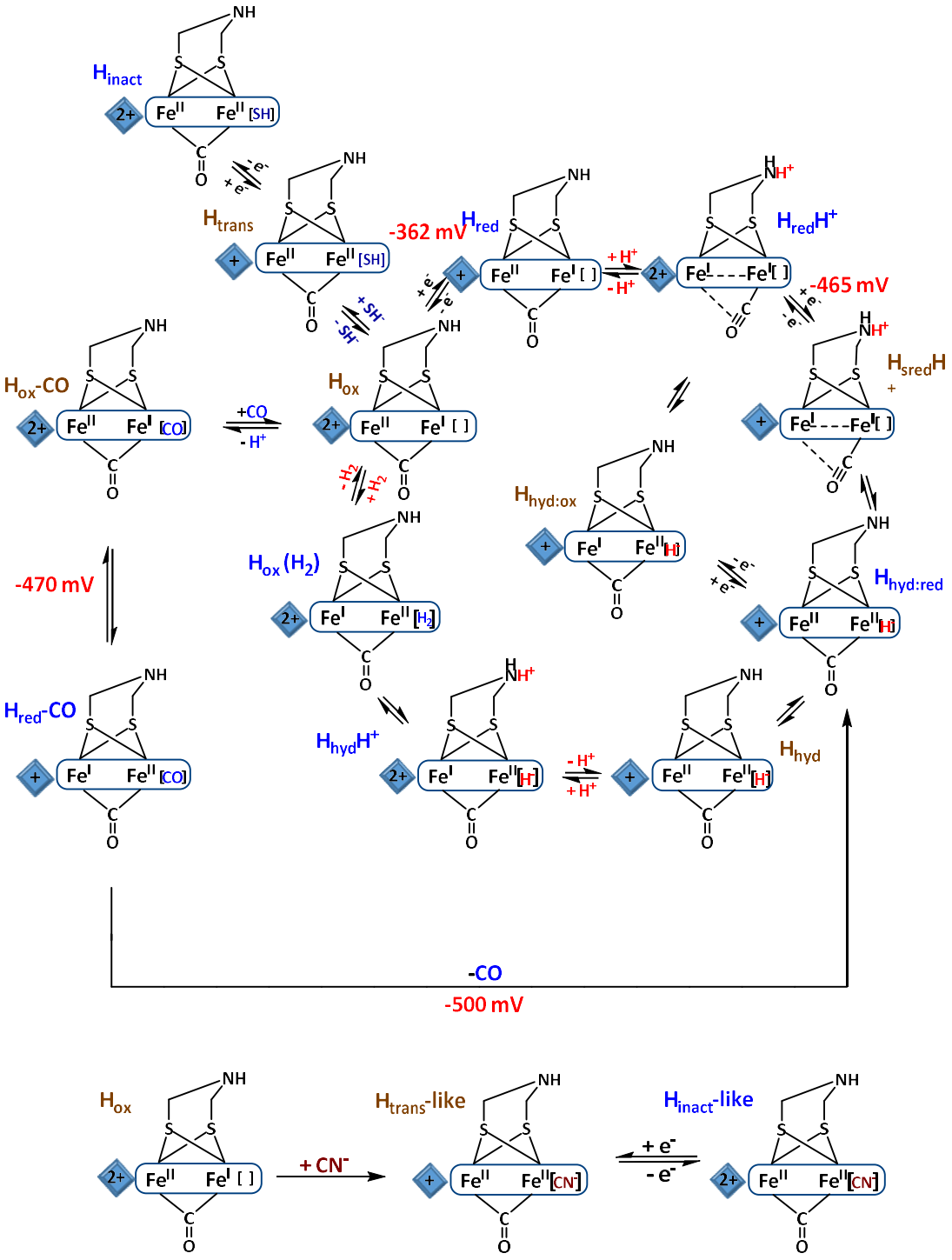


Figure 10: The catalytic cycle of [FeFe] hydrogenase with the seven active states (H_{ox}, H_{red}, $H_{red}H^+$, $H_{sred}H^+$, $H_{hyd:ox}$, $H_{hyd:red}$ and H_{hyd}), the CO inhibited inactive states (H_{ox}-CO and H_{red}-CO), H_{inact} and H_{trans} state as well as CN- inhibited states (H_{trans}-like and H_{inact}-like). The $[4Fe\text{-}4S]_H$ cluster is represented as

. The terminal CO and CN^- ligands are left off for simplicity. EPR-active states are highlighted in brown and EPR-silent states are highlighted in blue. The figure is adapted from reference[1] and was made using ChemDraw.

Inactive states

The air-stable inactive state (H_{inact}) of [FeFe] hydrogenases has been investigated intensively over the last decade as it provides insight into how to improve O_2 tolerance for highly efficient but O_2-sensitive [FeFe] hydrogenases to access and function under aerobic conditions, and for the design of better bio-inspired synthetic catalysts. The H_{inact} state in [FeFe] hydrogenase was first found in the O_2-sensitive and light-sensitive *Dd*HydAB (*Dd* is well-known as a sulfate reducing bacterium) isolated aerobically. It was shown that the H_{inact} state is air-stable and light-stable.[39] H_{inact} adopts a oxidised homovalent $Fe_p(II)Fe_d(II)$) configuration with the [4Fe-4S] subcluster oxidised (2+) (As shown in figure 10) . Thus, the H_{inact} state is diamagnetic and EPR silent. It was also shown that the two accessory clusters in the F-domain are also oxidised.[86] [87] Activation of the H_{inact} state to the H_{ox} state is achieved via two steps. [39] One electron reversible reduction of H_{inact} state led to H_{trans} state, where the [4Fe-4S] subcluster is reduced and the $[2Fe]_H$ stays in a homovalent $Fe_p(II)Fe_d(II)$) configuration. H_{trans} state is therefore paramagnetic and EPR-active. H_{ox} state can then be regained from H_{trans} state by transferring an electron from the [4Fe-4S] subcluster to the $[2Fe]_H$ and releasing a SH^- ligand. Nonetheless, it was not until recently that the crystal structure of *Dd*HydAB H_{inact} state was elucidated. H_{inact} state in *Dd*HydAB can be obtained from H_{ox} state via reduction with sodium dithionite NaDT and addition of sulfide Na_2S. It was also shown in this work that H_{inact} state could be formed in *Cr*HydA1, although to a much lesser extent, but not in *Cp*I[88] The crystal

structure of *Dd*HydAB H_{inact} state revealed that a sulfide ligand was bound to the open coordination site of the distal iron of $[2Fe]_H$[61] (see figure 11A). Interestingly, the crystal structure of H_{inact} state of another [FeFe] hydrogenase from *Clostridium beijerincki* (*Cb*)HydA1 revealed a Fe-S bond formed (3 Å) to the distal iron of $[2Fe]_H$ from the cysteine 367 ligand in the proton transfer pathway[89] (see figure 11B). The interconversion of H_{inact} state in *Cb*HydA1 to H_{ox} state was shown to be reversible without addition of sulfide. [90] [91] Spectroelectrochemistry of *Cb*HydA1 showed that this enzyme was able to trap H_{hyd} state at high proportion at low reduction potentials.[91]

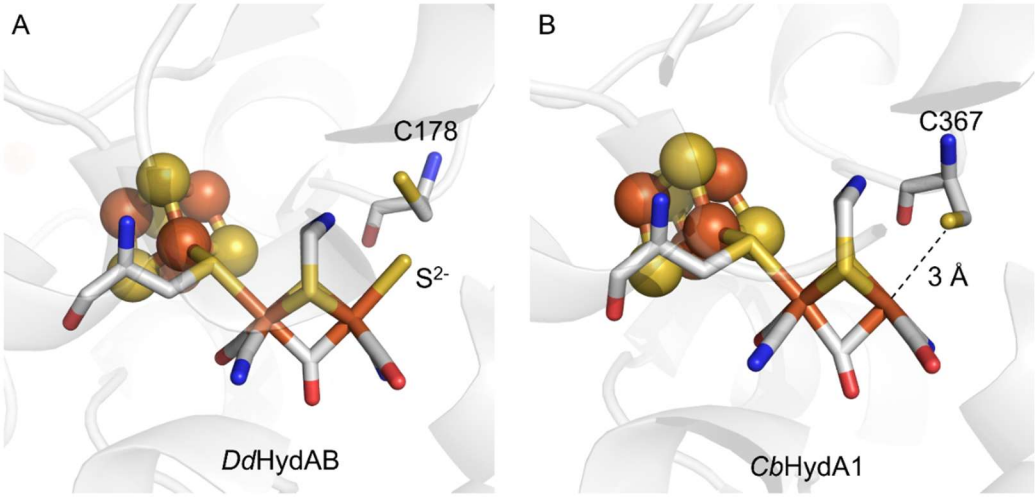


Figure 11: (A) X-ray crystal structures of H_{inact} state of *Dd*HydAB [FeFe] hydrogenase showing a sulfide bond to the distal iron of $[2Fe]_H$. (PDB:6SG2)[61] (B) X-ray crystal structures of H_{inact} state of *Cb*HydA1 [FeFe] hydrogenase revealing a FeS bond formed (3 Å) from C367 to the distal iron of $[2Fe]_H$. (PDB:6TTL)[89]. The figure was made using Pymol.

CN^- inhibited state

The crystal structure of CN^- inhibited state of [FeFe] hydrogenases from *Cp*I and *Dd*HydAB was reported recently.[92] [93] The result revealed that the CN^- ligand was bound to the open

coordination site of distal iron $[2Fe]_H$ and had resulted in a conformational change of amino residues (*Cp*I) in the proton transfer pathway which favours direct proton transfer between E279 and S319 ligands.[92] Interestingly, in *Dd*HydAB, C178A variant was isolated with CN^- inhibited to the open coordination site. The CN^- ligand is thought to be originated from the cannibalization of damaged $[2Fe]_H$. Detailed spectroscopy (FTIR and EPR) showed that the CN^- inhibited isolated state adopted a homovalant $Fe_p(II)Fe_d(II)$) configuration with the [4Fe-4S] subcluster oxidised (+), which is similar to the H_{trans} state observed in WT *Dd*HydAB (as shown in figure 9). Furthermore, it was shown that the H_{trans}-like state can be converted to H_{inact}-like state reversibly.[93]

1.6 The catalytic activity of [FeFe] hydrogenases

[FeFe] hydrogenases are highly active, and their catalytic characteristics and activities can be established by protein film electrochemistry (PFE). The catalytic activity can be measured from current. The catalytic activity of [FeFe] hydrogenases vary significantly amongst different organisms and types of enzymes. Figure 12A shows the cyclic voltammogram (CV) of the model [FeFe] hydrogenase from M2 type *Dd*HydAB.[40] The CV can be broken down into three regions. Region 1 is the H_2 production region below the H_2 thermodynamic potential (Figure 11, region 1, $E < E_{2H^+/H_2}$), the enzymes received electrons from electrodes and reduces H^+ to H_2. At the H_2 thermodynamic potential (E_{2H^+/H_2}), the H_2 production and H_2 oxidation currents reach equilibrium, hence zero current. Region 2 is the H_2 oxidation region above the H_2 thermodynamic potential (Figure 11, region 2, $E > E_{2H^+/H_2}$), the enzyme oxidises H_2 into

protons and electrons. [FeFe] hydrogenases are highly reversible catalysts (i.e. negligible overpotential for both directions). The third region represents high-potential inactivation (Figure 12, region 3). At high potentials, the oxidation current decreases which indicates the occurrence of inactivation of the enzyme. The catalytic current is nearly 100 % recovered during the return scan as the potential is swept back in the negative direction. E_{switch} (the potential at which the inactivation occurs) seemed to be dependent on the scan rate and pH.[94] M3-type *Ca*HydA1 [FeFe] hydrogenase seemed to display no high-potential inactivation at 'normal' scan rates (i.e. 20 mV/s), and the catalytic bias is more prone to H_2 production compared to M2 type *Dd*HydA1 (Figure 12B).

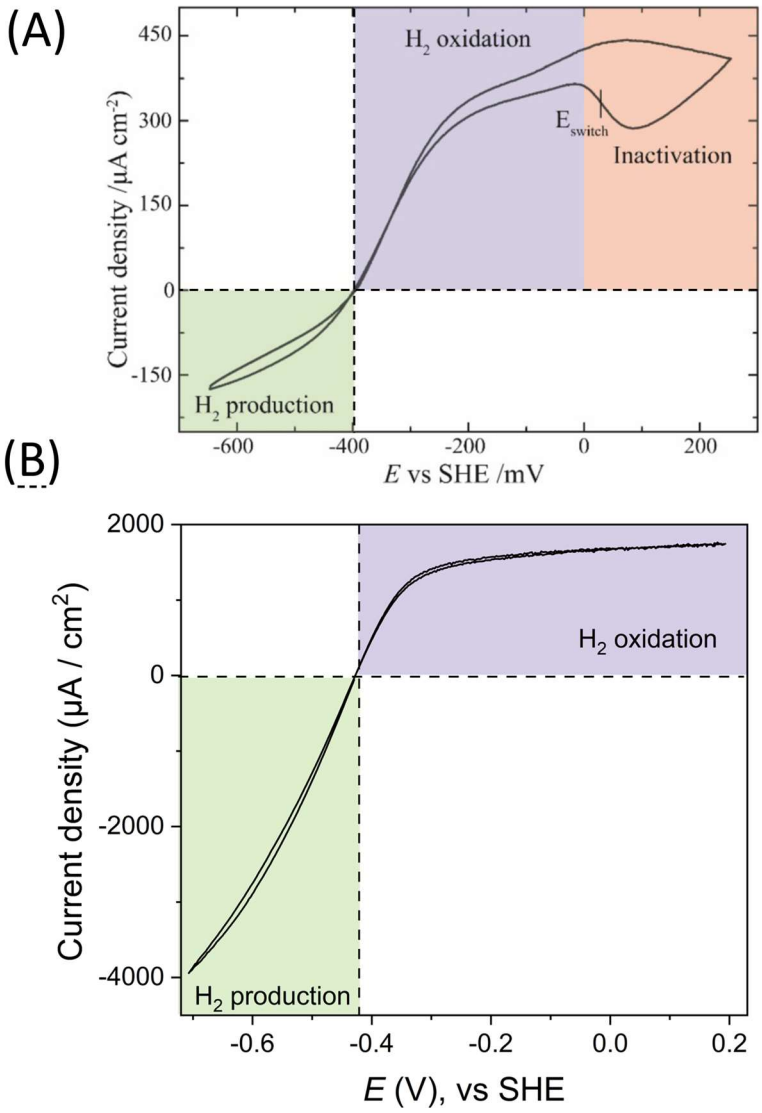


Figure 12: (A) Cyclic voltammogram (CV) of the [FeFe] hydrogenase from DdHydAB adsorbed onto a pyrolytic graphite electrode at pH 6.8, room temperature (RT), 100% H_2 (1 L/ min), 2000 rpm and 20 mV /s scan rate. The horizontal dashed line represents the zero current, and the vertical dashed line indicates the thermodynamic potential of the $2H^+/H_2$ couple under experimental conditions, figure reproduced from J. A. Birrell, K. Wrede, K. Pawlak, P. Rodriguez-Maciá, O. Rüdiger, E. J. Reijerse, W. Lubitz, Israel Journal of Chemistry 2016, 56, 852-863. © with the copy right permission.[95] (B)CV of the [FeFe] hydrogenase from CaHydA1 adsorbed onto a pyrolytic graphite electrode at pH 7.0, room temperature (RT), 100% H_2 (1 L/ min), 2000 rpm and 20 mV /s scan rate.

1.7 The aim and scope of this thesis

This DPhil project consists of mechanistic studies of [FeFe] hydrogenases, focusing on the model M3-type [FeFe] hydrogenase from *Clostridium acetobutylicum* (*Ca*HydA1). *Ca*HydA1 [FeFe] hydrogenase is one of the less studied [FeFe] hydrogenases. Its amino acid content is believed to be 70 % homologous to the well-studied *Cp*I [FeFe] hydrogenase.[96] These two [FeFe] hydrogenases exhibit higher O_2 tolerance compared to other [FeFe] hydrogenase such as *Dd*HydAB and *Cr*HydA1. *Ca*HydA1 and *Cp*I [FeFe] hydrogenases are both M3-type: they contain two additional clusters in the F-domain, so in total five FeS clusters. It has been suggested that these additional clusters (F-clusters) could facilitate electron transfer to the active site, thus when O_2 attacks and binds to the H-cluster, the F-clusters can quickly transfer two electrons to the H-cluster (together with two electrons from the H-cluster to give 4 electrons) to reduce O_2 to water and avoid the formation of reactive oxygen species (ROS). [97] [98]In addition, *Ca*HydA1 [FeFe] hydrogenase exhibits less pronounced high-potential inactivation compared to other M2-type and M1-type hydrogenases (As shown in figure 12B).[98] It will be interesting to know if the additional F-clusters influence the high-potential inactivation, and this will be investigated here. Another feature is that *Ca*HydA1 [FeFe] hydrogenase is strongly biased towards H_2 production. It has been suggested that the catalytic bias of the enzyme is directly related to the reduction potential of the most exposed FeS cluster.[99] However, it is still unclear which FeS cluster determines the catalytic bias in *Ca*HydA1, whether it is the His-ligated [4Fe-4S] cluster or the [2Fe-2S] cluster. In summary, this is a very interesting enzyme, which has a lot of potential but has been very little explored. The project combines molecular biology and biochemical, spectroscopic, electrochemical and

spectroelectrochemical methods to rationalize the role of the electron relay, i.e. the iron-sulfur (FeS) cluster cofactors, on the catalytic behaviour, the electron entry point and O_2 sensitivity of this [FeFe] hydrogenase. The overall aim is to understand the role of the FeS clusters on the active site properties, to develop design principles for the generation of new synthetic catalysts with improved catalytic properties properties such as inhibitor tolerance towards their application in H_2-driven biotechnological processes.

Chapter 3 will compare the heterologous overexpression of the *Ca*HydA1 [FeFe] hydrogenases in *E. coli* by two different methods: *1)* using an *in vivo* maturation system (i.e. maturases HydG, HydE and HydF) known in the literature[100] *2)* develop an *in vitro* maturation approach using artificial cofactors (i.e. artificial maturation). *Ca*HydA1 [FeFe] hydrogenases produced by the two different methods are compared spectroscopically and functionally. The artificial maturation system enables higher incorporation of the [2Fe] cofactor and allowed generation of high yields of very pure apo-enzyme (i.e. the protein containing the FeS cluster cofactors but lacking the active site), and enables maturation of apo-*Ca*HydA1 with various synthetic cofactors to generate a set of semi-synthetic enzymes.

In chapter 4, systematic truncations of the FeS cluster domain in the F-domain will be performed on *Ca*HydA1 [FeFe] hydrogenases generating 3 truncated variants (S75, D127 and S208). The preparation of truncated variants will be presented in detailed. Truncated variants were characterised functionally by activity assays and protein film electrochemistry to investigate the catalytic activity and characteristics of truncated variants and the effect of truncations of the FeS cluster domain on the catalytic behaviour on this enzyme. Next, truncated variants were studied spectroscopically by Infrared spectroscopy and electron

paramagnetic resonance (EPR) spectroscopy to study the electronic state of the H-cluster and potential long-range impact from truncating the FeS cluster on the H-cluster. Furthermore, activity assay of wild type (WT) and truncated variants with the physiological redox partner *Ca*Fd (ferredoxin) were performed to shine light on the binding site of the Fd on this enzyme.

Chapter 5 focuses on detailed electrochemical studies (protein film electrochemistry) on the WT and truncated variants. The catalytic bias of each variant was calculated at pH 6, 7 and 8. In all cases, the catalytic bias of truncated variants is shown to be more biased towards H_2 production compared to WT. At slow scan rate, distinguishable high-potential inactivation (HPI) previously unseen in *Ca*HydA1 [FeFe] hydrogenases can be found in its truncated variants but not in the WT enzyme. In this chapter, the inhibition of CO and O_2 in the activity of WT and truncated variants was also investigated. This provided insight into how truncating the FeS clusters domain impacts on the O_2 resistance of the enzyme as well as its affinity to bind CO.

In Chapter 6, the potential of the $[4Fe\text{-}4S]_H$ of the WT and truncated variants (maturated with PDT synthetic mimics) was determined using spectroelectrochemistry. In the PDT active site, the heterolytic splitting of H_2 is disabled as the N atom in native enzyme (ADT maturated) is replaced by C atom in PDT variant, effectively switching off the catalysis. PDT variants will only undergo one electron reduction on the $[4Fe\text{-}4S]_H$, which allows the determination the potential of the $[4Fe\text{-}4S]_H$ subcluster by plotting according to the Nernst equation.[78] FTIR and EPR suggest a new H_{ox} and H_{ox}-CO state in the wild type enzyme, which appears at more basic conditions (pH=10).

Chapter 2

Theory and Experimental Methods

Chapter 2: Theory and Experimental Methods

2.1 Molecular biology

2.1.1 Strains and plasmids

Table 1: Strains used in this thesis.

Strain	Description	Source
Top10	High efficiency cloning strain for miniprep to amplify DNA/plasmids	ThermoFisher Scientific, U.K
DH5α	High efficiency cloning strain for miniprep to amplify DNA/plasmids	ThermoFisher Scientific, U.K
Rosetta 2(DE3)	Rosetta 2 is a BL21 derivative. Specifically used for expression of eukaryotic proteins. The strain contain λDE3 carries the gene encoded for T7 RNA polymerase under control of lacUV5 promotor	Novagen, Sigma-Aldrich, U. S
BL21-A1	The strain contains a chromosomal insertion of gene encoding T7 RNA polymerase which is under control of *ara*BAD promotor. Specifically used for expression of toxic proteins.	ThermoFisher Scientific, U.K
BL21(DE3)*ΔiscR*	The strain contains a mutation to remove the genes for FeS cluster synthesis regulation. Kanamycin resistance.	Akbtar *et. al*[101] Gifted from Dr. Birrell from the University of Essex

	(UK)

Table 2: Plasmids used in this thesis.

Plasmid	Description	Source
pCaE2 and pCaFG	Ampicillin and streptomycin resistance. Plasmids for coexpression of apo-*Ca*HydA1 hydrogenase and maturases hydE, F, G	King *et.al.* [96] The plasmids were provided by Dr. S. Morra (University of Nottingham, UK).
pET-11b	Ampicillin resistance. Plasmid contains codon-optimised gene for expression of apo-*Ca*HydA1 hydrogenase Ampicillin resistance.	Merck Millipore
pET-21	Plasmid contains normal gene for expression of apo-*Ca*HydA1 hydrogenase and its truncated variants	The plasmids were provided by Dr. S. Morra (University of Nottingham, UK).

2.1.2 Cell growth and culture

Culture media

In this thesis, two types of cell culture media were used for cell growth: terrific broth (TB) and lysogeny broth (LB). The composition of TB media is consisting of 12 g/L tryptone, 24 g/L yeast

extract, 4 mL/L glycerol, 2.2 g/L KH_2PO_4, 9.4 g/L K_2HPO_4. LB media is commercially made with the composition of (10 g/L tryptone, 5 g/L yeast extract, 5 g/L NaCl). All diluted in milli-Q (ultrapure) water. All media were autoclaved to be sterile before inoculation.

LB agar plates for transformation of plasmids

LB agar plates for growing colony were made using LB media, 15 g/L agar was added before autoclaving. Different antibiotic stocks were prepared: 34 mg /mL chloramphenicol, 100 mg / mL ampicillin, 50 mg / mL kanamycin, and 50 mg / mL streptomycin. Chloramphenicol is diluted using ethanol whereas others were dissolved in Mili-Q water. The antibiotics were added at a final concentration of 1/1000 of the stock concentration.

Glycerol stocks

After successful transformation, the strains with the plasmid were stored as glycerol stocks for simpler cell growth and preservation purposes. The overnight culture containing 10 mL LB media was grown by inoculating a single colony from the agar plate supplemented with the corresponding antibiotics at 37 ^{o}C for 16 hours. Glycerol stocks are made by mixing 500 µL overnight culture with 500 µL 50 % (v/v) glycerol (Thermo Fisher Scientific) and flash frozen in liquid nitrogen and stored at – 80 ^{o}C. Plasmids can also be stored in DH5α and top10 competent cells as glycerol stocks. Glycerol stocks can be stored for many years. Old glycerol stocks can be revived by plating on a fresh LB agar plate and preparing new glycerol stocks using the method described above.

Preparation of BL21(DE3)*ΔiscR* competent cell

The BL21(DE3)*ΔiscR* stock was streaked on the agar plate supplemented with kanamycin and

placed overnight at 37 °C. 10 mL LB media was inoculated with a single colony grown on the agar plate and left shaking at 180 rpm overnight at 37 °C. This was followed by the main cell growth in 100 mL LB media until the optical density (OD) reached 0.4. The cell pellet was collected by centrifugation for 10 min at 6000 rpm, 4 °C. the supernatant was decanted, and the cell pellet was carefully suspended in 25 mL ice-cold 0.1 M $CaCl_2$. The cell suspension was incubated on ice for 30-60 min. Next, the cell pellet was collected again by centrifugation and resuspended in 5 mL of ice-cold 0.1 M $CaCl_2$, 15% (v/v) glycerol solution. The competent cell solution was separated into 50 µL aliquots which were flash frozen in liquid nitrogen, and stored at -80 °C.

Transformation of plasmid

Commercially available competent cells have their own transformation procedure, and the heat shock time would vary accordingly. For the transformation procedure for BL21(DE3)*ΔiscR* competent cells, the protocol is follows: First, 50 µL competent cell aliquot was thawed on ice for 10 min, Next, 1-2 µL of plasmid DNA was added to the competent cells, and they were incubated for 10-20 min on ice. Next, the cell-DNA mixture was heat shocked in a heat block at 42 °C for 45 seconds and was cooled down on ice for 2 minutes subsequently. Then, 1 mL of LB media was added to the transformed cell, and they were left to grow at 200 rpm, 37 °C for 1 hour. 100 µL of the grown cell was added to the prepared LB agar plate supplemented with antibiotic. Finally, the LB agar plate was incubated overnight at 37 °C. Visible colonies were typically seen in the agar plate the following day indicating a successful transformation. For the transformation procedure for DH5α competent cells for DNA amplification, the heat shock time should be 30 seconds at 42 °C.

'Miniprep', amplifying DNA

The plasmids were amplified using DH5α or Top10 competent cells. After successful transformation of plasmid to DH5α or Top10 competent cell. Overnight culture of 10 mL LB was inoculated with single colony from agar plate supplemented with antibiotics and grown overnight (16 hours) at 200 rpm, 37 ^{o}C. The next day, the cell pellet was harvested by centrifugation at 10000 ×g, 4 ^{o}C for 10 minutes. The desired plasmid was extracted from the cell pellet and purified using a Mini-prep kit (Quiagen QIAquick). Finally, the purified plasmid was dissolved in 30 µL autoclaved Mili-Q water and stored at -20 ^{o}C.

Measurement of DNA concentration

The DNA sample was diluted 50 times, and 1 µL of diluted DNA sample was then added to the NanoVue spectrophotometer (GE healthcare). The absorbance at 260 nm was measured and the concentration of the DNA sample was calculated by assuming the absorbance of 50 µg/mL dsDNA solution is 1.0 at 260 nm. Concentration of the DNA sample is typically in ng/µL.

Sequencing of DNA

The sequence of the DNA was checked by Sangar sequencing (Source Bioscience). The minimum DNA sample concentration required is 100 ng/µL.

2.1.3 Expression and purification of Protein

In the thesis, several proteins are expressed heterologously in *E. coli*. This method allows faster growth and production of protein (2-5 days) compared to native expression (2 weeks +).

More importantly, it allows production of larger amounts of protein with high purity.

Bacterial growth

Bacterial growth starts with bacterial division known as binary fission, where the bacterial cell grows and divides into two equally sized daughter cells, this process is also called cell proliferation.[102] Figure 1 shows a typical bacterial growth in culture medium. Bacterial growth can be divided into four phases: lag phase, log phase, stationary phase, and death phase.

During the lag phase, bacteria are adapting to the new conditions such as the growth media and temperature. The cell division is slow in this phase. The time length of the lag phase varies significantly. In this period, bacterial cells also synthesize RNA, enzyme and vital metabolite which could be absent form their new environment.

When the bacteria have adapted to the new conditions, they enter the log phase which is also known as the exponential growth phase. During this period, cells division occurs to be exponentially. The log of number of cells doubles in less than 30 minutes. Cells appear to be the most uniform and healthiest. Thus, when the optical density at this phase reaches 0.4-0.8 under normal growth conditions (200 rpm, 37 ^{o}C, LB media), it will be the best time to induce protein production.

In the stationary phase, cells have to adapt to the starvation condition. The cell concentration remains the same which means the growth of new cells start to be equal to the death of cells. Finally, when the nutrients in the medium have been consumed, or toxicity has developed in the medium by accumulation of by-products, the cell growth will stop, and cells will enter the death phase where the cell membrane is ruptured resulting in a decrease in cell concentration

(optical density).

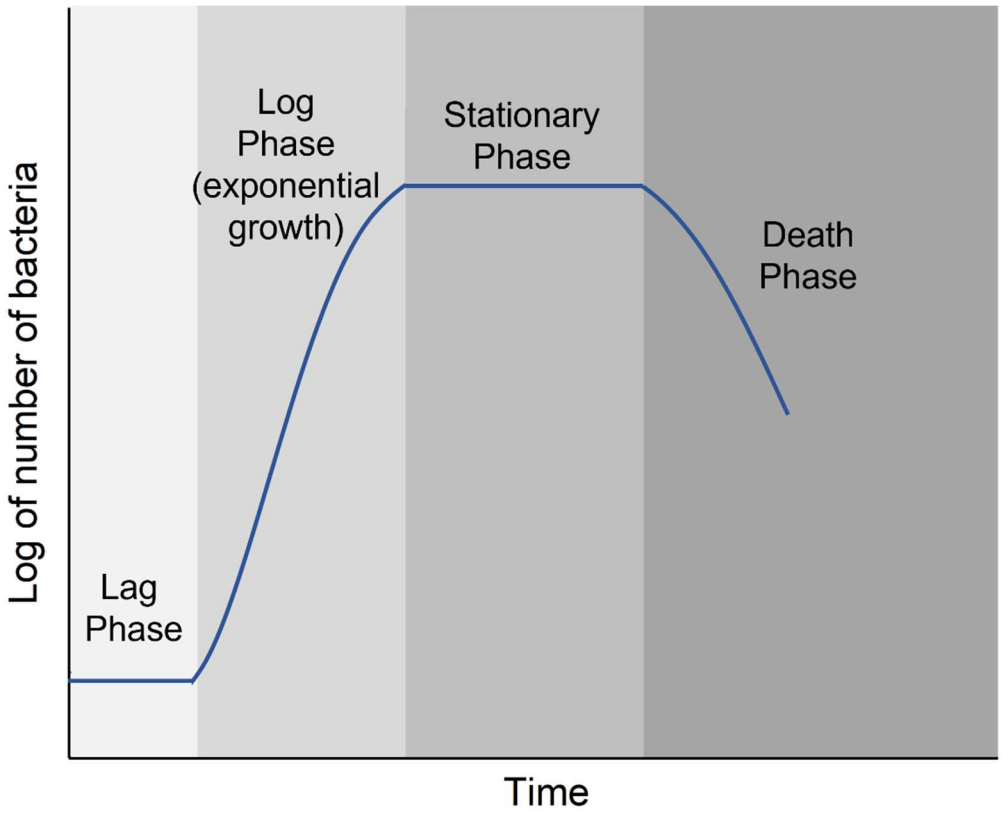


Figure 1: Graph of a typical bacterial growth curve in culture medium. The figure was made using PowerPoint.

Expression of apo-*Ca*HydA1 [FeFe] hydrogenase

A 10 mL preculture (LB media) was inoculated with a single colony from the LB-agar plate comprising BL21(DE3)*ΔiscR* cell (a strain that contains a mutation to remove the genes for FeS cluster synthesis regulation) with pET-21 plasmid incorporating the gene for apo-*Ca*HydA1 The medium supplemented with 50 µg /mL kanamycin and 100 µg /mL ampicillin. This overnight culture was left in the incubator shaking overnight (210 rpm, 37 °C). The following day, several 2 L conical flasks containing 1L LB media (20 g / L LB, 7.63 g/L K_2HPO_4, 5 g/L Na_2HPO_4) supplemented with 50 µg /mL kanamycin and 100 µg /mL ampicillin followed by 2 mM

ammonium ferric citrate (Fe Source), were inoculated with the overnight culture. The main culture media was left shaking (210 rpm, 37 ^{o}C) until OD_{600} reaches 0.4-0.8. The flasks with the culture media were cooled down in a water bath to slow down cell growth (maintain log phase). The culture was further supplemented with 0.5% w/v glucose and 2 mM cysteine (source of sulfur) and transferred to several 2L bottles and ready for deoxygenation. Next the bottle was bubbled with argon for 1 hour to keep it under anaerobic conditions for protein expression. Finally, the culture was injected with 1mM IPTG and additional 3 mM cysteine and left overnight stirring on the bench. The next day, the optical density of the media was checked and cells were harvested by centrifugation (6,500 x g, 4 °C, 30 min). The supernatant was decanted, and the pellet was stored at -80 °C ready for purification. A more detailed expression protocol is described in chapter 3.

Purification of apo-*Ca*HydA1 [FeFe] hydrogenase

The entire purification was done in the N_2-filled glove box under strictly anaerobic conditions. The pellet was thawed on ice for 30 minutes. After that, the thawed pellet was resuspended in 50 ml buffer W (100 mM Tris-HCl, 150 mM NaCl, pH 8.0) containing 30 mg of lysozyme which breaks down the cell wall of the bacteria. The cell solution after carefully suspended was lysed by sonication (Fisherbrand™ Q500 Sonicator, 2 second on and 5 second off for 15 minutes), followed by ultra-centrifugation (43,000 xg for 60 minutes) to separate the insoluble cell debris and protein containing supernatant. The supernatant was loaded to the pre-equilibrated strep-tactin superflow XT column (iba-lifesciences). The impurities were washed out by 2× column volume (CV) of buffer W. Apo-*Ca*HydA1 was obtained by eluting the column with the elution buffer containing biotin (100 mM Tris-HCl pH 8.0, 150 mM NaCl, 2.5 mM

biotin). The column can be regenerated by 2× CV of 3M $MgCl_2$ solution followed by 2× CV of buffer W.

Artificial Maturation

A 200 µM aliquot of Apo-*Ca*HydA1 [FeFe] hydrogenase (containing [4Fe-4S] cluster but lacking the $[2Fe]_H$ cluster) was incubated with 600 µM $[2Fe]^{adt}$ (three times excess) at 300 rpm, 15 °C overnight (>16 hours). On the following day, the maturated protein was loaded to a pre-equilibrated PD-10 column (desalting column) and washed with buffer (20 mM Tris-HCl 25 mM NaCl pH 8.0) to separate the excess unbound $[2Fe]^{adt}$ and elute the protein desired. The protein was further shaken at 300 rpm, 15 °C overnight (>16 hours) to release the CO bound to the maturated protein from the maturation process.

SDS-PAGE for protein separation and purity test

SDS-PAGE (sodium dodecyl sulfate polyacrylamide gel electrophoresis) is an analytical electrophoresis method that allows protein separation with different molecular masses between 5-250 kDa.[103] This method allows elimination of the influence due to structure and charge, and to separate the proteins solely based on their difference in molecular weights. SDS behaves as a surfactant, covering the intrinsic charge of the protein and conferring them with very similar charge-to-mass ratios. SDS carries negative charge, thus making the peptide chain negative. Upon applying constant electric field, proteins migrate towards to the anode. The larger the size of the protein, the more negative charges it will carry, and therefore the migration speed will be slower. Hence, this allows precise separation of proteins.

The protocol was followed: 20 µL protein was mixed with 20 µL loading buffer containing SDS

and DTT (Dithiothreitol, mild reducing agent to reduce disulfide bonds of proteins). Next the sample was denatured at 95 °C for 3 minutes. A 5-10 µL aliquot of sample was loaded onto the commercial SDS gel (Tris-glycine, Invitrogen), a pre-stained protein ladder (NEB) was also loaded as an indicator for molecular weights. The gel was electrophoresed at 220 V, 100 mA, 45 minutes in 1x Tris-Glycine Buffer. Finally, the gel was stained using instant blue (Expedeon) for 30 minutes, so that visible bands from the samples would be seen.

Table 3 Buffers for SDS-PAGE.

Buffer	Composition details
2x SDS-PAGE loading dye	4% SDS, 20% glycerol, 200 mM DTT, 0.01% bromo-phenol blue and 0.1 M Tris HCl, pH 6.8
5x SDS running buffer (1L Tris-Glycine Buffer)	15 g Tris-HCl, 72 g Glycine, 5 g SDS, pH 8.3

Bradford assay

The protein concentrations in this thesis were determined by Bradford assay. The Bradford assay is a colorimetric protein assay which follows the absorbance change at 595 nm of the Coomassie brilliant blue G-250 dye. Coomassie brilliant blue G-250 dye binds to the protein through the protein's carboxyl group via Van der Waals Forces and to the amino groups by electrostatic interactions, which causes a shift of colour from red to blue. [104] In order to determine the unknown concentration of a protein, one must use different concentrations of

BSA (Bovine Serum Albumin) as standards to plot a standard curve (absorbance at 595 nm against BSA concentration).[105]

The following protocol was used: several concentrations of BSA stock solutions were prepared (0-2000 μg/mL). The protein with unknown concentration was estimated and diluted 40×, 80×, and 160× (or accordingly lies in the region of 0-2000 μg/mL). 10 μL of three diluted samples and standards were loaded to the centre of the wells of a 96-well plate (Fisherbrand™); a triplicate of each sample was used to have a better estimation. Then, 300 μL of Bradford assay reagent was added to sample containing wells. The sample-Bradford assay reagent mixture was incubated for 15 minutes, before the absorbance of each sample was determined by UV-Vis. The protein concentration was determined by comparing to the standard curve, taking the average of the three triplicate points to calculate the error.

2.1.4 Hydrogenases solution activity assays

The solution activity assays of hydrogenases can be measured using an *in vitro* redox partner such as methyl viologen (MV) or physiological redox partner (For *Ca*HydA1 [FeFe] hydrogenase, this is *C. acetobutylicum* ferredoxin CAC0303 (*Ca*Fd)) to quantify the turnover frequencies. Both H_2 oxidation and evolution activities of [FeFe] hydrogenase were measured in 100 mM Tris-HCl, 150 mM NaCl, pH 8 buffer at 37 ^{o}C. For the activity assays for H_2 oxidation rate, methyl viologen or *Ca*Fd were used as electron acceptor. Briefly, the reduction of 10 mM MV or 30 μM *Ca*Fd by 1 nM enzyme in H_2 saturating buffer can be measured by UV-Vis spectroscopy. The absorbance of methyl viologen was followed at 604 nm (ε_{604} = 13.6 mM $^{-1}$ cm $^{-1}$) and *Ca*Fd

was followed at ε_{390} = 32.6 mM^{-1} cm^{-1} for 1 minute, the rates could be calculated by measuring the gradient. For the activity assays for H_2 evolution rate, the evolution of H_2 is monitored by gas chromatography (Agilent 7820A, purged packed inlet, Supelco Carboxen-1010 column, thermal conductivity detector, argon carrier gas) using either 10 mM reduced MV or 30 µM reduced *Ca*Fd as electron donor. The solution activity assay experiments were performed by collaborator Dr. Simone Morra at the University of Nottingham.

2.2 Electrochemistry

Electrochemistry studies the chemical changes as a result of the movement of electric charges (i.e. electric current) and the chemical reactions driven by the electrical potential difference. Thus, electrochemistry is often employed to study the thermodynamics and kinetics of electron transfers processes in redox active metalloenzymes.[106] [107] [108] In this thesis, electrochemistry will be applied to study the catalytic behaviour of [FeFe] hydrogenases.

2.2.1 Proton-Coupled Electron transfer

Proton-coupled electron transfer (PCET), which involves the transfer of electron and protons together, is important for numerous energy conversion processes, such as the oxidation and production of molecular hydrogen.[109] [110] [111] In nature, electron transfer is mediated by FeS clusters present in the hydrogenases and this is accompanied by proton transfers within the active site region of hydrogenases. There are two possible routes for proton/electron transfer:

1) the electron and proton are transferred in a stepwise manner; 2) the electron and proton are transferred in a concerted manner (PCET). Figure 2 shows these two possible routes.

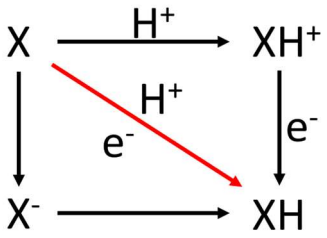


Figure 2: Two possible routes for electron/proton transfer: stepwise (Black arrow), concerted (PCET) (red arrow).

In an ideal situation, the concerted PCET reaction allows a considerably lower activation barrier.[112] Figure 3 shows that the energetic advantage of PCET compared to uncoupled proton and ET steps.

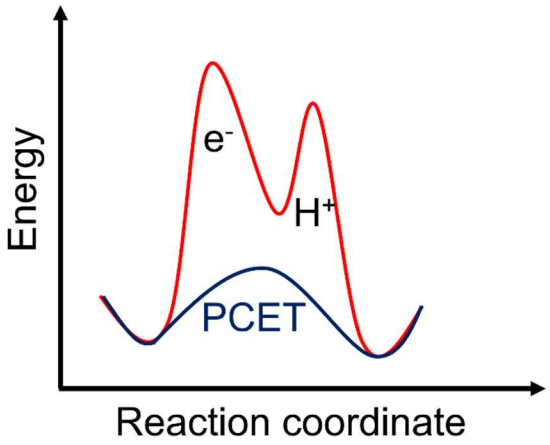


Figure 3: The reaction scheme of the energetic advantage of PCET compared to uncoupled proton and ET steps.[112]

2.2.2 The three-electrode system

In theory, electrochemistry can operate with only two electrodes (working electrode and counter electrode). However, in practice, it is hard to maintain a constant potential as large current passing through the counter electrode will alter its potential. In order to separate the role of monitoring and controlling the potential applied at the working electrode from balancing the current produced, a third electrode is required, termed a reference electrode.

The three-electrode system consists of a working electrode (WE), counter electrode (CE), and reference electrode (RE). Figure 3 shows the scheme of the circuit for a three-electrode system. The working electrode is where the redox processes of interest take place. The role of counter electrode is a current source collector to balance the current observed at the working electrode. The ammeter A is located between the working electrode and counter electrode measuring the current flow between these electrodes. The reference electrode's role is to act as a reference in controlling the potential of working electrode, with only a small current passed because the voltmeter V possesses a high input resistance. In a three-electrode system, the reference potential is much more stable. A reference electrode should have a fixed and known potential. Examples or reference electrodes commonly used in the lab are the Saturated Calomel Electrode (SCE) and the Ag/AgCl electrode.

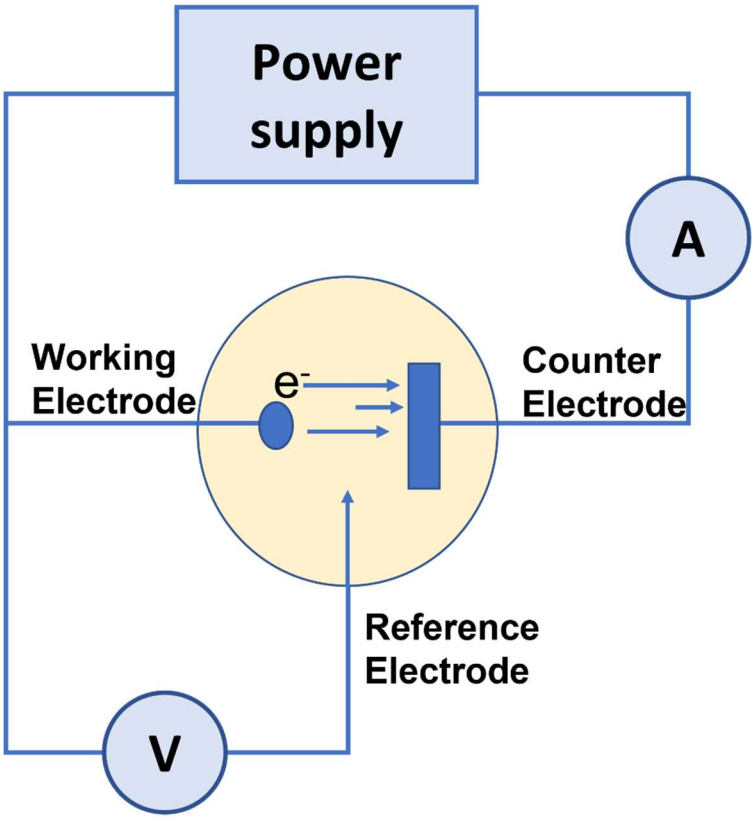


Figure 3: The scheme of the circuit for a three-electrode system consisting of working electrode (WE), counter electrode (CE), reference electrode (RE), ammeter (A) and voltmeter (V). The figure was made in PowerPoint.[107]

Cyclic voltammetry

Figure 4A illustrates how the applied potential in a cyclic voltammetry (CV) experiment is controlled. In a CV experiment, the applied potential on the working electrode is swept back and forth between two potentials, E_1 and E_2. (i.e., the potential will sweep back in the opposite direction to return to the original potential). These cycles can be repeated as many times as needed. The current flow through the working electrode can be plotted against the applied voltage to generate a trace of CV. Figure 4B shows an example of CV of $[Fe(CN)_6]^{3-}$. The CV of $[Fe(CN)_6]^{3-}$ displays a reversible CV wave, and the half-wave potential (redox potential) can be derived from the following equation (midpoint of the positive and negative peak potentials):

$$E_{1/2} = \frac{E_{p,a} + E_{p,c}}{2}$$

Where 'a' denotes the anodic peak (oxidation) and 'c' denotes the cathodic peak (reduction).

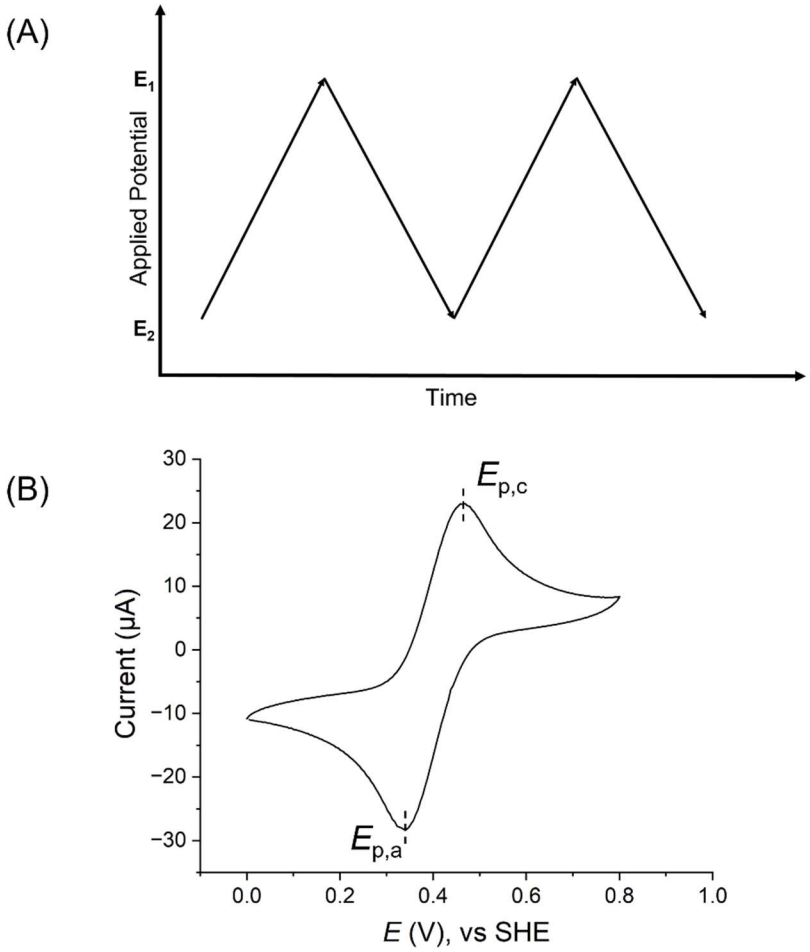


Figure 4: (A) Potential sweep between E_1 and E_2 potential in a cyclic voltammetry experiment representing the cyclic voltammetry waveform. (B) The CV of $[Fe(CN)_6]^{3-}$, Scan rate: 20 mV/s. Figure 4A was made in PowerPoint.

Chronoamperometry

Chronoamperometry (CA) experiments allow investigation of the effect of substrate concentration, potential inactivation and inhibitors on the catalytic activity in the case of redox

enzymes. In CA experiments, the applied potential is poised at a specific value for a period of time, in which the current at the working electrode is continuously measured. Figure 5 illustrated how the potential is stepped and the catalytic reductive current of a redox enzyme would respond to the applied potential as well as the investigation on the effect of addition of inhibitor on the enzyme's catalytic activity in a CA experiment.

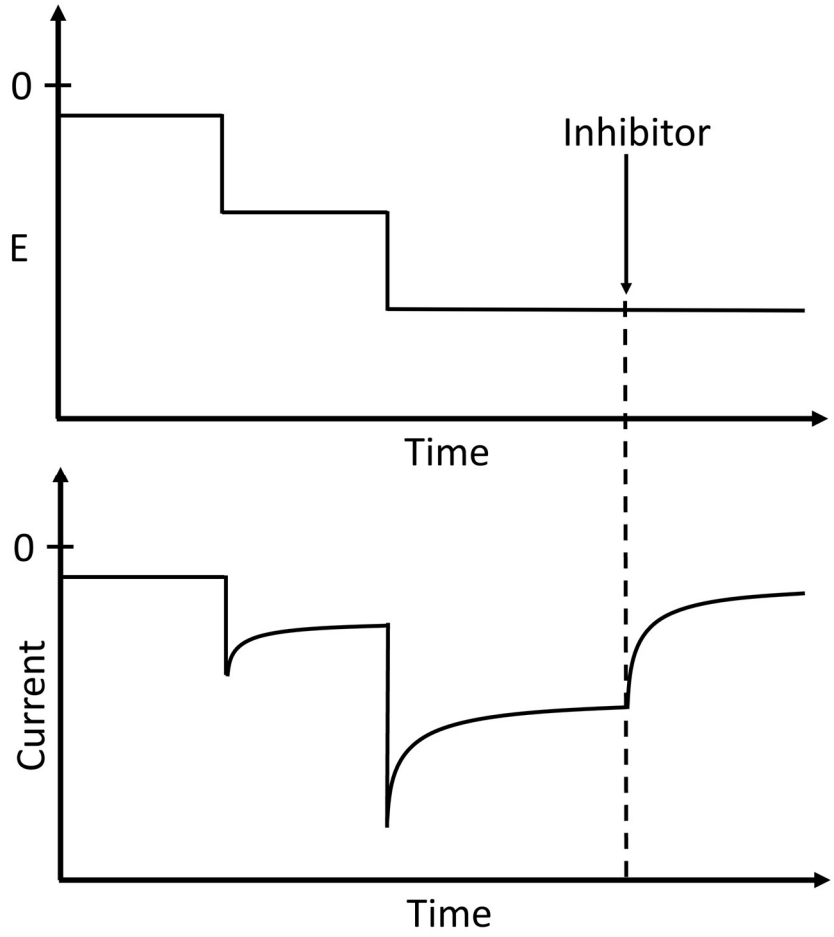


Figure 5: (A) Potential (E) poised and stepped over time in a CA experiment. The arrow represents the time point the inhibitor is added. (B) Current against time, the current measured changes with the applied potential and the loss of enzymatic reductive activity after addition of inhibitor. The figure was made using PowerPoint.

2.2.3 Protein film electrochemistry

Protein film electrochemistry (PFE) allows dynamic study of the catalytic behavior of a redox enzyme which is immobilised (either directly absorbed or covalently attached) to the surface of the electrode. The electrode acts as the redox partner for the enzyme (electron doner or accepter).[113] There are several advantages of using the PFE technique. Firstly, the electron transfer is not limited by protein diffusion to the electrode, making it possible to gain thermodynamic and kinetic information about the enzyme quantitatively in real time. Secondly, little sample is required for each PFE experiment. [114] Thirdly, PFE enables fast and direct control of the electrode potential, and this enables investigation of hydrogenases containing numerous redox active states and inactive states that are sensitive to the change of potential.

Figure 6 shows the electrochemical setup for PFE. To study O_2-sensitive [FeFe] hydrogenases, PFE experiments were carried out in anaerobic conditions in a N_2-filled glovebox (Belle Technology). The electrochemical measurements were run using an Autolab potentiostat (PGSTAT128N) controlled by Nova software (Metrohm Autolab). The temperature of the experiment was controlled by water flow in and out of a jacket around the cell, and was set to 25 ^oC for PFE experiments. Gas mixtures could be controlled by mass flow controllers (Sierra Instruments). In the case of PFE experiments with [FeFe] hydrogenases, 100 % H_2 (1 L/min) was used. The three-electrode system was used for PFE for various reasons discussed before. The Platinum wire (Surepure chemetals, 99.95 %, 0.4 mm diameter) was used as counter electrode and was submerged into the buffer solution. A SCE electrode was employed as reference electrode submerged in 0.1 M NaCl solution which was separated from the main

cell but still connected via Luggin capillary. The reference electrode potential was checked to determine any offset and working electrode was a pyrolytic graphite edge (PGE) rotating disk electrode. The PGE electrode was polished by sandpaper, and then 2 µL of protein sample was added to the PGE surface, and allowed to partially dry for 5 minutes. In the meantime, the main cell was filled with buffer (mixed buffer). The enzyme modified PGE electrode was submerged into the buffer and rotated at a constant speed (ω = 1000–3000 rpm). A CV experiment was then run to check the correct connection of the electrical circuit.

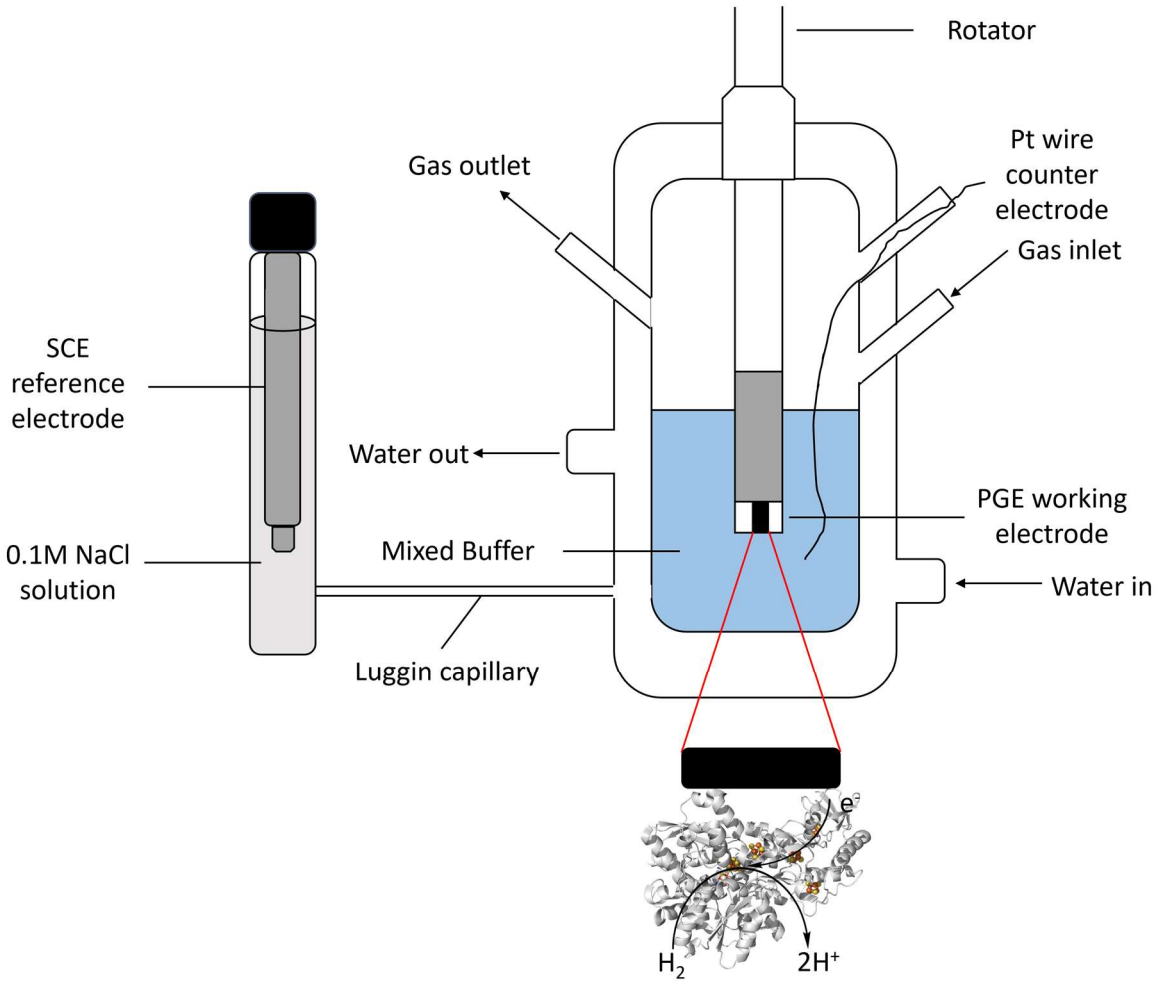


Figure 6: Protein film electrochemistry set up consisting of a three-electrode system: PGE working

electrode, a platinum counter electrode and the SCE reference electrode submerged in 0.1 M NaCl separated from the main electrochemical cell. The mixed buffer was prepared containing 15 mM MES, HEPES, TAPS, CHES, sodium acetate and 0.1 M NaCl. The figure was made in PowerPoint.

In the context of redox enzyme, the electric current recorded is proportional to the enzymatic catalytic activity. k_{cat} is the turnover frequency of the enzyme with respect to the electrode potential. F is the Faraday constant (96485 C/mol), A is the area of the electrode in cm^2.[115]

$$i = nFA\Gamma k_{cat}$$

Where Γ is the electrode surface coverage of the redox enzyme in mol/cm^2.

The electrode surface coverage of the redox enzyme can be calculated by measuring the non-turnover signals, following the equation:

$$\Gamma = \frac{S}{nFAv}$$

Where S is the area under the peak of the on non-turnover signal (cm^2), v is the scan rate (V/s).

Figure 7A shows the reversible catalysis of *Ca*HydA1 [FeFe] hydrogenase and the enzyme is biased towards H_2 production and shows an efficient catalysis as no overpotential is introduced. Comparison of reversible (Blue trace) and irreversible catalysis (Red trace) is shown in figure 7B. No overpotential is introduced in the reversible system (it operates very close to the thermodynamic potential, thus very efficient). In contrast, the irreversible system does require extra energy to start the reaction introducing overpotential.

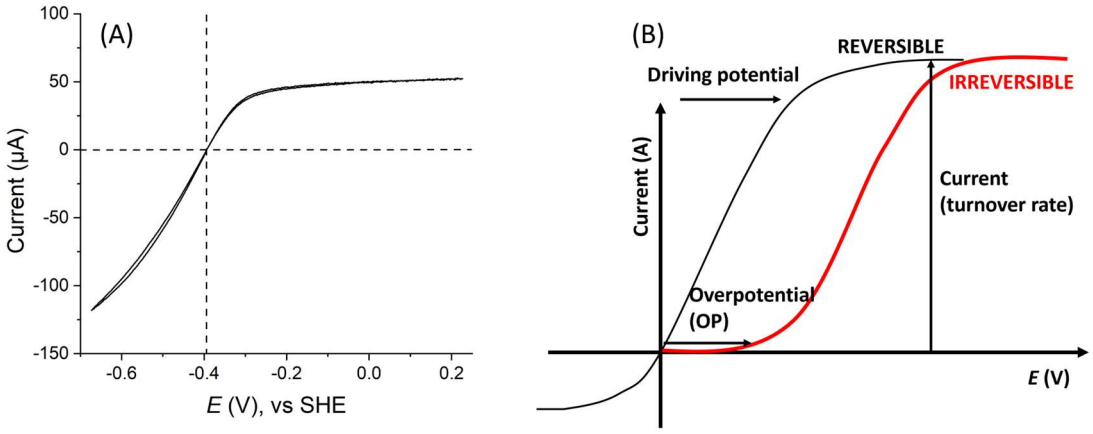


Figure 7: (A) CV of *Ca*HydA1 [FeFe] hydrogenase adsorbed onto a pyrolytic graphite electrode at pH 7, room temperature (RT), 100% H_2 (1 L/ min), 2000 rpm and 20 mV /s scan rate. The horizontal dashed line represents the zero current, and the vertical dashed line indicates the thermodynamic potential of the $2H^+/H_2$ couple corrected for the experimental conditions. (B) Schematic representation of reversible and irreversible catalysis showing overpotential. The figure 7B was adapted from reference [116] [27-62] in PowerPoint.

2.3 Infrared spectroscopy

2.3.1 Theory of infrared spectroscopy

Infrared (IR) spectroscopy is commonly used to study the vibrations in a molecule as a result of the interaction with IR radiation. When a molecule absorbs the IR radiation, an oscillating electric dipole is created that triggers bonds vibrations within the molecule. Fourier-transform infrared spectroscopy (FTIR) allows the generation of actual spectra from raw data (recorded as an interferogram) by Fourier transformation (a mathematical process).[117] There are numerous vibrational modes in a sample when it interacts with IR radiation. In order to be IR-active, the selection rule requires a change in the dipole moment. Figure 8 shows two typical

vibrational modes in a water molecule: stretching (change of bond length) and bending (change of bond angle).

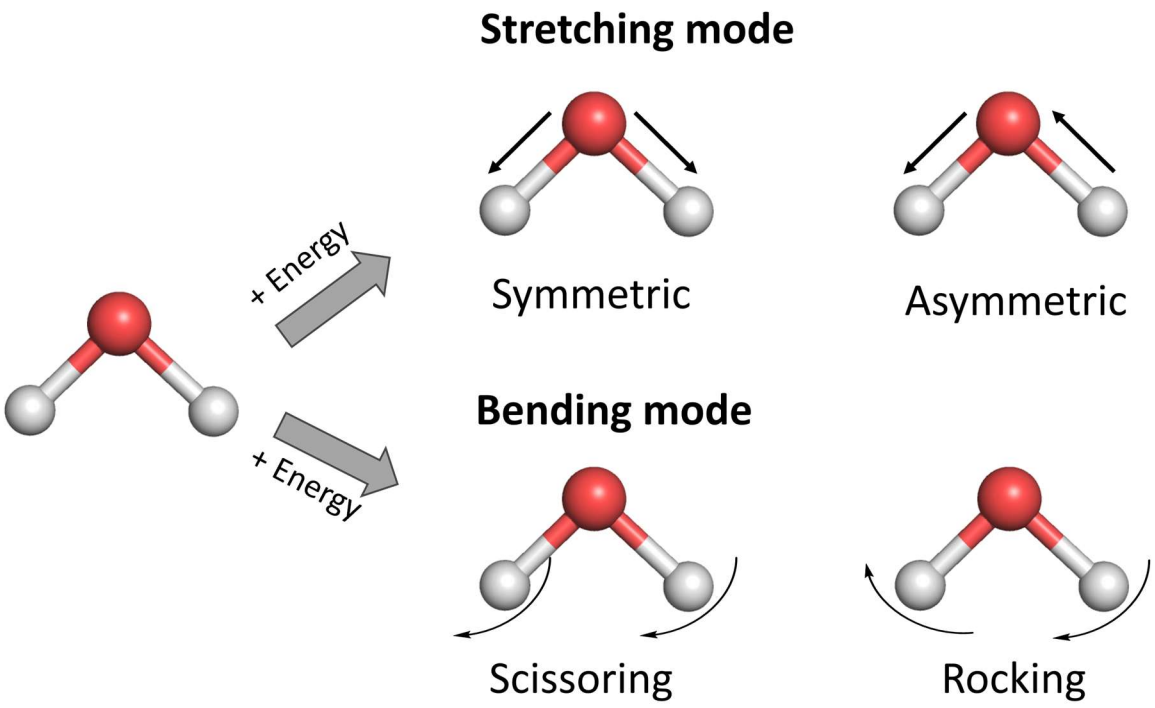


Figure 8: IR vibrational modes in a water molecule showing symmetric and asymmetric stretching vibrations as well as scissoring and rocking bending vibrations. The figure was adapted from reference [27] made using PowerPoint.

2.3.2 Infrared spectroscopy applied to hydrogenases

IR spectroscopy is able to identify common functional groups in inorganic chemistry such as strong field CO and CN^- ligands. Therefore, IR spectroscopy is a very useful technique to study hydrogenases as the active site contains CO and CN^- ligands. The strong field ligands CO and CN^- keep the iron core of the hydrogenase in a low spin state and low oxidation state. Importantly, protonation of the side chain and change of oxidation state on the metal centre can be sensed by a subtle shift in the CO and CN^- vibrational bands in IR spectroscopy. Thus, IR spectroscopy provides important information for the mechanistic study of hydrogenases.

In hydrogenase, the ν_{CO} stretching absorption bands lie in the region 2050-1750 cm^{-1}. In contrast, the ν_{CN} bands lie in the region 2200-2000 cm^{-1}. CO is a better π-accepter and poorer σ-donor compared to CN^-, greater π-back bonding to the anti-bonding orbital of the CO weakening the C≡O bonding, vice versa for CN^- ligand.[117] In addition, the frequency is proportional to $1/\sqrt{\mu}$, where μ is the reduced mass ($\frac{M_1 M_2}{M_1+M_2}$), μ is larger for CO than CN, thus ν_{CO} stretching bands is always smaller than ν_{CN} bands.

In [FeFe] hydrogenases, each state in the catalytic cycle consists of five bands shown in figure 9. Three bands are originated from the CO ligands, ν_{CO} stretch lies in the lower wavenumber region of 2050-1750 cm^{-1}. The bridging CO appears at even lower wavenumber at around 1800 cm^{-1} for H_{ox} state as greater π-back bonding from two iron atoms to the anti-bonding orbital of the CO further weakens the C≡O bonding. Another two bands are originated from the CN ligands, with the ν_{CN} stretch at the higher wavenumber in the region of 2200-2000 cm^{-1}. In reduced states, the electron density increases in the active site resulting in more π-back bonding from the iron atoms to the anti-bonding orbital of the CO, further weakening the C≡O bonding.

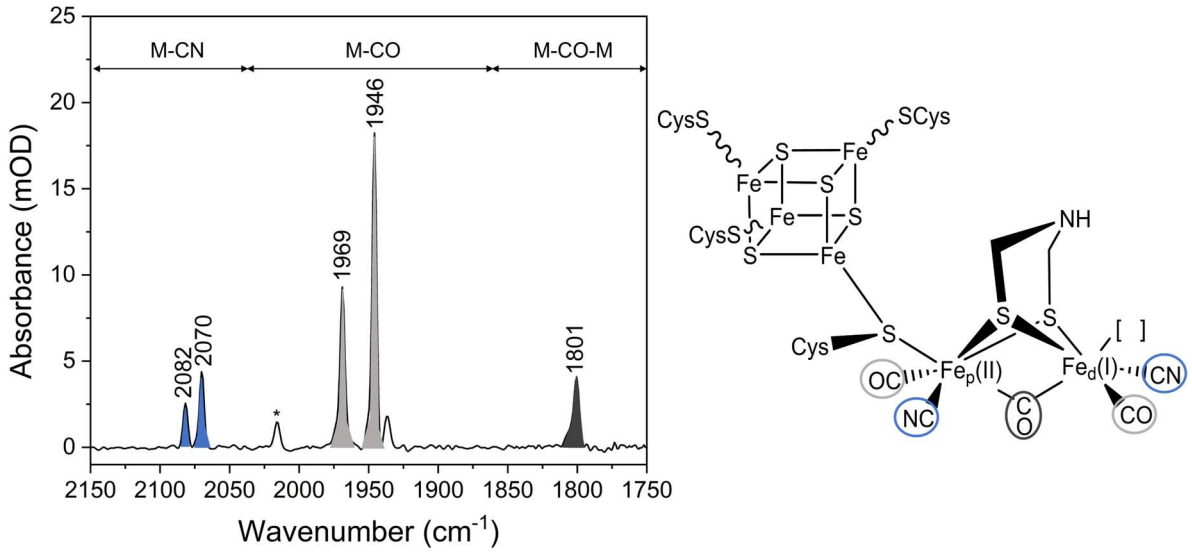


Figure 9: IR spectrum of H_{ox} state of *Ca*HydA1 [FeFe] hydrogenase, the structure of the H_{ox} state of the active site is shown on the right. The CN peaks are highlighted in blue, CO peaks are highlighted in grey and bridging CO peak is highlighted in black. *represents a small proportion of H_{ox}-CO state.

2.3.2 IR spectroeletrochemistry

IR spectroeletrochemistry is often applied to hydrogenases to explore the catalytic intermediate states, in which the potential can be poised at different values while IR spectra can be measured. This requires a specialised IR Spectro-electrochemical cell (SEC): The reflection-absorption cell was built in-house and involves a three-electrode system (1 mm diameter glassy carbon working electrode (WE) surrounded by a platinum counter electrode (CE) ring, and a commercial Ag/AgCl reference electrode (RE)). The IR light reflects off the polished glassy carbon and passes to the detector. The protein crystals/solution was mixed with approximately 10 µL crystallisation buffer containing 1 mM redox mediator cocktail, and then loaded onto the glassy carbon working electrode (WE) anaerobically. The three electrodes were covered with buffer to make electrochemical connection and a 25 µm spacer was added to maintain a stable thin layer thickness in the cell. The important role of the

mediator cocktail is to facilitate electron transfer. A cocktail of mediators is chosen covering the range of relevant potentials, -600 to +300 mV vs Standard Hydrogen Electrode (SHE). Figure 10 illustrates the setup of the IR Spectro-electrochemical cell (SEC).

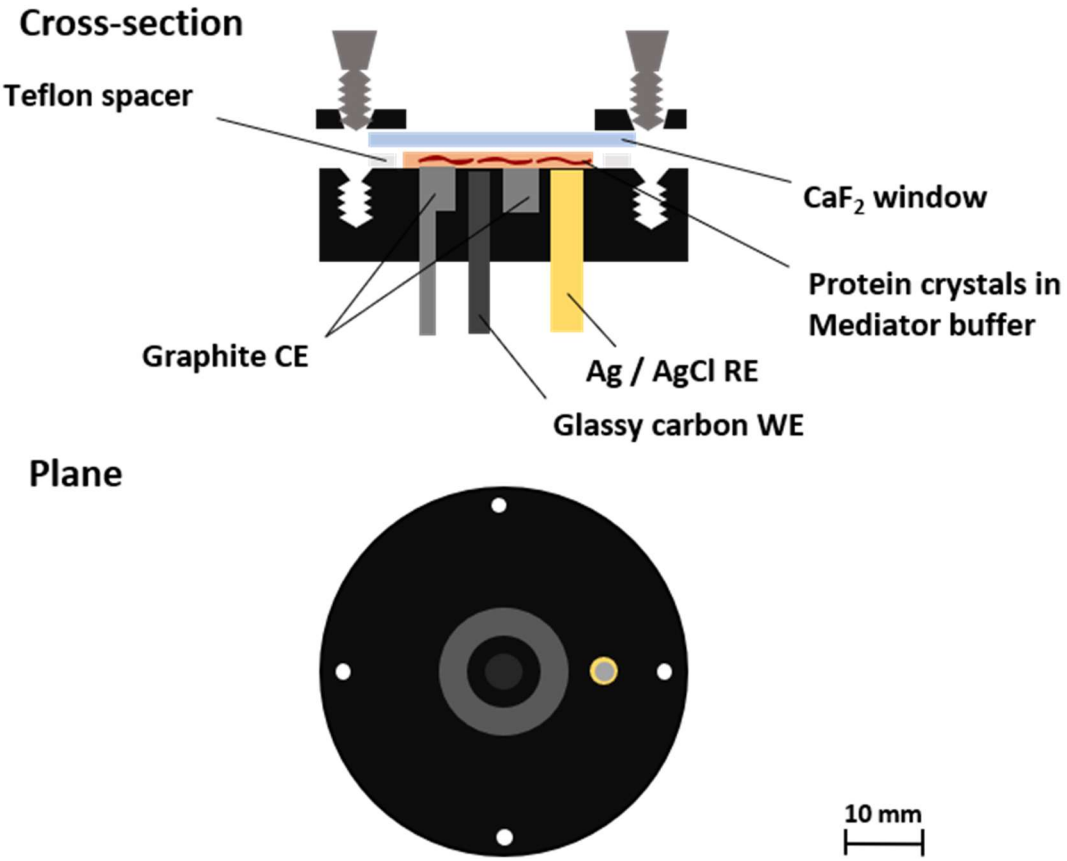


Figure 10: The setup of the IR Spectro-electrochemical cell (SEC) used for studying protein crystals or hydrogenases in solution. The figure was made in PowerPoint, adapted from reference.[118]

2.4 Electronic paramagnetic resonance (EPR)

2.4.1 Theory of electron paramagnetic resonance (EPR) spectroscopy

EPR spectroscopy is a technique used to study the unpaired electrons of species (paramagnetic states). As a result of the Zeeman effect, energy levels of the spins split into several components in the presence of an external magnetic field. In the absence of the external magnetic field (B_0), the energy levels are degenerate. In the presence of the external magnetic field (B_0), the energy levels split (electron Zeeman splitting) so that the electrons' magnetic moment orients itself in either parallel ($m_s = +\frac{1}{2}$) or antiparallel ($m_s = -\frac{1}{2}$) fashion as regards to the applied magnetic field (Figure 11). The difference between the energy levels is proportional to the external magnetic field (B_0). The transitions between energy levels stimulated by microwave radiation can then be excited by absorbance of a photon. This process is also known as resonance. In continuous wave electronic paramagnetic resonance (CW-EPR), the microwave frequency is maintained at the same value while sweeping the external magnetic field until the resonance condition is accomplished. The separation of upper state and lower state energy can be described by:

$$\Delta E = hv = g_e \mu_B B_0$$

Where h is the Planck's constant (6.6×10^{-34} J·s); v is the frequency; g_e is the so called g-factor, which is dimensionless and describes the proportionality of the resonance energy as regards to B_0. The g value for the free electron is 2.0023;[119] μ_B is the Bohr magneton (9.27x10 -24 J/T) and B_0 is the applied magnetic field.

Figure 11(B) shows the simulated EPR absorption spectrum fulfilling resonance conditions, and the typical first derivative of the EPR absorption spectrum, which is commonly used to report CW-EPR.

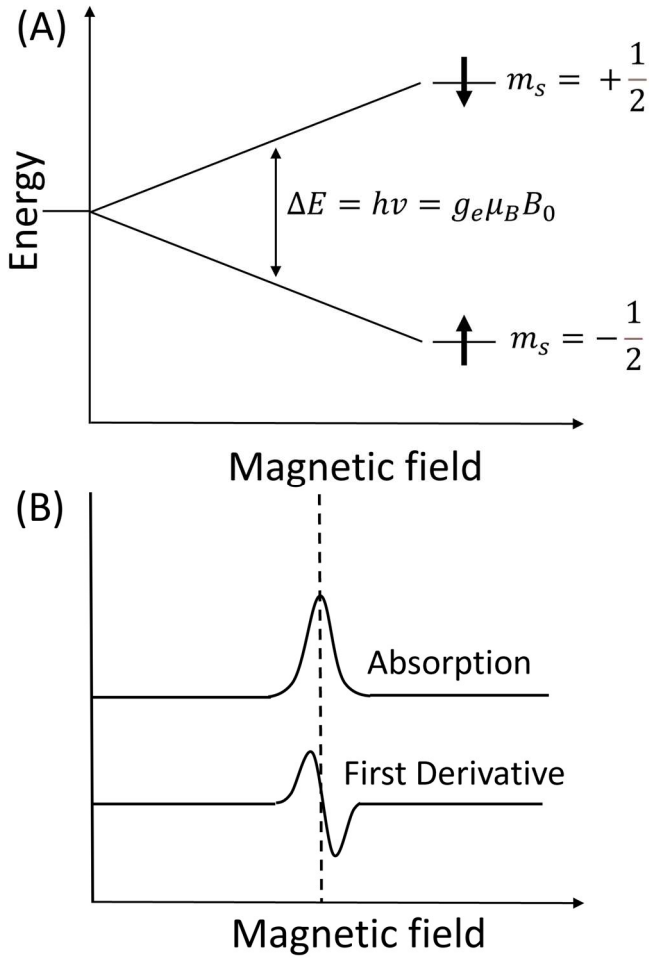


Figure 11: (A)Electron Zeeman splitting for electron spin *S*=1/2 system under an external magnetic field (B_0). (B) simulated EPR absorption spectrum fulfilling resonance conditions, and First derivative of the EPR absorption spectrum. The figure was adapted from reference [27] using PowerPoint.

2.4.2 EPR spectroscopy of metalloproteins

EPR spectroscopy of FeS cluster containing metalloproteins requires the protein sample solution to be frozen in solution (due to their relaxation times) in which the molecules are randomly oriented. The EPR spectrum of a metalloprotein captures superposition of spectra of all orientations of the molecules; each paramagnetic species will carry its own g-factor. Based on the symmetry of the spin system, there are three forms can be detected in EPR-spectra: isotropic (having all g-values identical, $g_1 = g_2 = g_3$), axial when having two anisotropic signals (two of the g-values identical, $g_1 \neq g_2 = g_3$) and rhombic (all g-values different, $g_1 \neq g_2 \neq g_3$). In metalloproteins such as hydrogenases, signals originating from the FeS-clusters present are commonly found to be in axial or rhombic forms as the unpaired electrons are present in the molecular orbitals that are non-spherical. Figure 12 (A),(B) shows the typical rhombic and isotropic signal respectively.

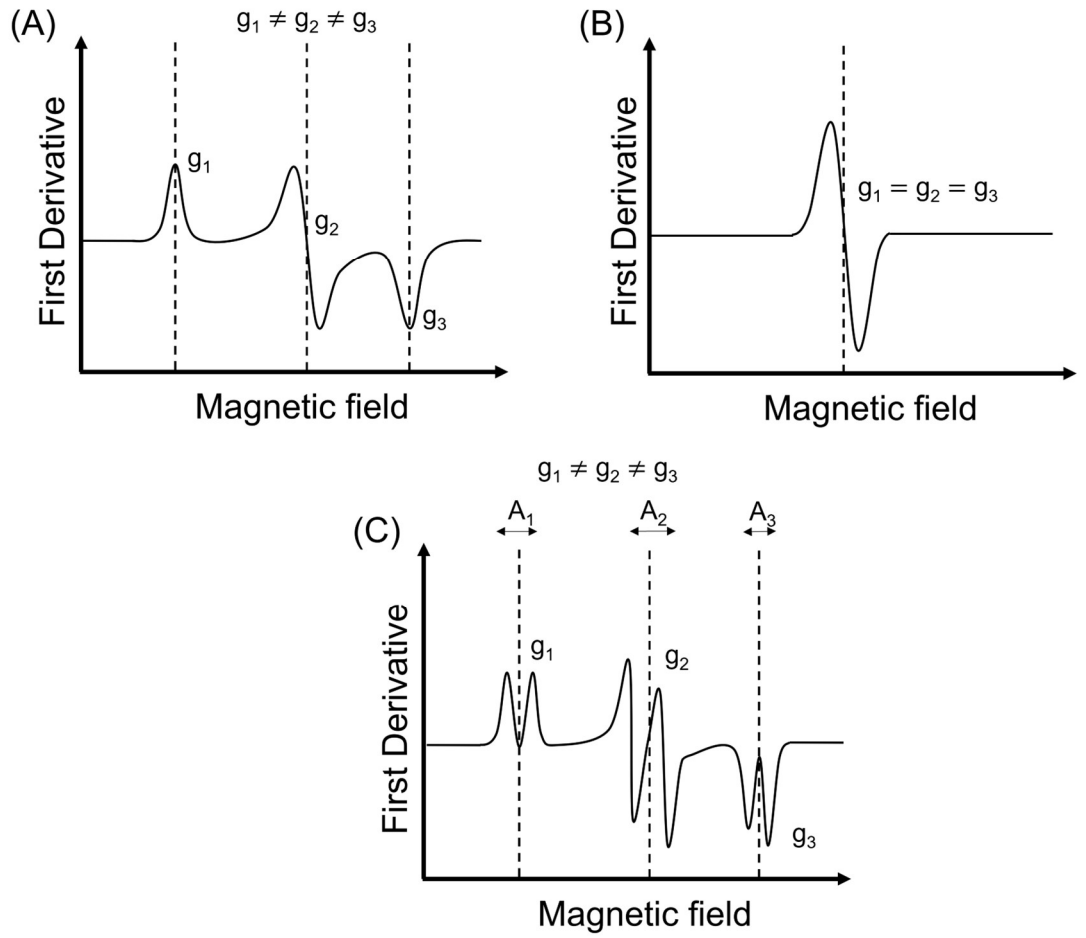


Figure 12: (A) First derivative EPR absorption spectrum of a typical rhombic signal (B) First derivative EPR absorption spectrum of a typical isotropic signal. (C) First derivative EPR absorption spectrum of a rhombic signal with hyperfine splitting. The figure is adapted from reference[27] made using PowerPoint.

Figure 12 (C) shows a rhombic signal with hyperfine splitting ($I = \frac{1}{2}$ nucleus). The hyperfine splitting further splits the energy levels due to coupling of unpaired electrons with nearby nucleus. The hyperfine interactions can be better studied with more than one microwave frequency as they are independent of the magnetic field strength frequencies. X band, Q band and W band are the most commonly used frequency bands at 9.5, 34 and 95GHz respectively in EPR spectroscopy.

In [FeFe] hydrogenases, there are many active site states that are EPR active in the catalytic cycle: H_{ox}, H_{ox}-CO, $H_{sred}H^+$, H_{hyd} and H_{trans}. EPR spectroscopy is a technique which aids interpretation of the FTIR spectroscopy to probe the mechanism of the catalytic cycle as it could sense the electronic environment close to the active site as well as identifying different oxidation states or catalytic states, etc. In addition, hyperfine splitting can be observed in [FeFe] hydrogenases, which can be resolved by electron nuclear double resonance (ENDOR) and hyperfine sublevel correlation (HYSCORE) providing information of the interactions of the unpaired electrons with nearby nucleus or electrons and coupling between the clusters and binuclear site. [120]

2.5 UV-Vis spectroscopy

UV-visible (UV-Vis) spectroscopy is used to study the absorbance spectra of compounds solution or can directly measure semi-transparent solids. The majority of molecules or ions absorb energy in the UV-Vis region (termed chromophores), in which the electrons are excited to higher energy orbitals (ground state to the first singlet excited state). The absorbance spectroscopy can be described by the Beer-Lambert Law:

$$A = \varepsilon CL$$

Where A is the absorbance; ε is the molar extinction coefficient (M^{-1} cm^{-1}); L is the path length of the cuvette (commonly 1 cm).

In cell biology, UV-Vis spectroscopy can be used to quantify nucleic acids to determine average

concentration of DNA or RNA in samples via absorbance at 260 nm (as described in section 2.1.2). Sample purity can be deduced by measuring A260:A280 ratios as protein could be present as a contaminant for DNA sample (aromatic amino acid residues in proteins absorbs at 280 nm). In protein samples, amino acid residues such as tryptophan, tyrosine and phenylalanine absorb at 280 nm. Protein concentration can be estimated by Bradford assay based on UV-Vis spectroscopy (as described in section 2.1.3). Many FeS clusters-containing metalloproteins such as [FeFe] hydrogenases are weakly coloured (brown). Typical absorbance bands for FeS clusters arise between 300-600 nm due to ligand metal charge transfer (LMCT). The absorption band for $[4Fe\text{-}4S]^{2+}$ clusters can be found around 410 nm.[121]

Chapter 3

Development of a heterologous overexpression system for apo-CaHydA1 [FeFe] hydrogenase and in vitro maturation with synthetic cofactors

Chapter 3: Development of a heterologous overexpression system for apo-CaHydA1 [FeFe] hydrogenase and in vitro maturation with synthetic cofactors

3.1 Introduction and aim of this chapter

3.1.1 Classification of [FeFe] hydrogenases

All [FeFe] hydrogenases feature an H-domain, and most also harbour additional accessory FeS clusters known as F-clusters. F-clusters function as an electron relay, enabling electron transfer between the buried H-cluster and the protein surface, and are believed to have long-range impacts on the catalytic behaviour. Based on Meyer's classification of [FeFe] hydrogenases[48] (see Figure 1), these enzymes are divided into three main types. The simplest form, the M1-type, consists solely of the catalytic centre (H-cluster) within the H-domain. M2-type [FeFe] hydrogenases consist of both the H-domain and the F-cluster domain, the latter of which contains two bacterial-type ferredoxin [4Fe-4S] clusters to facilitate electron transfer from the buried active site to the protein surface. An example of an M2-type hydrogenase is *Dd*HydAB[49]. The M3-type [FeFe] hydrogenases also feature an H-domain and an F-cluster domain, but they possess two additional N-terminal cluster-binding motifs in the F-domain. Examples include *Cp*I[122] and *Ca*HydA1[51] [52]. One of these motifs contains a [4Fe-4S] cluster coordinated by one histidine residue and three cysteine residues, while the other harbours a plant-type ferredoxin [2Fe-2S] cluster.

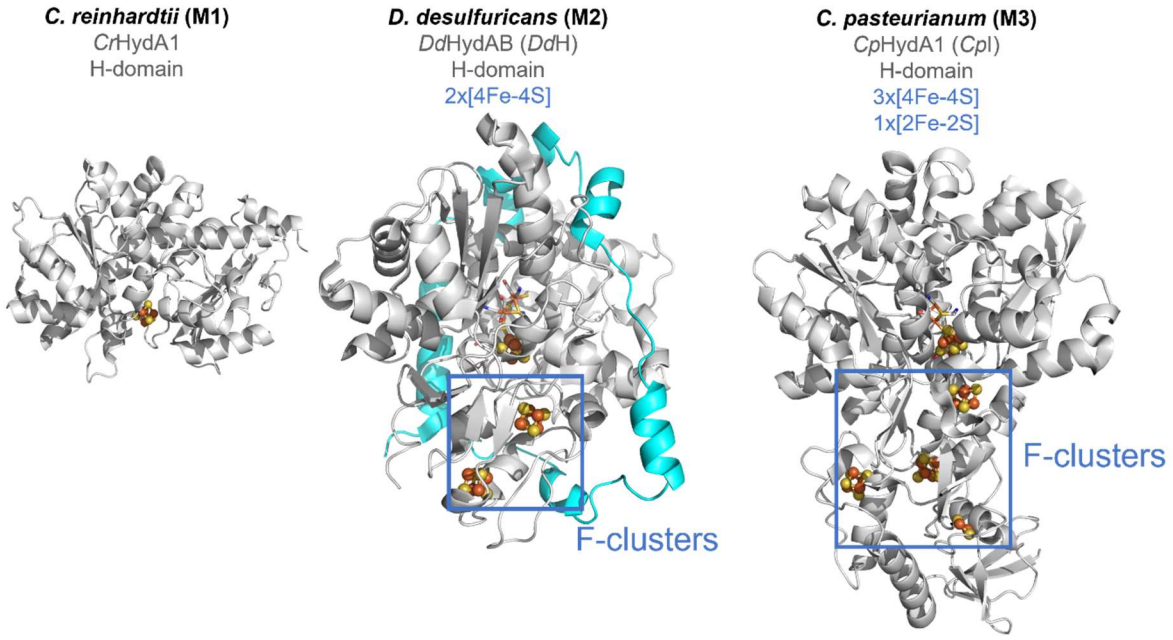


Figure 1: Meyer's classification for [FeFe] hydrogenases[48]: X-ray crystal structures of [FeFe] hydrogenases from M1-type: *Chlamydomonas reinhardtii* (*Cr*HydA1),(PDB 3LX4) [60]; M2 type: *Desulfovibrio desulfuricans* (*Dd*HydAB), (PDB 6SG2)[61]; M3 type: *Clostridium pasterianum* (*Cp*I), (PDB 3C8Y). [44] This figure was made in Pymol.

Research into [FeFe] hydrogenases would be difficult to carry out without important technical advances in the expression of these enzymes. Two novel advances are recombinant expression in *E. coli* [123] [96] [124] and production of semi-synthetic hydrogenases via artificial maturation. [65] [125]

3.1.2 *In vivo* maturation of [FeFe] hydrogenase

[FeFe] hydrogenases maturation *in vivo* requires three maturases (HydE, HydF and HydG). It was not until 2004 that the accessory genes encoding HydE, HydF and HydG were first identified in *Chlamydomonas reinhardtii.* [126] Native expression of [FeFe] hydrogenases is

often low yield and requires longer time for expression. In recent years, research on heterologous overexpression of HydA in *E. coli* was carried out to advance the production of [FeFe] hydrogenases, and it was shown that the expression of HydA alone gives inactive enzyme. It requires the co-expression of maturases HydE, HydF and HydG to obtain an active form.[96] It was also shown that the heterologous expression of the HydA without the co-expression of either HydE or HydG or HydF resulted in an inactive hydrogenase. More importantly, later research showed that it was possible to achieve *in vitro* activation of apo-protein with the *E. coli* cell extract in which HydE, HydF and HydG were expressed (as shown in Figure 2). [127]This evidence strongly supports that the maturases HydE, HydF, HydG are responsible for H-cluster assembly via their actions with ubiquitous substrates present in the cellular lysates. Subsequent research on characterising the simplest M1 type Apo-*Cr*HydA1 expressed with the HydA alone using UV-Vis, EPR and Mössbauer spectroscopy reveal that $[4Fe4S]_H$ is intact in the protein. [128] It was shown that the apo-protein with the $[4Fe4S]_H$ cluster chelated can no longer be activated by the cell extract containing HydE, HydG, and HydF maturases. These results demonstrated the H-cluster assembly requires a preassembled $[4Fe4S]_H$ cluster synthesised by the Iron-Sulfur Cluster (ISC) machinery in the cell. Later research by Kuchenreuther and co-workers further supports this mechanism by studying electron paramagnetic resonance (EPR) and Nuclear resonant vibrational spectroscopy (NRVS) on *Cp*I.[129] It was reported that when ^{56}Fe HydA was *in vitro* activated with ^{57}Fe-labeled HydE, HydF and HydG maturases, only the $[2Fe]_H$ consisted of ^{57}Fe. This was confirmed by the crystal structure of the apo-*Cr*HydA1 expressed with the HydA alone in *E. coli*, where $[4Fe4S]_H$ is present in the apo-*Cr*HydA1 but the $[2Fe]_H$ subcluster is missing[60]. It was reported that the

apo-CrHydA1 contains an electropositive channel likely supporting the electrostatic interaction with the negatively charged [2Fe] subcluster. These all demonstrated that the HydE, HydF and HydG are exclusively responsible for the biosynthesis of the $[2Fe]_H$ subcluster, which can later can be incorporated into the preassembled $[4Fe4S]_H$ cluster to form the assembled H-cluster, yielding an active [FeFe] hydrogenase.

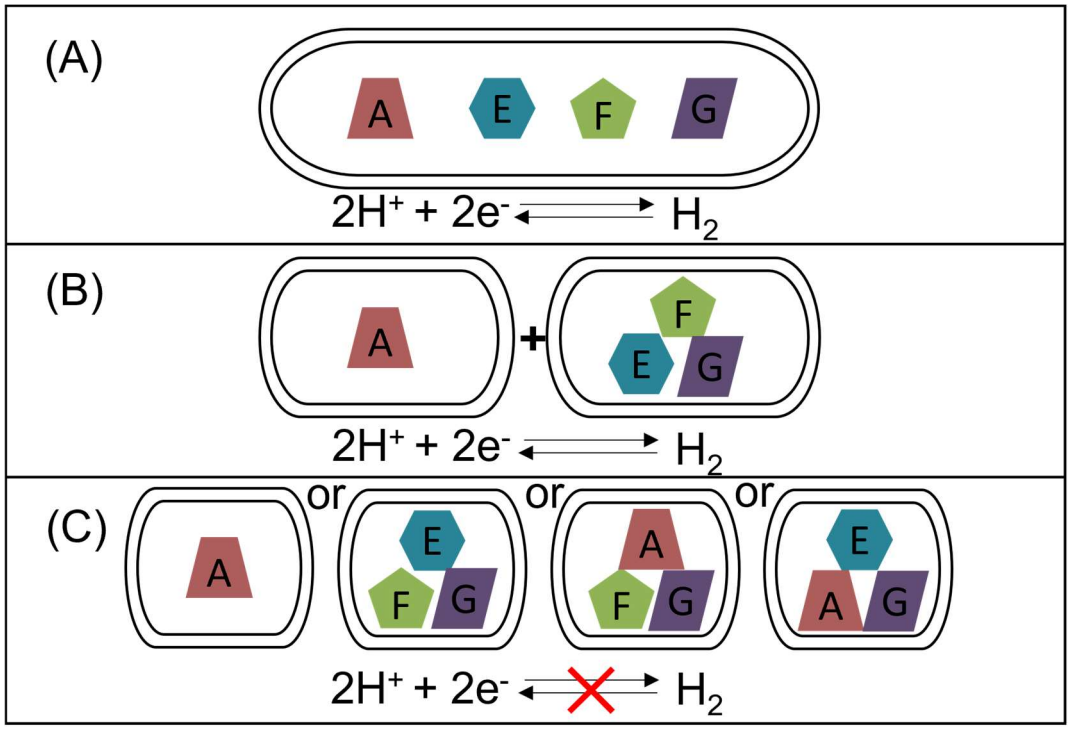


Figure 2: Whole cell extracts hydrogenase activation results: (A) Co-expression of HydAEFG yielded an active hydrogenase; (B) *In vitro* activation of HydA with HydEFG Cell extracts showed an active hydrogenase; (C) Lack of either one of the three maturase enzymes cannot activate hydrogenase.

It is essential to understand these maturase enzymes, HydE, HydG and HydF, to know their individual roles in the biosynthesis of the H-cluster. Figure 3 shows a schematic representation of the individual role of each maturase enzyme and the origin of atoms in the H-cluster. HydG is a radical S-adenosylmethionine (rSAM) enzyme that is shown to consume tyrosine to

form the CO and CN^- ligands of the $[2Fe]_H$ subcluster through rSAM based radical chemistry with the tyrosine substrate. [130] [131] It was also evidenced by stopped flow FTIR that a $Fe(CO)_2CN$ synthon exists, as only two CO and one CN^- were detected [132] These studied concluded that the 2Fe2S core of the $[2Fe]_H$ subcluster is sourced from its synthon $[Fe(CO)_2CN(cysteinate)]^-$, an organometallic complex.[133] HydE is also an rSAM enzyme, and it was demonstrated that it is able to convert the $[Fe(CO)_2CN(cysteinate)]^-$ synthon to a new $[Fe(CO)_2(CN)S]$ centre and form a $[Fe_2(CO)_4(CN)_2S_2]$ dimer.[134] Additionally, it enables the formation of the dithiolate bridge between two iron atoms. Maturase HydF differs from the other two maturases in that it is not an rSAM enzyme. It was demonstrated that it plays a role in synthesising the bridging amine group in the $[2Fe]_H$ subcluster from serine[63] and later transporting the $[2Fe]_H$ subcluster to the apo-protein to form the complete H-cluster.[135]

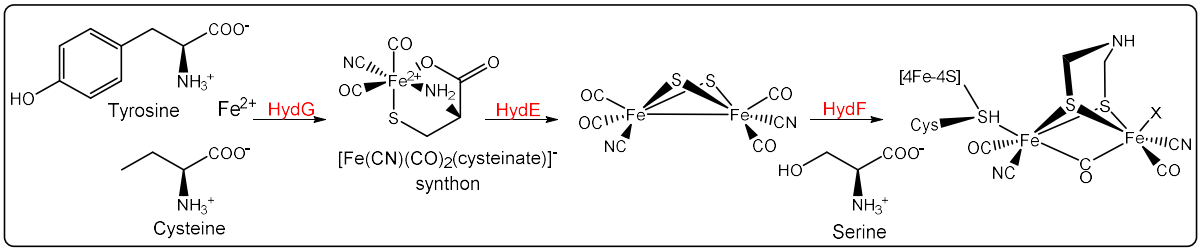


Figure 3: Schematic representation of individual role of each maturase enzyme and origins of atoms in the biosynthesis of H-cluster.[133] The scheme is adapted from reference[64] and was made in ChemDraw.

3.1.3 *In vitro* maturation of [FeFe] hydrogenase

In 2013, Berggren and co-workers demonstrated that [FeFe] hydrogenases could be maturated *in vitro*, making a significant breakthrough the field. They showed that Apo-HydA and HydF could be overexpressed in *E. coli,* and subsequently combined *in vitro* with an artificially

synthesised cofactor ADT. HydF facilitated the transfer the ADT to the apo-hydrogenase, resulting in the formation of a fully assembled, active H-cluster to form holo [FeFe] hydrogenase. This artificially maturated holo [FeFe] hydrogenase was found to be functionally and spectroscopically identical to the native protein produced *in vivo*. [65]

Interestingly, it was shown that apo-HydA could achieve complete maturation with ADT alone, without the assistance of HydF. [125] These findings open the door to engineering synthetic variants of [FeFe] hydrogenases by manipulating both the protein scaffold and the active-site cofactor as illustrated in the introduction chapter. This approach simplifies site-directed mutagenesis since the apo-proteins can be produced in *E.coli*, a system with well-established molecular biology tools. Additionally, artificial maturation yields high purity proteins in large quantities. Figure 4 shows the schematic representation of artificial maturation of [FeFe] hydrogenase. During *in vitro* maturation, the synthetic cofactor binds spontaneously to the $[4Fe\text{-}4S]_H$ cluster. This process results in the loss of one CO ligand and the migration of another CO ligand into a bridging position between the two Fe atoms, creating a vacant site at the apical position on Fe_d, which is trans to the bridging CO. Furthermore, the CO/CN^- ligands reorganise into an octahedral coordination at each Fe atom. Each of the two Fe atoms adopts perpendicular equatorial planes, accomodating the mixed valence Fe(II)Fe(I) state of H_{ox}. [65]

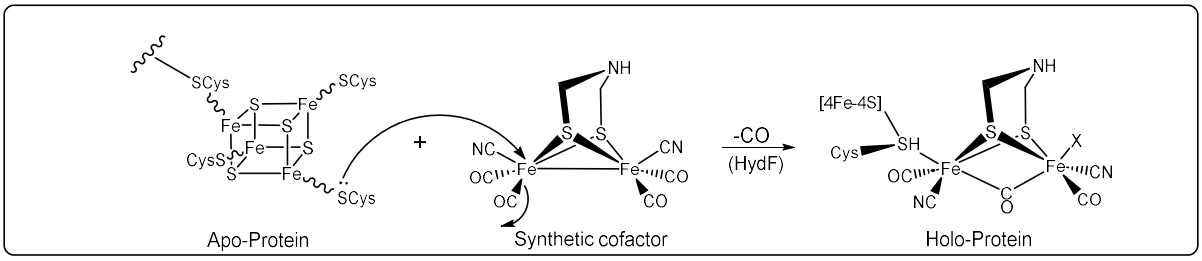


Figure 4: Schematic representation of artificial maturation of [FeFe] hydrogenase. The figure was made using ChemDraw.

3.1.4 The aim of the chapter

In this chapter, I will focus on the overexpression of an excellent H_2 producer, M3 type *Ca*HydA1 [FeFe] hydrogenase. This enzyme is reported to be less O_2 sensitive compared to many other hydrogenases such as M1 type *Cr*HydA1 and M2 type *Dd*HydAB [98], and its excellent performance on the electrode gives potential for biotechnological applications such as bio-fuel cells. My goal in this chapter is to develop a recombinant overexpression of apo-*Ca*HydA1 in *E. coli*, and this will make it possible for *in vitro* maturation with various synthetic cofactors. I will compare the overexpression of M3 type *Ca*HydA1 [FeFe] hydrogenase using the *in vivo* maturation method and the *in vitro* (artificial) maturation method in terms of yield and the purity of the protein. Additionally, I will also compare functional and spectroscopic characterisation of the protein prepared by two different methods. Figure 5 shows the homology model of the M3 type *Ca*HydA1 [FeFe] hydrogenase.

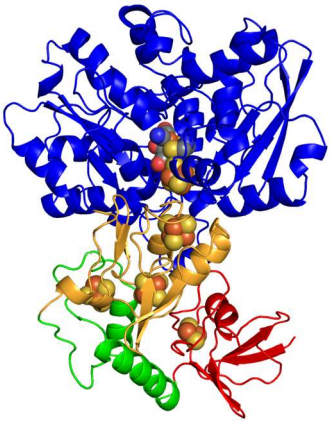
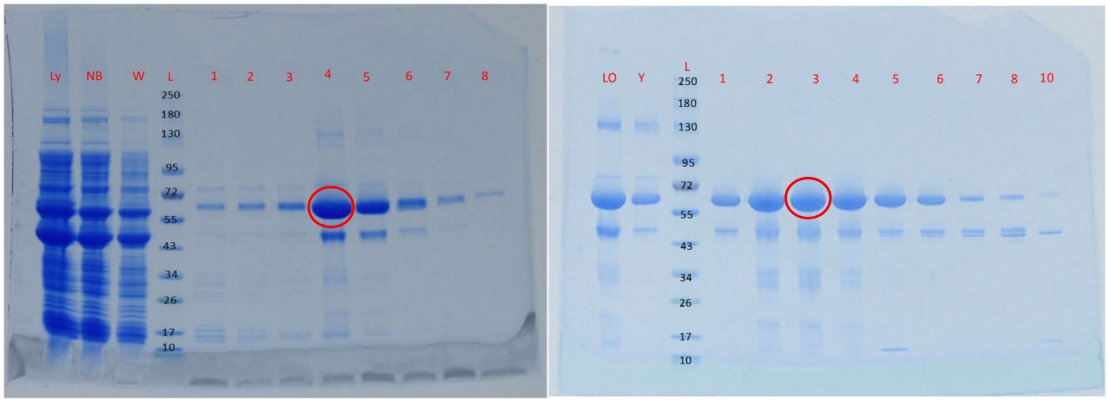


Figure 5: Homology model of M3 type *Ca*HydA1 [FeFe] hydrogenase was prepared based on the *Cp*I [FeFe] hydrogenase (70 % homologous) using Pymol. Blue colour represents the H-domain with H-cluster intact and the other shows the F-domain with accessory F-clusters intact. The figure is adapted from T. Lai *et al* in preparation.[136]

3.2 Recombinant expression of holo-*Ca*hydA1 [FeFe] hydrogenase - *In vivo* maturation

We employed the expression method developed by Morra and coworkers. [52] The plasmids, provided by Dr. S. Morra (University of Nottingham, UK), pCaE2 and pCaFG, encode for apo-*Ca*HydA1 [FeFe] hydrogenase and maturases *Ca*HydE, *Ca*hydF and *Ca*HydG. These were co-transformed into *E. coli* Rosetta2(DE3) and grown on LB plates containing 100 μg/mL ampicillin, 50 μg/mL streptomycin and 34 μg/mL chloramphenicol. The preculture was inoculated by picking a colony of bacteria and was left to grow at 37 °C overnight. Bacteria were added to several 1 L containers containing terrific broth (TB) (12 g/L tryptone, 24 g/L yeast extract, 4 mL/L glycerol, 2.2 g/L KH_2PO_4, 9.4 g/L K_2HPO_4) supplemented with antibiotics (100 μg/mL ampicillin, 50 μg/mL streptomycin, 34 μg/mL chloramphenicol) and 2 mM ammonium ferric citrate. When the OD_{600} reached ~ 0.6, the culture was supplemented with 2 mM cysteine, 25 mM fumarate, 0.5% w/v glucose and induced with 0.5 mM IPTG. After induction, the culture was purged with pure argon to remove O_2 and incubated overnight. The culture was then harvested by centrifugation (10,000 rpm, 10 min, 4 °C), ready for protein isolation and purification. The cell pellet was lysed using lysis buffer containing standard wash buffer 100 mM Tris-HCl and 150 mM NaCl at pH8, 1% v/v Triton X-100 as detergent to break the cell membrane, 1mg/mL Lysozyme to break the cell wall, 10 mM sodium dithionite (NaDT) to scavenge trace O_2, 2 mM dithiothreitol (DTT) and 0.1 % avidin solution to improve protein purity.

The expressed protein possesses a Strep-TagII at the C-terminal. A strep tag affinity column was used to purify the protein, and the protein was collected as 1 mL aliquots to separate unwanted proteins. Sodium dodecyl sulfate polyacrylamide gel electrophoresis (SDS-PAGE) was run to test the purity of aliquots of eluted protein (as shown in Figure 6A). Aliquots 3-6, showing the darkest bands in the SDS-PAGE, were collected as they contain more concentrated protein. The band at 65 kDa corresponds to the *Ca*HydA1 enzyme. Another observed band on the SDS-PAGE at 46 kDa represents a small impurity (*Ca*HydF). The protein purified by one single affinity column could be used for functional and spectroscopic characterisation. However, for structural studies, a size exclusion column was used for further purification. Due to the O_2 sensitivity of the protein, size exclusion chromatography was run in the glove box with a constant purge of N_2 to maintain an anaerobic atmosphere. After the size exclusion column, 1 mL aliquots of protein were collected, and SDS-PAGE was run to determine the purity. In Figure 6B, impurities above 65 kDa disappeared, and the *Ca*HydF impurity (46 kDa) became paler but still present. Therefore, no completely pure sample could be obtained after two purification steps. The overall mass after two purification steps was 5.15 mg from a 4 L fermentation batch, resulting in an overall yield of 1.29 mg/L. The concentration of the protein was assayed with the Bradford assay using bovine serum albumin as standard [137].



(A) (B)

Figure 6: The SDS-PAGE of the *Ca*HydA1 [FeFe] hydrogenase (*in vivo* maturated) (A) after the strep tag affinity column, and (B) after the size exclusion column. Red circle indicates the desired band for the protein at 65 kDa.

3.3 Overexpression of apo-*Ca*HydA1 [FeFe] hydrogenase and *in vitro* maturation with synthetic cofactors

3.3.1 Overexpression of apo-*Ca*HydA1 using codon optimised gene

Initially, a codon optimised gene in pET11b vector for *E. coli* was designed to optimise the expression of apo-*Ca*HydA1 [FeFe] hydrogenase (shown in Figure 7A). The codon optimised gene, together with the pET11b vector containing the ampicillin resistance gene, was digested by BamHI and NdeI endonucleases. Agarose gel electrophoresis was run to separate both products (shown in Figure 7B and 7C). The gene and the vector were isolated by gel extraction kits and ligated by T4 DNA ligase. Finally, the product was verified by DNA sequencing. This

plasmid pET11b for apo-*Ca*HydA1 was transformed into *E. coli* BL21(DE3) *ΔiscR* cells and grown on LB plates containing 50 μg/mL kanamycin and 100 μg/mL ampicillin. The *E. coli* BL21(DE3) *ΔiscR* strain was given as a gift by Dr. J. Birrell and Prof. S. DeBeer (MPI-CEC, Germany). The colony was inoculated to the LB preculture and left to grow at 37 ^{o}C shaking overnight. The following day, the main media was inoculated by adding 10 mL of bacterial preculture to several 1 L containers containing Lysogeny Broth (LB) (10 g/L tryptone, 5 g/L yeast extract, 5 g/L NaCl, 7.63 g/L K_2HPO_4, 5 g/L Na_2HPO_4) supplemented with antibiotics (50 μg/mL kanamycin, 100 μg/mL ampicillin), 2 mM ammonium ferric citrate. However, the OD growth of the media reaches around 0.3 after several hours and decreased to 0.1. This suggested that apo-*Ca*HydA1 expressed using the plasmid pET11b could be toxic to the *E. coli* BL21(DE3)*ΔiscR* cells leading to cell death. The gene encoding for the repressor IscR is deleted in *E. coli* BL21(DE3)*ΔiscR* cells to improve the synthesis of FeS clusters and thus will be better suited for the 5 FeS cluster-containing *Ca*HydA1.

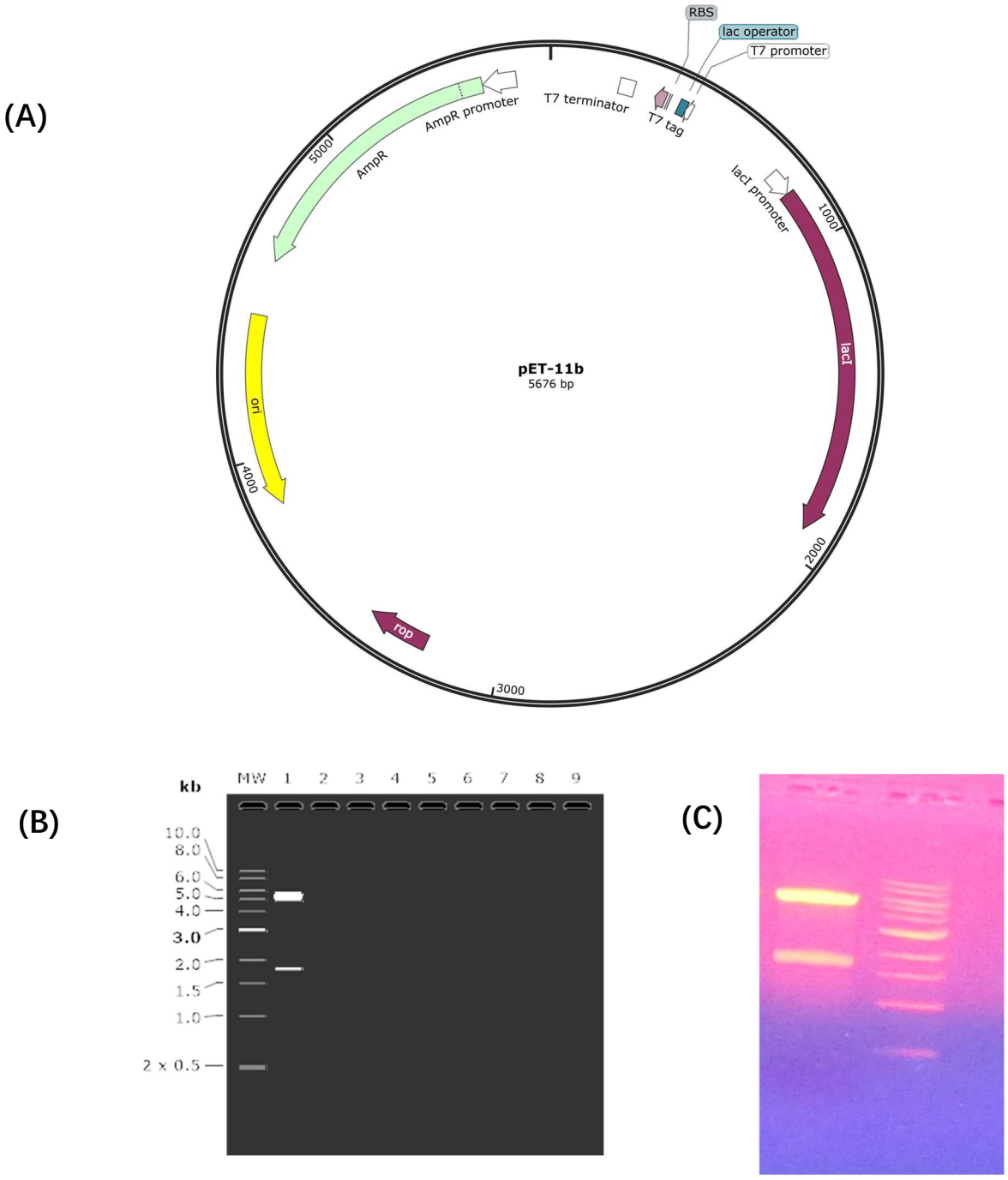


Figure 7: (A) Graphical structure of the plasmid pET11b for apo-CaHydA1 [FeFe] hydrogenase, (B) simulated gel image after digest with BamHI and NdeI, (C) agarose gel after digestion with BamHI and NdeI.

In the second attempt, the pET11b plasmid was transformed to *E. coli* BL21A1 cells, and cells were grown using the same protocol. This time, the OD_{600} of the media reached ~ 0.6, and

0.5% w/v glucose and 2 mM cysteine were added to the culture. The culture was then bubbled with argon for 1h to make it anaerobic. After bubbling, protein production was induced with 0.5 mM IPTG and stirred overnight on the bench (room temperature, RT) with gentle shaking. The culture was harvested the following day by centrifugation (6,500 rpm, 30 min, 4 ^{o}C) and was ready for protein isolation and purification. However, no protein could be harvested in soluble form when lysing the cell using sonication (30 % amplitude, 2s on 10s off, 15 min). SDS-PAGE (Figure 8) was run showing that the protein was insoluble and was found in the pellet.

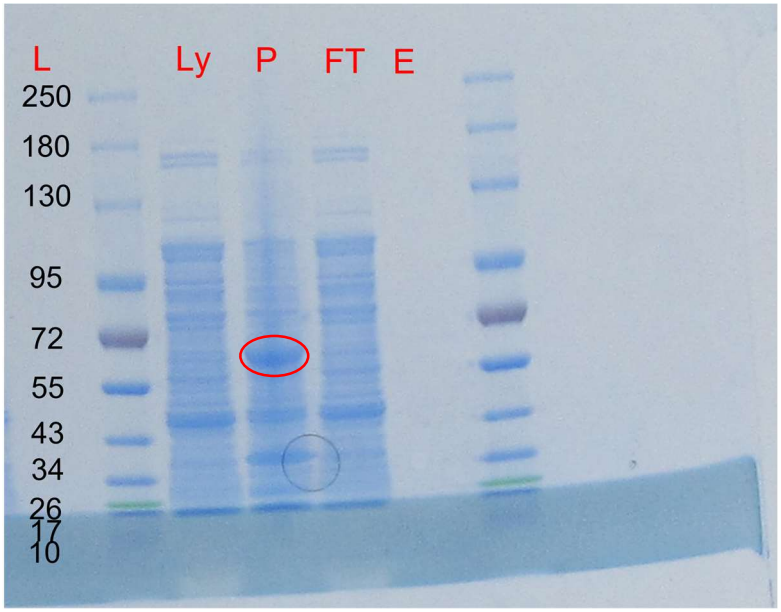


Figure 8: The SDS-PAGE of insoluble apo-*Ca*HydA1 [FeFe] hydrogenase expressed in BL21A1, Red circle indicates the desired band for the protein at 65 kDa. Ladder indicator is represented as L, Cell lystate is Ly, pellet is represented as P, Flow though is FT and E is protein elution.

3.3.2 Overexpression of apo-*Ca*HydA1 using native gene

After several attempts to express the codon optimised gene encoding apo-*Ca*HydA1, it was found that this gene led to incorrect folding of the protein, causing toxicity to the cell. Therefore, the decision was made to focus on the native gene. The vector pET21 was chosen for this gene (as shown in Figure 9).

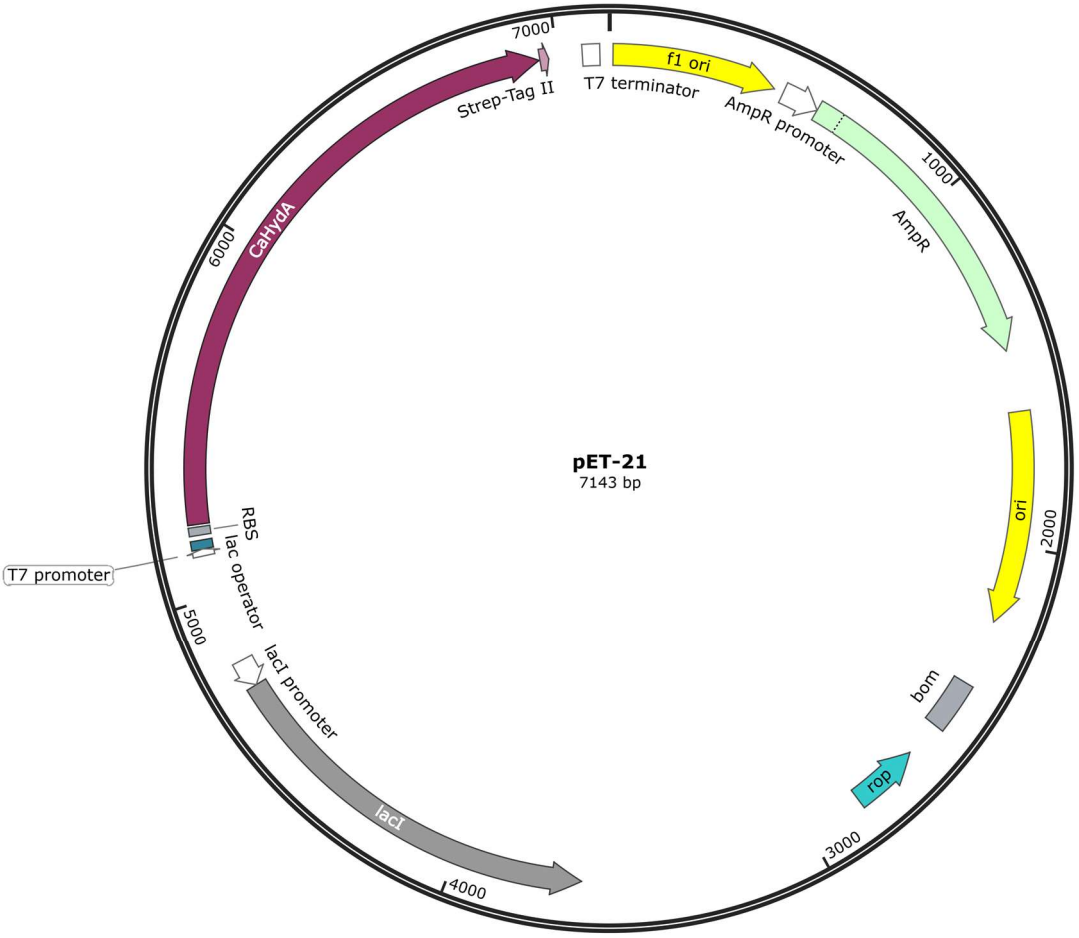


Figure 9: Graphical structure of the plasmid pET21 for apo-*Ca*HydA1 [FeFe] hydrogenase.

The plasmid pET21 for apo-*Ca*HydA1 was transformed into *E. coli* BL21(DE3)*ΔiscR* cells and grown on LB plates containing 50 μg/mL kanamycin and 100 μg/mL ampicillin. A preculture of

the bacteria was left to grow at 37 °C shaking overnight. The following day, the main media was inoculated by adding 10 mL of bacterial preculture to several 1 L containers containing Lysogeny Broth (LB) (10 g/L tryptone, 5 g/L yeast extract, 5 g/L NaCl, 7.63 g/L K_2HPO_4, 5 g/L Na_2HPO_4) supplemented with antibiotics (50 μg/mL kanamycin, 100 μg/mL ampicillin), 2 mM ammonium ferric citrate. When the OD_{600} reached ~ 0.6, 0.5% w/v glucose and 2 mM cysteine were added to the culture. The culture was then bubbled with argon for 1h to make it anaerobic. After bubbling, protein production was induced with 0.5 mM IPTG and stirred overnight on the bench (room temperature, RT) with gentle shaking. The culture was then harvested the following day by centrifugation (6,500 rpm, 30 min, 4 °C) and was ready for protein isolation and purification, stored at -80°C until its subsequent use. The protein was isolated by lysing the cell with sonication (30 % amplitude, 2s on 10s off, 15 min) and was harvested by ultra-centrifugation (43,000 rpm). Finally, a strep-tag affinity column was used to purify the apo-protein, and SDS-PAGE was run to test the purity, as shown in Figure 10.



Figure 10: SDS-PAGE of the apo-*Ca*HydA1 [FeFe] hydrogenase after the strep tag affinity column. Red circle indicates the desired bands for the protein at 65 kDa. Ladder indicator is represented as L, Cell lystate is Ly, pellet is represented as P, Flow though is FT and E is protein elution.

A band is present at around 65 kDa, as expected for *Ca*HydA1 (Figure 10). It can also be seen that the Elutent (E) lane is much cleaner than the one obtained via the *in vivo* system, and only some very small impurities can be seen in the artificially maturated enzyme. The overall yield of the apo-*Ca*HydA1 after the strep-tag affinity column was about 5 mg/ L culture, almost 5 times higher than the yield obtained for the *in vivo* maturated holo-*Ca*HydA1 (1.29 mg/L).

The FeS clusters in the apo-protein can be confirmed by UV-Visible spectroscopy (as shown in Figure 11). The broad band around 410 nm arises from the oxidised [4Fe4S] cluster (via metal-ligand charge transfer)

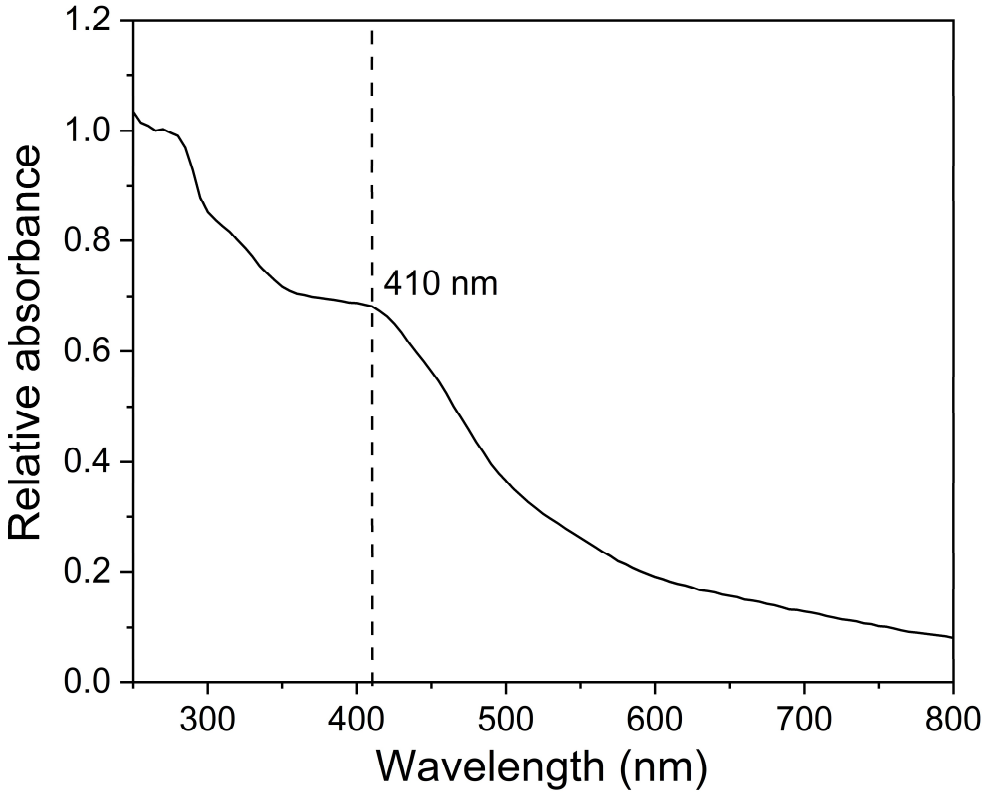


Figure 11: The UV-Visible (UV-VIs) absorption spectrum of purified apo-*Ca*HydA1. This absorbance represents a 10 µM apo-*Ca*HydA1 in 100 mM Tris-HCl, 150 mM NaCl, pH8 buffer.

The expression of apo-*Ca*HydA1 [FeFe] hydrogenase using recombinant expression methods

offers benefits such as that it allows the production of a large amount of protein with very high purity. Secondly, this system allows quicker growth, and it is a much easier system for performing site-directed mutagenesis. Thirdly, for easy purification, tag sequences can be inserted so the protein can be purified using affinity column. In this work, the *Ca*HydA1 [FeFe] hydrogenase (both, *in vivo* maturated via the maturases and apo-*Ca*HydA1) has been recombinantly expressed in *E. coli* with a C-terminal strep-tag II.

3.3.3 *in vitro* maturation of apo-*Ca*HydA1 with synthetic cofactors

For the artificial maturation, 200 µM of apo-*Ca*HydA1 [FeFe] hydrogenase was incubated with 600 mM of ADT solution for 1 h at 25 °C. Afterward, the mix was run through a desalting column (PD-10). The first eluted band is the desired holo-protein, and the second eluted band is the excess ADT. The protein was left shaking for 1 day under a N_2 atmosphere to release the CO. The maturation time was tested by incubating the apo-*Ca*HydA1 [FeFe] hydrogenase with ADT solution in the transmission cell in which FTIR spectra can be obtained with different incubation times (as shown in Figure 12). Incubation of apo-*Ca*HydA1 with ADT solution for 1 h achieved 95 % of maturation, and at 10 h, maturation was 100 % shown by no further change in the IR spectra. Therefore, it was decided to use 1 h incubation time compared to 10 h as the extra time needed was not justified by the small gain in incorporation ratio of ADT cofactor.

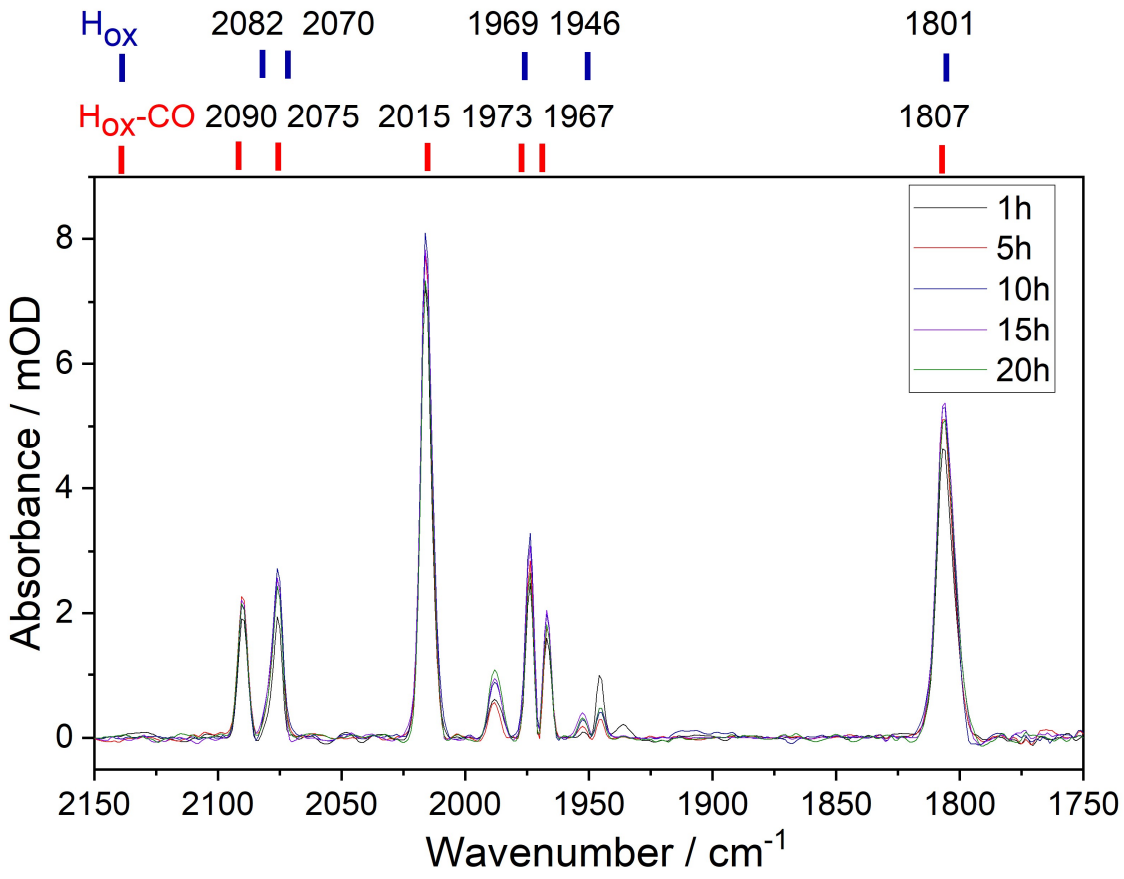


Figure 12: FTIR spectra of the 200 µM apo-*Ca*HydA1 [FeFe] hydrogenase maturated with native ADT cofactor at different incubation times with 600 µM ADT solution.

3.4 Functional characterization of wild-type *Ca*HydA1 [FeFe] hydrogenase: Comparison between *in vivo* and *in vitro* maturated enzyme

FTIR spectroscopy was utilized to identify the CO (1800-2020 cm^{-1}) and CN (2040-2100 cm^{-1}) vibrations in the [2Fe] sub-cluster, allowing differentiation between different redox states present in the H-cluster. The comparison of FTIR spectra of the *Ca*HydA1 [FeFe] hydrogenases prepared by *in vivo* maturation and artificial maturation (Figure 13 A) suggests, judging by the

intensity of the bands, that the artificially maturated sample enables higher incorporation of the active-site cofactor, while the in vivo maturated sample appears to have much lower active site incorporation. Consequently, solution activity assays using methyl viologen as a redox partner show higher H2 uptake rates for the artificially maturated sample (Figure 13 B). Electrochemical characterisation of both samples via cyclic voltammetry (CV) (Figure 13 C) also shows higher current densities for the artificially maturated sample. Note that caution is needed when attributing significance to absolute currents in electrochemistry, specifically in protein film voltammetry (PFV), as it reflects not only the intrinsic enzyme catalytic activity but also the enzyme coverage on the electrode surface.

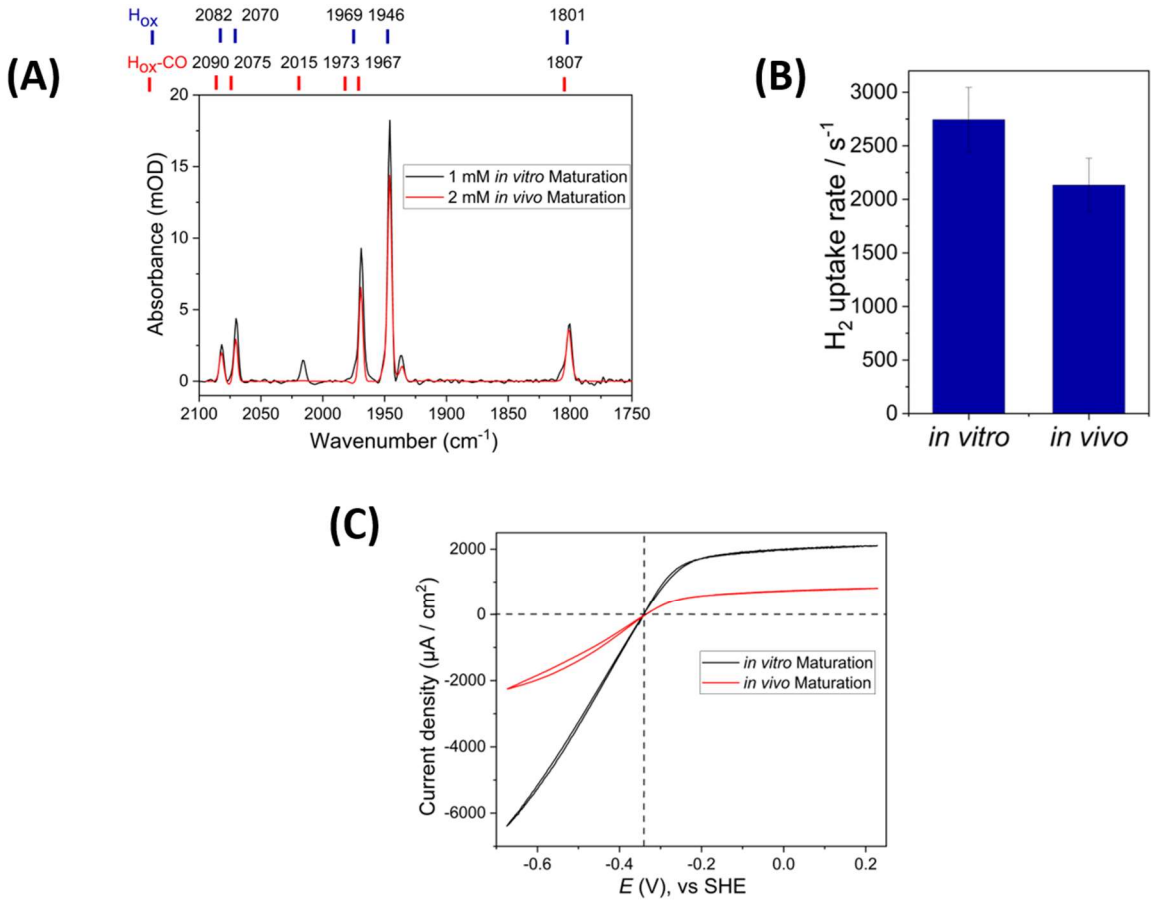
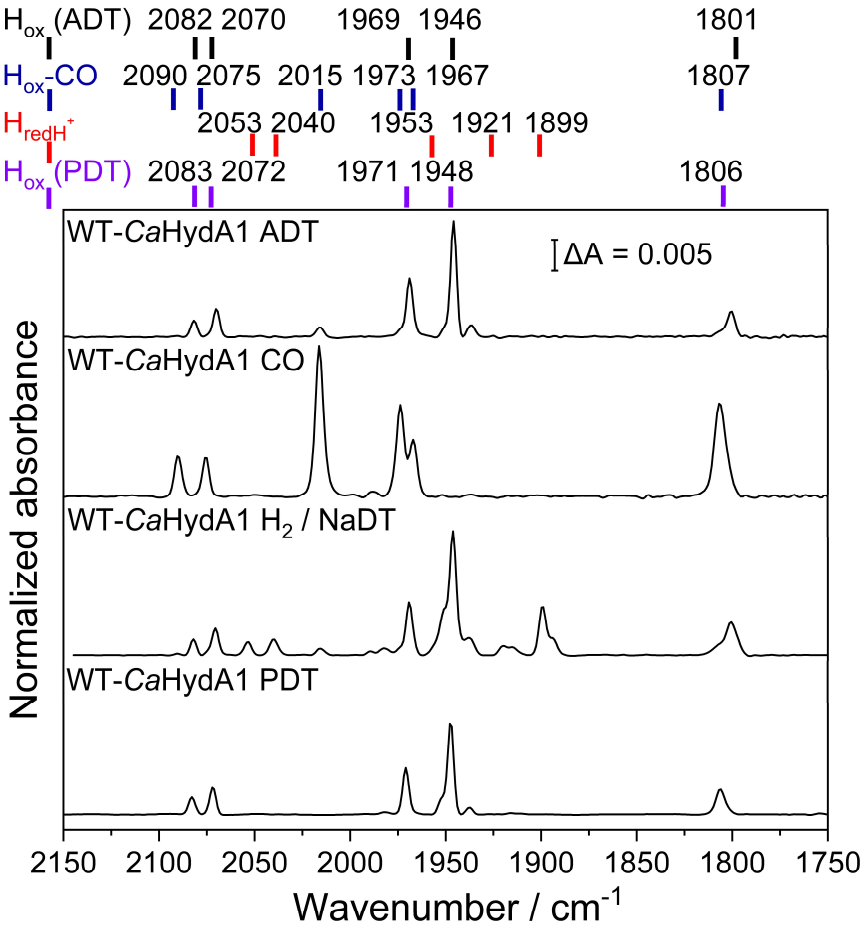


Figure 13 A) Fourier-transform infrared (FTIR) spectra of *Ca*HydA1 [FeFe] hydrogenase generated by artificial maturation (black) 1 mM and by the *in vivo* maturases system (red) 2 mM at pH 8, showing mainly the H_{ox} state. The main bands of H_{ox} and H_{ox}-CO are indicated on top in blue and red respectively. B) H_2 uptake rates calculated from solution activity assays of *Ca*HydA1 with *in vitro* and *in vivo* samples. The H_2 oxidation rate was measured by following the reduction of methyl viologen by the enzyme in a H_2-saturated solution. C) Cyclic voltammogram (CV) of the *Ca*HydA1 [FeFe] hydrogenase generated by *in vitro* artificial maturation (black) and by the *in vivo* maturases system (red), both adsorbed onto a pyrolytic graphite electrode, measured at pH 6. Conditions: room temperature (RT), 100% H_2 (1 L/ min), 2000 rpm and 20 mV /s scan rate. The horizontal dashed line represents the zero current, and the vertical dashed line indicates the thermodynamic potential of the $2H^+/H_2$ couple at pH 6.

The FTIR spectrum for the as isolated full-length enzyme (WT) is shown in Figure 14 with majority of H_{ox} state and a small composition of the H_{ox}-CO state present in the spectrum, in

which an additional CO is bound to the open coordination site on the binuclear part of the H-cluster. To achieve a pure H_{ox}-CO state, the sample was flushed with excess CO. The most pronounced 2015 cm^{-1} band has been assigned to the extrinsic CO ligand. Treatment with H_2 and sodium dithionite results in the formation of reduced states, with a very pronounced 1899 cm^{-1} peak corresponding to the $H_{red}H^+$ state.

The sample was also maturated with PDT ($Fe_2(pdt)(CO)_4(CN)_2]^{2-}$) to show that the apo protein can be maturated with different metal cofactors. This yielded a very pure, only H_{ox} containing spectrum. These results are in excellent agreement with previous work on *Ca*HydA1 produced *in vivo* using natural maturases Hyd EFG.[137]



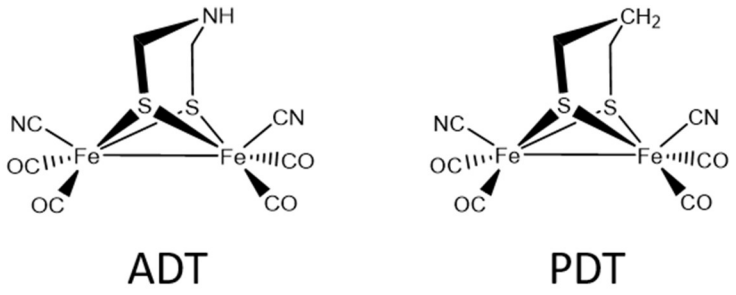


Figure 14: FTIR spectra of WT CaHydA1: ADT maturated sample; ADT maturated sample treated with CO (H_{ox}-CO); ADT maturated sample treated with H_2 (100 %) and 10 mM Na-dithionite (NaDT); PDT-maturated sample. The chemical structure of ADT and PDT are listed in the figure.

Figure 15 (A) shows the EPR spectrum of *Ca*HydA1 maturated with ADT. The EPR spectrum for H_{ox} shows spin-coupling between $[4Fe\text{-}4S]_H$ and $[2Fe]_H$ subcluster shown by the g values and a small fraction of H_{ox}-CO state resulting from the degradation of the H-cluster by O_2 damage. The spectrum also revealed a signal corresponding to spin coupling of $[2Fe\text{-}2S]^+$ cluster. The raw data was fitted by simulation of H_{ox}, H_{ox}-CO and [2Fe-2S] signals using MATLAB software. The EPR assignments of H_{ox} and H_{ox}-CO of WT *Ca*HydA1 are in good agreement with previous work from Morra and coworkers.[137] The EPR experiments were measured in CAESAR in collaboration with Dr. Will Myers. The EPR simulations were performed using Easyspin which is run in Matlab.[138]

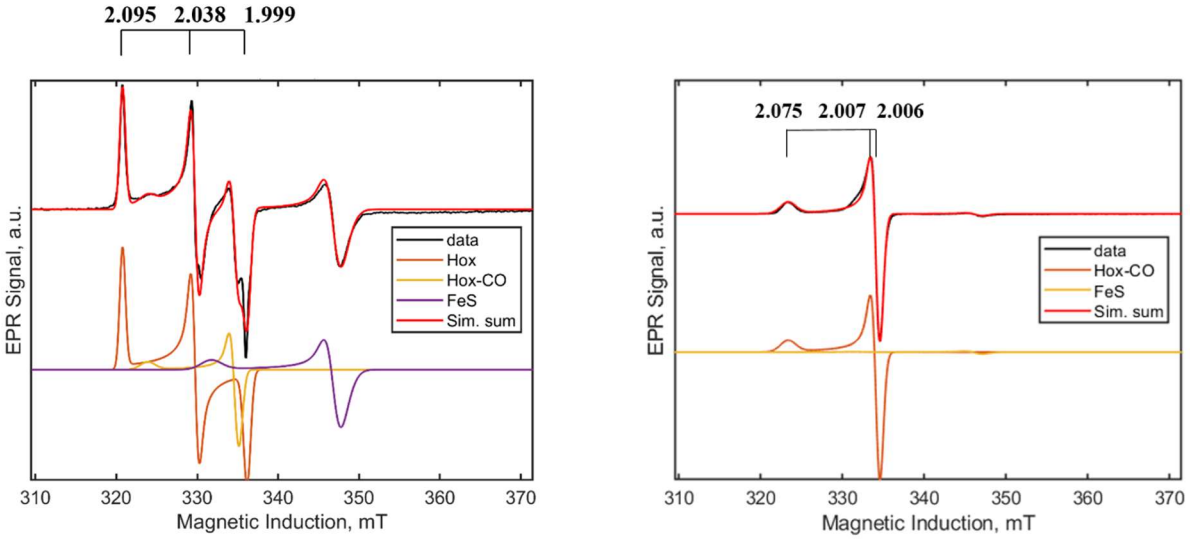


Figure 15: (A) Electron paramagnetic resonance (EPR) spectrum of *Ca*HydA1 maturated with ADT (B) EPR spectra of sample treated with CO (H_{ox}-CO). The raw data are shown in black, spectrum simulated for H_{ox} is shown in red, H_{ox}-CO spectrum is simulated in yellow, spectrum corresponding to [2Fe2S] is shown in purple and overall simulated spectrum to fit the raw data is shown in red. The g values are presented on top of the curve. The simulation and figure make up was done with the help of Dr Will Myers.

3.5 Discussion and Conclusion

The goal of this chapter was to develop a recombinant overexpression of M3 type apo-*Ca*HydA1 in *E. coli,* and to enable maturation with various synthetic cofactors. The protocol from morra and coworkers' [52] for overexpression of holo-*Ca*HydA1 [FeFe] hydrogenase using maturase enzymes systems was initially reproduced. In this system, plasmids pCaE2 and pCaFG encoding HydA and maturase enzymes HydEFG were co-expressed in *E. coli* Rosetta2(DE3). After a two- step purification (affinity column followed by size exclusion

column), SDS-PAGE showed a major band at 65 kDa corresponding to holo-*Ca*HydA1 and a distinct band at 46 kDa consistent with *Ca*HydF. The overall yield was 1.29 mg per litre of culture. However, the maturase *Ca*HydF present as an impurity for the desired protein, appeared to hinder the crystallization of this protein. As discussed before, all the maturases are essential for the biosynthesis of the $[2Fe]_H$ subcluster, so avoiding the contamination of the protein expressed using this system is challenging, which makes it difficult for protein crystallization.

For this reason, work was therefore carried out to develop the artificial maturation system for this protein. A similar approach was adopted to the artificial maturation system developed for *Dd*HydAB [95], in which a codon optimised *Dd*HydAB plasmid and *E. coli* BL21(DE3)*ΔiscR* strain was used to optimise the yield of protein expression. However, after several attempts with the codon optimised *Ca*HydA1 plasmid pET11b with both *E. coli* BL21(DE3)*ΔiscR* and *E. coli* BL21A1 strains, it was found that the codon-optimised *Ca*HydA1 plasmid may cause toxicity to the cell leading to cell death, and in the latter case, resulting in a decrease in solubility of the protein and unfolding of the protein.

In response to this, it was decided to focus on the native gene and find a plasmid suited for this native gene. pET21 was selected for the native gene, and *E. coli* BL21(DE3)*ΔiscR* strain was used. The desired protein could be isolated in a soluble form. After one single strep-tag affinity column, SDS-PAGE showed a distinct band at 65 kDa and little impurity present. The yield for the apo-*Ca*HydA was 5 mg per liter of culture.

We showed that the apo-*Ca*HydA1 could be maturated quite readily by incubating apo-

*Ca*HydA1 with ADT solution for 1 h to achieve 95 % incorporation of the $[2Fe]_H$ subcluster, as shown by the FTIR. Additionally, the apo-*Ca*HydA1 could also be maturated with PDT cofactor, yielding a very pure H_{ox} spectrum. Comparing the functional and spectroscopic characterisations of both systems suggested that the artificial maturation system allows 100 % incorporation of the $[2Fe]_H$ subcluster. The electronic structure of the H-cluster is the same for this protein produced by two different methods, confirmed by FTIR and EPR spectroscopy.

In conclusion, we have developed a recombinant overexpression of M3 type apo-*Ca*HydA1 in *E. coli* with the increased yield and purity. We showed that the protein can be maturated with various synthetic cofactors, and we proved that this system is better, as it allows 100 % incorporation of the $[2Fe]_H$ subcluster. Next, this system will be applied to expressing truncated variants to investigate the effect of the electron relay (accessory F-clusters) on the electronic structure, catalytic behaviour, O_2 sensitivity and cluster potential of [FeFe] hydrogenase.

Chapter 4

Functional and spectroscopic characterization of the truncated variants and comparison with the wild-type enzyme

Chapter 4: Functional and spectroscopic characterization of the truncated variants and comparison with the wild-type enzyme

4.1 Introduction and aim of this chapter

4.1.1 The role of FeS clusters in the metalloenzymes

Iron-sulfur (FeS) clusters are important cofactors in metalloenzymes, they function as electron relays supporting electron transfer (ET) and storage in various biological pathways, such as respiration and photosynthesis.[139] Some of the most common and characterized clusters in the metalloproteins are prototypical cubane [4Fe-4S], [3Fe-4S] and [2Fe-2S] clusters (Figure 1A-C). The reduction potential of [4Fe-4S] cluster lies in the -250 mV to -650 mV region, with an average of -400mV. The typical reduction potential of [3Fe-4S] ranges from -50 mV to -450 mV, with an average of -100 to -150 mV Typical reduction potential of 4cys-[2Fe-2S] lies in -150 mV to -450 mV. [140] [141] The iron ions are in tetrahedral geometry and often chelated by multiple sulfide groups or amino acids. In most cases, the iron ions are chelated by cysteine, with exceptions of $[4Fe\text{-}4S]_{His}$ chelated by three cysteine and one histidine ligated, which can be found in M3 type [FeFe] hydrogenases such as *Ca*HydA1 and *Cp*I. Two other examples are NEET- and Rieske-type [2Fe-2S] containing 3Cys: 1His and 2Cys: 2His respectively (Figure 1A and C).

In nature, enzymes are designed to contain multiple FeS clusters to catalyze essential multi-

electron redox reactions, such as activation of nitrogen (N_2), carbon dioxide (CO_2), carbon monoxide (CO), nitrite (NO_2^-), sulfite (SO_3^{2-}) and dihydrogen (H_2). The electron relay FeS-clusters are often coupled to an active center/ cofactor such as nickel, selenium, vanadium, or iron. FeS cluster-containing [NiFe] and [FeFe] hydrogenases, in addition to the [Fe] hydrogenases, are responsible for the activation of H_2 in microorganisms.[142] Standard [NiFe] hydrogenases, such as *E. coli* hydrogenase 2 (Hyd 2), consist of a proximal [4Fe-4S] cluster, a [3Fe-4S] cluster in the medial position and also a distal [4Fe-4S] cluster. However, in the case of membrane bound [NiFe] hydrogenase, such as *Ralstonia eutropha* (*Re*MBH), the proximal cluster is a [4Fe-3S] cluster, (Fig. 1D), which is thought to contribute to oxygen tolerance of this hydrogenase. [143] [144] The proximal [4Fe-3S] cluster in O_2-tolerant [NiFe] hydrogenases can access three redox states with rapid transfer of two electrons to the active site to reduce O_2 into water molecules with two additional electrons supplied from the electron relay of the hydrogenase to give in total 4 e^-.[145] This demonstrates how the redox properties of the FeS relay clusters can affect catalytic behaviour at an enzyme active site.

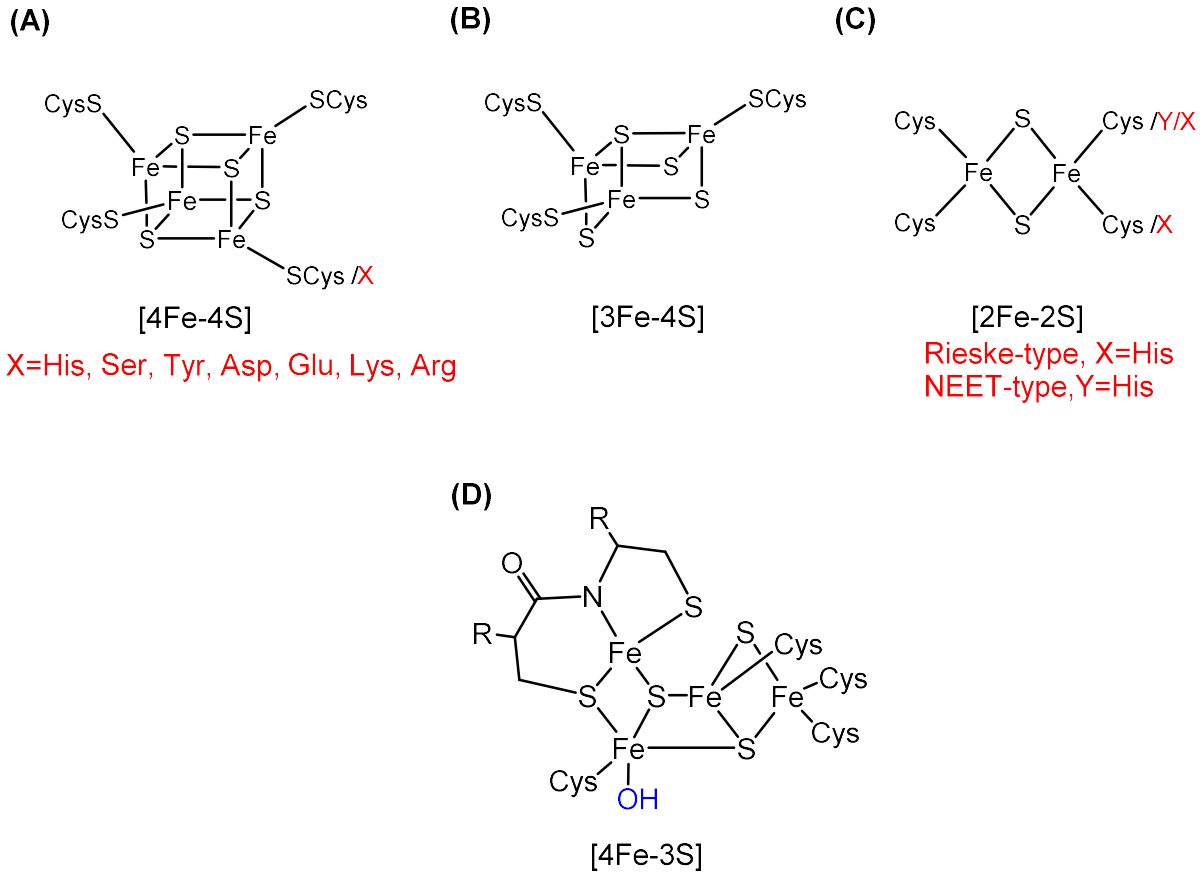


Figure 1: Structures of most common and best characterized FeS clusters. (A) prototypical cubane [4Fe-4S] cluster, X in red represents various cluster ligation; (B) [3Fe-4S] cluster; (C) [2Fe-2S] cluster including Rieske (labeled in red, X=Histidine) and NEET-type (labeled in red. Y=Histidine); (D) [4Fe-3S] proximal cluster of the oxygen tolerant membrane bound (MBH) [NiFe] hydrogenase containing a hydroxyl group heighted in blue. The figure was made using ChemDraw.

4.1.2 The role of FeS clusters in [FeFe] hydrogenases

The active site of [FeFe] hydrogenases, named the H-cluster, consists of a cubane $[4Fe\text{-}4S]_H$ cluster coupled with a $[2Fe]_H$ subcluster. Most [FeFe] hydrogenases also harbor additional FeS clusters in the F-domain named F-clusters, these FeS clusters are positioned approximately 11 Å apart, forming an electron transfer chain that facilitates efficient electron transfer. H_2 is

oxidized in the active center and electrons are transferred by the electron transfer chain to the protein surface (where they are usually passed to an physiological redox partner in the microorganism) or the reverse. The M1 type [FeFe] hydrogenase *Cr*HydA1 contains only the H-cluster without additional accessory FeS clusters. It was reported that modification of the His-ligated $[4Fe\text{-}4S]_H$ by site-directed mutagenesis changes the catalytic bias of the enzyme, suggesting the cubane $[4Fe\text{-}4S]_H$ cluster and $[2Fe]_H$ subcluster are strongly redox coupled.[146] M2 type *Dd*HydAB consists of two extra FeS clusters in the F-domain. Importantly, *Dd*HydAB can form the H_{inact} state by artificially adding sodium sulfide (Na_2S), and the crystal structure confirms the binding of the sulfide ligand at the open coordination site of the distal iron. [88] [147] The H_{inact} state protects the active site of the protein from being attacked by O_2 and can be reactivated in reducing conditions. A similar H_{inact} state can also be obtained in *Cb*A5H of *Clostridium beijerinckii*. Recently, the crystal structure revealed that in *Cb*A5H there was sulfide from the conserved cysteine residue in the local environment bound to the open coordination site of distal iron.[90] [89] The overall structure of *Cb*A5H is similar to *Cp*I and *Dd*HydAB. The H- and F- domain of *Cb*A5H harbor three [4Fe-4S] cluster the same as *Dd*HydAB, interestingly, the N-terminal domain (termed SLBB domain) harbours an additional His-ligated [4Fe-4S] cluster which is more than 20 Å away from any other [4Fe-4S] cluster. The role of this particular cluster in this protein is still unknown. M3 type [FeFe] hydrogenase *Ca*HydA1 harbours a His-ligated [4Fe-4S] cluster and an additional [2Fe-2S] cluster in the N-terminal domain (Figure 2). M3 type [FeFe] hydrogenases are excellent H_2 producers; it was thought that the catalytic bias is governed by the reduction potential of the distal FeS cluster, which could rationalize why this type of [FeFe] hydrogenases is prone to H_2 production.[99] The

additional FeS clusters present in the F-domain are also thought to provide two extra e^- to allow this enzyme to readily reduce O_2 to water when O_2 attacks the active site.

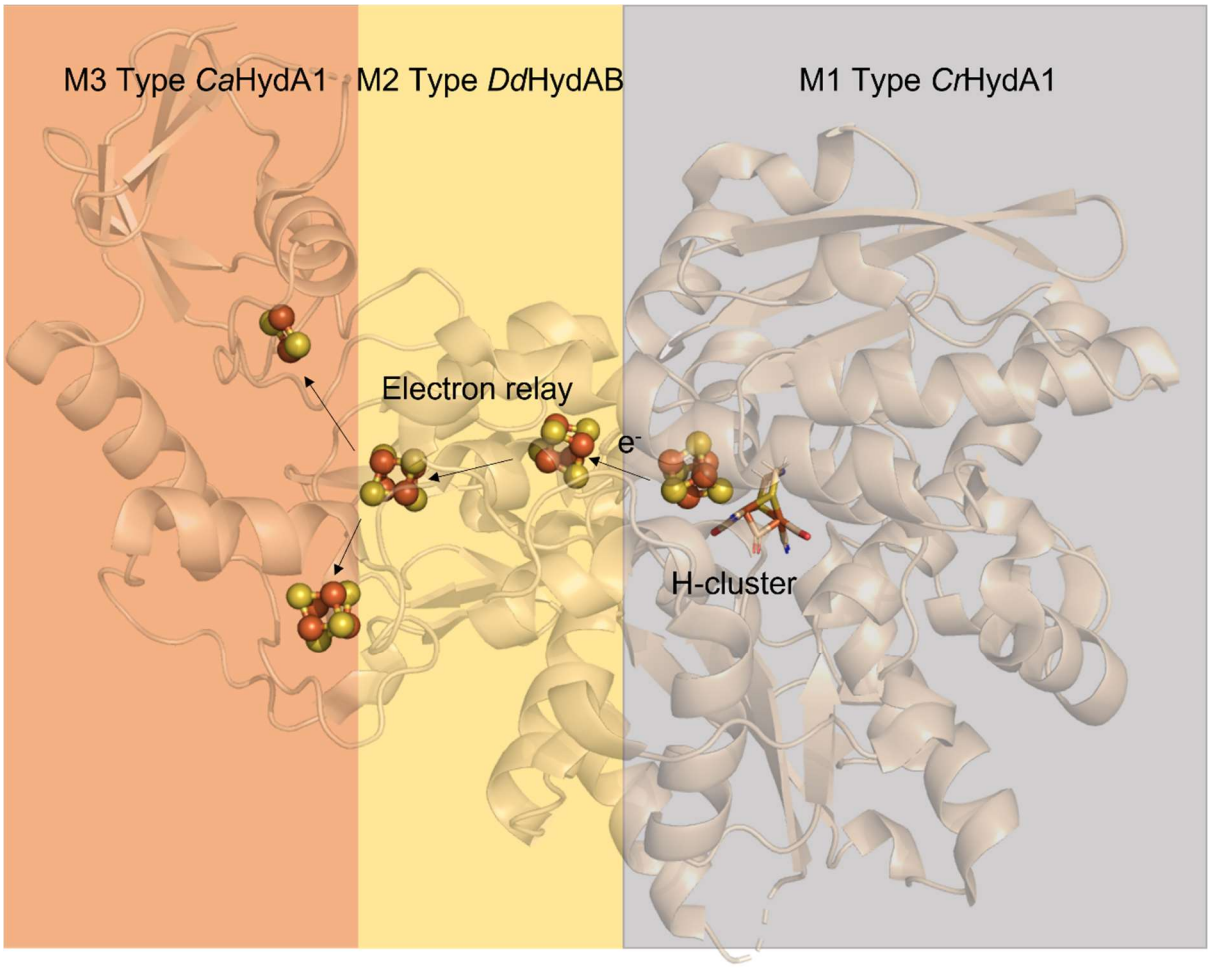


Figure 2: Schematic representation of *Cp*I [FeFe] hydrogenase, PDB code: 4XDC. *Cp*I [FeFe] hydrogenase is used to model other types of [FeFe] hydrogenases. The different colors showing the major three types of [FeFe] hydrogenases, the gray color represents M1 type [FeFe] hydrogenase, yellow color shows the additional domain present in a M2 type hydrogenase and the brown color shows the further additional domain present in an M3 type hydrogenase.

Table 1 lists the group A prototypical [FeFe] hydrogenases and their types according to Meyers' classification. Figure 3 illustrates the structural models and schemes, indicating different domains in this group of [FeFe] hydrogenases.

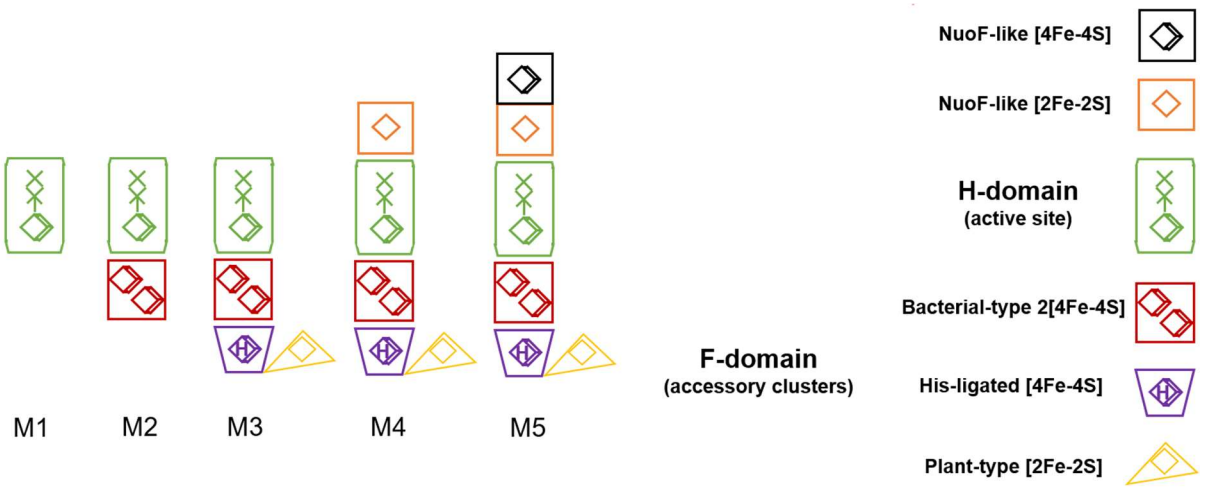


Figure 3: Schematic representation of classifications of prototypical [FeFe] hydrogenase (M1-M5 type), the different colours refers to both structural models and schemes, indicating different domains in group A prototypical [FeFe] hydrogenases, the green colour represents the H-cluster, red colour shows the bacterial type [4Fe-4S] clusters, purple colour illustrates the His-ligated [4Fe-4S] cluster and yellow colour represents the plant type [2Fe-2S] cluster. Additional NuoF-like [4Fe-4S] and [2Fe-2S] clusters were shown in black and orange, respectively. [53]

Table 1: Group A prototypical [FeFe] hydrogenases and their types according to Meyers' classification[148].

Type of [FeFe] hydrogenases	Name of [FeFe] hydrogenases
M1 type	(*Chlamydomonas reinhardtii*) *Cr*HydA1
M2 type	(*Desulfovibrio desulfuricans*) *Dd*HydAB
M2 type	(*Megasphaera elsdenii*) *Me*HydA
M3 type	(*Clostridium pasteurianum*) *Cp*I
M3 type	(*Clostridium acetobutylicum*) *Ca*HydA1
M3 type	(*Chlorella variabilis*) *Cv*HydA
M4 type	(*Thermotoga (T.) maritima*) *Tm*HydABC
M5 type	*Nyctotherus ovalis*[148]

Recent research on the roles of FeS clusters of [FeFe] hydrogenases highlights significant functionalities of the FeS clusters. Gauquelin and coworkers investigated cluster removal in *Ca*HydA1 [FeFe] hydrogenase by site directed mutagenesis. Their results showed that the catalytic activities of the mutants were significantly reduced and suggested that the removal of F-clusters could have a thermodynamic effect on the potential of the H-cluster leading to more bias towards H_2 production.[149] One of the controversies in M3 type [FeFe] hydrogenases is that the electron entry point could be either the His-ligated [4Fe-4S] cluster or the [2Fe-2S] cluster. The result from Gauquelin and co-workers showed that the removal of the [2Fe-2S] cluster resulted in a more significant decrease in the *in vitro* activity with physiological redox partner (ferredoxin) than the removal of the His-ligated [4Fe-4S] cluster, strongly supporting the electron entry point could be the [2Fe-2S] cluster. Notably, they also performed truncation on the *Ca*HydA1 [FeFe] hydrogenase to the M1-type like, the H-domain containing hydrogenase. They showed that the truncated protein had low catalytic activity in both solution assays and when absorbed to an electrode, but further data were not reported. The truncation of the M2 type *Me*HydA from *Megasphaera elsdenii* to only H-cluster containing *Me*H-HydA (M1 type like) by removing the entire F-domain was done by Caserta *et al*, and their results displayed that the truncated protein without accessory F-clusters retained well-assembled and active H-cluster as well as O_2 resistance. Moreover, they also showed that the truncation led to much more bias towards H_2 production. [150] It is evident that in both scenarios, the F-clusters are a key factor in tuning catalytic bias. Artz and coworkers investigated the reduction potentials of [FeFe]-hydrogenase accessory FeS clusters by EPR titration experiment. They found that the reduction potential of the His-ligated [4Fe-4S]

cluster is much more negative than the [2Fe-2S], which is thermodynamically favourable when reduced ferredoxin (Fd_{red}) binds and provides electrons through the electron transfer chain to the active site to reduce protons to H_2. Therefore, their results support the idea that the electron entry point is the His-ligated [4Fe-4S] cluster.[151] A site-directed mutation (histidine to cysteine) was done in the His-ligated [4Fe-4S] cluster in *Ca*HydA1, which resulted in a drastic decrease in catalytic activity shown by both *in vitro* and *in vivo* activity assay and a small negative shift in the midpoint potential (E_m) of ~65 mV of the [4Fe-4S] cluster. Their results tend to imply that the electron entry point is the His-ligated [4Fe-4S] cluster.[152] Furthermore, Artz and coworkers investigated the catalytic properties of *Cp*I, *Cp*II and *Cp*III. Both *Cp*II and *Cp*III have two [4Fe-4S] clusters in the F-domain as well as H-domain containing the H-cluster. However, they exert completely different catalytic bias, *Cp*II favors H_2 oxidation and *Cp*III is prone to H_2 evolution. They attributed the bias difference to the reduction potential of the distal cluster (much more positive -180 mV for *Cp*II compared to much more negative for *Cp*I and *Cp*III). [153]

4.1.3 The aim of the chapter

Comparison between naturally occurring enzymes has allowed some degree of speculation on the role of the F-domain, but the difference observed may as well be a consequence of other variations within the H-domain. In this chapter, I will focus on systematic truncations on *Ca*HydA1 using the overexpression system we developed in the last chapter. I aim to understand the specific role of each FeS cluster by a systematic truncation on the model

enzyme *Ca*HydA1.

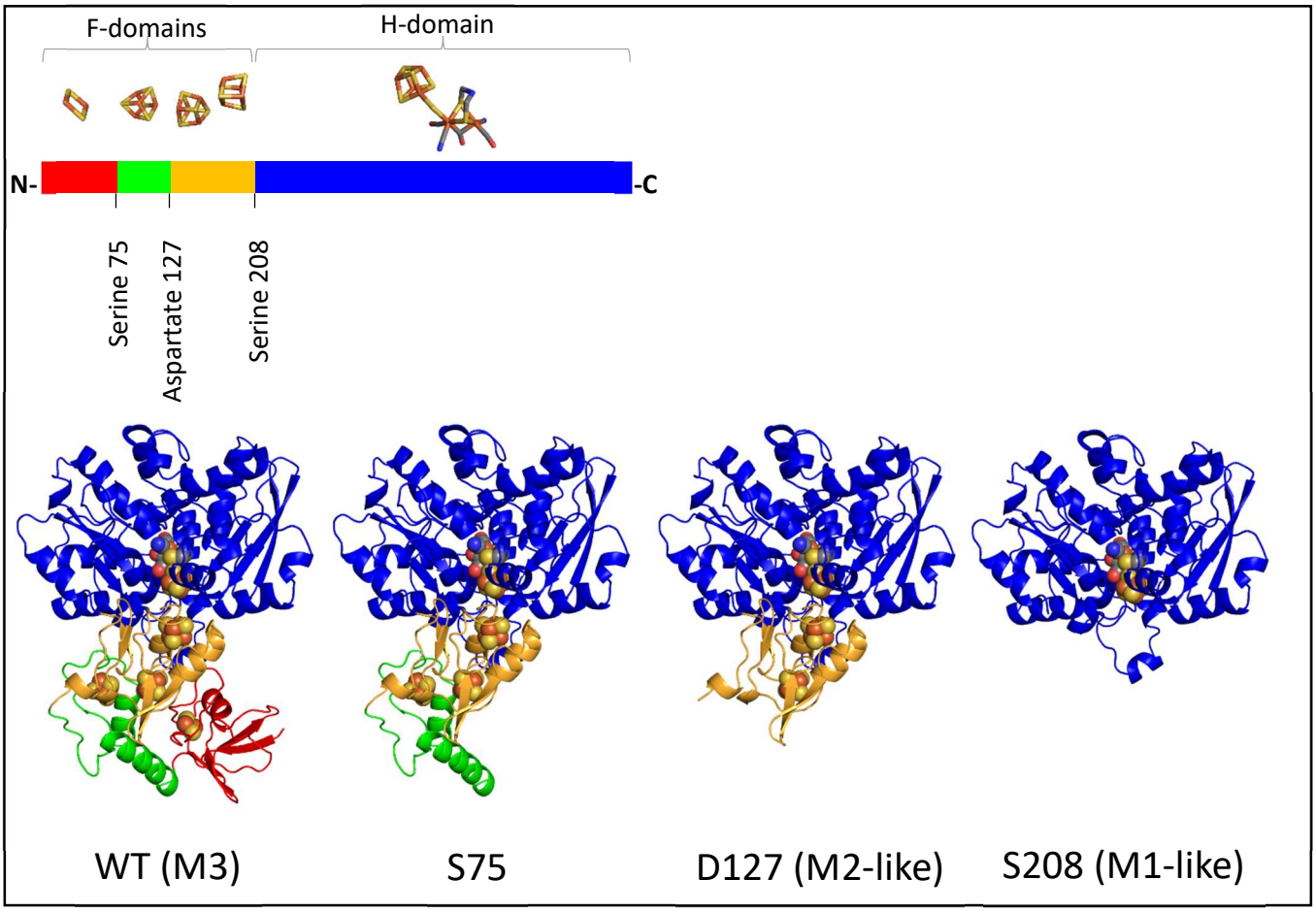


Figure 4: The structural (homology) model of *Ca*HydA1 [FeFe] hydrogenase presenting the systematic truncation of the F-domain we have done in this work: with the red colour showing the N-terminal domain containing a [2Fe-2S] cluster. The His-ligated [4Fe-4S] cluster-containing domain is coloured in green, the two additional [4Fe-4S] cluster domains are shown in yellow, and the H-domain containing the active site is shown in blue. From left to right showing WT *Ca*HydA1 and S75, D127 and S208 truncated *Ca*HydA1 proteins. The figure is adapted from T.Lai *et al* in preparation[136]

4.2 Systematic truncation of the F-domain in *Ca*HydA1 [FeFe] hydrogenases

4.2.1 Overexpression of *Ca*HydA1- S75 [FeFe] hydrogenase

As shown in Figure 4, the aim for this variant is to remove the [2Fe-2S] cluster in the F-domain, therefore we aim to truncate the entire N-terminal domain for this protein without interfering other domains. CaHydA1-S75 truncation position was identified by mapping the domains on InterPro (https://www.ebi.ac.uk/interpro/). The N-terminal domain containing [2Fe-2S] cluster corresponds to the first 74 amino acids of the protein. This domain is homologous to the plant-type or mammalian-type ferredoxins. Thus, the first 74 amino acids were truncated by removing the DNA sequence corresponding to the amino acids in the gene. The truncated gene for *Ca*HydA1-S75 was amplified by PCR using following Primer: CTTTAAGAAGGAGATATACATATGTCCGATGAAGTAAAAGAACGAATC. rev: AGTGGTGGTGGTGGTGGTGCTCGAGTTATTTTTCAAATTGAGGATGACTCC. The plasmid pET21 was suited well for WT apo-*Ca*HydA1 shown in chapter 3, therefore, the gene was cloned into pET21 vector using the NEBuilder HiFi assembly cloning kit (NEB) and verified by DNA sequencing (Figure 5). The molecular biology for preparation of the S75 plasmid was performed by collaborator Dr Simone Morra at the University of Nottingham. My part was to overexpress the variant and perform its functional and spectroscopic characterization.

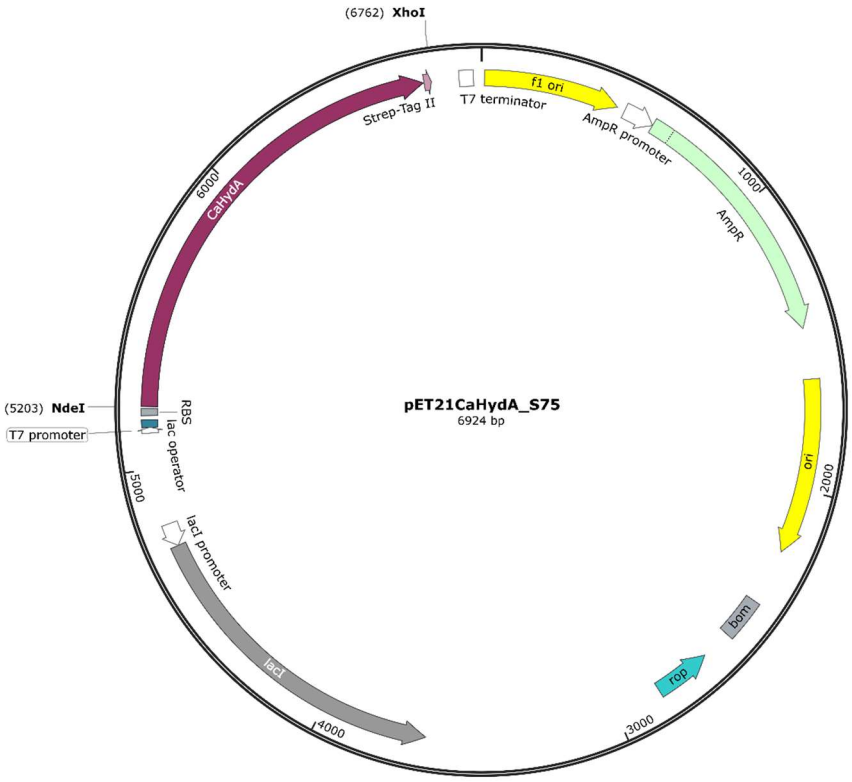
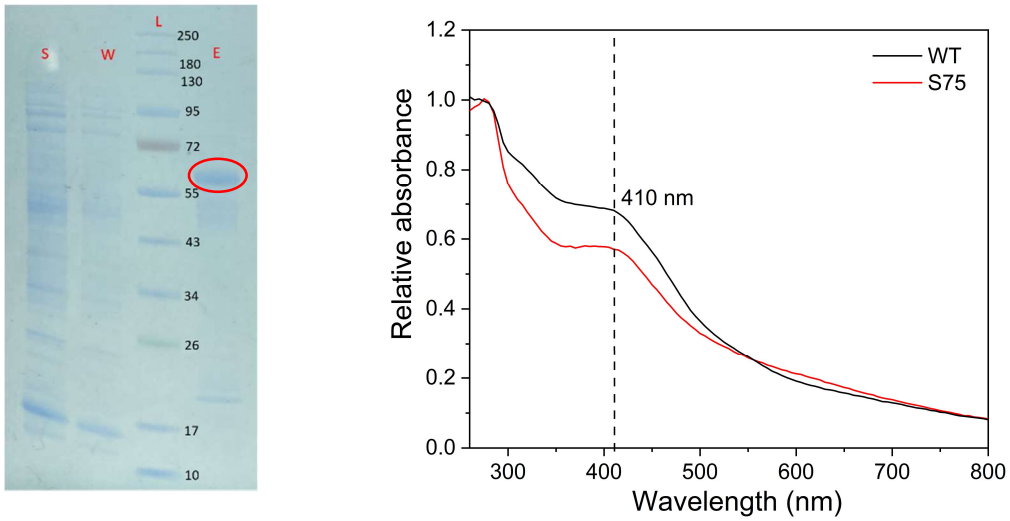


Figure 5: Graphical structure of the plasmid pET21 for apo-CaHydA1-S75 truncated variant.

The plasmids were transformed into *E. coli* BL21ΔiscR cells and the protein was expressed and purified following the same method described for the full-length protein. The protein was isolated successfully, yielding 3 mg per liter of culture. The purity of the protein was determined by SDS-PAGE, where the red circle corresponds to S75 at 57.5 kDa (Figure 6A). The FeS clusters for the S75 truncated variant was confirmed by UV-Visible spectroscopy (as shown in figure 6A), where a decrease of the band around 420 could be seen, agreeing with the removal of the [2Fe-2S] cluster. The iron content of S75 was confirmed by Inductively Coupled Plasma Mass Spectrometry (ICP-MS) (table 2). The ICP-MS experiments were performed by collaborator Dr Simone Morra at the University of Nottingham.



(A) (B)

Figure 6: (A) SDS-PAGE of the apo-CaHydA1-S75 [FeFe] hydrogenase after the strep tag affinity column. Red circle indicates the desired bands for the protein at 57.5 kDa. (B) The UV-Visible (UV-Vis) absorption spectrum of purified apo-CaHydA1-S75 and WT-CaHydA1. This absorbance represents a 10 µM apo-CaHydA1-S75 and WT apo-CaHydA1 in 100 mM Tris-HCl, 150 mM NaCl, pH 8 buffer.

Table 2: Determination of the Fe content by ICP-MS and expected Fe content of the WT holo-CaHydA1 and truncated variant (CaHydA1-S75)

	WT *Ca*HydA1	*Ca*HydA1-S75
Fe content	22.0 ± 1.4	18.5 ± 1.2
Fe content / expected	20	18

The maturation condition of apo-*Ca*HydA1-S75 was tested with PDT cofactor, and the peak 1953 cm^{-1} representing the most pronounced peak of H_{ox} (PDT) reached maximum intensity after 15-20 h (as shown in Figure 7). Interestingly, it required a longer incubation time compared with WT, which achieved 90 % maturation after 1h. It could be that the removal of

N-terminal domain affects the electropositive channel, resulting in a weaker interaction of the apo-protein with the negatively charged PDT cofactor. Thus, the maturation of apo-*Ca*HydA1-S75 was done with a 20 h incubation of synthetic cofactors to ensure complete maturation following similar protocol with the WT enzyme.

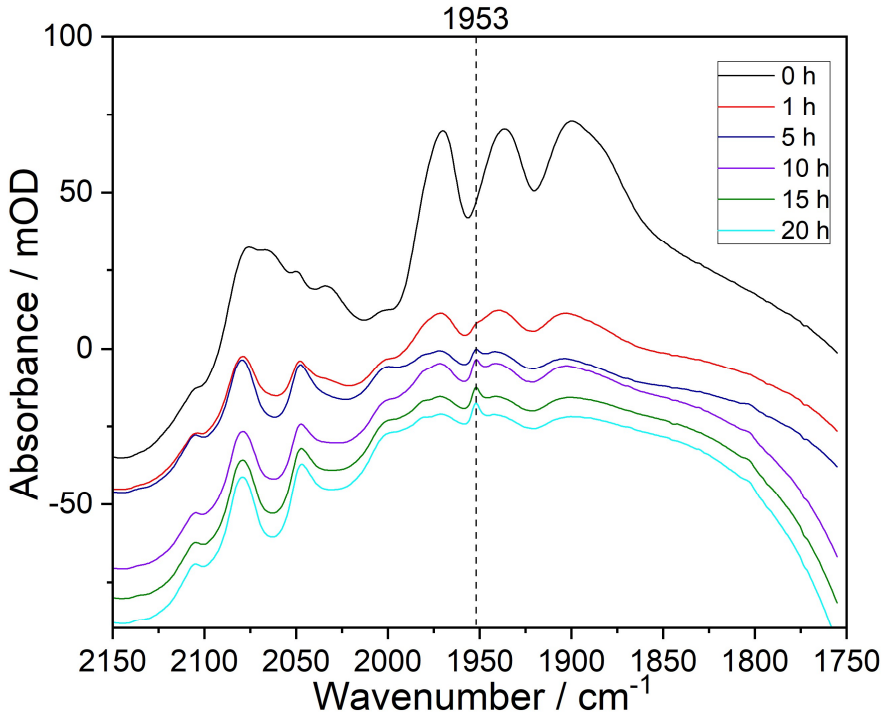


Figure 7: FTIR spectra of the apo-CaHydA1-S75 [FeFe] hydrogenase maturated with native PDT cofactor at different incubation times with PDT solution. The broad peaks arise from the free PDT cofactor. The dash line represents the most pronounced peak of H_{ox}(PDT) at 1953 cm^{-1}.The baseline is not baseline corrected due to a large proportion of free PDT.

4.2.2 Overexpression of M2 type like *Ca*HydA1- D127 [FeFe] hydrogenase

The aim for this variant is to mimic the M2 type [FeFe] hydrogenases, where two [4Fe-4S] clusters can be found in the F-domain alongside the H-domain (Figure 4). *Ca*HydA1-D127

truncation position was identified by mapping the domains on InterPro (https://www.ebi.ac.uk/interpro/). The N-terminal domain containing the [2Fe-2S] cluster and the His-ligated [4Fe-4S] cluster domain corresponds to the first 127 amino acids of the protein. Thus, the first 127 amino acids were selected to be truncated by removing the DNA sequence corresponding to the amino acids in the gene. The truncated gene for CaHydA1-D127 was amplified by PCR using following Primer: CTTTAAGAAGGAGATATACATATGGATAAGGATGCTCTAGTTGATAATAG. rev: AGTGGTGGTGGTGGTGGTGCTCGAGTTATTTTTCAAATTGAGGATGACTCC. The gene was cloned into pET21 vector using the NEBuilder HiFi assembly cloning kit (NEB) and verified by DNA sequencing (Figure 8). The molecular biology for preparation of the D127 plasmid was performed by collaborator Dr Simone Morra at the University of Nottingham. My part was to overexpress the variant and perform its functional and spectroscopic characterization.

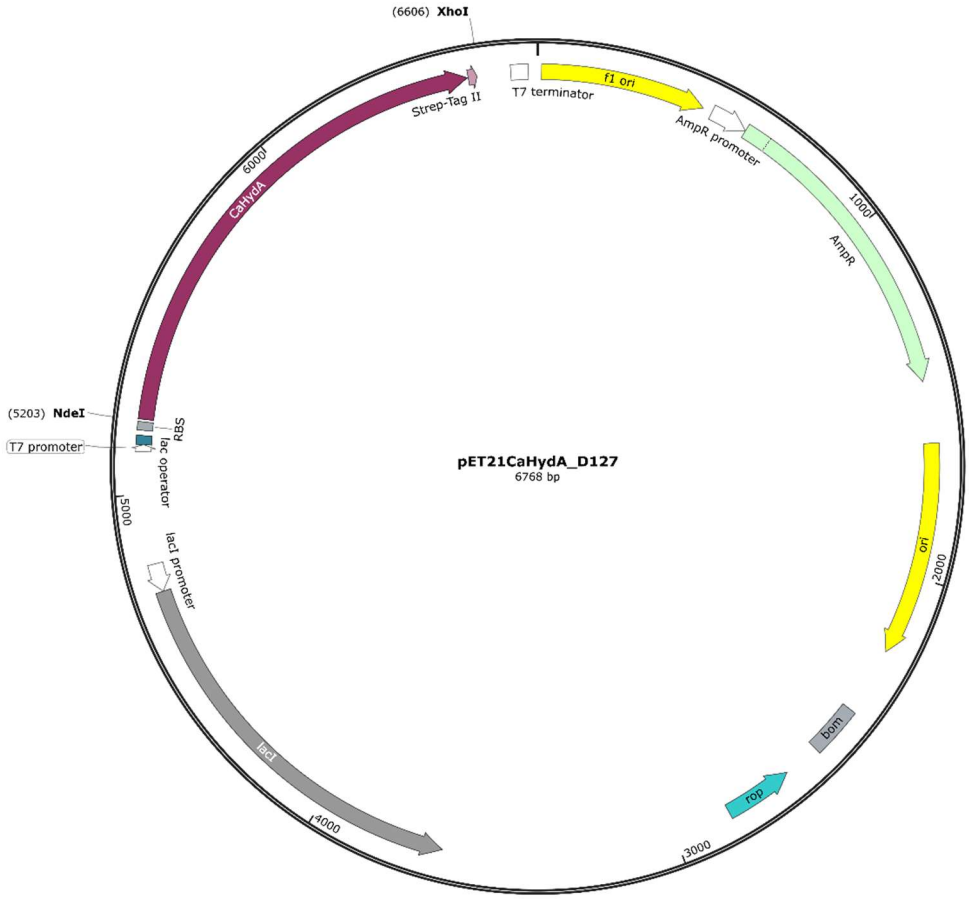
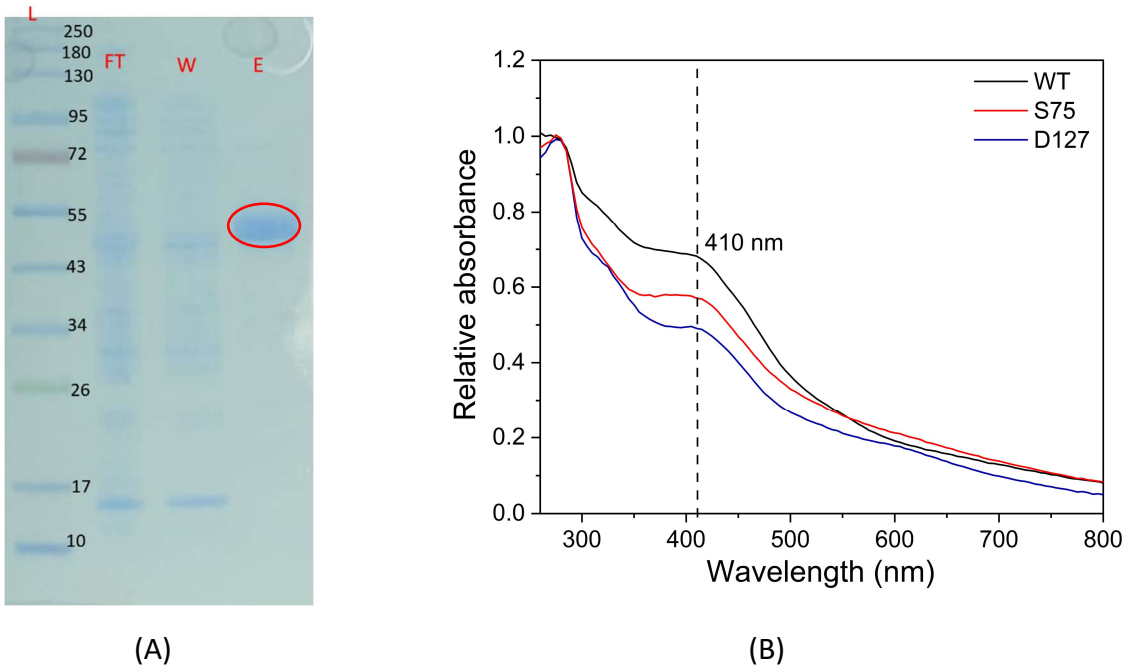


Figure 8: Graphical structure of the plasmid pET21 for apo-CaHydA1_D127 truncated variant.

The plasmids were transformed into *E. coli* BL21ΔiscR cells and the protein was expressed and purified following the same method described for the full-length protein. The protein was isolated successfully, yielding 20 mg per liter of culture. The purity of the protein was determined by SDS-PAGE, where the red circle corresponds to D127 at 51.4 kDa (figure 9A). The FeS clusters for D127 truncated variant was confirmed by UV-Visible spectroscopy (as shown in figure 9B), where a successive decrease of the bands around 400 nm could be seen, agreeing with removing the [2Fe-2S] cluster and His-ligated [4Fe-4S] cluster. The iron content of D127 was confirmed by ICP-MS (Table 3). The ICP-MS experiments were performed by collaborator Dr Simone Morra at the University of Nottingham.



(A) (B)

Figure 9: (A) SDS-PAGE of the apo-CaHydA1-D127 [FeFe] hydrogenase after the strep tag affinity column. Red circle indicates the desired bands for the protein at 51.4 kDa. (B) The UV-Visible (UV-Vis) absorption spectrum of purified apo-CaHydA1-D127, WT-CaHydA1 and S75. This absorbance represents a 10 µM apo-CaHydA1-D127 in 100 mM Tris-HCl, 150 mM NaCl, pH8 buffer shown in blue, WT apo-CaHydA1 shown in black, S75 shown in red.

Table 3: Determination of the Fe content by ICP-MS and expected Fe content of the WT holo-CaHydA1 and truncated variant (CaHydA1-D127)

	WT *Ca*HydA1	*Ca*HydA1-D127
Fe content	22.0 ± 1.4	10.6 ± 0.5
Fe content / expected	20	14

The maturation condition of apo-CaHydA1-D127 was tested with ADT cofactor, the peak 2013

cm^{-1} representing the most pronounced peak of H_{ox}-CO reached maximum intensity after 10 h. However, only about 60 % of protein was maturated after 1 h incubation, which is less than that of WT enzyme (90 %) (as shown in Figure 10). This suggests that truncation has affected the maturation process, but the reason is not clear. The maturation of apo-CaHydA1-D127 was performed with a 10 h incubation of synthetic cofactors following a similar protocol as described previously.

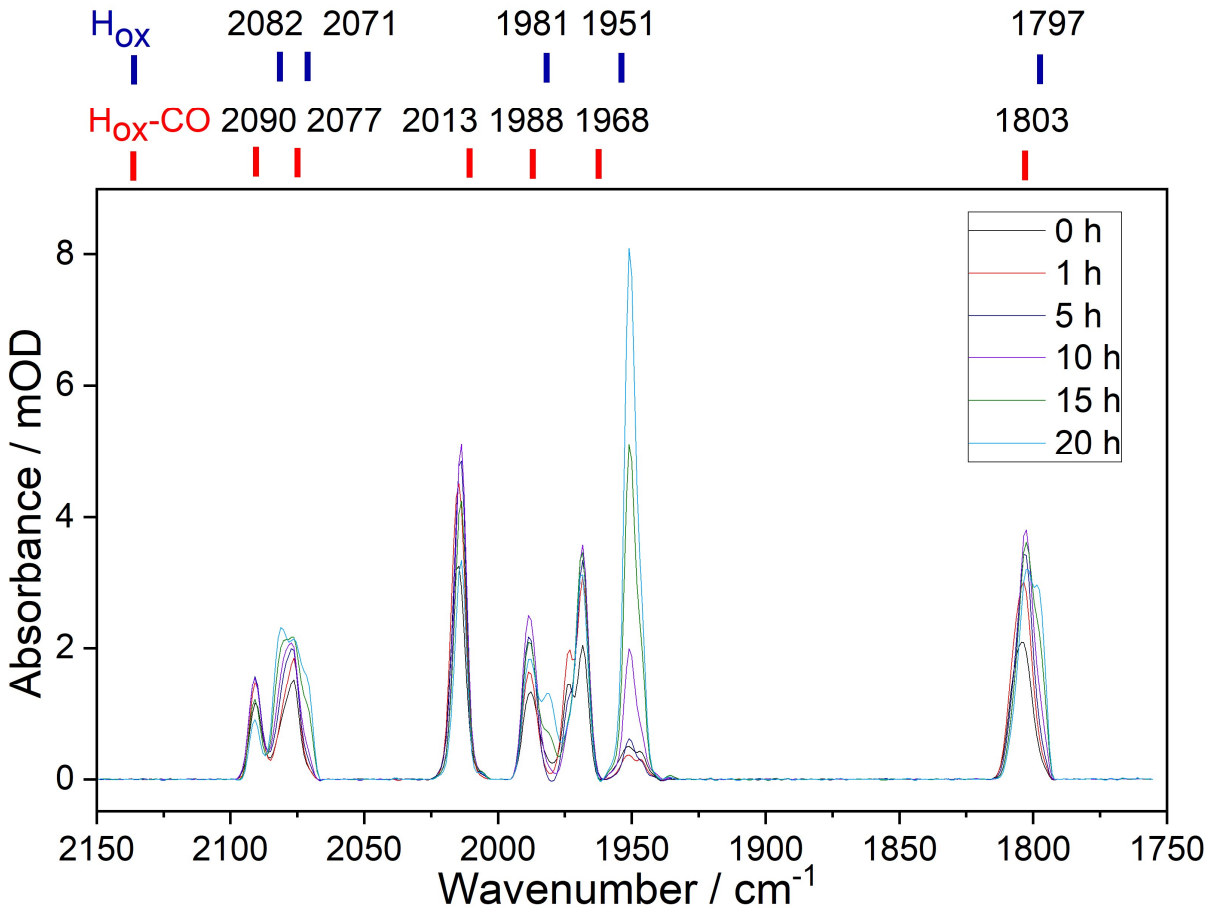


Figure 10: FTIR spectra of the apo-CaHydA1-D127 [FeFe] hydrogenase maturated with native ADT cofactor in different incubation time with ADT solution.

4.2.3 Overexpression of M1 type like *Ca*HydA1- S208 [FeFe] hydrogenase

The aim for this variant is to mimic the M1 type [FeFe] hydrogenases, with only H-domain present for this protein. *Ca*HydA1-S208 truncation position was identified by mapping the domains on InterPro (https://www.ebi.ac.uk/interpro/). The entire F-domain containing the three [4Fe-4S] cluster and one [2Fe-2S] cluster corresponds to the first 208 amino acids of the protein. Thus, the first 208 amino acids were selected to be truncated by removing the DNA sequence corresponding to the amino acids in the gene. The truncated gene for CaHydA1-S208 was amplified by PCR using the following Primer: CTTTAAGAAGGAGATATACATATGTCCCATATAGAAAAAGTTCAAG. rev: AGTGGTGGTGGTGGTGGTGCTCGAGTTATTTTTCAAATTGAGGATGACTCC. The gene was cloned into pET21 vector using the NEBuilder HiFi assembly cloning kit (NEB) and verified by DNA sequencing (Figure 11). The molecular biology for preparation of the S208 plasmid was performed by collaborator Dr Simone Morra at the University of Nottingham. My part was to overexpress the variant and perform its functional and spectroscopic characterization.

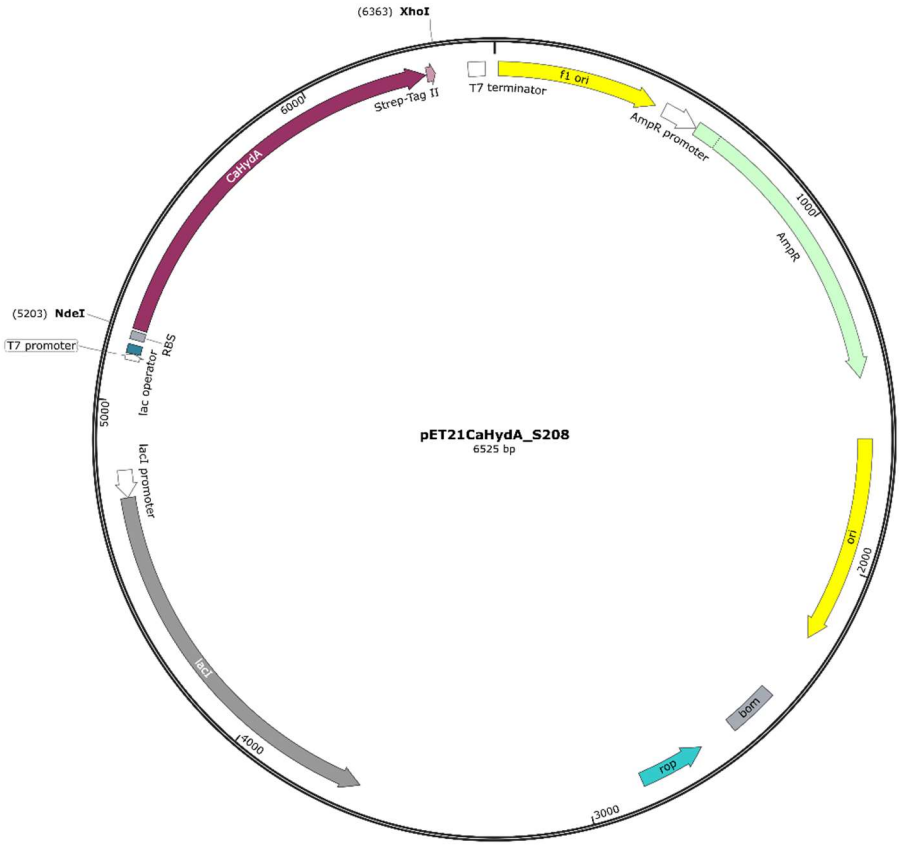
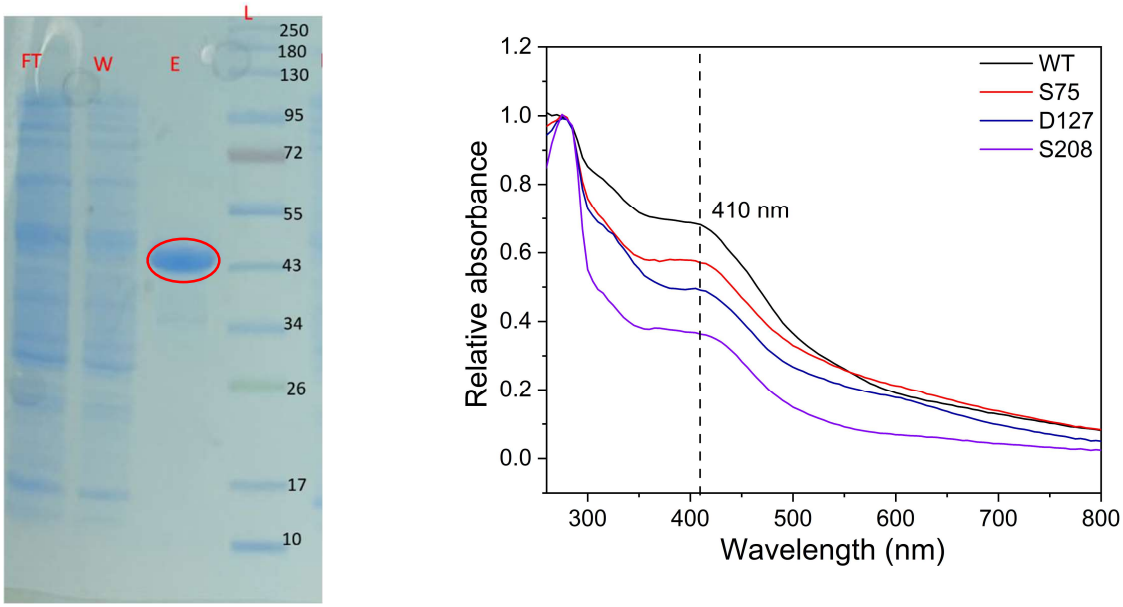


Figure 11: Graphical structure of the plasmid pET21 for apo-CaHydA1-S208 truncated variant.

The plasmids were transformed into *E. coli* BL21ΔiscR cells and the protein was expressed and purified following the same method described for the full-length protein. The protein was isolated successfully, yielding 28 mg per liter of culture. The purity of the protein was determined by SDS-PAGE, where the red circle corresponds to S208 at 42.8 kDa (Figure 12A). The FeS cluster ($[4Fe\text{-}4S]_H$) for S208 truncated variant can be confirmed by UV-Visible spectroscopy (as shown in Figure 12B), in which a further decrease of the band for S208 around 400 nm could be seen, this agreed with removing the entire F-domain containing three [4Fe-4S] clusters and one [2Fe-2S] cluster. The iron content of S208 was confirmed by ICP-MS (Table 4). The ICP-MS experiment was performed by collaborator Dr Simone Morra in the University of Nottingham.



(A) **(B)**

Figure 12: (A) SDS-PAGE of the apo-CaHydA1-S208 [FeFe] hydrogenase after the strep tag affinity column. Red circle indicates the desired bands for the protein at 42.8 kDa. (B) The UV-Visible (UV-Vis) absorption spectrum of purified apo-CaHydA1-S208, WT-CaHydA1, S75 and D127. This absorbance represents a 10 µM apo-CaHydA1-S208 in 100 mM Tris-HCl, 150 mM NaCl, pH 8 buffer shown in purple, WT apo-CaHydA1 shown in black, S75 shown in red and D127 shown in blue.

Table 4: Determination of the Fe content by ICP-MS and expected Fe content of the WT holo-CaHydA1 and truncated variant (CaHydA1-S208)

	WT *Ca*HydA1	*Ca*HydA1-S208
Fe content	22.0 ± 1.4	6.7 ± 0.3
Fe content / expected	20	6

It is interesting to parallel the expression yields of truncated variants (Table 5), it seems that the yield increases when we truncate the protein further, except for the S75 variant. The reason could be that the protein contains fewer FeS clusters when we truncate more of the

protein, making it more readily biosynthesised (insertion of FeS clusters by ISC machinery). In the case of S75, the yield is the lowest at 3 mg per liter of culture. It could be related to the N-terminal domain that is crucial for the solubility of the protein and could potentially affect the folding of the protein.

Table 5: Yield of the WT apo-CaHydA1 and apo-truncated variants (CaHydA1-S75, CaHydA1-D127 and CaHydA1-S208)

	WT apo-*Ca*HydA1	*Ca*HydA1-S75	*Ca*HydA1-D127	*Ca*HydA1-S208
Yield / mg L^{-1} of culture	5 ± 1	3 ± 1	20 ± 4	28 ± 5

4.3 Functional characterisation of truncated *Ca*HydA1 [FeFe] hydrogenases

4.3.1 Solution activity assay with artificial redox partner

The catalytic activity of truncated *Ca*HydA1 variants was assessed through solution activity assays using methyl viologen as an electron mediator (artificial redox partner). Both H_2 oxidation and evolution activities were measured in 100 mM Tris-HCl, 150 mM NaCl, pH 8 buffer at 37 ^{o}C. For the activity assays for H_2 oxidation rate, methyl viologen was used as the electron acceptor. Briefly, the reduction of 10 mM methyl viologen by 1 nM enzyme in a H_2 saturating buffer can be measured by UV-Vis spectroscopy. The absorbance of methyl viologen was followed at 604 nm (ε_{604} = 13.6 mM $^{-1}$ cm $^{-1}$) for 1 minute, and the rates could be

calculated by measuring the gradient. For the activity assays for H_2 evolution rate, the evolution of H_2 is monitored by gas chromatography (GC) using methyl viologen as the electron donor. The gas chromatography (Agilent 7820A, purged packed inlet, Supelco Carboxen-1010 column, thermal conductivity detector, argon carrier gas) was performed at the University of Nottingham by collaborator Dr. Morra.

In general, the catalytic activities of truncated *Ca*HydA1 [FeFe] hydrogenases measured by solution activity assays are drastically lower than that of the WT *Ca*HydA1 [FeFe] hydrogenases in both H_2 oxidation and H_2 evolution rates (Figure 13 and Table 6). The H_2 evolution rates are in general lower than H_2 oxidation rate. Interestingly, the activity appears to increase within the truncations. A rationale to this could be that the charge on the protein surface is changed with the truncations, which affect the interaction between the protein and methyl viologen (effectively changing the K_m for methyl viologen, K_m is a Michaelis constant that serves as a quantitative measure of enzymes' affinity for the substrates, electron transfer to the protein maybe influenced). In addition, since the electron entry changes in each truncated variant, the potential of the distal cluster may vary. Thus, the potential mismatch between methyl viologen and distal cluster of the truncated variants may cause a significant reduction in values. Regardless, the change in electronic characteristics within the active site could largely alter the catalytic rates of the truncated variants.

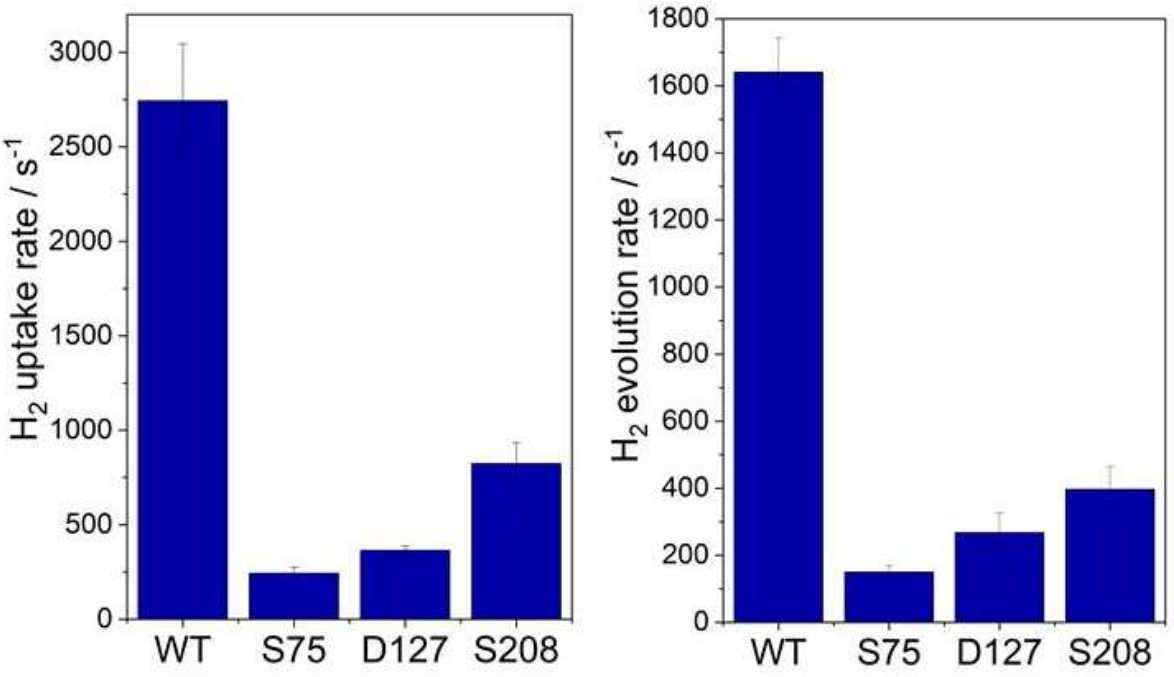


Figure 13: Solution activity assays of WT *Ca*HydA1 and truncated variants. The H_2 oxidation rate was measured by following the reduction of methyl viologen by the enzyme in a H_2-saturated solution. The H_2 evolution rate was measured by gas chromatography (GC) using methyl viologen as electron donor. All rates are measured in 100 mM Tris-HCl, 150 mM NaCl, pH 8 with 10 mM methyl viologen, 37 °C. Rates are given in s^{-1}, as U/mg would be inaccurate due to change in enzyme size.

Table 6: Solution activity assays of WT CaHydA1 and truncated variants. Data shows the exact numbers, the activities relative to WT and bias between H_2 evolution and uptake. Evol/upt represents H_2 evolution against H_2 uptake.

	H_2 uptake	Relative to WT	H_2 evolution	Relative to WT	Bias (evol/upt)
WT	2744.0 ± 301.7		1640.9 ± 111.0		59.8%
S75	243.7 ± 32.4	8.9%	149.7 ± 18.0	9.1%	61.4%
D127	364.9 ± 23.7	13.3%	267.4 ± 51.5	16.3%	73.3%
S208	823.6 ± 111.1	30.0%	396.6 ± 48.2	24.2%	48.2%

4.3.2 Solution activity assays with the physiological redox partner

One of the major objectives of this project is to determine the electron entry point of M3 type [FeFe] hydrogenase, as this tunes the reversibility of intermolecular and intramolecular electron transfer for reversible catalytic H_2 activation.[152] *In vivo*, *Ca*HydA1 is responsible for the reoxidation of ferredoxin resulting in H_2 evolution. The key redox partner for *Ca*HydA1 is a two [4Fe-4S] cluster containing bacterial type ferredoxin. The electron transfer between the ferredoxin and *Ca*HydA1 is an essential step for biological H_2 evolution [154]. We engineered M3 type *Ca*HydA1 [FeFe] hydrogenase by removing the FeS cluster containing domain in the F-domain. It would be interesting to investigate the H_2 evolution and oxidation activities of the truncated variants when interacting with physiological redox partner compared to the wild type enzyme since we are significantly truncating the domains of the protein (which could affect the binding site of the protein).

The physiological redox partner for *Ca*HydA1 [FeFe] hydrogenase used was *C. acetobutylicum* ferredoxin (*Ca*Fd, gene ID CAC0303). *Ca*Fd is a typical clostridial ferredoxin which efficiently interacts with *Ca*HydA1 in both H_2 oxidation and H_2 evolution *in vivo*. [155] Both H_2 oxidation and evolution activities were measured in 100 mM Tris-HCl, 150 mM NaCl, pH 8 buffer at 37 ^oC. For the activity assays for H_2 oxidation rate, oxidised *Ca*Fd was used as the electron acceptor. Briefly, the reduction of 30 μM oxidised *Ca*Fd by 1 nM enzyme in a H_2 saturating buffer can be measured by UV-Vis spectroscopy. The solution activity assay experiment with

the physiological redox partner was performed at the University of Nottingham by collaborator Dr. Morra. The absorbance of oxidised *Ca*Fd was followed at 390 nm (ε_{390} = 32.6 mM^{-1} cm^{-1}) for 1 minute, and the rates could be calculated by measuring the gradient. For the activity assays for H_2 evolution rate, the evolution of H_2 is monitored by gas chromatography (GC) using reduced *Ca*Fd as the electron donor. Strikingly, we found that only WT *Ca*HydA1 showed activity when interacting with *Ca*Fd with 281.4 ± 32.3 s^{-1} and 1055 ± 12 s^{-1} for H_2 oxidation and H_2 evolution respectively. For truncated proteins, we observed negligible specific catalytic activities for S75, D127 and S208 for both H_2 oxidation rates and H_2 evolution rates (Table 7 and Figure 14). Notably, it seems that the activity for WT and all truncated variants are more biased towards H_2 evolution when interacting with *Ca*Fd. This could rationalise why *Ca*HydA1 is considered to be responsible for H_2 production *in vivo*. These data clearly suggest that the N-terminal domain, which is missing in S75, is essential for the physiological redox partner *Ca*Fd to bind, supporting that the binding site would be more likely to be the N-terminal domain containing the [2Fe-2S] cluster. Absence of the N-terminal domain disrupts the interfacial electron transfer between both proteins. This also supports the [2Fe-2S] cluster being the electron entry point of this enzyme.

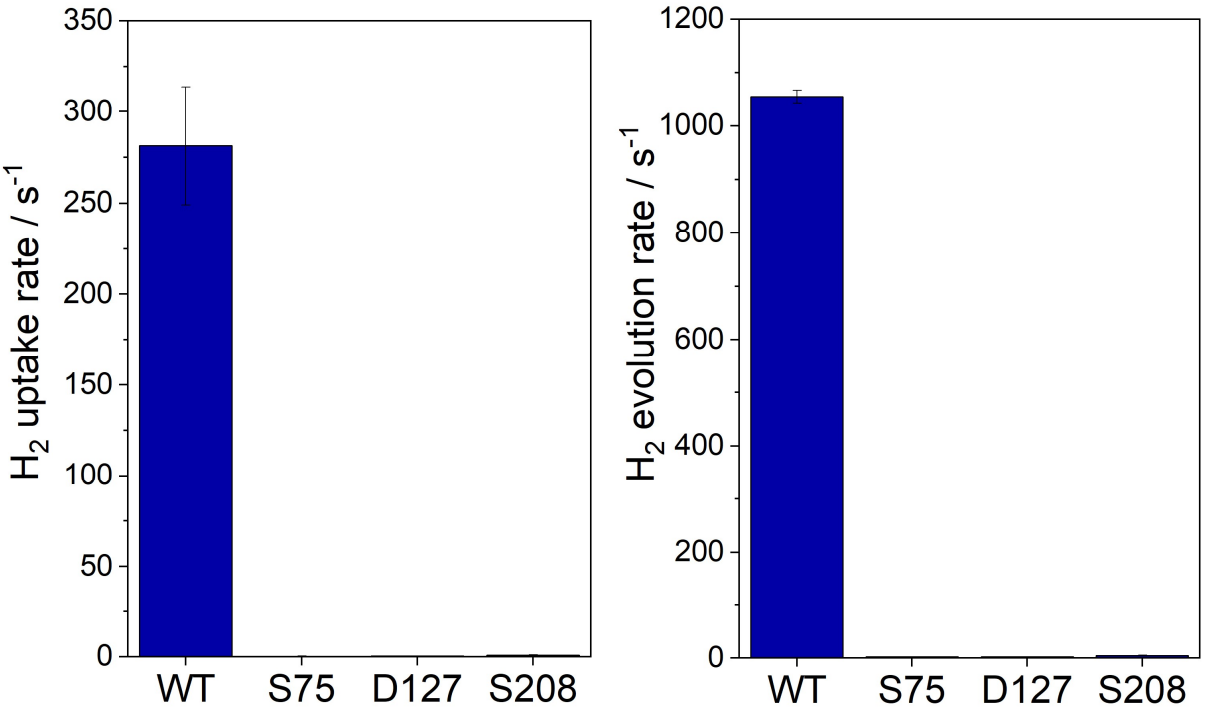


Figure 14: solution activity assays of WT *Ca*HydA1 and truncated variants using 30 µM of the physiological redox partner *Ca*Fd. The H_2 oxidation rate was measured by following the reduction of methyl viologen by the enzyme in a H_2-saturated solution. The H_2 evolution rate was measured by gas chromatography (GC) using methyl viologen as electron donor. All rates are measured in 100 mM Tris-HCl, 150 mM NaCl, pH 8 with 10 mM methyl viologen, 37 °C. Rates are given in s^{-1}, as U/mg would be inaccurate due to change in enzyme size.

Table 7: Solution activity assays of WT CaHydA1 and truncated variants using physiological redox partner CaFd. Data shows the exact numbers, the activities relative to WT and bias between H_2 evolution and uptake. Evol/upt represents H_2 evolution against H_2 uptake.

	H_2 uptake	Relative to WT	H_2 evolution	Relative to WT	Bias (evol/upt)
WT	281.4 ± 32.3		1055 ± 12		375%

S75	0.2 ± 0.1	0.08%	2.2 ± 0.2	0.21%	961%
D127	0.3 ± 0.1	0.11%	2.4 ± 0.4	0.22%	784%
S208	0.8 ± 0.2	0.29%	4.8 ± 0.9	0.45%	580%

4.3.3 Electrochemistry

The catalytic behaviour (the shape of the cyclic voltammogram (CV)) of all truncated proteins are very similar to WT *Ca*HydA1 (Figure 15). Interestingly, the current densities are fairly comparable for WT and truncated proteins (the current is influenced by both the catalytic activity as well as electrode coverage, thus, direct interpretation of current should be done carefully). Very Importantly, all the truncated forms also worked very efficiently without displaying overpotential in any direction, and they seemed to be more biased towards H_2 production (the overpotential and catalytic bias of these truncated proteins will be discussed in more detail in chapter 5). The current densities of these variants increase down the truncation series, which is similar to that observed in the solution activity assays, although as noted above, this could be due to differences in coverage on the electrode rather than inherent activity.

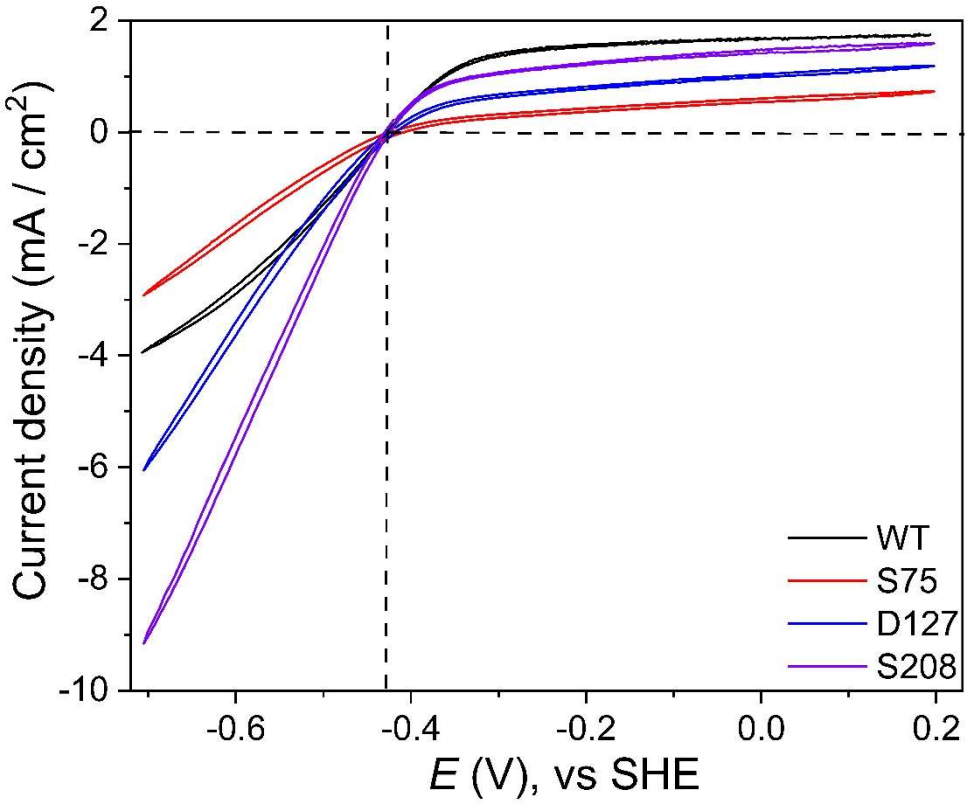


Figure 15: Cyclic voltammetry (CV) of the WT and truncated CaHydA1 [FeFe] hydrogenases adsorbed onto a pyrolytic graphite electrode at pH 7, room temperature (RT), 100% H_2 (1 L/ min), 2000 rpm and 20 mV /s scan rate. The horizontal dashed line represents the zero current, and the vertical dashed line indicates the thermodynamic potential of the $2H^+/H_2$ couple, under the experimental conditions.

4.4 Spectroscopic characterisation of truncated *Ca*HydA1 [FeFe] hydrogenases

4.4.1 IR spectroscopic assignment for truncated *Ca*HydA1 [FeFe] hydrogenases

All truncated proteins have nearly identical FTIR spectra (Figure 16). The as isolated WT sample ('As is') contains mainly the H_{ox} state, with the most pronounced peak at 1946 cm^{-1}.

For all the truncated variants, the main peak of the 'As is' spectrum is blue-shifted to 1951 cm^{-1}. The other CO band has shifted from 1969 cm^{-1} to 1981 cm^{-1}. One of the CN ligands is shifted from 2070 cm^{-1} to 2071 cm^{-1}, while the other CN band remains the same. Despite the blue shift of all ligands, the bridging CO band has slightly shifted toward lower wavenumber (red-shift) and appears at 1797 cm^{-1} compared with 1801 cm^{-1} in the WT. This suggests a long-range effect of the FeS clusters in the F-domain on the electron density of the H-cluster. Interestingly, the ratio between the two CO bands (1969 cm^{-1} and 1946 cm^{-1}) in WT enzyme is slightly larger than the ratio of 1981 cm^{-1} and 1951 cm^{-1} in all truncated variants. In all truncated variants, only small peak intensity arises for 1981 cm^{-1} but dominates for 1951 cm^{-1}. This could indicate a conformational change in the active site region. In all cases, the spectra contain very pure H_{ox} state with small amount of H_{ox}-CO state, likely formed by a 'cannibalisation' process, in which some active sites break down and release CO ligands that inhibit some of the intact active sites (this arises from the degradation of the $[2Fe]_H$). [39] In summary, IR spectra demonstrated that the electronic environment is consistent between truncated variants but differs slightly from the WT enzyme suggesting a long-range effect of the FeS clusters in the F-domain on the electronic structure of the H-cluster. This could indicate a local change in the coordination environment of the H-cluster in the truncated proteins, which in turn affects its active site region.

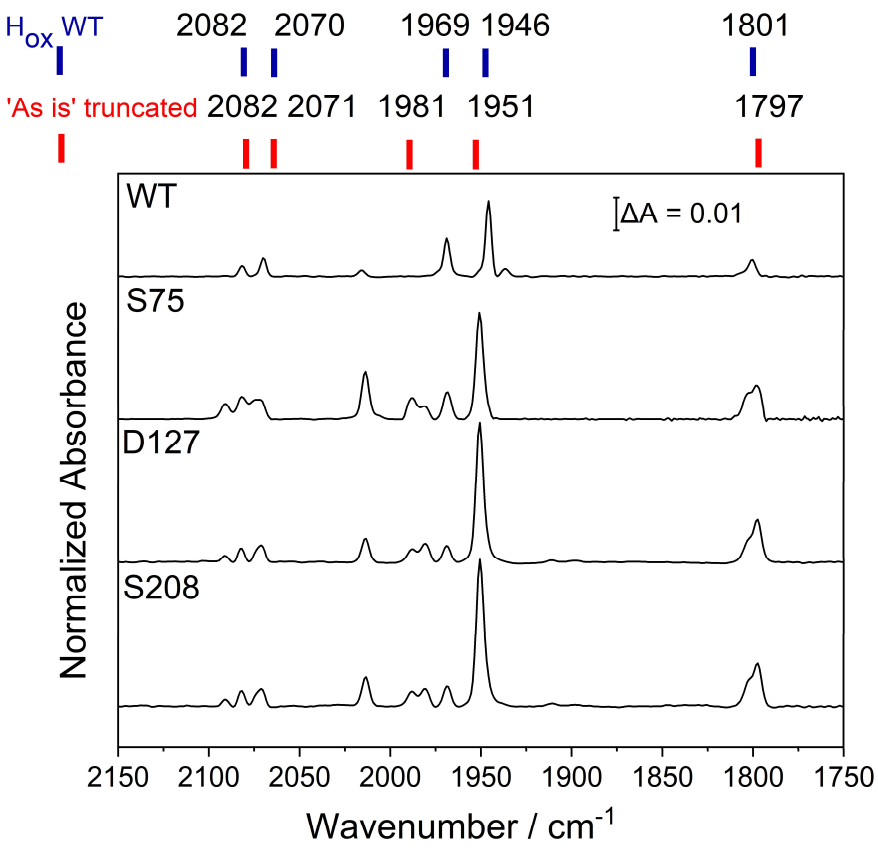


Figure 16: The FTIR spectrum of 1-2 mM of WT and truncated proteins as isolated (maturated with ADT cofactors) at pH 8. The H_{ox} (ADT) state and 'As is' truncated state are highlighted with blue and red respectively. The spectra is baseline corrected by subtracting the water vapour peaks.

To further investigate the characteristics of the active site, all truncated variants were maturated with unnatural synthetic cofactor (PDT), showing a blue shift of all ligands compared to that maturated with native cofactor (ADT) (Figure 17). This is due to the substitution of a nitrogen atom with a carbon atom on the bridgehead, leading to lower electron density in the H-cluster. Therefore, less π-back bonding from the iron atom to the CO and CN ligands results in stronger bonds of CO and CN. The CN peaks shifts from 2082 and 2070 cm^{-1} to 2083 and 2072 cm^{-1}. In addition, the two CO peaks are shifted from 1981 and 1951 cm^{-1} to 1981 and 1953 cm^{-1}. Similar observations can be seen in PDT variants (blue shifts

of all ligands except bridging CO band). This further confirms a long-range effect caused by removing FeS cluster domains on the the H-cluster. In all cases, the spectra contain very pure H_{ox} (PDT) state. The PDT maturated truncated variants are inactive, however, these PDT maturated truncated variants enable us to study the potential of the $[4Fe\text{-}4S]_H$ cluster of the H-cluster as it effectively switches off the catalysis and will facilitate understanding of the impact of accessory FeS clusters components on the active site potential and catalysis. (i.e. one electron reduction on $[4Fe\text{-}4S]_H$ cluster), which will be further investigated in chapter 6.

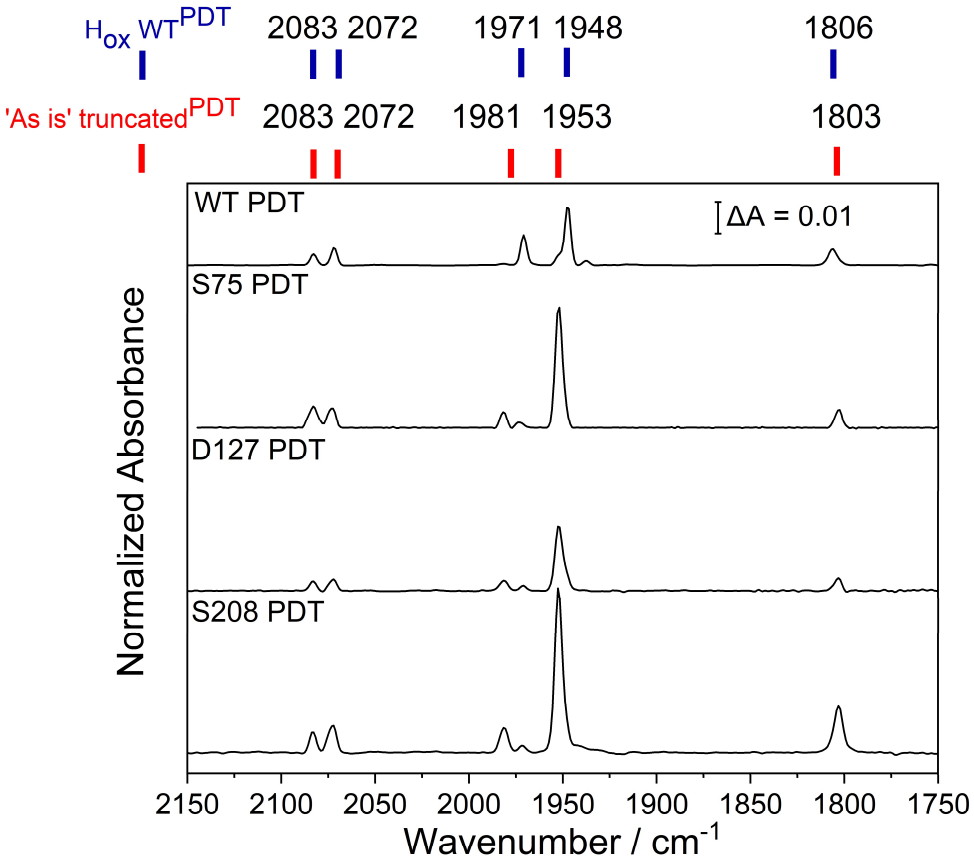


Figure 17: The FTIR spectrum of 1-2 mM WT and truncated proteins as isolated (maturated with PDT cofactors) at pH 8. The H_{ox} (PDT) state and 'As is' truncated state are highlighted with blue and red respectively. The spectra is baseline corrected by subtracting the water vapour peaks.

Pure CO inhibited states could be obtained by flushing CO to WT and truncated variants for 30 mins (Figure 18). All truncated variant CO inhibited states are very similar, and dramatically different from the H_{ox}-CO state in the WT enzyme. In this state, two CN ligands, two terminal CO ligands, a bridging CO ligand as well as an exogenous CO ligand can be found. The most pronounced peak (2013 cm^{-1}) of CO inhibited state of the truncated proteins arises from exogenous CO bound to the open coordination site of distal iron. This peak has slightly shifted towards lower wavenumber compared to the WT enzyme (2015 cm^{-1}). One of the CN peaks is shifted towards a higher wavenumber from 2075 cm^{-1} to 2077 cm^{-1}. In addition, the two terminal CO peaks have shifted towards higher energy, while the bridging CO has shifted towards lower energy. Overall, all the peaks have blue shifts to higher wavenumber except red shifts of exogenous CO and bridging CO. Interestingly, the two terminal CO peaks are separated further apart in terms of wavenumber in truncated variants compared to WT. Clearly, this demonstrates a change of around the active site for the truncated variants.

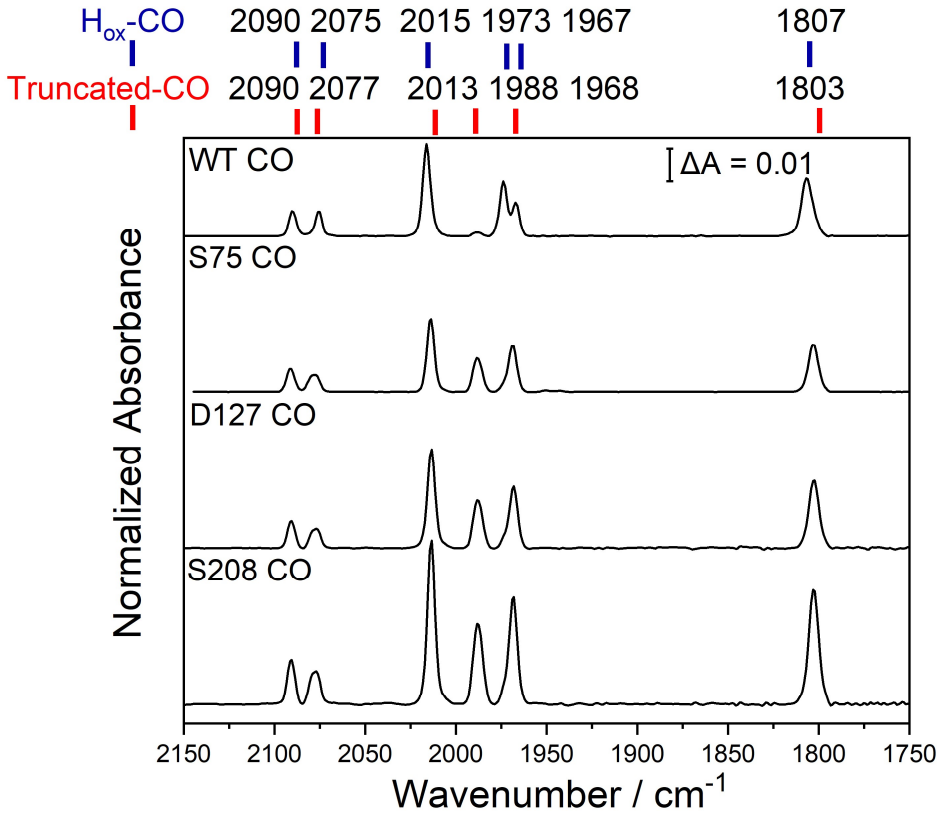


Figure 18: The FTIR spectrum of 1-2 mM WT and truncated proteins inhibited with CO at pH 8. The H_{ox}-CO state and truncated CO inhibited state are highlighted with blue and red respectively. The spectra is baseline corrected by subtracting the water vapour peaks.

The reduced states of WT and truncated variants could be achieved by flushing with H_2, followed by the addition of 10 mM sodium dithionite (NaDT) (Figure 19). Interestingly, the H_{redH}^+ states could be obtained in all truncated variants, and showed very similar spectroscopic characteristics (displaying the same wavenumbers) compared to WT enzyme. Two CN peaks are at 2054 cm^{-1} and 2040 cm^{-1}, and the most pronounced peak is 1899 cm^{-1}, corresponding to terminal CO. The other terminal CO peak at 1921 cm^{-1} seems to be missing for S75 and S208. It was not until recently that one electron reduced H_{redH}^+ state and two electron reduced H_{sredH}^+ state have been confirmed to operate exclusively bridging CO instead of bridging hydride, studied by low temperature IR spectroscopy and nuclear resonance vibrational

spectroscopy (NVRS) together with density functional study (DFT) calculations [85]. The bridging CO peak of this state was then suggested to be 1801 cm^{-1} following the previous work by Ratzloff and coworkers on low temperature IR spectroscopy of *Ca*HydA1 [FeFe] hydrogenase [156]. Interestingly, the ratio between the resting state (H_{ox} / 'As is' truncated states) and the most pronounced peak of H_{redH}^{+} state varies. D127 variant shows nearly a 1:1 ratio between two states, WT displays a 2:1 ratio, and S75 and S208 variants exhibit a 3:1 ratio. A noticeable difference is that the truncated proteins seem to be H_{red} and H_{sredH}^{+} states silent, and in the WT enzyme, visible shoulder peaks of H_{red} and H_{sredH}^{+} states could be seen. Previous work on the spectroelectrochemistry of *Cr*HydA1 and *Dd*HydAB suggested that the *Dd*HydAB is 150 mV more negative compared to F-cluster missing M1 type *Cr*HydA1. *Dd*HydAB exerts redox anti-cooperativity (i.e. the reduction of one cluster disfavours reduction of the neighbouring cluster, possibly caused by the electrostatic repulsion between the clusters). In *Dd*HydAB, when the proximal F-cluster gets reduced, the H_{red} state was converted to $H_{red}H^{+}$ state showing that the proximal cluster could directly influence the proton coupled electronic rearrangement in the H-cluster. In F-cluster free *Cr*HydA1, proton reduction must operate with doubly reduced H-cluster in the $H_{red}H^{+}$ states. However, in *Dd*HydAB, formation of $H_{sred}H^{+}$ state is not necessary as the second electron can be stored in the F-cluster and provided to the H-cluster when H_2 is formed. This could rationalise why it was seen that H_{red} and $H_{sred}H^{+}$ states are stable in *Cr*HydA1 but unstable in *Dd*HydAB[157] [77] [78] [158]. However, an opposite is noted when comparing the spectra of the 4 F-cluster containing WT and F-cluster free S208. In the S208 variant, the peaks from H_{red} and H_{sredH}^{+} states are not seen but are present in the WT enzyme. This will need to be confirmed by spectroelectrochemistry to fully understand the

proton coupled electron transfer (PCET) and redox anti-cooperativity effect in this enzyme. More importantly, the H_{hyd} state can be seen for all truncated protein but is not observed in the WT enzyme. A major characteristic of H_{hyd} state is that the peaks appear in the 1860-1870 cm^{-1} region. We can see two small peaks at 1860 cm^{-1} and 1867 cm^{-1} in all truncated variants.

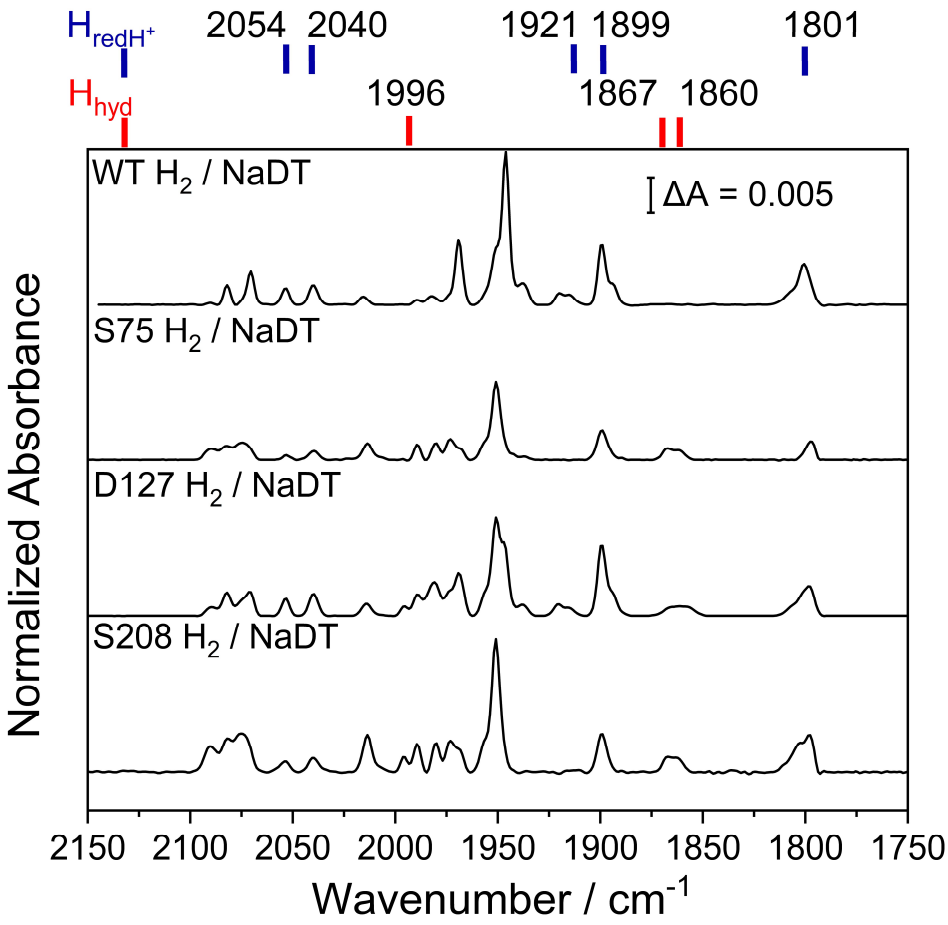


Figure 19: The FTIR spectrum of 1-2 mM WT and truncated proteins flushed with H_2 followed by addition of 10 mM sodium dithionite (NaDT) at pH 8. The H_{redH}^+ state and H_{hyd} state are highlighted with blue and red respectively. The spectra is baseline corrected by subtracting the water vapour peaks.

Overall, it seems to be that removing only the N-terminal domain containing a [2Fe-2S] cluster, as in S75 variant, results in a long-range effect on the active site electronic structure, as shown

by IR spectroscopy. This suggests the importance of the [2Fe-2S] cluster in tuning the catalysis of the enzyme, and this adds to the argument that the [2Fe-2S] cluster is more likely to be the electron entry point of the enzyme supporting interfacial electron transfer between redox partners and enzyme. It clearly illustrates that removing F-cluster domains or even the ferredoxin domain as a result of truncations has no effect on the redox properties and catalytic properties of the enzyme showing that the active site enviorment of truncated variants remains intact.

4.4.2 EPR spectroscopic assignment of truncated *Ca*HydA1 [FeFe] hydrogenases

The electron paramagnetic resonance (EPR) raw data of the WT enzyme and truncated variants were simulated and fitted by multiple compositions: H_{ox} state, H_{ox}-CO and FeS cluster signals using MATLAB software with the help of Dr. Myers. Both H_{ox} and H_{ox}-CO states in WT enzymes are paramagnetic and can be detected by EPR spectroscopy. The H_{ox} state features a rhombic signal (paramagnetic $[2Fe]_H$ with Fe(II)Fe(I) (S = 1/2) configuration coupled with diamagnetic oxidised $[4Fe\text{-}4S]_H$ (2+ state). [159]The resting states and CO inhibited state of truncated variants appeared to be paramagnetic and therefore could be observed by EPR (Figure 20). The EPR spectroscopy of as isolated truncated variants were measured in 25 K, 50 µW, detailed description can be found in chapter 2. The EPR spectra of as isolated truncated variants have similar signal characteristic compared to the WT enzyme (all appeared to have

typical H_{ox} rhombic signal). This similarity suggests that the resting state of truncated variants and H_{ox} state in the WT enzyme are in the same oxidation states for both $[4Fe\text{-}4S]_H$ cluster and $[2Fe]_H$ cluster. One of the major differences is the signal corresponding to the reduced [2Fe-2S] cluster in the WT enzyme, which further confirms that the [2Fe-2S] cluster has been successfully removed in all truncated variants. All truncated variants contain mainly H_{ox}-like state signal and a significant amount of CO-inhibited state signal as a result of CO released from the degradation of $[2Fe]_H$ cluster inhibiting the active H-cluster ('cannibalisation' process) caused by the rapid freezing of samples using liquid nitrogen (truncated variants are less robust towards this process) (Figure 21). The g values of the resting state of all truncated variants appeared to be lower compared to the WT enzyme (g=2.093, 2.034, 1.996 for S75; g=2.094, 2.036, 1.997 for D127; g=2.094, 2.036, 1.997 for S208 compared to g=2.095, 2.038, 1.999 for WT). A similar observation could be seen in the truncated version of *Me*HydA (*Me*H-HydA only containing the H-domain) where they found that the g value of the resting state of *Me*H-HydA is lower than that of *Me*HydA. [150] The change of the g values by truncation also suggests a change in electronic structure of the H-cluster.

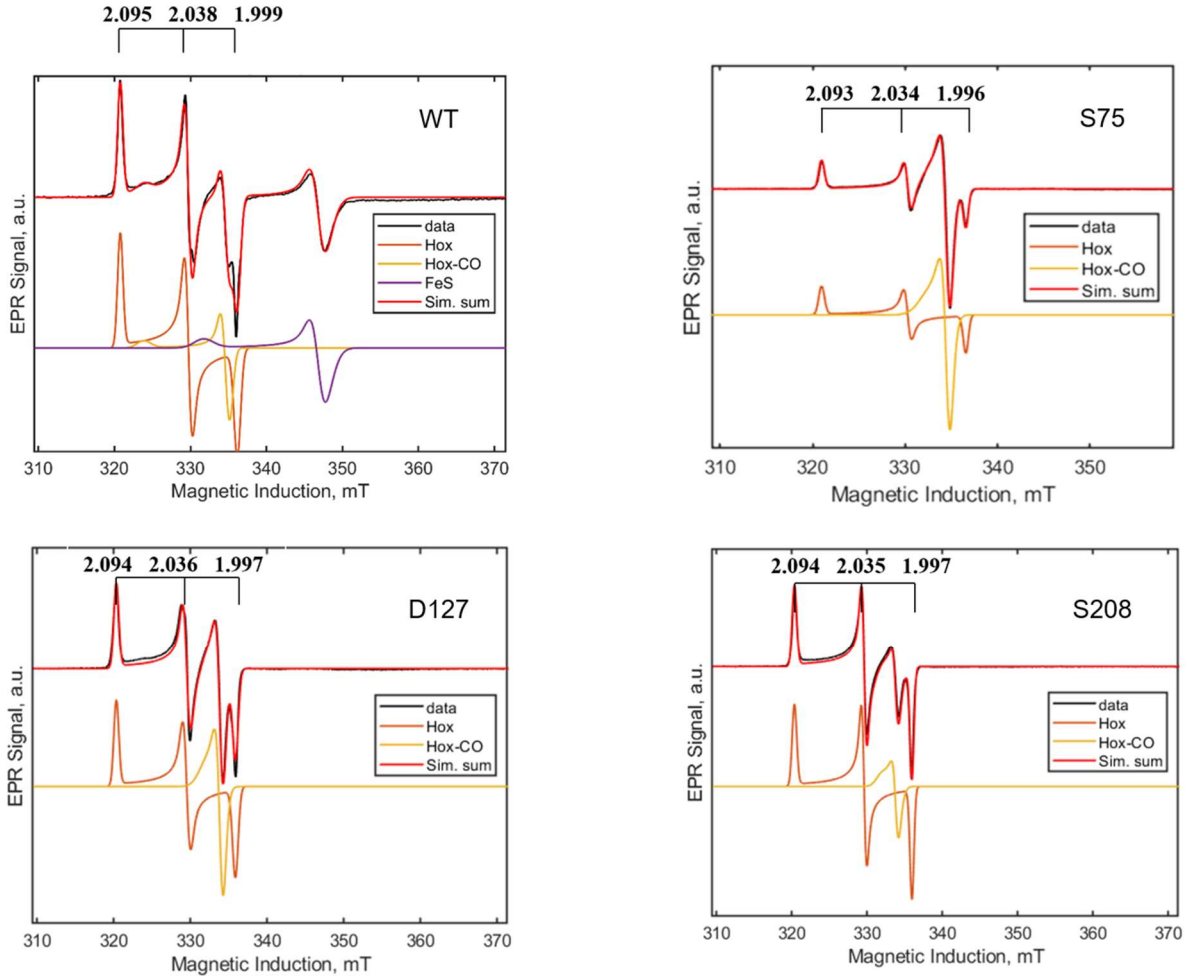


Figure 20: The EPR spectra of 200 µM WT and truncated proteins in the resting state at pH 8 measured at X-band. The EPR spectra for WT and truncated protein is displayed in black trace. Simulated H_{ox} is shown in brown, H_{ox}-CO spectrum is simulated in yellow, spectrum corresponding to [2Fe2S] is shown in purple and overall simulated spectrum to fit the raw data is shown in red. The g values are presented on top of curves. The simulations and plots are performed with the help of Dr. William Myers.

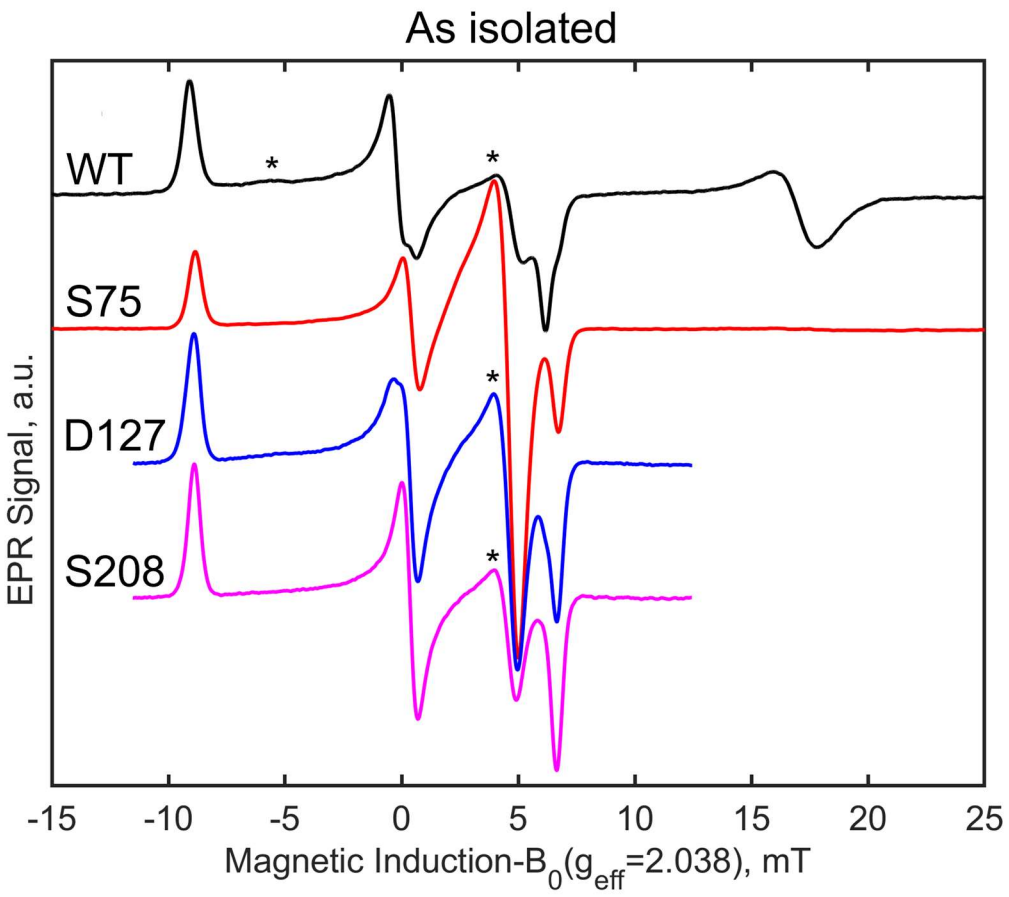


Figure 21: Stacked EPR spectra of 200 µM WT (H_{ox}) and truncated proteins (Truncated as isolated) at pH 8 measured at X-band. The traces i-iv are wild type, S75, D127 and S208 truncated proteins, respectively. The peaks marked with * correspond to the H_{ox}-CO state. The simulations and plots are performed with the help of Dr. William Myers. The figure is adapted from T.Lai *et. al,* in preparation.[136]

The H_{ox}-CO state features a paramagnetic $[2Fe]_H$ with Fe(I)Fe(II) (S = 1/2) configuration coupled with diamagnetic oxidised [4Fe (Figure 22). The CO inhibited state in truncated variants appeared to be much less anisotropic than the H_{ox}-CO state in the WT enzyme (the g values shifted from g = 2.075, 2.007, 2.006 in WT enzyme to 2.021, 2.009, 2.008 in truncated variants (S208, D127), in the case of S75, the g value is 2.020, 2.009, 2.008 (Figure 24). Similarly, in the truncated version of *Me*HydA (*Me*H-HydA), a very similar EPR spectrum of the CO inhibited state could be seen with almost identical g values (g=2.020,2.009,2.008) even though the IR

spectra of the CO inhibited states of *Me*H-HydA and *Ca*HydA1 truncated variants are significantly different.[150] Heghmanns and coworkers reported an unknown radical signal ($R^{\cdot ox}$) in the oxygen-resistant [FeFe] hydrogenase *Cb*A5H[160]. Interestingly, the EPR spectrum of this radical signal ($R^{\cdot ox}$) shows nearly identical features (g values, g =2.019, 2.010, 2.006) to the *Ca*HydA1 truncated variants and *Me*H-HydA. The EPR spectrum of $R^{\cdot ox}$ exhibits a nearly isotropic signal at 2.010. They showed that *Cb*A5H reacting with O_2 or mild oxidant hexamine ruthenium (III) chloride (HAR) led to the formation of $R^{\cdot ox}$. They excluded the H_{inact} state being the source of the $R^{\cdot ox}$ by substituting the cys367 (crucial for the formation of H_{inact}) to aspartate and showing that $R^{\cdot ox}$ still formed. Undoubtedly, the lack of the FTIR assignment of $R^{\cdot ox}$ has kept this a mystery. A bit later, Corrigan *et al.* reported that the CO inhibited state of *Cb*A5H can be isolated as two forms: H_{ox}-CO(1) and H_{ox}-CO(2).[161] The slow-relaxing EPR signal H_{ox}-CO form (H_{ox}-CO(1)) looks identical to $R^{\cdot ox}$, whereas fast-relaxing H_{ox}-CO(2) resembles typical H_{ox}-CO signal detected in many other [FeFe] hydrogenases, like H_{ox}-CO in WT *Ca*HydA1. They assign $R^{\cdot ox}$ species to H_{ox}-CO(1), but further experiments are needed to elucidate the relationship between these two species. H_{ox}-CO and H_{ox} states also exist in two forms in WT *Ca*HydA1, this will be discussed in detail in chapter 6.

It is interesting to parallel the three very similar EPR spectra, the EPR signals of all three scenarios appear to be nearly isotropic, which could be rationalised as a result of the broken symmetry of the $[4Fe\text{-}4S]_H$ and $[2Fe]_H$.[161] Nonetheless, it is very interesting to relate the CO inhibited *Ca*HydA1 truncated variants to the O_2-resistant *Cb*A5H (H_{ox}-CO(1) and [160] [161] as this may aid in the understanding of the O_2 protecting mechanism of [FeFe] hydrogenases and perhaps imply why *Ca*HydA1 is relatively less O_2 sensitive than many other [FeFe]

hydrogenases.

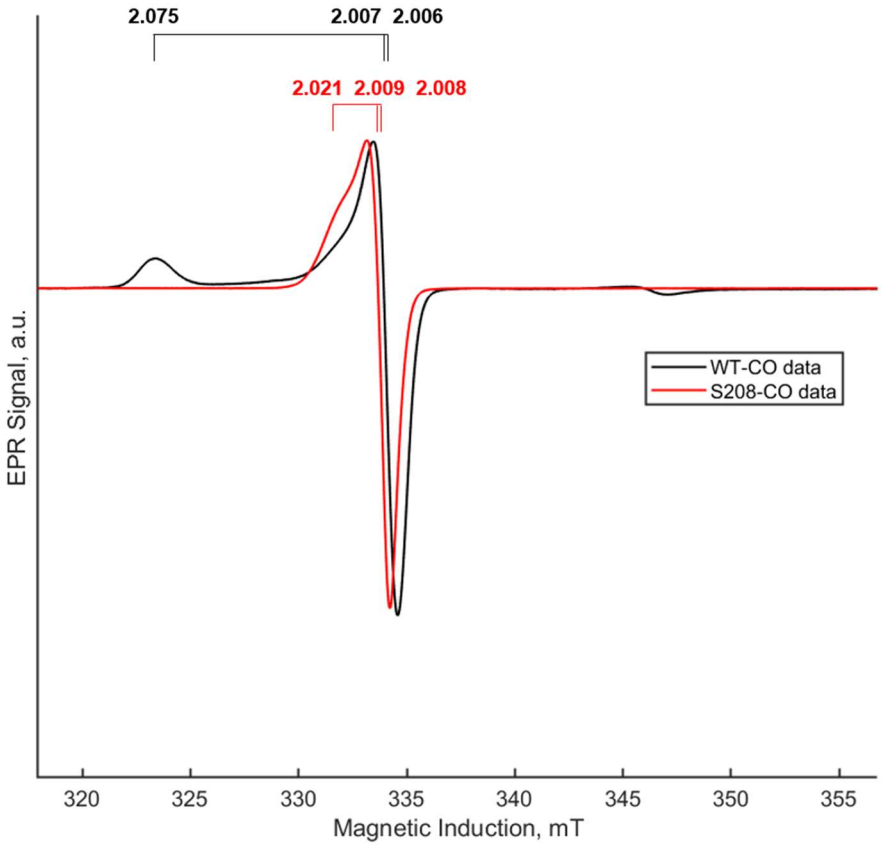


Figure 22: The overlay of EPR spectra of 200 µM WT (H_{ox}-CO) and truncated protein (S208) treated with CO (Truncated-CO) at pH 8 measured at X-band. The EPR spectrum of WT inhibited by CO is displayed as a black trace and representative truncated (S208) CO inhibited spectrum is in a red trace. The g values are presented on top of both curves. Simulations and plot performed with the help of Dr Meyers

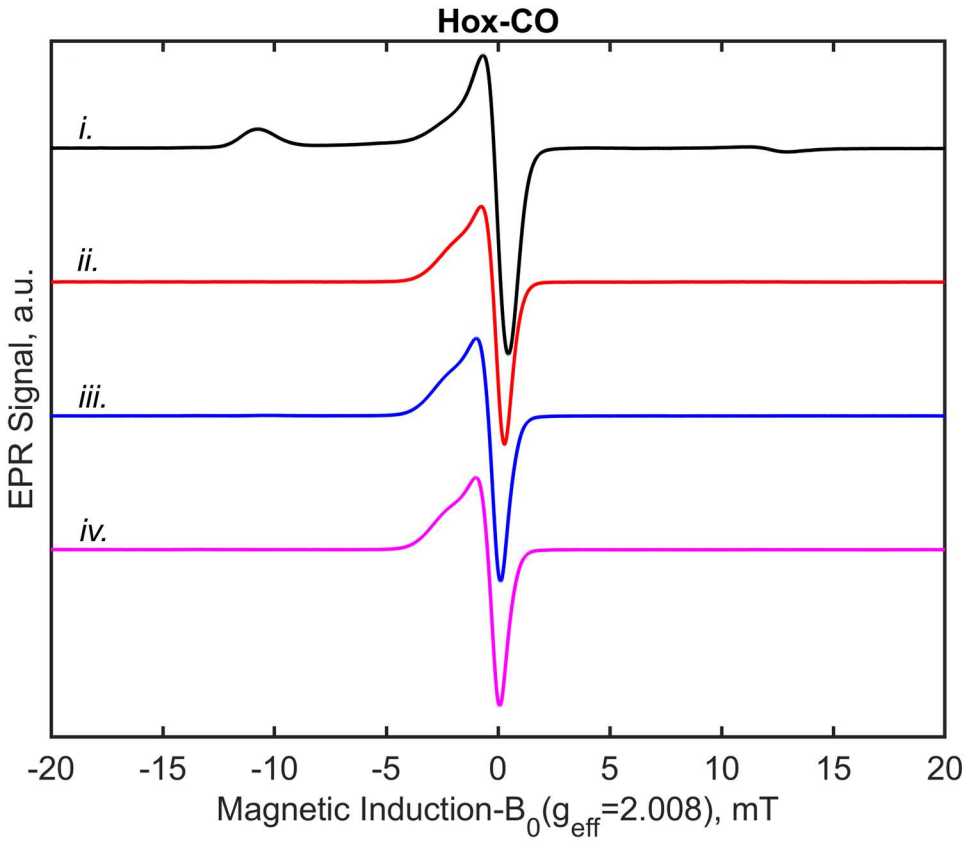


Figure 23: Stacked EPR spectra of 200 µM WT (H_{ox}-CO) and truncated proteins (Truncated-CO) treated with CO at pH 8 measured at X-band. The traces i-iv are wild type, S75, D127 and S208 truncated proteins, respectively. The simulations and plots are performed with the help of Dr. William Myers.

4.5 Discussion and conclusion

4.5.1 Systematic truncation of the F-domain in CaHydA1 [FeFe] hydrogenases

Comparing naturally occurring [FeFe] hydrogenases allows for some speculations on the role of F-clusters between different types of [FeFe] hydrogenases, but differences in the H-domain

could also contribute to observed variations. The primary goal of this chapter is to engineer the excellent H_2 producer M3 type *Ca*HydA1 [FeFe] hydrogenase through systematic truncations to study the long-range effect of the electron relay (the F-clusters) on the active site catalysis. The first objective was to design the protein constructs. The truncation positions of three truncated variants were selected by mapping the domains on InterPro. In the S75 variant, the [2Fe-2S] cluster containing N-terminal domain is removed, serving to explore the importance of this domain on the long-range effect on active site catalysis, potentially acting as a key cluster supporting interfacial electron transfer with redox partners (electron entry point). In the D127 variant, both the [2Fe-2S] cluster containing N-terminal domain and the His-ligated [4Fe-4S] cluster domain are removed to mimic the M2 type [FeFe] hydrogenases. This is to investigate the effect of removal of ferredoxin domain on the catalytic behaviour of the enzyme. Finally, in the S208 variant, the entire F- domain was removed, making it a M1 type like [FeFe] hydrogenase. Comparing the WT hydrogenase with the truncated variant removing all F-clusters is of particular interest.

All truncated variants were successfully isolated in very pure forms using a similar protocol developed for the WT enzyme in the previous chapter. The expression yield increases down the truncated series, except for S75 variant. This could be explained by the decrease of FeS clusters content, as this requires ISC machinery, making the protein more readily expressed. In the case of S75, lacking the N-terminal domain might significantly impact the solubility of this protein. The integrity of FeS clusters in each variant was confirmed by ICP-MS and UV-Vis spectroscopy. Additionally, maturation of each variant was tested: all truncated variants displayed a slower maturation process compared to the WT enzyme, with the S75 variant

being the slowest. One rationale could be that the removal of N-terminal domain or truncations affects the electropositive channel, resulting in a weaker interaction of the apo-protein with negatively charged synthetic cofactors.

4.5.2 Functional characterizations of truncated *Ca*HydA1 [FeFe] hydrogenases

Solution activity assays of truncated *Ca*HydA1 [FeFe] hydrogenases with the artificial redox partner methyl viologen revealed that all truncated variants were lower in activity in both H_2 oxidation and evolution rates compared to WT enzyme. In particular, S75 shows the lowest activity implying the importance of [2Fe-2S] cluster to the catalytic activity of the enzyme. Interestingly, the activity seemed to increase when the protein was further truncated. The reason could be that the charge on the protein surface was changed upon truncation, which would affect the interaction between the protein and methyl viologen (effectively changing the K_m). On the other hand, the active site of the protein is more exposed in truncated variants, enabling more interaction between the protein and methyl viologen, which could explain why in S208 variant, the activity was the highest amongst all truncated variants.

Solution activity assays of WT and truncated variants with the physiological redox partner *Ca*Fd (CAC0303) strikingly showed that only WT had activity in both H_2 oxidation and evolution with the physiological redox partner. The [2Fe-2S] cluster containing N-terminal domain removed in the S75 variant displayed negligible residual activity in both H_2 oxidation and evolution rates, indicating that the [2Fe-2S] cluster containing N-terminal domain is crucial for

the physiological redox partner to bind and could be the natural binding site of the protein. This, in turn, suggests that the electron entry point could be the [2Fe-2S] cluster instead of the His-ligated [4Fe-4S] cluster. Further support from the docking models showed that *Ca*Fd tends to bind with *Ca*HydA1 on the [2Fe-2S] cluster containing N-terminal domain.

4.5.3 Spectroscopic characterisation of truncated *Ca*HydA1 [FeFe] hydrogenases

The FTIR spectra of truncated variants maturated with ADT revealed a long-range effect of truncating the FeS clusters on the H-cluster as all IR bands were shifted compared to WT enzyme. All IR bands were blue shifted towards higher wavenumber except bridging CO band, which blue shifted to a lower wavenumber compared to WT enzyme. This could indicate a conformational change in the active site environment in all truncated proteins. However, this will need to be confirmed by X-ray crystallography. Importantly, the IR spectra of all truncated variants were identical, indicating the significance of [2Fe-2S] cluster containing N-terminal domain on tuning the active site catalysis. The FTIR spectra of truncated variants maturated with PDT cofactor displayed a blue shift of all ligands as expected (exchange of bridge head atom of more σ-donating nitrogen atom in ADT to the less σ-donating carbon atom in PDT), compared to that maturated with ADT cofactor. Similarly, all IR bands were shifted towards higher wavenumber except the bridging CO band which shifted to a lower wavenumber compared to WT enzyme, confirming a long-range effect by removing FeS cluster domains on the H-cluster. Furthermore, the FTIR spectra of truncated variants inhibited by CO showed that all IR bands were shifted. Overall, all the peaks have shifted to higher wavenumbers, except for red shifts of exogenous CO and bridging CO. Notably, the IR bands

of terminal CO ligands were more separated compared to the WT enzyme. Finally, the FTIR spectra of reduced states of truncated variants revealed that the reduced states H_{redH}^{+} and H_{hyd} remained at similar wavenumbers compared to WT enzyme. All truncated variants seemed to exist exclusively in these two reduced states. However, in the WT enzyme, H_{red} and H_{sredH}^{+} states can be found in a relatively small proportion, which contradicts the previous argument that the anti-cooperativity of F-clusters plays a role in the proton coupled electronic rearrangement of the H-cluster to destabilise the formation of H_{red} and H_{sredH}^{+}[158]. Further investigation through spectroelectrochemistry is needed. Interestingly, all truncated variants could trap a small amount of H_{hyd} state, whereas H_{hyd} state could not be observed in the WT enzyme.

EPR spectroscopy of truncated variants revealed that the resting state of truncated variants is in similar oxidation state for both $[4Fe\text{-}4S]_H$ and $[2Fe]_H$ clusters to the H_{ox} state in WT enzyme, featuring diamagnetic $[4Fe\text{-}4S]_H$ (2+) cluster and paramagnetic $[2Fe]_H$ cluster in the Fe(II)Fe(I) electronic configuration (S = 1/2) as the signal characteristics were similar to that of H_{ox} in WT enzyme (a typical rhombic signal). The g values of truncated variants are slightly shifted towards lower numbers compared to that of WT enzyme, indicating a change in the electronic structure of H-cluster, although the overall EPR signal characteristics are similar. These EPR spectra of as isolated truncated variants agreed well with the IR spectra. More interestingly, the EPR spectra of CO-inhibited truncated variants displayed nearly isotropic signals. The massive change in the EPR signals of CO inhibited truncated variants could be related to the IR spectra where a major shift could be seen. Similar observations were seen in truncated *Me*HydA (*Me*H-HydA) and the radical signal of O_2-resistent CbA5H ($R^{\cdot ox}$)[150] [160]. In the case of

truncated variants in *Ca*HydA1 and *Me*HydA, the nearly isotropic EPR signal arises from the protein inhibited with CO. However, in CbA5H, $R^{\cdot ox}$ appeared when it was exposed to O_2. The result excludes the H_{inact} being the source of $R^{\cdot ox}$ despite H_{inact} being dominant when exposed to O_2, as shown by IR spectra. The lack of definitive IR assignment of this $R^{\cdot ox}$ perturbs the understanding of its origin. Nonetheless, the isotropic signal could be rationalised as a result of the broken symmetry of the $[4Fe\text{-}4S]_H$ and $[2Fe]_H$. [161] It is interesting to relate the CO inhibited *Ca*HydA1 truncated variants to the O_2-resistant CbA5H ($R^{\cdot ox}$) as this may help understand the O_2 protecting mechanism of [FeFe] hydrogenases and may explain why *Ca*HydA1 is relatively less O_2 sensitive than many other [FeFe] hydrogenases.

4.5.4 Conclusion

In this chapter, we engineered the excellent H_2 producer M3 type *Ca*HydA1 [FeFe] hydrogenase via systematic truncations aiming to study the role of the F-clusters on the [FeFe] hydrogenase. All truncated variants could be isolated successfully using a similar protocol for WT enzyme. In addition, functional and spectroscopic characterizations were performed on truncated variants, showing a substantial change in the catalytic behavior, catalytic activity, and electronic characteristics of the H-cluster. Notably, solution activity assay with the physiological redox partner and docking models suggests that the natural binding site is likely to be the [2Fe-2S] cluster containing N-terminal domain implying that the electron entry point is the [2Fe-2S] cluster. Furthermore, removing only the [2Fe-2S] cluster containing N-terminal domain has a long-range effect on the electronic characteristics of H-cluster as shown by FTIR and EPR spectroscopy, and a substantial change in the catalytic behavior and activity shown by solution activity assay and electrochemistry. Overall, this result is indicative that the [2Fe-

2S] cluster plays an important role in the interfacial electron transfer with redox partners and controlling electron transfer in and out of the protein, leading to a long-range effect on the active site catalysis.

Interesting isotropic EPR signals of CO inhibited truncated variants relates to the O_2-resistant CbA5H ($R^{\cdot ox}$), driving interest to investigate the O_2 sensitivity of these enzymes. In the next chapter, the catalytic behavior of truncated variants will be explored in detailed using protein film electrochemistry (PFE) as well as their reactivities towards competitive inhibitors, O_2 and CO.

Chapter 5

Comparing the Catalytic Activity of Truncated Variants and WT Enzyme, and Their Tolerance Towards Competitive Inhibitors

Chapter 5: Comparing the Catalytic Activity of Truncated Variants and WT Enzyme, and Their Tolerance Towards Competitive Inhibitors

5.1 Introduction and aim of the chapter

5.1.1 Electrocatalytic mechanism and Catalytic activity of [FeFe] hydrogenases

The catalytic behaviour of [FeFe] hydrogenases from each of the major classes of M1-M3 types exhibit completely different catalytic behaviours, as shown by the protein film electrochemistry (PFE). The interpretation of the electrocatalytic mechanism of [FeFe] hydrogenases is rather challenging.

It has been suggested that the accessory F-clusters may influence the catalytic bias. Furthermore, It was previously hypothesised by Hexter *et al.* that the catalytic bias of hydrogenases is governed by the reduction potential of the most distal cluster (the entry/exit point of the electrons) [99]. Their investigation was based on a serious of different [NiFe] and [FeFe] hydrogenases (Hydrogenase 1 from *E. coli* (*Ec*Hyd1), Hydrogenase 2 from *E. coli* (*Ec*Hyd2), *Cr*HydA1 and *Ca*HydA1). Based on the simplified model (figure 1), they argued that the interfacial electron transfer between the enzyme and the electrode is the determining factor for catalytic activity. Furthermore, they revealed that the reduction potential of the electron relay centre (distal FeS cluster, site at which electrons leave or enter the catalytic cycle) of *Ca*HydA1 was at -400 mV, therefore, more negative than the reduction potential of the H^+/H_2 couple at pH 6.0 (-360 mV). This could explain why *Ca*HydA1 is strongly biased

towards H_2 evolution. In addition, the distal clusters of the two [NiFe] hydrogenases, *Ec*Hyd2 and *Ec*Hyd1, exhibited reduction potentials of -300 mV and -190 mV, respectively. These aspects could account for why *Ec*Hyd2 is strongly biased towards H_2 oxidation, and *Ec*Hyd1 does not evolve H_2 except at very low pH and requires an overpotential to oxidise H_2. Their model places emphasis on the role of the reduction potential of the distal cluster in tuning the catalytic bias. Nonetheless, this model ignores significant details of the intramolecular electron transfer chain and its possible impact on the potential-determining step. Additionally, they were only able to compare enzymes from different classes of hydrogenases from various organisms in which their active centres and amino acid residues around the active site are dramatically different, which perturbs the understanding of the electrocatalytic mechanism of these enzymes.

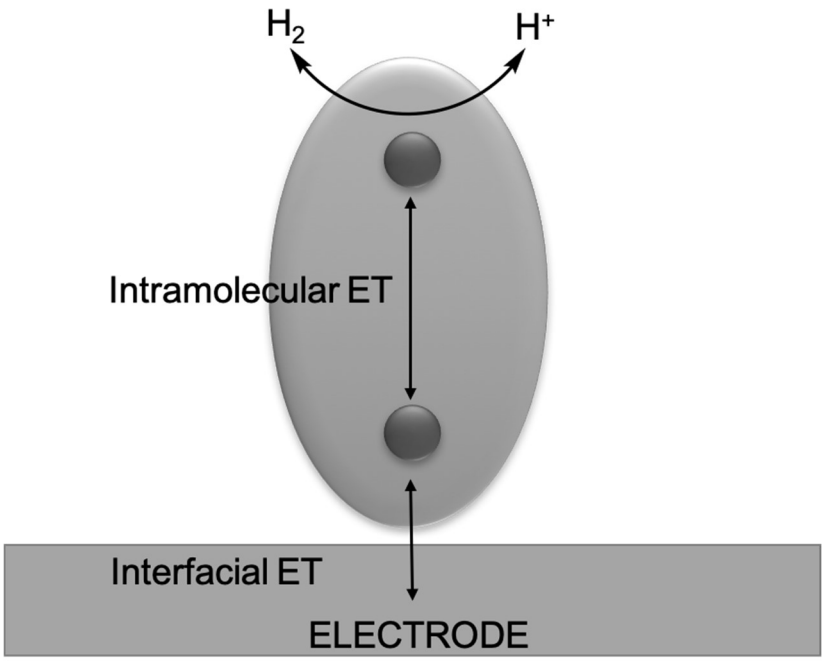


Figure 1: A schematic model of intermolecular and intramolecular electron transfer through an enzyme attached to an electrode. The Figure is reproduced from Hexter *et al* [99] made using PowerPoint.

Another interesting aspect is that changes of proton transfer pathway (PTP) in the [FeFe] hydrogenases greatly affects the catalytic wave shape and catalytic reversibility of [FeFe] hydrogenases, as demonstrated by Lampret and coworkers[112]. Importantly, they highlighted that substituting glutamate with aspartate in either of two positions in the PPT at long range in *Cp*I and *Cr*hydA1 [FeFe] hydrogenases effectively slows down the proton transfer (PT) for both catalytic directions and diminishes catalytic reversibility, thus influencing catalysis. With respect to catalytic bias, it was suggested that the suppression of rate in either direction may be rigidly related to chemical in origin. It was shown in [NiFe]-hydrogenases from *Desulfovibrio fructosovorans (Df)* that narrowing the gas diffusion channel greatly affects the catalytic bias, suggesting that a rate-limiting chemical effect tunes the catalytic bias[162] [163] [164].Thus, supressing the ability to capture or transport protons from solvent in PTP variants influences the capability of functioning as H_2 producers at high pH. However, surprisingly, for the direction of H_2 oxidation, at high pH, a favourable proton gradient from the active site to solvent seems to have no influence on PTP variants. More importantly, the catalytic reversibility of PTP variants was greatly affected, as a rather large inflection was seen close to the $2H^+/H_2$ thermodynamic potential at certain pHs. This result suggests that the long-range electron transfer process is tightly coupled to PT. In addition, these inflections appear because of a change in the PTP rather than electron transfer (ET) chain implying that PT is limiting the rate of ET. Interestingly, the catalytic wave shape of PTP disrupted E279D *Cp*I variant is nearly identical to that of *Cp*II reported by Artz and coworkers[153]. They rationalised that the catalytic bias of *Cp*II strongly towards H_2 oxidation, and the requirement of considerable overpotential by high reduction potential of the distal cluster of *Cp*II (-180 mV in *Cp*II vs (-450 mV in *Cp*I),

cause a lower internal driving force for H_2 evolution.[153] [165] [151] However, in E279D *Cp*I, by simply disrupting the PTP without affecting the FeS relay of ET chain, a similar catalytic waveshape to *Cp*II is observed, which clearly suggests that the catalytic bias of [FeFe] hydrogenase certainly need to take into account cooperativity between the PT and ET pathways.

5.1.2 Tolerance of [FeFe] hydrogenases towards competitive inhibitors

Competitive inhibitors are molecules that can bind competitively to the active site of the enzyme, preventing the substrate from binding. In the case of [FeFe] hydrogenases, CO and O_2 are both competitive inhibitors. It was shown in the previous chapter that CO can bind to the open coordination site of Fe_d of [FeFe] hydrogenases, forming H_{ox}-CO state. In a combined density functional theory (DFT) and PFE study, it was shown that CO could also bind to the reduced state H_{red} state and irreversibly inactivate the enzyme.[166] Despite [FeFe] hydrogenases being such efficient H_2 producing catalysts, they suffer from O_2 inactivation, thus, the investigation on the O_2 inactivation mechanism has become a major field of research[97]. O_2 first enters the [FeFe] hydrogenases via the gas diffusion channel[167], and the initial attack occurs on the open coordination site of distal iron (Fe_d), leading to the formation of reactive oxygen species (ROS)[98] [168] [169] [170] [171]. However, the mechanism following the first O_2 attachment to the Fe_d remains unclear. Esselborn and coworkers exposed *Cp*I crystals to O_2, revealing fast degradation on the $[2Fe]_H$, particularly with the Fe_d degrading much faster

compared to proximal iron (Fe_p). Additionally, it was also shown that the $[4Fe\text{-}4S]_H$ ultimately degraded, leaving the accessory F-clusters essentially unaffected. Furthermore, they also showed that apo-*Cp*I is rather stable when exposed to O_2 [172] . This suggests that ROS species formed from binding to the Fe_d diffuse towards the $[4Fe\text{-}4S]_H$ and destroy it[169] [173].

A useful and comprehensive technique, protein film electrochemistry, has been applied to investigate the kinetics of O_2 inhibition of [FeFe] hydrogenases as the catalytic activity can be measured from the current when the enzymes are exposed to a controlled flow of O_2.[98] [168] Interestingly, it was shown that the M3 type *Ca*HydA1 [FeFe] hydrogenases exhibited reversibility when exposed to a flow of O_2 and retained most of their catalytic activity after bursts of O_2. However, in the M1 and M2 type hydrogenases such as *Cr*HydA1 and *Dd*HydAB, controlled bursts of O_2 led to irreversible degradation as the catalytic current quickly reached zero[98]. This is certainly indicative that the accessory F-clusters in [FeFe] hydrogenases play a role in O_2 perhaps by reducing O_2 to water. They could act as an electron reservoir, providing electrons when O_2 diffuses to the H-cluster. But it may just be the difference in the size of the gas channels in these [FeFe] hydrogenases that affects the rate and extent of O_2 inhibition. Nonetheless, comparing the naturally occurring [FeFe] hydrogenases has provided some degree of speculation, but their active site environment and the amino residues around the active site are significantly different, making it difficult to draw concrete conclusions.

5.1.3 Aim of the chapter

In this chapter, I will compare and contrast the electrochemistry of truncated variants and WT enzyme with respect to the electrocatalytic behaviour, catalytic bias, high-potential

inactivation and redox potentials of the most distal FeS cluster of each variant and WT protein. Additionally, the O_2 and CO inhibition of truncated variants and WT enzyme will also be investigated.

5.2 Electrocatalytic characterisation of WT enzyme and truncated variants

The significance of protein film electrochemistry in investigations of electron-mediated metalloproteins lies in its ability to control and measure catalytic electron flow instantaneously and to relate the catalytic activity to different properties (catalytic redox states or activation, inactivation) of the enzyme. The catalytic activity of the enzyme can be measured form the current, which is proportional to the rate of catalytic electron flow. The effect of changing conditions (such as pH, substrate concentration) in any kinetic study could provide substantial information on distinguishing a change in catalytic rate due to kinetic factors or thermodynamic driving force[114].

5.2.1 Electrocatalytic characterisation of WT enzyme and truncated variants under different pH values

Protein film electrochemistry (PFE) was used to investigate the electrocatalytic behaviour of WT enzyme and truncated variants at pH 6, 7, and 8. Figure 2 shows cyclic voltammograms (CV) for the WT enzyme and truncated variants adsorbed onto a pyrolytic graphite electrode at pH 7. The CV curve for WT protein showed reversible behaviour (no overpotential, no extra energy required to start a reaction in either direction) with a small bias (≈1.3) towards H_2 production direction compared to the H_2 oxidation direction when considering the current

density ± 100 mV vs $E(2H^+/H_2)$ (Figure 3). Interestingly, the CV curves of the truncated proteins displayed similar electrocatalytic behaviour compared to WT enzyme in general: they are highly reversible with a strong bias (≈3.0) towards the H_2 production direction compared to the H_2 oxidation direction when calculating the current density (figure 3). When wired to the electrode, it seemed that the truncated proteins (particularly D127 and S208) displayed higher catalytic activities compared to WT enzyme. This might be due to differences in the electrode coverage as the truncated proteins are smaller in size and may also have differences in the surface charge due to the domains being removed. However, the solution assays shown in chapter 4 also showed an increase in activity between the truncated variants, with S75 being the least active and S208 the most active.

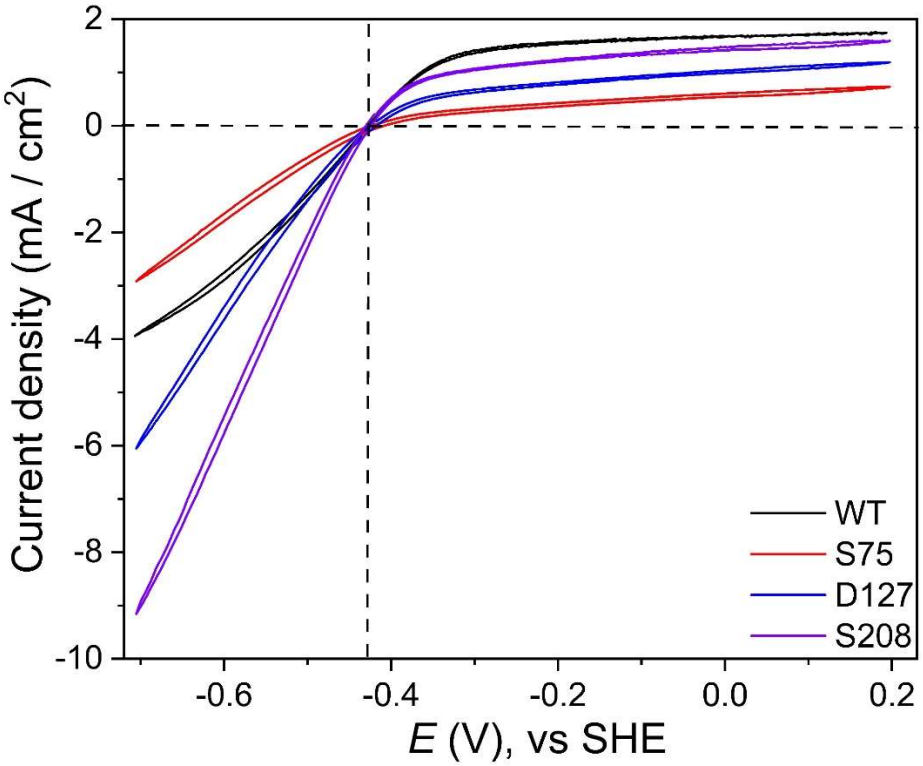


Figure 2: Cyclic voltammograms of the WT and truncated CaHydA1 [FeFe] hydrogenases adsorbed

onto a pyrolytic graphite electrode at pH 7, room temperature (RT), 100% H_2 (1 L/ min), 2000 rpm and 20 mV /s scan rate. The horizontal dashed line represents the zero current, and the vertical dashed line indicates the thermodynamic potential of the $2H^+/H_2$ couple.

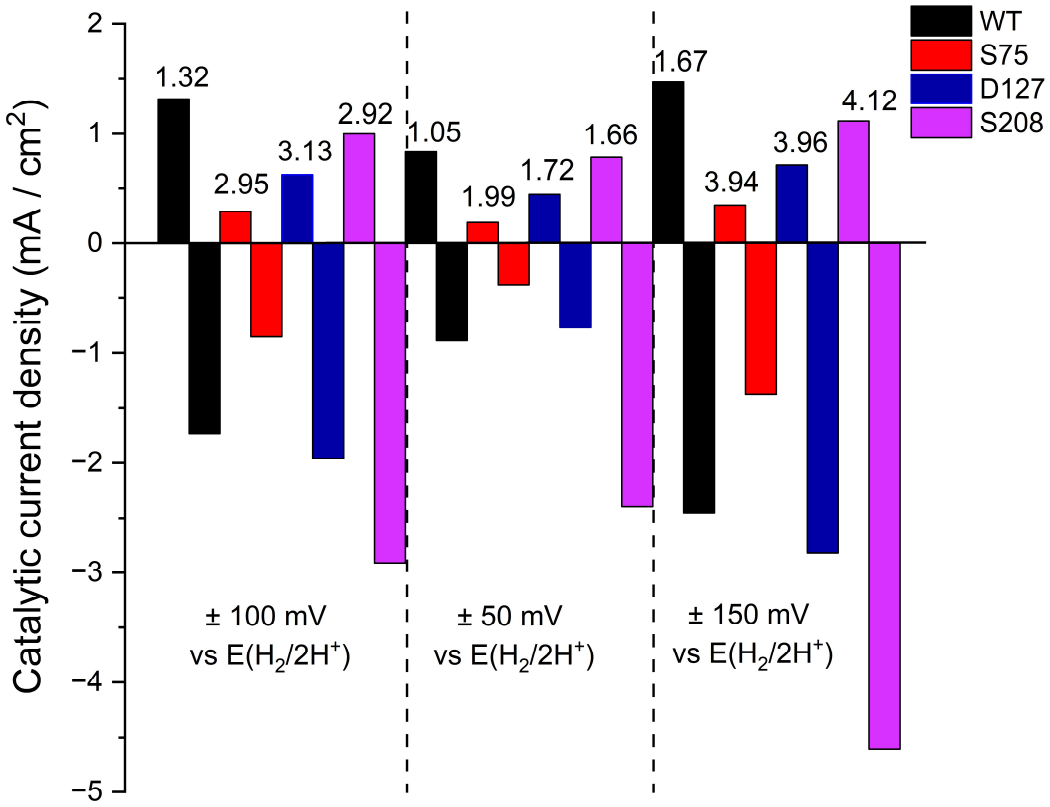


Figure 3: Determination of the catalytic bias at three different overpotentials for WT, truncated *Ca*HydA1 [FeFe] hydrogenases from protein film electrochemistry at pH 7 (by calculating the ratio of catalytic current density on the reduction direction / oxidation direction, values are indicated the top of at each column) at ± 100 mV vs *E*($2H^+/H_2$), ± 50 mV vs *E*($2H^+/H_2$) and ± 150 mV vs *E*($2H^+/H_2$). WT and S75, D127 and S208 variants are highlighted in black, red, blue and purple respectively.

In a boarder context, hydrogenase operates very close to *E*($H_2/2H^+$) under physiological conditions, thus milder potential bias values (e.g. ± 50 mV vs *E*($H_2/2H^+$)) are more relevant. For biotechnological applications where larger potential was applied, larger potential bias values (e.g. ± 150 mV) might be more relevant. When calculating the catalytic bias of WT protein and truncated variants using current density ± 50 mV vs *E*($H_2/2H^+$) (as shown in

figure 3), the catalytic bias of WT protein and truncated variants appeared to be less biased towards H_2 production. (≈1.0 for WT enzyme and ≈1.7 for truncated variant). On the other hand, when calculating the catalytic bias of WT protein and truncated variant using current density $\pm$ 150 mV vs $E(H_2/2H^+)$ (as shown in figure 3), the catalytic bias of WT protein displayed more bias towards H_2 production (≈1.7 for WT enzyme and ≈4 for truncated variants). The CV curves of truncated variants and WT enzymes are all steeper in the H_2 production direction compared to H_2 oxidation direction, thus when looking at potentials further from $E(H_2/2H^+)$, WT protein and truncated variants all displayed higher catalytic bias towards H_2 production direction compared to H_2 oxidation direction.

The overall waveshape of CV curve of WT enzyme displayed a visible curvature in H_2 production direction, and it reached plateau early at high-potential in the H_2 oxidation direction. In contrast, in the truncated variants, the shape of the CV curves appeared to be steeper in the H_2 production direction compared to the WT enzyme, and the oxidation current does not reach a plateau at higher potential in the H_2 oxidation direction. The maximum current when reaching a plateau in the case of WT enzyme may not be a characteristic of the electrocatalyst but it may reflect limited transportation of H_2 in the H_2 oxidation direction. [174]

The CVs of WT protein and truncated variants can be normalised to provide a better view of overall waveshapes. Figure 4 shows the CVs of WT protein and truncated variants normalised to the current at (A) -400 mV and (B) the highest oxidation current respectively. From the normalised CV curve (Figure 4 (A), (B)), it is more evident that all truncated variants are more biased towards H_2 production compared to WT enzyme. In addition, a curvature is clear for WT enzyme. In the H_2 oxidation direction, similar to what is shown in raw data, the

WT protein reached a plateau early very close to the $E(H_2/2H^+)$, but the truncated variants do not seem to reach a plateau.

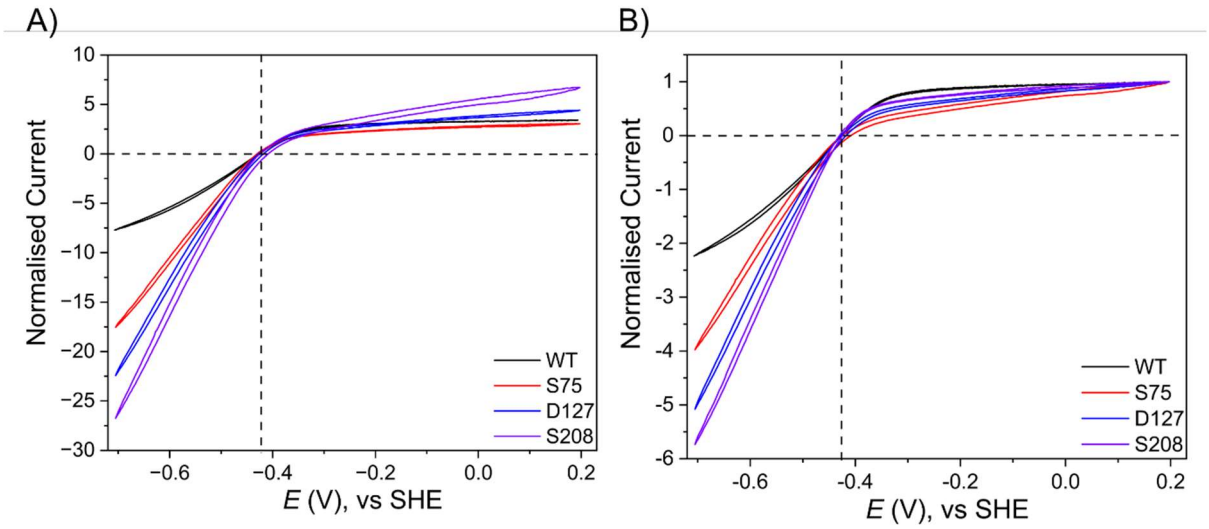


Figure 4: Normalised CVs of WT *Ca*HydA1 and truncated proteins absorbed onto a pyrolytic graphite electrode at pH 7. All measured in buffer mix, 25 °C, 2000 rpm rotation rate, 20 mV/s scan rate, and under 1 atm of H_2. A) Normalisation at -400 mV. B) Normalisation using the highest H_2 oxidation current. The horizontal dashed line represents the zero current, and the vertical dashed line indicates the thermodynamic potential of the $2H^+/H_2$ couple at the given pH.

Figure 5 shows the electrochemical characterisation of WT protein and truncated variants under a more acidic condition, pH 6 (Figure 5 A) and a more basic condition, pH 8 (Figure 5 B). The thermodynamic potential of the $2H^+/H_2$ couple at different pH values can be described by the Nernst equation:

$$E = E^o - \frac{RT}{nF}\ln\frac{[Red]}{[Ox]}$$

$$E = -0.059\mathrm{pH}$$

Where E is the cell potential; E^o is the standard cell potential; R is the universal gas constant: $R = 8.314$ J K^{-1} mol^{-1}; n is the number of electrons involved in the cell reaction;

F is the Faraday constant, F = 96485 C mol^{-1}. The thermodynamic potential $E(H_2/2H^+)$ of different pH values can be derived based from Nernst equation, Temperature=25 °C, E^o = 0 in a standard hydrogen electrode.

Therefore, under a more acidic condition such as pH 6, the thermodynamic potential $E(H_2/2H^+)$ is -354 mV vs SHE, and for pH7 and more basic condition pH8, the thermodynamic potentials $E(H_2/2H^+)$ are -413 mV and -472 mV vs SHE, respectively (as shown in table 1).

Table 1: The thermodynamic potential E(H_2/$2H^+$) at different pH values in otherwise standard conditions.

	pH 6	pH 7	pH 8
$E(H_2/2H^+)$ / mV vs SHE	-354	-413	-472

PFE experiments allow measurement of potential dependence of catalytic activity. A change in pH results in a change in the thermodynamic driving force, and a change in catalytic rate can be rationalised from the effect of changing the thermodynamic driving force.[114] At pH 6 condition, the reduction current density appeared to be the highest. This is consistent with greater availability of H^+ in more acidic conditions. At pH 8, the reduction current density is the lowest. However, in the direction of H_2 oxidation, the current density remained the same at all pH values.

The overall waveshapes of CVs of WT protein and truncated variants measured at pH 6 are similar to those measured at pH 7. All truncated variants have higher electrocatalytic activities compared to WT enzyme, especially for S208, reaching 12 mA /cm^{-2} current density. In the

oxidation direction, all truncated proteins reach a plateau, which is more evident compared to that at pH 7. In the case of pH 8 condition, very visible plateau is seen for WT enzyme, indicating limited transportation of H_2 in a H_2 oxidation reaction, whereas truncated variants seemed to be less steep (less reversible) in the H_2 oxidation direction and do not seem to have a plateau, implying that the transportation of H_2 in a H_2 oxidation reaction is not limited under these conditions.

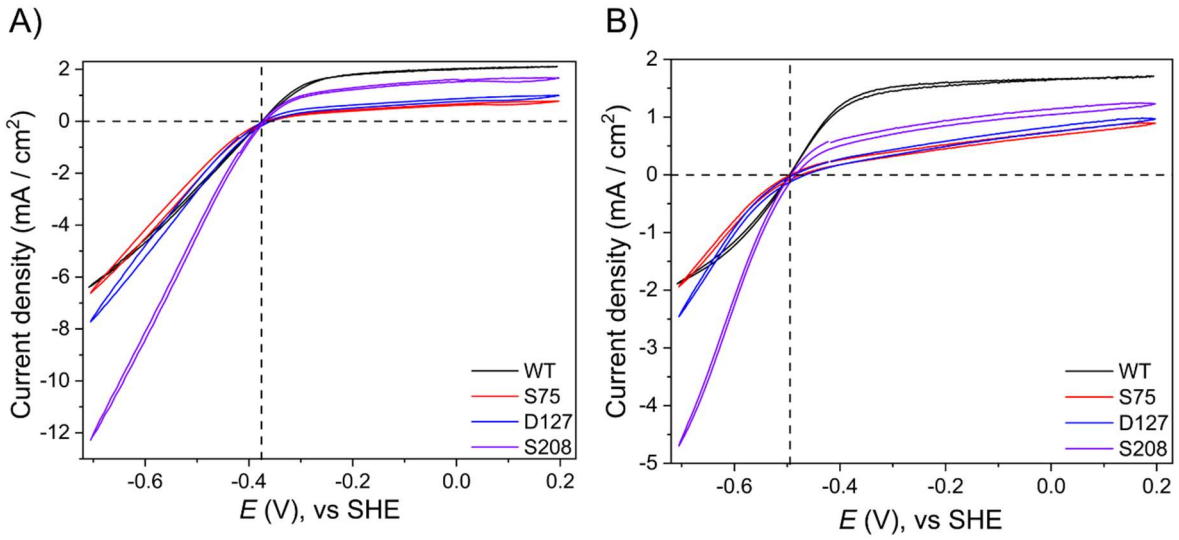


Figure 5: Comparison of the electrochemical behaviour at different pH values for WT *Ca*HydA1 and truncated proteins. A) absorbed onto a rotating pyrolytic graphite electrode at pH 6; and B) at pH 8. All measured in buffer mix at the desired pH, 25 °C, 2000 rpm rotation rate, 20 mV/s scan rate, and under 1 atm of H_2 (1000 mL/ min). The horizontal dashed line represents the zero current, and the vertical dashed line indicates the thermodynamic potential of the $2H^+/H_2$ couple at the given pH.

5.2.2 Electrocatalytic characterisation of WT enzyme and truncated variants: high-potential inactivation

High-potential inactivation is often seen in [NiFe] hydrogenases [175] [176] [177]and some [FeFe] hydrogenases such as prototypical M1 type and M2 type hydrogenases, *Cr*HydA1 and

*Dd*HydAB[178] [94]. E_{switch} is a thermodynamic-kinetic parameter that indirectly reflects the inactivation/reactivation potential (potential at which the inactivation occurs) and seems to be dependent on the scan rate and pH.[94] The origin of high-potential inactivation for [FeFe] hydrogenases is still not fully understood. It was shown that halide (Cl^- and Br^- ions) present in the buffer solution used to measure PFE causes the appearance of high-potential inactivation for [FeFe] hydrogenases.[179] And this could rationalise why CVs of isolated *Cr*HydA1 and *Dd*HydAB have high-potential inactivation. The reports suggested that Cl^- or Br^- ions are necessary for the inactivation to proceed for [FeFe] hydrogenases[180].They suggest that the Cl- bind in the 2nd coordination sphere interacting with the NH via H-bonding. Interestingly, M3 type [FeFe] hydrogenases such as *Ca*HydA1 does not seem to have visible high-potential inactivation in the presence of halides (See figure 1, 20 mV/s scan and figure 7, 5mV/s scan). The high-potential inactivation could correlate to the number of F-clusters present in the [FeFe] hydrogenase.[80]

Figure 7 shows that CVs of WT enzyme and truncated variants in 5 mV/s scan. High-potential inactivation is not present in the WT enzyme, but clear high-potential inactivation can be seen in all truncated variants.

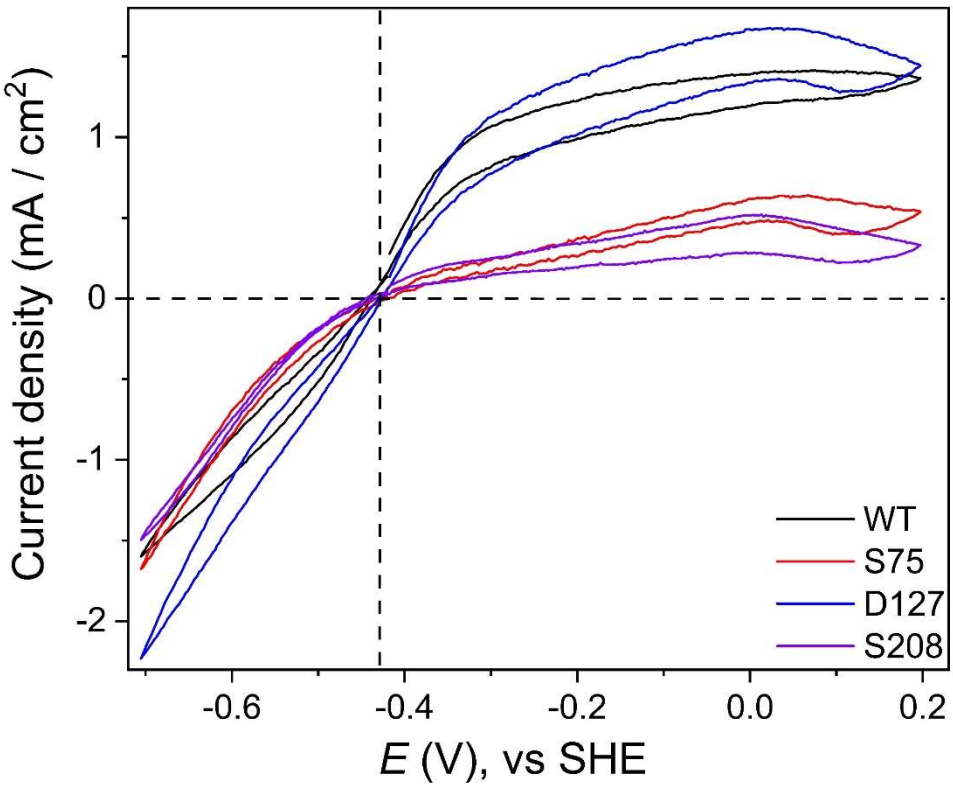


Figure 7: CV of WT *Ca*HydA1 and truncated proteins absorbed onto a pyrolytic graphite electrode at pH 7 measured at a slow scan rate. All measured in buffer mix, 25 °C, 2000 rpm rotation rate, 5 mV/s scan rate, and under 1 atm of H_2. The horizontal dashed line represents the zero current, and the vertical dashed line indicates the thermodynamic potential of the $2H^+/H_2$ couple at the given pH.

E_{switc} at 5 mV/s of truncated variants were determined to be +78 mV, +73 mV and +65 mV vs SHE for S75, D127, and S208 respectively by taking account to the minimum 1st derivative. E_{swit} of *Cr*HydA1 and *Dd*HydAB were determined to be +60 mV and +40 mV vs SHE respectively. In the same report, it was shown that when Na_2S was added to the enzyme, E_{swit} values of *Cr*HydA1 and *Dd*HydAB were shifted 100 mV more negative compared to the experiment with no Na_2S. [88]

Table 3: Determination of the E_{swtich} for WT and truncated CaHydA1 [FeFe] hydrogenase from protein film electrochemistry at pH 7, 5 mV/s scan rate after calculating the minimum in the first derivative from figure 5 from the sweep towards negative potentials.

	WT *Ca*HydA1	S75	D127	S208
E_{swtich} / mV, vs SHE	NA	78	73	65

5.3 Comparing tolerance towards competitive inhibitors in WT enzyme and its truncated variants

5.3.1 O_2 inhibition during H_2 oxidation

Traditional methods such as activity assay are not feasible because O_2 readily oxidises redox partner, and the rate of O_2 inactivation requires the activity to be sampled at a fast frequency. Direct electrochemistry is exceptionally helpful for kinetic studies of inhibition of hydrogenases with O_2 because the current can be measured simultaneously when the enzyme transfers electrons to an electrode. In addition, the potential can be controlled and poised at a potential so that O_2 reduction by the electrode is slow without interfering with the measurement.[98]

The inactivation of the WT and truncated variants by O_2 was studied by PFE by

chronoamperometric experiments by monitoring O_2 inactivation of electrocatalytic H_2 oxidation by the enzymes after injection of small amounts of O_2-saturated buffer (Figure 8). The normalization is done by taking account the highest current as 1, and zero current as 0. The cell potential was set to + 40 mV (a potential more positive than the reduction potential of O_2 at graphite to avoid direct reduction at the electrode surface) to monitor any effect of O_2 on the electrocatalytic H_2 oxidation by each enzyme. The injection of O_2 caused an immediate drop in electrocatalytic current for all the proteins. In both WT and truncated variants, ≈ 10 % of activity was lost. WT enzyme shows some recovery of activity (as previously reported)[98] as O_2 is displaced from the electrochemical cell by the flow of H_2. The S75 variant, displays a similar degree of reversibility to WT, while the D127 and S208 variants did not show any sign of recovery of activity after O_2 exposure.

This strongly suggests that removal of the F-clusters has a negligible effect on the inactivation by O_2 but does have a direct influence on the recovery of current (i.e. reversibility). This indicates that the F-clusters are not directly involved in protecting the enzyme against O_2 attack (i.e. in the initial O_2 binding step) but they are involved in providing a 'defense' mechanism for the active site to avoid the formation of reactive oxygen species (ROS) by providing enough electrons to reduce O_2 to water. [150] [181] [182] [97] [183] It is likely that the His-ligated [4Fe-4S] cluster controls the reversibility of oxygen inactivation in *Ca*HydA1, as the variants D127 and S208 do not show any recovery.

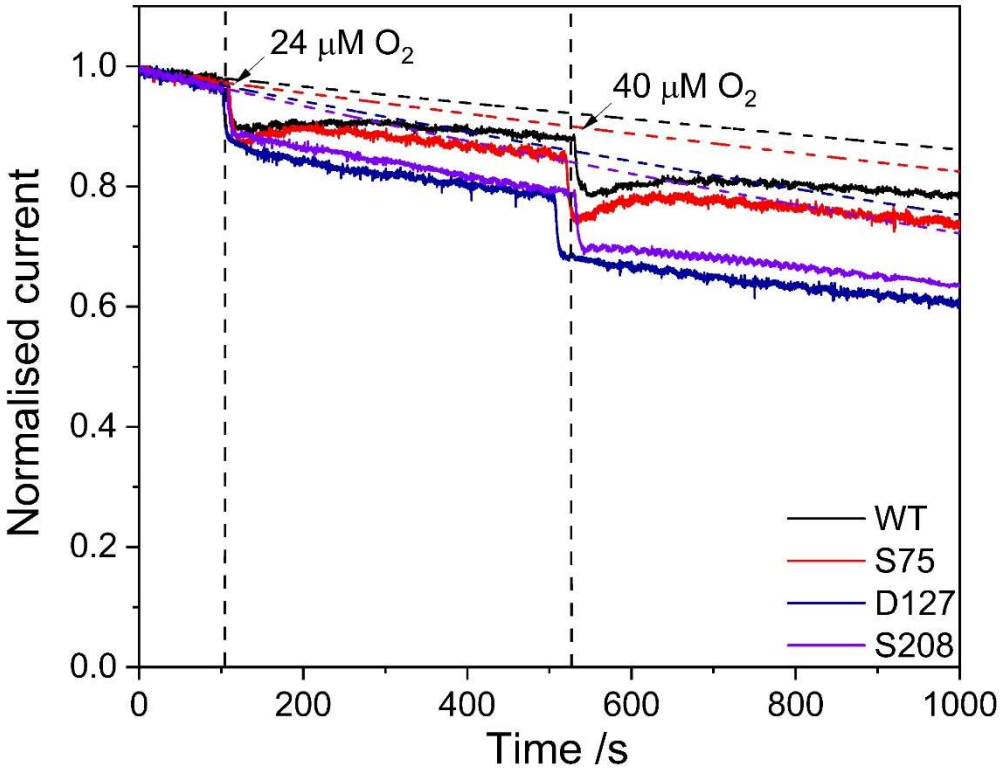


Figure 8 Normalised chronoamperograms showing the aerobic inactivation of WT *Ca*HydA1 and its truncated variants. The enzymes were adsorbed onto the rotating pyrolytic graphite electrode and poised at +40 mV vs SHE under a 100% H_2 atmosphere to avoid direct reduction of O_2 on the electrode surface. The H_2 oxidation current was monitored vs time following the injection of small amounts of O_2 in the electrochemical cell. The solid lines are the experimental data and dotted lines are the projected current baselines extrapolated from the anaerobic part of the data (recorded in first 100 seconds) by fitting to an exponential function. [150] [184]The vertical dashed line indicates the points where O_2 was added to the electrochemical cell.

Comparing the anaerobic inactivation of D127 and S208 variants with their native counterpart prototypical M1 type *Cr*HydA1 and M2 type *Dd*HydAB, showed superior O_2 resistance for D127 and S208 variants as both *Cr*HydA1 and *Dd*HydAB lost activity when small amount of O_2 injected (As shown in Figure 9).

We hypothesize that the enhanced O_2 tolerance of the M3-type [FeFe] hydrogenases may

relate to differences in the gas channel rather than the FeS clusters, and that the overpotential may be governed by the potentials of the $[4Fe\text{-}4S]_H$ cluster and the $[2Fe]_H$ subsite rather than by the number of FeS clusters in the F-domain or by the potential of the most exposed cluster.

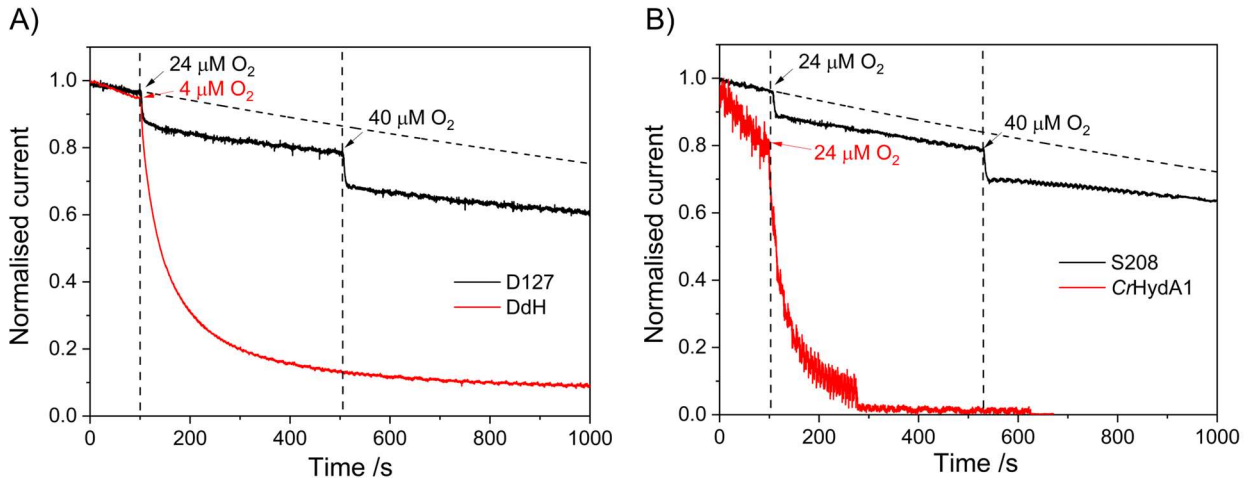


Figure 9: Normalised chronoamperograms showing the aerobic inactivation comparison between (A) M2-type like D127 and the enzyme *Dd*HydAB and (B) M1-type like S208 and CrHydA1. Enzymes were absorbed onto a PGE and the potential was poised at +40 mV vs SHE under 100% H_2 atmosphere. The H_2 oxidation current was monitored vs time following the injection of small amounts of air-saturated buffer into the electrochemical cell. The solid lines are the experimental data and dotted lines are the projected current baselines extrapolated from the anaerobic part of the data (recorded in first 100 seconds) by fitting to an exponential function. [150] [184] Vertical dash lines indicate the points where O_2 was added to the electrochemical cell.

5.3.2 CO inhibition during H_2 oxidation

The inhibition of the WT and truncated variants by CO was studied by PFE by chronoamperometric experiments, monitoring O_2 inactivation of electrocatalytic H_2 oxidation of the enzymes after injection of small amounts of CO-saturated buffer (Figure 10). The normalization is done by taking account the highest current as 1, and zero current as 0. The

cell potential was set to -160 mV to monitor any effect of CO on the electrocatalytic H_2 oxidation by each enzyme. The extent of inhibition of CO for WT and truncated variants is similar. The H_2 oxidation currents fully recover after CO is flushed away by H_2, taking into account the estimated loss of activity due to film loss from the electrode over this time span. This suggests that truncating the FeS cluster domain has a negligible effect on the CO inhibition, indicating that this is due to the gas channel remaining unchanged and not affecting the gas diffusion into the active centre.

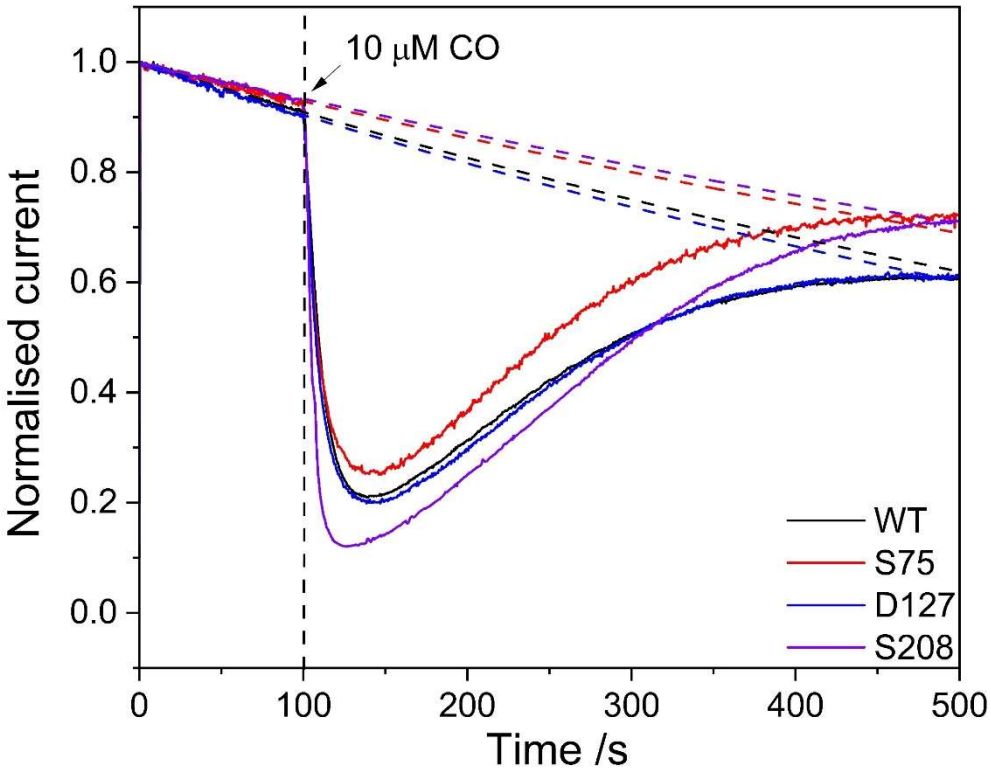


Figure 10 Normalised chronoamperograms showing the CO inhibition of WT *Ca*HydA1 and its truncated variants. The enzymes were adsorbed onto the rotating pyrolytic graphite electrode and poised at -160 mV vs SHE under a 100% H_2 atmosphere. The H_2 oxidation current was monitored vs time following the injection of CO-saturated buffer in the electrochemical cell. The solid lines are the

experimental data and dotted lines are the projected current baselines extrapolated from the anaerobic part of the data (recorded in first 100 seconds) by fitting to an exponential function. [150] [184] The vertical dashed line indicates the points where CO was added to the electrochemical cell.

5.4 Discussion and conclusion

5.4.1 Electrocatalytic characterisation of WT enzyme and truncated variants

The aim of this chapter was to electrochemically characterise a set of truncated variants of *Ca*HydA1 by protein film electrochemistry, comparing their activities, electrocatalytic behaviour and catalytic biases, in order to study the electron relay within this protein.

CVs of truncated proteins showed that they maintain similar catalytic waveshapes compared to WT enzyme. However, all of them are more biased towards the H_2 production direction and this effect has been strengthened at lower pH conditions. Another interesting observation is that WT enzyme seems to reach a plateau at high H_2 oxidation current, whereas truncated protein seemed to have no limitations. Notably, when directly comparing the H_2 production currents, S208 and D127 seemed to have greater electrocatalytic activities than WT enzyme, making them potential candidates for bio-applications such as bio-fuel cells. It is notable that this differs to the results of solution activity assays (shown in chapter 4) where WT shows the highest catalytic turnover frequency and truncated variants have drastically lower catalytic turnover frequencies. This might be due to the fact that when wired to the electrode, smaller proteins would have more active sites available thus higher electrode coverage compared to WT enzyme. Another aspect could be the change in the electrostatic potential of the exposed

surface when truncating the protein, leading to a poorer interaction with artificial redox partners such as methyl viologen in solution activity assays.

High-potential inactivation could be seen in all truncated variants but not clearly seen in WT enzyme although it is unclear why. The variants have a E_{switch} value of around 70 mV vs SHE, very similar to that of *Dd*HydAB and *Cr*HydA1.

5.4.2 Comparing tolerance towards competitive inhibitors in WT enzyme and its truncated variants

O_2 sensitivity is a highly heated topic for the class of [FeFe] hydrogenases, as they are highly active for reversible catalysis of protons to H_2, yet are very O_2 sensitive, hindering their applications in biotechnology. The O_2 sensitivity of WT enzyme and truncated variants was studied by PFE. A fraction of O_2-saturated buffer was injected to the electrochemical cell, which caused an initial decrease of catalytic currents (~ 10 %) of WT enzyme and truncated variants. WT enzyme and S75 showed some recovery of catalytic currents when O_2 is flushed away with H_2, but D127 and S208 do not show any sign of recovery of catalytic currents. This suggests that the F-clusters may not participate in the initial attack by the O_2 to prevent O_2 inactivation, but rather provide a 'defense' mechanism for the active site to avoid the formation of reactive oxygen species (ROS) by supplying enough electrons to reduce O_2 to water. It can be tentatively concluded that the His-ligated [4Fe-4S] cluster controls the reversibility of oxygen inactivation in *Ca*HydA1, as the variants D127 and S208 do not show any recovery. Overall, the enhanced O_2 tolerance of the M3-type [FeFe] hydrogenases

compared to other types of [FeFe] hydrogenases may relate to differences in the gas channel rather than the F-clusters.

CO inhibition of WT enzyme and truncated variants was also examined by PFE. All WT enzyme and truncated variants showed a rapid decrease of catalytic currents when CO-saturated buffer was added to the electrochemical cell. Subsequently, the catalytic currents were recovered completely after CO was displaced by H_2. This indicates that removal of F-cluster domain has a negligible effect on the competitive inhibition of the enzyme.

5.4.3 Conclusion

In this chapter, the catalytic activity of truncated variants and WT enzyme were compared, and their tolerance towards competitive inhibitors was investigated using protein film electrochemistry. The electrocatalytic activities of the truncated proteins are comparable to that of WT enzyme. Truncation has made the enzyme more biased towards H_2 production without introducing overpotential.

O_2 sensitivity of truncated variants and WT enzyme was kinetically studied by protein film electrochemistry. The results indicate that the F-clusters may not facilitate preventing the initial attack by the O_2, but provide a 'defense' mechanism for the active site by supplying enough electrons to reduce O_2 to water to avoid the formation of reactive oxygen species (ROS). It is likely the His-ligated [4Fe-4S] cluster controls the reversibility of O_2 inactivation, as the variants D127 and S208 do not show any recovery. Taken together, the O_2 sensitivity in various types of [FeFe] hydrogenases may relate to the differences in the gas channel rather

than the F-clusters. Similar CO inhibition effects were observed in truncated variants and WT enzyme, suggesting the removal of F-cluster domain has no impact on the competitive inhibition of the enzyme.

Chapter 6

IR Spectroelectrochemical Studies of the CaHydA1 [FeFe] Hydrogenase and its Truncated Variants – isolation of new active-site States

Chapter 6: IR Spectroelectrochemical Studies on the redox behavior of $[4Fe\text{-}4S]_H$ in *Ca*HydA1 [FeFe] Hydrogenase and its Truncated Variants, and New Active-site States

6.1 Introduction and aim of the chapter

6.1.1 Redox potential of FeS cluster in [FeFe] hydrogenases

FeS clusters are essential electron relays for transporting electrons to and from the buried active centre to the protein surface, enabling efficient catalysis in [FeFe] hydrogenases. Thus, it is important to know the energetics of each of the FeS clusters. Artz and coworkers approximated the redox potential of each of the FeS clusters in the F domain in *Cp*HydA1 [FeFe] hydrogenase using EPR redox titrations. [151] They showed that the His-ligated [4Fe-4S] cluster has the most negative reduction potential (≤ -450 mV vs SHE) and all the other FeS clusters are more positive in reduction potential (~ -366 mV vs SHE). They proposed that the His-ligated [4Fe-4S] cluster controlled the interfacial electron transfer in and out of the protein, as this is the thermodynamically more favorable route compared to the [2Fe-2S] cluster. Rodríguez-Macia and coworkers investigated the redox behavior of $[4Fe\text{-}4S]_H$ using IR spectro-electrochemical titrations in *Dd*HydAB [FeFe] hydrogenase maturated with PDT (which effectively switches off catalysis i.e. allowing only one-electron reduction of the $[4Fe\text{-}4S]_H$ cluster). [77] Their results showed that the accessory F-clusters influence the catalytic properties of the enzyme as they present as strongly coupled to the $[4Fe\text{-}4S]_H$ cluster. This strong interaction magnifies proton-coupled electronic rearrangement within the H-cluster. Redox anticooperativity could be observed as electrostatic repulsion between the F-clusters

and H-cluster or conformational change in the protein as a result of redox coupling. The F-cluster and H-cluster couple mediate an electron, and equilibrates within the F-cluster and $[4Fe\text{-}4S]_H$. A second electron at lower potential reduces the remaining clusters. The mid-point potential of $[4Fe\text{-}4S]_H$ in the M2 type *Dd*HydAB [FeFe] hydrogenase maturated with PDT was shown to be around -500 mV vs SHE.

The redox behavior of $[4Fe\text{-}4S]_H$ in M1 type CrHydA1 and M3 type *Cp*HydA1 [FeFe] hydrogenases maturated with PDT was also studied using IR spectro-electrochemical titrations.[78] The mid-point potential of $[4Fe\text{-}4S]_H$ in the M1 type CrHydA1 [FeFe] hydrogenase maturated with PDT are the same (around – 360 mV vs SHE) for pH 6 and pH 8, which agrees with the 1 H^+/ e^- proton coupled electron transfer (PCET) process[146] [185] and supports that $[4Fe\text{-}4S]_H$ does not participate in PCET and that reduction of $[4Fe\text{-}4S]_H$ does not coupled with protonation. The mid-point potential of $[4Fe\text{-}4S]_H$ in the M3 type *Cp*HydA1 [FeFe] hydrogenase maturated with PDT also show a pH-independent redox potential of the $[4Fe\text{-}4S]_H$ subcluster (around – 490 mV vs SHE). The behavior of oxidized state H_{ox}^{PDT} and reduced state H_{red}^{PDT} measured by IR spectroelectrochemistry was fitted according to the Nernst equation. The M1 type CrHydA1 [FeFe] hydrogenase fitted well to n=1, whereas the M3 type *Cp*HydA1 [FeFe] hydrogenase fitted to $n \approx 0.5$. The non-Nernstitian behavior observed in IR spectroelectrochemical titration in *Cp*HydA1 suggested that the redox anticooperativity between F-clusters and H-cluster was present in CpHydA1 similar to what has been observed in *Dd*HydAB [FeFe] hydrogenase.

6.1.2 Two active-site states observed in *Cb*HydA1 [FeFe] hydrogenase

*Cb*HydA1 [FeFe] hydrogenase was extensively studied in recent years due to its unusual ability to maintain intact active site when exposed to O_2 and to convert reversibly to an O_2-stable inactive state, H_{inact} .[90] [89] It has been suggested that cysteine 367 is key for the formation of the H_{inact} state. The crystal structure of *Cb*HydA1 [FeFe] hydrogenase showed that an FeS bond was formed between the distal Fe and S atom from Cys367. [89] However, it was argued that the resolution of the crystal structure was fairly low (2.9 Å resolution) and the FeS bond distance in this case (3.1 Å) was further apart than a typical bond distance between iron and sulfur (2.4 Å).[186] Interestingly, a recent study revealed that structural flexibility of the active site could be seen in *Cb*HydA1, as both H_{ox} and H_{ox}-CO displayed two distinct forms in EPR spectroscopy.[91] It was shown that interconversion of the two forms were pH-dependent which suggested that the heterogeneity of these two forms originated from a specific perturbation of the coordination environment of the $[4Fe\text{-}4S]_H$ subcluster without altering the $[2Fe]_H$ subcluster, as only one form could be detected in IR spectroscopy and EPR HYSCORE.[161] It was proposed that the protein conformations in the H-cluster of *Cb*HydA1 switches rapidly: one form is related to the bidirectional catalysis of the enzyme, while the other promotes formation of the H_{inact} state under oxidising conditions.

6.1.3 Aim of the chapter

In this chapter, the redox behavior of $[4Fe\text{-}4S]_H$ of *Ca*HydA1 [FeFe] hydrogenases and

truncated variants maturated with PDT were studied using IR spectro-electrochemical titration to determine the midpoint potentials of $[4Fe\text{-}4S]_H$ and their Nernst behaviours. One electron reduction on the $[4Fe\text{-}4S]_H$ causes a small shift of *v*(CO) towards lower wavenumbers due to a small change in electron density at the $[2Fe]_H$. It is thought that the F-clusters are important for interfacial and intramolecular electrons transfer and the effect of removal of F-clusters in the F-domain in truncated variants on the redox behaviour will be studied. In addition, two active-site states in the 'as is' state of the WT enzyme (similar to what has been observed in *Cb*HydA1 [FeHe] hydrogenase) will be studied by IR, EPR spectroscopy and PFE under various pH conditions to investigate their formation and stabilization as well as the coordination environment of the $[4Fe\text{-}4S]_H$ and the $[2Fe]_H$ subclusters in the new isolated states.

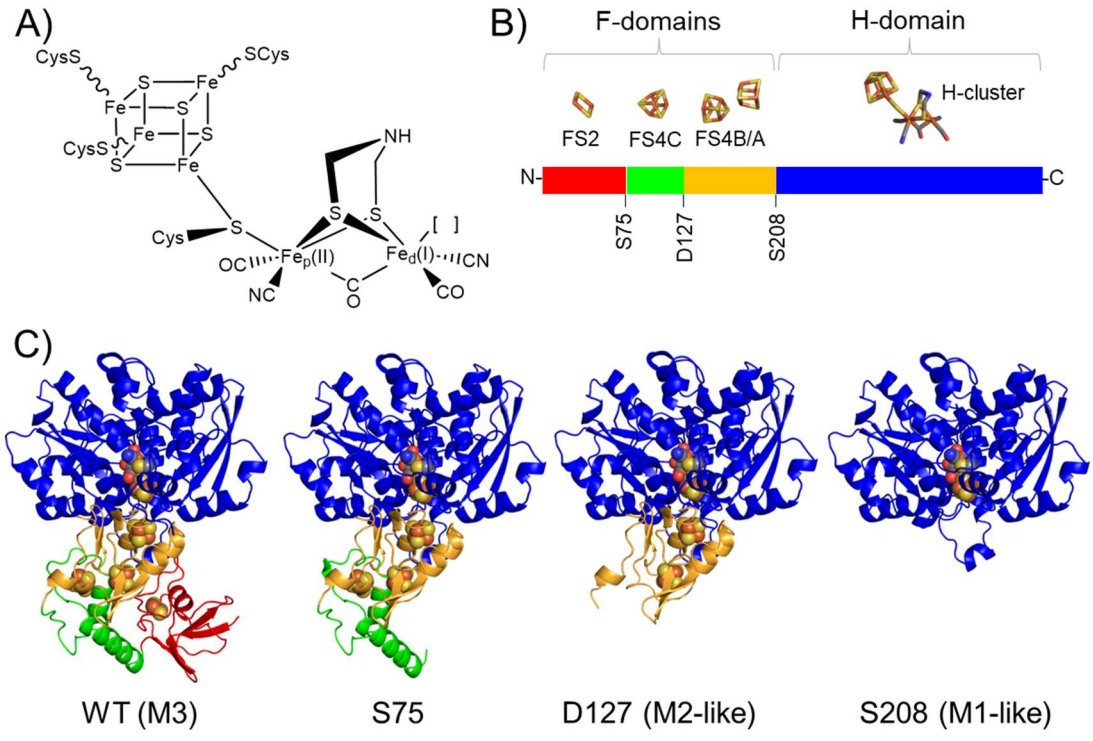


Figure 1: A) Schematic representation of the H-cluster in the H_{ox} state. B) schematic representation of *Ca*HydA1 structure highlighting the residues selected for each truncation. C) AlphaFold models for WT and truncated *Ca*HydA1 variants. The figure is adapted from T.Lai *et al* in preparation [136]

6.2 Redox behaviours of $[4Fe\text{-}4S]_H$ in *Ca*HydA1 [FeFe] hydrogenase and truncated variants

6.2.1 Redox behaviour of $[4Fe\text{-}4S]_H$ in *Ca*HydA1 [FeFe] hydrogenase

The enzyme maturated with PDT allows investigations on the $[4Fe\text{-}4S]_H$, as it only allows a one electron reduction on the $[4Fe4S]_H$ but no catalysis, which enables us to directly measure the E_m of the $[4Fe4S]_H$.[78] IR spectroelectrochemistry was carried out on *Ca*HydA1^{PDT} at pH 8 and pH 6 to observe any differences between two different pH values. Figure 2A and B show the IR spectra of *Ca*HydA1^{PDT} at high potential (-220 mV vs SHE), intermediate potential (-500 mV vs SHE) and low potential (-640 mV vs SHE). The spectra are virtually identical at each of the two pH values except for different intensity due to differences in concentration. At high potential, pure H_{ox}^{PDT} can be observed （1948 cm^{-1} for the most intense CO band, CO at Fe_d）, and this shifts to 1938 cm^{-1} when fully reduced indicating pure H_{red}^{PDT} at low potential, representing a 10 cm^{-1} red shift. This is consistent with a typical one electron reduction of $[4Fe\text{-}4S]_H$ (≈10 cm^{-1} shift in the CO on $[2Fe]_H$), while reduction of $[2Fe]_H$ typically resulted in a larger shift (≈50 cm^{-1}). At -460 mV, roughly equal peak intensities for H_{ox}^{PDT} and H_{red}^{PDT} were seen. By plotting the peak intensity against the applied potential (Figure 2 C, D), the midpoint

potentials (E_m) of $[4Fe4S]_H$ in both pH conditions were determined by fitting to the Nernst equation, and we observed that the E_m (pH8) = -515 ± 20 mV vs SHE and E_m (pH6) = -505 ± 20 mV vs SHE, fitted with n = 0.44 and n=0.48 respectively. The mid-point potentials at the two pH values were nearly identical, which is consistent with the E_m is independent of the pH shown in *Cr*HydA1 and *Cp*HydA1.[78] The difference in E_m between *Ca*HydA1 and *Cp*HydA1 (≈20 mv vs SHE) might be due to the difference in the H-cluster secondary coordination environment as *Ca*HydA1 is 70 % homologous to *Cp*HydA1. The non-Nernstian behaviour observed in both pH conditions is similar to that of *Cp*HydA1, which was fitted with n ≈0.5.[78] This indicates that redox anti-cooperativity between F-cluster and H-cluster was also seen in WT *Ca*HydA1.

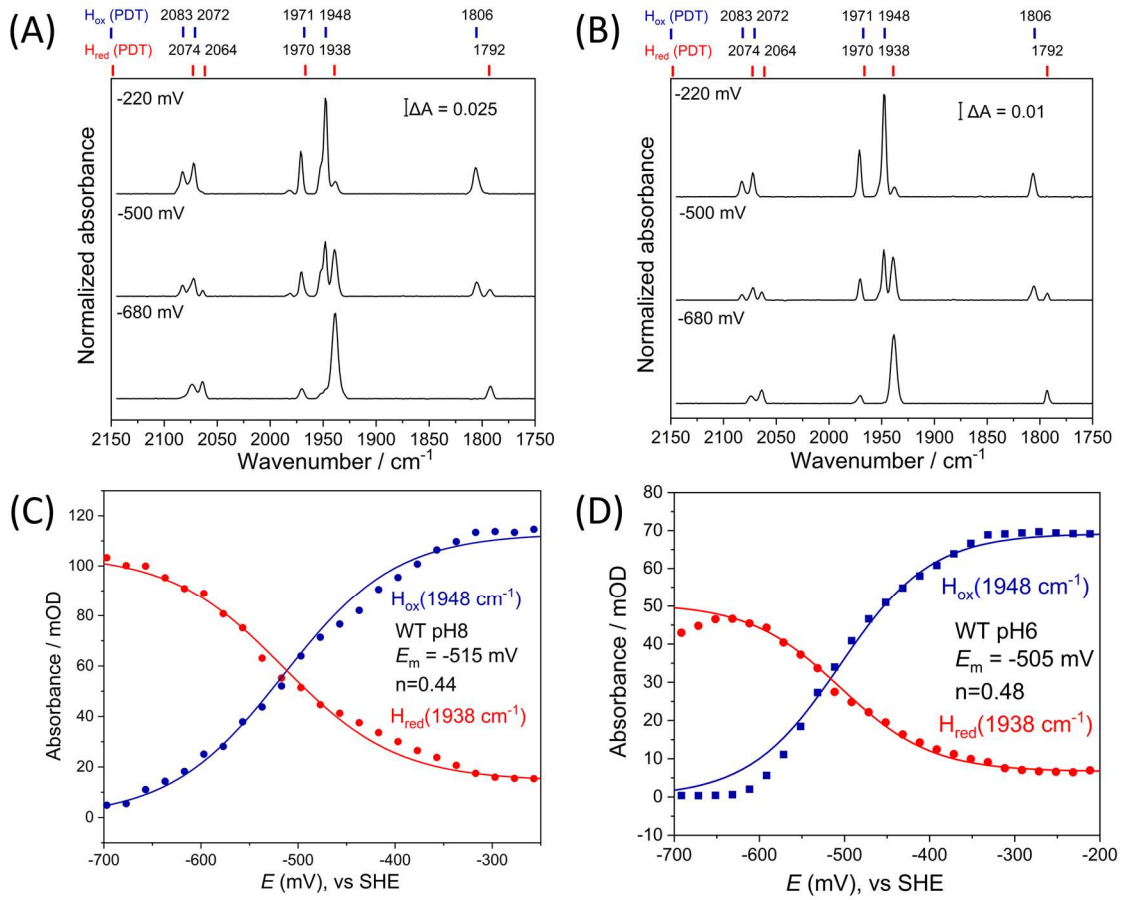


Figure 2: IR spectroelectrochemistry of *Ca*HydA^{PDT} at pH 8 and pH 6. (A) selected IR spectra ≈2mM *Ca*HydA^{PDT} in 100 mM Tris-HCl, pH 8 containing 150 mM NaCl as the supporting electrolyte at different applied potentials showing H_{ox}^{PDT} (blue peaks), H_{red}^{PDT} (red peaks) states. (B) selected IR spectra ≈2mM *Ca*HydA^{PDT} in 100 mM MES, pH 6 containing 150 mM NaCl as the supporting electrolyte at different applied potentials showing H_{ox}^{PDT} (blue peaks), H_{red}^{PDT} (red peaks) states. (C) Redox titration plot of the most intense feature in the H_{ox}^{PDT} and H_{red}^{PDT} states, fitted according to the Nernst equation, as represented by blue and red lines. (D) Same as (C), but at pH=6. The fitting include redox anticooperativity in the fitting models[158]

6.2.2 Comparison of the redox behavior of $[4Fe\text{-}4S]_H$ in WT *Ca*HydA1 [FeFe] hydrogenase and its truncated variants

To observe the effect of accessory F-clusters on the redox behavior of the $[4Fe\text{-}4S]_H$. We performed IR spectroelectrochemistry on the S75, D127 and S208 truncated variants. Figure 3 A, C and E shows the IR spectra of *Ca*HydA^{PDT} S75, D127 and S208 truncated variants at high potential (-220 mV vs SHE), intermediate potential (-550 mV vs SHE) and low potential (-640 mV vs SHE). At high potential, pure H_{ox}^{PDT} can be observed at 1953 cm^{-1} for the most intense CO band (CO at Fe_d), and shifts to 1940 cm^{-1} when fully reduced to pure H_{red}^{PDT} at low potential, with a 13 cm^{-1} red shift, which is a slightly larger shift compared to WT enzyme. Plots of the intensity of most intense feature in the H_{ox}^{PDT} (1953 cm^{-1}) and H_{red}^{PDT} (1940 cm^{-1}) with the applied potential and their Nernst fittings are shown in figure 3 B, D, F. The E_m(pH 8) = -535 mV ± 20 vs SHE for S75, E_m(pH 8) = -560 mV ± 20 vs SHE for D127, and E_m(pH 8) = -538 mV ± 20 vs SHE for S208, all fitted with n = 1. The E_m values of all truncated variants are more negative in potential (≥ 25 mV) compared to that of WT enzyme. D127, in particular, has a potential 50 mV more negative than WT enzyme. This suggested that removal of the F-cluster in the F-domain has a long range effect on the mid-point potential of the $[4Fe4S]_H$. Interestingly, a shoulder peak of $H_{ox\ 1948}$ state (the most intense CO band at 1948 cm^{-1} seen in WT enzyme) was observed in D127 at high potential, (-220 mV vs SHE), and got fully converted to pure $H_{ox\ 1953}$ state (the most intense CO band at 1953 cm^{-1} in all truncated protein) when potential became more negative. Subsequently, the truncated H_{ox} state was then converted to truncated H_{red} state at low potential. This may explain why D127 has a slightly more negative potential than the other two truncated variants which are similar in E_m value. The

interesting two forms of H_{ox} state in D127 and WT enzyme will be discussed in the following section. Surprisingly, all truncated variants displayed Nernst behavior as they were fitted well to n=1. This suggests that truncating the F-cluster domain in the F-domain has disrupted the anti-cooperativity between the F-cluster and H-cluster. Removal of [2Fe-2S] cluster domain in the F-domain in S75 variant has caused a large change in the Nernst behavior. This again highlights the importance of [2Fe-2S] cluster in controlling interfacial and intramolecular electron transfer. Truncating the [2Fe-2S] cluster domain in the F-domain has resulted in a negative shift of the mid-point potential of $[4Fe\text{-}4S]_H$ in all truncated variants.

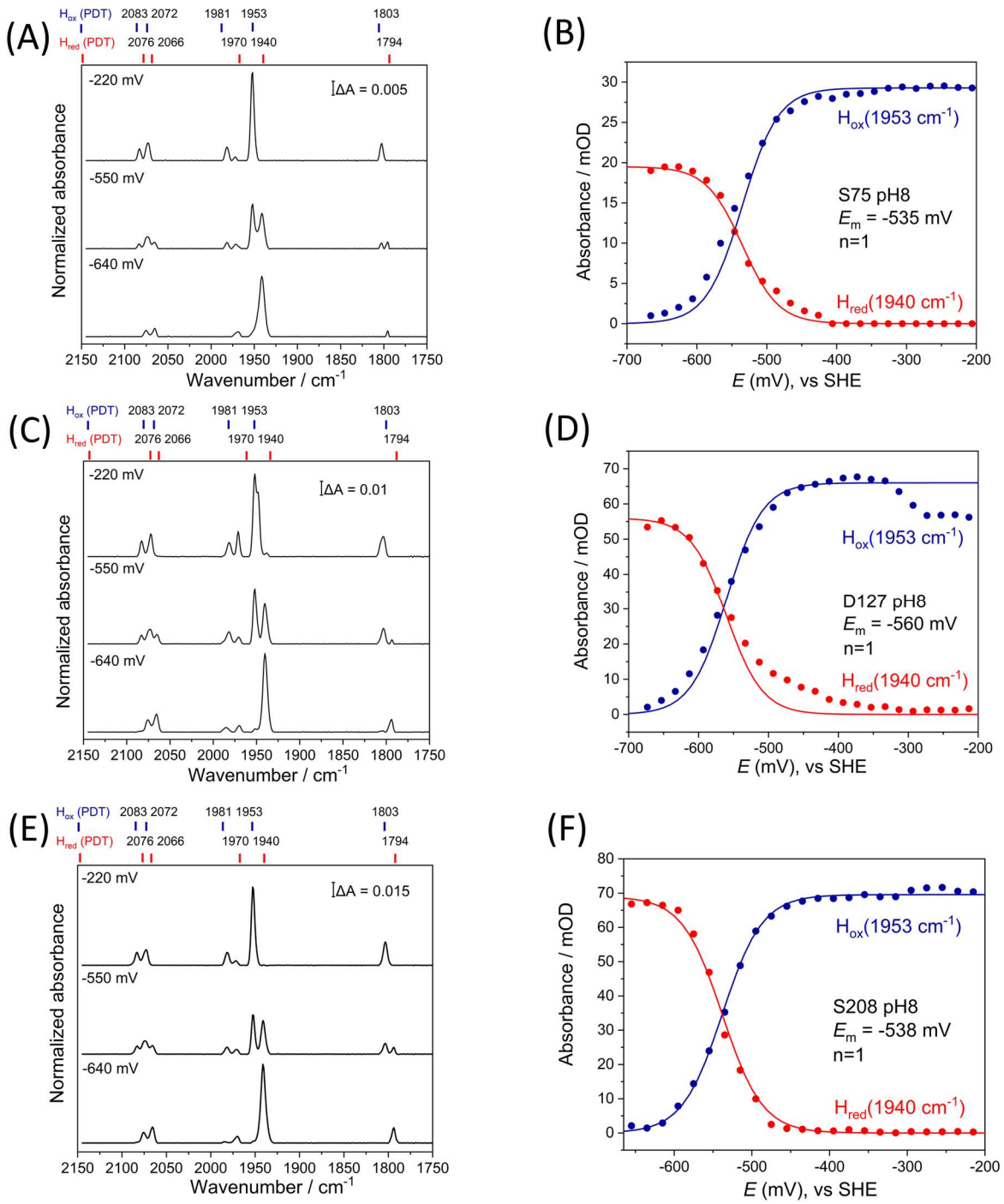


Figure 3: IR spectroelectrochemistry of *Ca*HydA^{PDT} truncated variant at pH 8. (A) Selected IR spectra ≈2 mM S75 *Ca*HydA^{PDT} in 100 mM Tris-HCl, pH 8 containing 150 mM NaCl as the supporting electrolyte at different applied potentials showing H$_{ox}^{PDT}$ (blue peaks), H$_{red}^{PDT}$ (red peaks) states. (B) Redox titration plot of the most intense feature in the H$_{ox}^{PDT}$ and H$_{red}^{PDT}$ states of S75, fitted to the Nernst equation (blue and red lines). (C) Redox titration plot of the most intense feature in the H$_{ox}^{PDT}$

and H_{red}^{PDT} states, fitted to the Nernst equation (blue and red lines). (C) Selected IR spectra ≈2 mM D127 *Ca*HydA^{PDT} at different applied potentials showing H_{ox}^{PDT} (blue peaks), and H_{red}^{PDT} (red peaks) states. (D) Redox titration plot of the most intense feature in the H_{ox}^{PDT} and H_{red}^{PDT} states of D127, fitted to the Nernst equation (blue and red lines). (E) Selected IR spectra ≈2mM S208 *Ca*HydA^{PDT} at different applied potentials showing H_{ox}^{PDT} (blue peaks), and H_{red}^{PDT} (red peaks) states. (D) Redox titration plot of the most intense feature in the H_{ox}^{PDT} and H_{red}^{PDT} states of S208, fitted to the Nernst equation (blue and red lines). The fitting include redox anticooperativity in the fitting models[158]

6.3 New active-site States

6.3.1 Two active-site states observed in the 'as is' state in D127 truncated variants

Observation of two forms of the H_{ox} state of D127 maturated with PDT were seen in the previous section. Similar observations could also be seen in the D127 variant maturated with ADT (See figure 4 and figure 6d). The D127 variant maturated with ADT was isolated with two forms of H_{ox} state at pH 8 as observed by IR spectroscopy: $H_{ox\ 1951}$ state (the most intense CO band at 1951 cm^{-1}) and $H_{ox\ 1946}$ state (the most intense CO band at 1951 cm^{-1}). It was also shown in EPR spectroscopy from a second derivative signal (Figure 6d) that the H_{ox} state consists of two components in the D127 variant. The $H_{ox\ 1951}$ state of D127 truncated variant could be enriched when buffer was exchanged to pH 9. This suggests that the change in coordination environment around $[4Fe\text{-}4S]_H$ and $[2Fe\text{-}2S]_H$ in D127 variant is pH dependent, revealing an atypical structural flexibility of the active site surrounding in the D127 variant. Interestingly, only one form of H_{ox} state ($H_{ox\ 1951}$ state) could be observed in S75 and S208

truncated variants (Figure 6c, e; Table 1). In contrast to *Cb*HydA1, the CO adduct H_{ox}-CO state of the truncated variants is only present in one form (Figure 7c-e; Table 1).

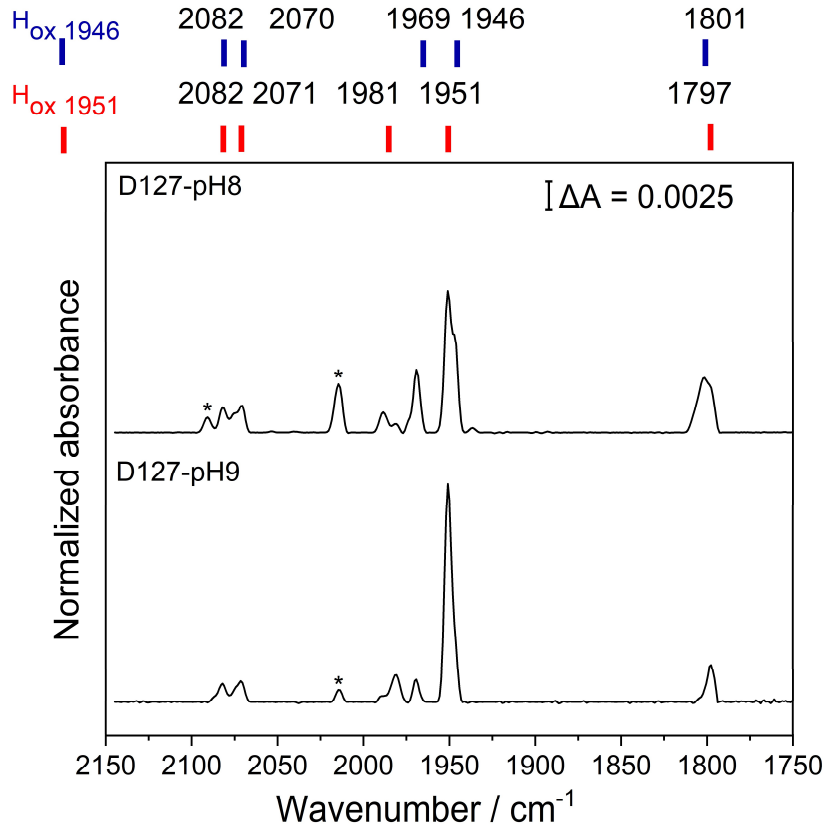


Figure 4: The FTIR spectrum of 1-2 mM of D127 truncated proteins as isolated (maturated with ADT cofactors) at pH8 and pH9. Two forms of H_{ox} states : $H_{ox\ 1946}$ state and $H_{ox\ 1951}$ state are highlighted with blue and red respectively.

6.3.2 pH dependent interconversion of the two active-site states in the 'as is' state of the WT enzyme

H_{ox} state in WT enzyme in pH 8 also exists in two forms in the 'as is' samples shown by IR and

EPR spectroscopy (Figure 5 and Figure 6b). The major form in pH 8 is $H_{ox\ 1946}$ state and minor form in $H_{ox\ 1951}$ state which is seen in all truncated proteins. The $H_{ox\ 1951}$ state can be enriched in higher pH conditions with almost 1:1 ratio in pH 9 condition and can be 100 % enriched in pH 10 observed by IR spectroscopy. To investigate if this is reversible, WT enzyme in pH 10 was buffer exchanged to 8 and 6 respectively. The WT state can be recovered 50 % in pH 8 and it was shown that it can be almost recovered in pH 6 condition. The interconversion of two forms of WT state is pH dependent, suggesting that the change of the coordination environment of $[4Fe\text{-}4S]_H$ and $[2Fe\text{-}2S]_H$ is pH dependent. The observation of two forms in WT *Ca*HydA1 enzyme is similar to that of *Cb*HydA1. However, there is no pH dependence in the case of *Cb*HydA1 in both H_{ox} state and H_{ox}-CO state and that only one form can be observed in *Cb*HydA1 from IR spectroscopy. This suggests the change in the coordination environment for *Ca*HydA1 enzyme involves a proton movement within the H-cluster and its closed proximity (as the wavenumber shift is within 10 cm^{-1}), whereas *Cb*HydA1 does not involve a proton movement. Secondly, the change in the coordination environment for *Cb*HydA1 is possibly only close to the $[4Fe\text{-}4S]_H$ subcluster without having an influence on the $[2Fe\text{-}2S]_H$ subcluster, whereas the change in coordination environment for *Ca*HydA1 does have an impact on the $[2Fe\text{-}2S]_H$ subcluster, therefore could be detected by FTIR spectroscopy. The two forms of H_{ox} and H_{ox}-CO states could be further confirmed by EPR spectroscopy (Figure 6b, 7b; Table 1), as the second derivative signal showed that both H_{ox} and H_{ox}-CO state consist of two components in the WT enzyme.

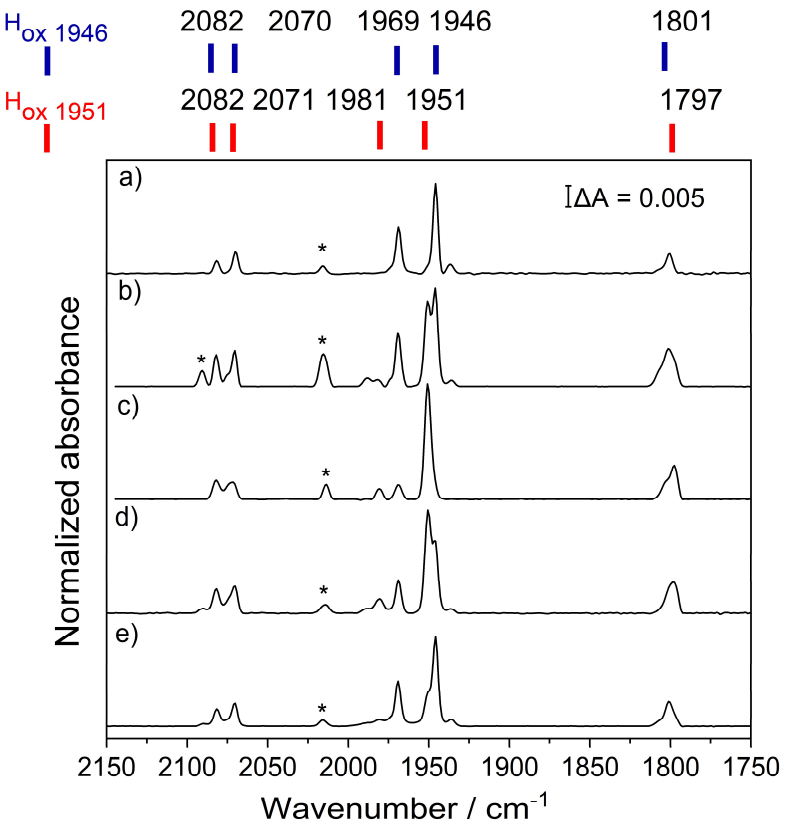


Figure 5: The FTIR spectrum of 1-2 mM of WT *Ca*HydA1 proteins as isolated (maturated with ADT cofactors) a) at pH 8, b) at pH 9 and c) at pH 10; d) buffer exchanged from pH 10 to pH 8 and e) buffer exchanged from pH 10 to pH 6. Two forms of H_{ox} states: $H_{ox\ 1946}$ state and $H_{ox\ 1951}$ state are highlighted with blue and red respectively.

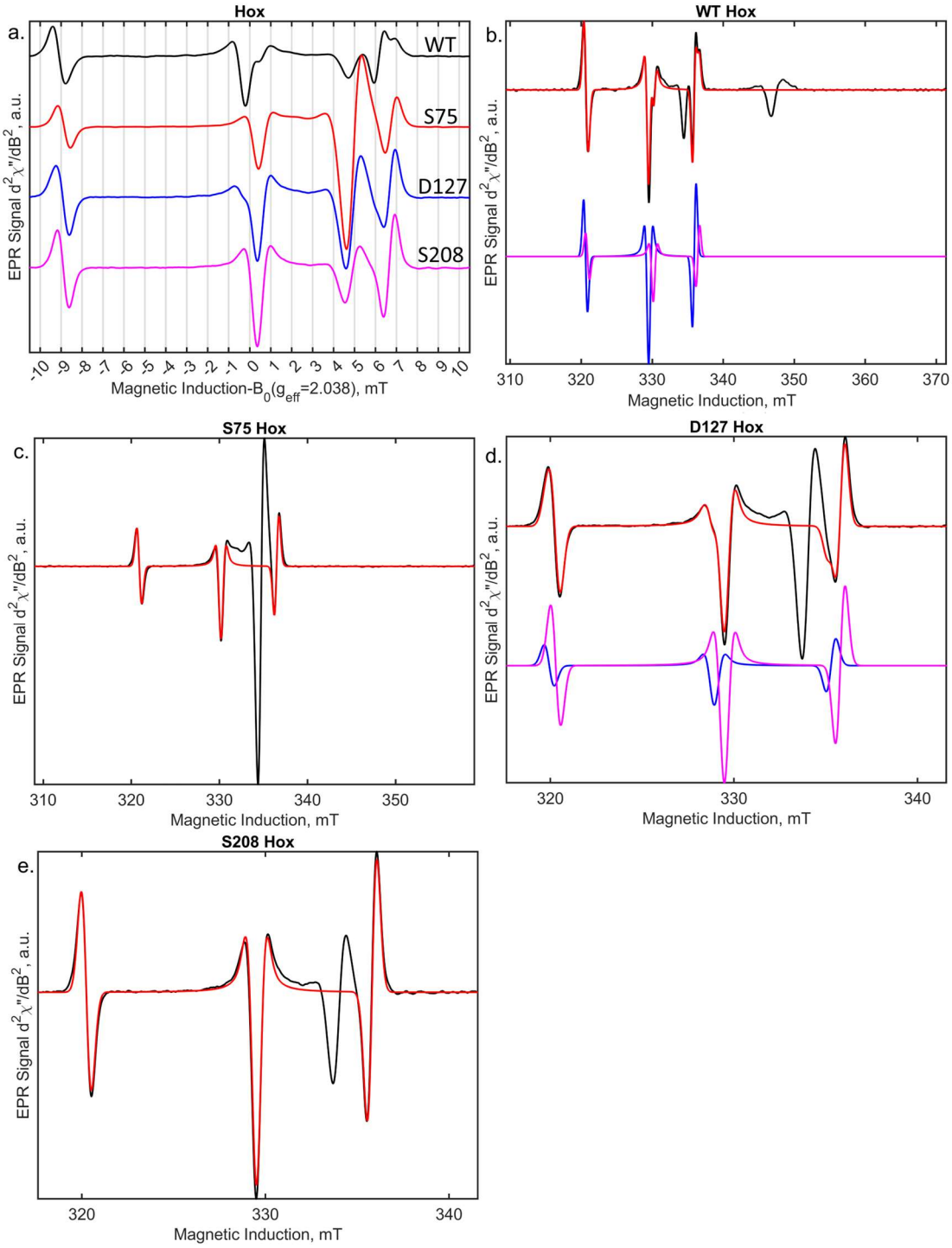


Figure 6: Simulations of the H_{ox} state of numerical second derivatives via 0.5 mT pseudomodulation of CW-EPR spectra at X-band of 200 µM wild type (WT) and truncated variants S75, D127, and S208. Panel a. shows all data as second derivatives, whilst panels b-e have corresponding total simulations in red and components in blue and violet. All samples contain fractional H_{ox}-CO states, while WT additionally contains a $[2Fe\text{-}2S]^{+}$ signal. The spectra are made by collaborator Dr. Will Myers.

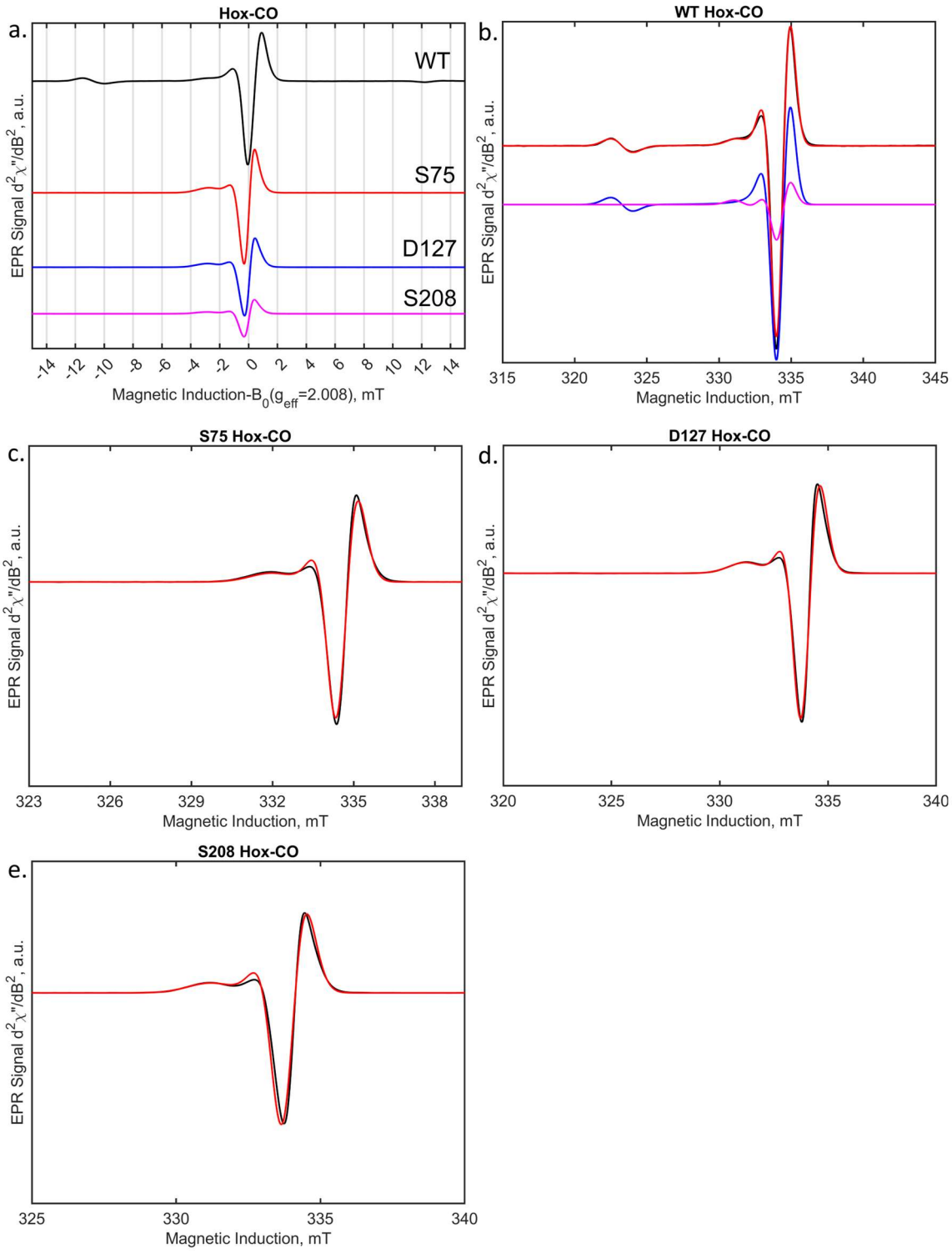


Figure 7: Simulations of the H_{ox}-CO state of numerical second derivatives via 0.5 mT pseudomodulation of CW-EPR spectra at X-band of 200 µM wild type (WT) and truncated variants S75, D127, and S208. Panel a. shows all data as second derivatives, whilst panels b-e have corresponding total simulations in red and components in blue and violet. All samples contain mainly H_{ox}-CO states, while WT additionally contains a $[2Fe\text{-}2S]^{+}$ signal. The spectra are made by

collaborator Dr. Will Myers.

Table 1： ***Ca*HydA1 [FeFe] hydrogenase variants EPR simulation parameter values.** **[a]Linewidths were $\sigma_{1,2,3}$ =7.9,7.9,7.2 MHz [b]An axial g-matrix is assumed. Linewidths were $\sigma_{1,2,3}$= 25,13,13 MHz**

State	Protein		Component fraction	g_1	g_2	g_3	g_{iso}
H_{ox} [a]	WT	Comp 1	F=0.7	2.096	2.0395	2.0005	2.0453
		Comp 2	F=0.3	2.0942	2.0355	1.9975	2.0424
	S75	Comp 1	F=1	2.0930	2.0342	1.996	2.0411
	D127	Comp 1	F=0.25	2.0965	2.0392	2.0005	2.0454
		Comp 2	F=0.75	2.0942	2.0358	1.9975	2.0425
	S208	Comp 1	F=1	2.0946	2.0357	1.9975	2.0426
H_{ox}-CO [b]	WT	Comp 1	F=0.9	2.075	2.0069	2.0069	2.0296
		Comp 2	F=0.1	2.0225	2.0069	2.0069	2.0121
	S75	Comp 1	F=1	2.02	2.008	2.008	2.012
	D127	Comp 1	F=1	2.022	2.009	2.009	2.0133
	S208	Comp 1	F=1	2.022	2.0095	2.0095	2.0137
Apo-protein	Apo	$[2Fe\text{-}2S]^+$	F=1	2.025	1.935	1.935	1.965

Since the $H_{ox\ 1946}$ state in WT enzyme could be enriched to $H_{ox\ 1951}$ state 100 % in pH 10, the electrochemistry of both states in the WT enzyme could be directly compared. WT enzyme buffer-exchanged to pH 10 (containing only $H_{ox\ 1951}$ state) and WT enzyme at pH 8 were both loaded to electrochemical cell containing Mixed buffer pH 8 (containing only $H_{ox\ 1946}$ state) showed a dramatic difference in the catalytic waveshape of CV curves (see figure 8). The CV of WT enzyme buffer-exchanged to pH 10 exerted similar catalytic characteristic to that of truncated variants, which indicates the change in the electronic structure (potential) of the H-cluster may have influenced the downstream reduction potential of the accessory F-clusters according to 'electrostatic' effects, which in turn affects the catalytic bias.

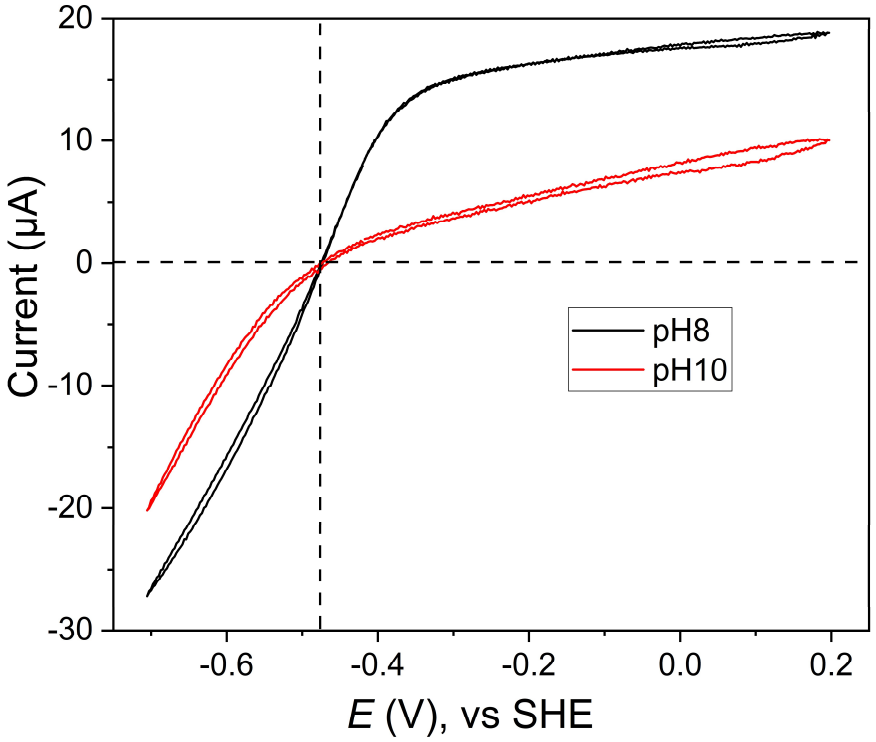


Figure 8: Cyclic voltammetry (CV) of the WT *Ca*HydA1 [FeFe] hydrogenases at pH 10 (red), and WT *Ca*HydA1 at pH 8 (black) adsorbed onto a pyrolytic graphite 'edge' electrode using mixed buffer at pH 8, room temperature (RT), 100% H_2 (1 L/ min), 2000 rpm and 20 mV /s scan rate. The horizontal dashed line represents the zero current, and the vertical dashed line indicates the thermodynamic potential of the $2H^+/H_2$ couple under experimental conditions.

6.4 Discussion and conclusions

6.4.1 Redox behaviors of $[4Fe\text{-}4S]_H$ in *Ca*HydA1 [FeFe] hydrogenases and its truncated variants

Enzyme maturated with PDT cofactor enables measurements of the mid-point potential of $[4Fe\text{-}4S]_H$ of [FeFe] hydrogenases (effectively switches off the catalysis) using IR spectroelectrochemistry. The E_m of $[4Fe\text{-}4S]_H$ of [FeFe] hydrogenases could be derived by fitting the Nernst equation of the peak intensity against the applied potential plot. Similar E_m values of $[4Fe\text{-}4S]_H$ of *Ca*HydA1 [FeFe] hydrogenase in pH6 and pH8 were obtained (E_m (pH 8) = -515 ± 20 mV vs SHE and E_m (pH6) = -505 ± 20 mV vs SHE, fitted to n = 0.44 and n=0.48 respectively). This suggests that $[4Fe\text{-}4S]_H$ does not play a role in PCET and a proton was not involved in the reduction of $[4Fe\text{-}4S]_H$. In addition, anti-cooperativity between accessory F-clusters and H-cluster in *Ca*HydA1 was observed as both plots were fitted to n $\approx$ 0.5 representing non-Nernst behaviour.

IR spectroelectrochemistry of truncated variants revealed E_m values of $[4Fe\text{-}4S]_H$ with E_m(pH 8) = -535 mV ± 20 vs SHE for S75, E_m(pH 8) = -560 mV ± 20 vs SHE for D127, and E_m(pH 8) = -538 mV ± 20 vs SHE for S208, all fitted to n = 1. All E_m values of $[4Fe\text{-}4S]_H$ of truncated variants are more negative compared to that of WT enzyme ($\geq$ 25 mV), indicating a long-range effect of truncating the F-clusters domain on the potential of the $[4Fe\text{-}4S]_H$. Interestingly, all truncated variants were fitted to n=1 following a standard Nernst behaviour, suggesting that the anti-cooperativity between accessory F-clusters and H-cluster is disrupted by truncating the F-clusters domain. Truncating the [2Fe-2S] cluster domain only in S75 has a significant impact

on the potential of the $[4Fe\text{-}4S]_H$ and Nernst behaviour of the enzyme, highlighting the role of the [2Fe-2S] cluster in controlling interfacial and intramolecular electron transfer in *Ca*HydA1.

6.4.2 New Active-site State in WT Enzyme

Two forms of H_{ox} states ($H_{ox\ 1946}$ state and $H_{ox\ 1951}$ state which is seen in WT enzyme) were observed in D127 variants shown by both IR and EPR spectroscopy. The $H_{ox\ 1946}$ state could be enriched to $H_{ox\ 1951}$ state 100 % in D127 truncated variant upon buffer exchanged to pH 9. This suggests that the change in coordination environment around $[4Fe\text{-}4S]_H$ and $[2Fe\text{-}2S]_H$ in D127 variant is pH dependent and possibly involves a proton movement. However, H_{ox} state only exists in one form for S75 and S208 truncated variants. H_{ox}-CO only exists in one form for truncated variants, which differs to *Cb*HydA1.

We found that H_{ox} state in WT *Ca*HydA1 also exists in two forms: $H_{ox\ 1946}$ state and minor form of $H_{ox\ 1951}$ state which is seen in all truncated variants, shown by both IR and EPR spectroscopy. The $H_{ox\ 1946}$ state in WT enzyme can be enriched in a more alkaline condition (pH 10) and reconverted to WT H_{ox} state in a more acidic condition (pH 6). The pH dependence of the interconversion between both forms indicates the involvement of proton movement in the coordination environment around $[4Fe\text{-}4S]_H$ and $[2Fe\text{-}2S]_H$, revealing an atypical structural flexibility of the active site surrounding in WT enzyme. In addition, two forms of H_{ox}-CO state in WT could be detected by EPR spectroscopy. Protein film electrochemistry further confirms the existence of both forms in WT enzyme as two distinct waveshapes were seen. The CV of WT enzyme at pH 10 exerted similar catalytic characteristic to that of truncated variants, suggesting that the catalytic bias of [FeFe] hydrogenases may relate to the redox state of the

H-cluster rather than reduction potential of the distal cluster. Alternatively, the change in the electronic structure (potential) of the H-cluster in WT enzyme may have influenced the downstream reduction potential of the accessory F-clusters according to 'electrostatic' effect, which in turn affects the catalytic bias.

6.4.3 Conclusion

In this chapter, redox behaviors of $[4Fe\text{-}4S]_H$ of *Ca*HydA1 [FeFe] hydrogenases and its truncated variants, as well as new catalytic state in WT *Ca*HydA1 were studied. IR spectroelectrochemistry of WT enzyme in pH 6 and pH 8 revealed similar E_m potential of $[4Fe\text{-}4S]_H$, suggesting that the $[4Fe\text{-}4S]_H$ does not play a role in PCET and a proton was not involved in the reduction of $[4Fe\text{-}4S]_H$. All truncated variants showed more negative E_m potential values ($\geq$ 25 mV) compared to WT enzyme, indicating a long-range effect of removal of F-cluster domain on the E_m potential of $[4Fe\text{-}4S]_H$.

Two forms of H_{ox} state and its CO adduct H_{ox}-CO state in WT *Ca*HydA1 could be confirmed by FTIR and EPR spectroscopy. The interconversion of the two forms of H_{ox} state is pH-dependent, which suggests the change in coordination environment around $[4Fe\text{-}4S]_H$ and $[2Fe\text{-}2S]_H$ involves a proton movement, revealing an atypical structural flexibility of the active site surrounding of WT enzyme.

Chapter 7

Conclusion and Outlook

Chapter 7: Conclusion and Outlook

7.1 Conclusion

Iron-sulfur (FeS) clusters function as electron relays in metalloenzymes, which are essential for the intermolecular and intramolecular electron transfer from the protein surface to the buried active site, enabling efficient catalysis. This project has focused on engineering the electron relay on one of the best H_2 producers among [FeFe] hydrogenase, the M3 type *Ca*HydA1 [FeFe] hydrogenase, to understand its effect on catalytic behaviour, O_2 sensitivity and the long-range influence on the active site's electronic characteristics. The ultimate goal is to study from nature to design a better biocatalyst or synthetic catalyst suited for future bio-applications.

7.1.1 Development of a heterologous overexpression system for apo-*Ca*HydA1 [FeFe] hydrogenase and *in vitro* maturation with synthetic cofactor

Chapter 3 focused on the establishment of a heterologous overexpression system for the apo-form of *Ca*HydA1 [FeFe] hydrogenase, enabling subsequent *in vitro* maturation with synthetic cofactors. The development of the *in vitro* maturation system for *Ca*HydA1 [FeFe] hydrogenase sets the groundwork for the advanced work in this project.

Heterologous expression for *Ca*HydA1 [FeFe] hydrogenases using maturases system was first performed, yielding 1.15 mg/L of relatively not pure protein after a two-step purification. In comparison, the heterologous expression for apo-*Ca*HydA1 [FeFe] hydrogenases using the *in vitro* maturation system produced 5.05 mg/L of purer protein after a single-step strep-tag

purification. Further characterization using FTIR, Protein film electrochemistry and solution activity assay all showed that *in vitro* maturation system enables higher incorporation of $[2Fe]_H$ binuclear site compared to the maturases system. FTIR and EPR spectroscopy showed that *Ca*HydA1 [FeFe] hydrogenases produced using *in vitro* maturation system are consistent with previously reported data. These findings suggest that *in vitro* maturation system is a better approach for the production of *Ca*HydA1 [FeFe] hydrogenases.

7.1.2 Functional and spectroscopic characterization of the truncated variants and comparison with the wild-type enzyme

The successful establishment of the *in vitro* maturation system for *Ca*HydA1 [FeFe] hydrogenase allows the generation of highly active enzymes, and it also eases the genetic modification of the enzyme. *Ca*HydA1 [FeFe] hydrogenase was engineered by truncating the F-cluster domains, with the aim of removing the accessory F-clusters one by one to generate three truncated variants (S75, D127 and S208). The production of three truncated variants as well as functional and spectroscopic characterizations of these variants are detailed in chapter 4.

All truncated variants were isolated and maturated successfully, showing an intact active site and visible catalytic activities, verified by FTIR, EPR and solution activity assays, respectively. Notably, the enzyme production yield increased with more extensive truncation, especially for the S208 variant, yielding 28 mg/L, which is almost 6 times of the WT enzyme (5.05 mg/L). Spectroscopic techniques (FTIR and EPR) revealed a long-range effect of truncating the F-

cluster domain on the active site's electronic characteristics. The catalytic activities of truncated variants, assessed by solution activity assays, showed drastically lower activities compared to WT enzyme. However, this differed from results shown by electrochemistry, where all truncated variants exhibited higher activities when wired to the electrode. Notably, the S208 showed twice the activity compared to the WT enzyme. This discrepancy may arise from changes in the protein surface charge due to truncations, which influences the interaction between the protein and methyl viologen (effectively affecting the K_m for methyl viologen) and how well the proteins were absorbed to the electrode. In addition, solution activity assays with the physiological redox partner indicated that the natural binding site is likely the [2Fe-2S] cluster-containing N-terminal domain, suggesting that the electron entry point is the [2Fe-2S] cluster instead of His-ligated [4Fe-4S] cluster. Removing the [2Fe-2S] cluster domain only in the S75 has resulted in substantial changes in the active site's electronic characteristics and catalytic behavior. This result implies that [2Fe-2S] cluster controls the interfacial electron transfer of *Ca*HydA1 [FeFe] hydrogenase and has a long-range effect on the active site catalysis.

7.1.3 Comparing the catalytic activity of truncated variants and WT enzyme, and their tolerance towards competitive inhibitors

Chapter 5 compared the electrochemistry of truncated variants and WT enzyme to study the electrocatalytic behaviour, catalytic bias, high-potential inactivation and the redox potentials of the most distal FeS cluster of truncated variants and WT enzyme. Additionally, the tolerance of truncated variants and WT enzyme towards competitive inhibitors such as O_2 and CO_2 was

also investigated.

All truncated variants showed comparable electrocatalytic activities to WT enzyme, with the S208 displaying twice the electrocatalytic activity of WT enzyme, as studied by protein film electrochemistry. All truncated variants were more biased towards H_2 production than the WT enzyme without introducing overpotential. This also suggests the [2Fe-2S] cluster is the most distal cluster (electron entry point), as truncating the [2Fe-2S] cluster domain in S75 variant alone has resulted in these effects. The truncated variants retained similar O_2 sensitivity compared to the WT enzyme. The results suggest that the His-ligated [4Fe-4S] cluster controls the reversibility of O_2 inactivation, as the reversibility ceased in D127 variant. We conclude that the O_2 sensitivity may relate to the differences in the gas channels rather than the electron relay (F-clusters) in [FeFe] hydrogenases. Similar CO inhibition effect was observed in truncated variants and WT enzyme.

7.1.4 IR spectroelectrochemical studies of the redox behavior of $[4Fe\text{-}4S]_H$ in *Ca*HydA1 [FeFe] hydrogenase and its truncated variants, new active-site statess

The redox potential of $[4Fe\text{-}4S]_H$ of *Ca*HydA1 [FeFe] hydrogenase and its truncated variants could be determined by IR spectroelectrochemistry. The E_m values of $[4Fe\text{-}4S]_H$ of [FeFe] hydrogenases were derived by fitting the Nernst equation tof the peak intensity versus the applied potential plot. Similar E_m values of $[4Fe\text{-}4S]_H$ could be obtained at pH 6 and pH 8 of WT enzyme, suggesting that the $[4Fe\text{-}4S]_H$ does not participate in (proton coupled electron transfer) PCET and that a proton is not involved in the reduction of $[4Fe\text{-}4S]_H$. In addition, the

E_m values of $[4Fe\text{-}4S]_H$ of truncated variants were ≥25 mV more negative than WT enzyme, confirming a long-range effect of the removal of F-cluster domain on the E_m potential of $[4Fe\text{-}4S]_H$.

FTIR and EPR spectroscopy revealed two forms of H_{ox} state and its CO adduct H_{ox}-CO state in WT *Ca*HydA1. The interconversion of the two forms of H_{ox} state is pH-dependent, suggesting that a proton movement is associated with the change in coordination environment around $[4Fe\text{-}4S]_H$ and $[2Fe\text{-}2S]_H$, revealing an atypical structural flexibility of the active site surrounding of WT enzyme.

Overall, the work presented in this thesis contributes a systematic study on the long-range effect of the electron relay (accessory F-clusters) on the catalysis in *Ca*HydA1 [FeFe] hydrogenase. The catalytic behavior (including catalytic bias and catalytic activity), redox potentials of $[4Fe\text{-}4S]_H$ and most distal cluster, and O_2 sensitivity were explored in detail. Furthermore, this work provides important insights into the electron relay and the binding site of ferredoxin in *Ca*HydA1. More generally, it demonstrates how the electron relay in [FeFe] hydrogenases can be engineered to produce variants with specific properties.

7.2 Outlook

Future experiments to further understand the mechanistic details and functional properties of *Ca*HydA1 [FeFe] hydrogenase and its truncated variants should include obtaining structural information using X-ray crystallography or Cryo-EM (Cryo-electron microscopy), which would provide comprehensive insight into changes in the secondary amino acid environment around the active site, as well as general conformational changes in the protein structure following

protein truncation. Although *Ca*HydA1 and its truncated variants might be too small for Cryo-EM. However, the resolution of small proteins using cryo-EM has been made possible through the use of nanobody-binding scaffolds and advancements in computational techniques.[187] [188] In addition, alphafold3 can also be a powerful tool to predict the structure with a very high accuracy.

Furthermore, the catalytically active $H_{red}H^+$ and H_{hyd} states, previously unseen in WT enzyme but present in truncated variants under reducing condition, warrant further investigation. IR spectroelectrochemistry of the WT enzyme and its truncated variants, maturated with ADT, will further elucidate the influence of truncating the F-clusters domain on the populations of various catalytic states (in particular, $H_{red}H^+$, H_{hyd} states) under electrochemical control *in-situ*. This would provide valuable information on the influence of proton couple electron transfer (PCET) and redox anti-cooperativity effect in this enzyme.

References

[1] W. Lubitz, H. Ogata, O. Rüdiger, E. Reijerse, *Chem. Rev.* **2014**, *114*, 4081-4148.

[2] D. Sokolova, K. A. Vincent, *Chem. Commun.* **2024**, *60*, 13667-13677.

[3] S. Joseph Srinivasan, S. E. Cleary, M. A. Ramirez, H. A. Reeve, C. E. Paul, K. A. Vincent, *Angew Chem Int Ed Engl* **2021**, *60*, 13824-13828.

[4] S. Joseph Srinivasan, S. E. Cleary, M. A. Ramirez, H. A. Reeve, C. E. Paul, K. A. Vincent, *Angew. Chem. Int. Ed.* **2021**, *60*, 13824-13828.

[5] M. A. Ramirez, S. Joseph Srinivasan, S. E. Cleary, P. M. T. Todd, H. A. Reeve, K. A. Vincent, *Front. catal* **2022**, *2*.

[6] D. Sokolova, T. C. Lurshay, J. S. Rowbotham, G. Stonadge, H. A. Reeve, S. E. Cleary, T. Sudmeier, K. A. Vincent, *Nat. Commun.* **2024**, *15*, 7297.

[7] M. Frey, *ChemBioChem* **2002**, *3*, 153.

[8] J. Szczesny, J. A. Birrell, F. Conzuelo, W. Lubitz, A. Ruff, W. Schuhmann, *Angew. Chem. Int. Ed.* **2020**, *59*, 16506-16510.

[9] Y. Liu, C. Pulignani, S. Webb, S. J. Cobb, S. Rodríguez-Jiménez, D. Kim, R. D. Milton, E. Reisner, *Chem. Sci.* **2024**, *15*, 6088-6094.

[10] E. Rosenberg, *The Prokaryotes: Prokaryotic Biology and Symbiotic Associations* **2013**, vii.

[11] M. W. W. Adams, *J. Biol. Chem.* **1987**, *262*, 15054-15061.

References

[12] M. W. W. Adams, J. F. Holden, A. L. Menon, G. J. Schut, A. M. Grunden, C. Hou, A. M. Hutchins, F. E. Jenney, C. Kim, K. Ma, G. Pan, R. Roy, R. Sapra, S. V. Story, M. F. J. M. Verhagen, *J. Bacteriol.* **2001**, *183*, 716-724.

[13] P. C. Hallenbeck, J. R. Benemann, *Int. J Hydrogen. Energ.* **2002**, *27*, 1185-1193.

[14] M. Jokel, S. Kosourov, Y. Allahverdiyeva, in *Climate Change, Photosynthesis and Advanced Biofuels: The Role of Biotechnology in the Production of Value-added Plant Bio-products* (Eds.: A. Kumar, Y.-Y. Yau, S. Ogita, R. Scheibe), Springer Singapore, Singapore, **2020**, pp. 237-253.

[15] S. I. Allakhverdiev, V. Thavasi, V. D. Kreslavski, S. K. Zharmukhamedov, V. V. Klimov, S. Ramakrishna, D. A. Los, M. Mimuro, H. Nishihara, R. Carpentier, *J. Photochem. Photobiol. C-Photochem. Rev.* **2010**, *11*, 101-113.

[16] J. M. Odom, H. D. Peck, *FEMS Microbiol. Lett* **1981**, *12*, 47-50.

[17] Y. Nicolet, C. Piras, P. Legrand, C. E. Hatchikian, J. C. Fontecilla-Camps, *Structure* **1999**, *7*, 13-23.

[18] G. Fauque, H. D. Peck, Jr., J. J. Moura, B. H. Huynh, Y. Berlier, D. V. DerVartanian, M. Teixeira, A. E. Przybyla, P. A. Lespinat, I. Moura, et al., *FEMS Microbiol Rev* **1988**, *4*, 299-344.

[19] R. Hedderich, *J. Bioenerg. Biomembr.* **2004**, *36*, 65-75.

[20] J. D. Fox, R. L. Kerby, G. P. Roberts, P. W. Ludden, *J. Bacteriol.* **1996**, *178*, 1515-1524.

[21] J. D. Fox, Y. He, D. Shelver, G. P. Roberts, P. W. Ludden, *J Bacteriol* **1996**, *178*, 6200-6208.

[22] H. Nishihara, Y. Miyashita, K. Aoyama, T. Kodama, Y. Igarashi, Y. Takamura, *Biochem Biophys Res Commun* **1997**, *232*, 766-770.

[23] U. Deppenmeier, *J. Bioenerg. Biomembr.* **2004**, *36*, 55-64.

[24] K. Schuchmann, V. Müller, *J. Biol. Chem.* **2012**, *287*, 31165-31171.

[25] H. Q. Loh, V. Hervé, A. Brune, *Front Microbiol* **2020**, *11*, 635786.

[26] M.-L. Chong, N. A. Abdul Rahman, R. A. Rahim, S. A. Aziz, Y. Shirai, M. A. Hassan, *Int. J. Hydrogen. Energ.* **2009**, *34*, 7475-7482.

[27] P. Rodriguez-Macia, Doctoral thesis, Ruhr-Universität Bochum, Bochum. **2017**.

[28] P. Wulff, C. C. Day, F. Sargent, F. A. Armstrong, *Proc. Natl. Acad. Sci.* **2014**, *111*, 6606-6611.

[29] H. Ogata, T. Kramer, H. X. Wang, D. Schilter, V. Pelmenschikov, M. van Gastel, F. Neese, T. B. Rauchfuss, L. B. Gee, A. D. Scott, Y. Yoda, Y. Tanaka, W. Lubitz, S. P. Cramer, *Nat. Commun.* **2015**, *6*, 8.

[30] C. Zirngibl, R. Hedderich, R. K. Thauer, *FEBS Letters* **1990**, *261*, 112-116.

[31] C. Zirngibl, W. Van Dongen, B. Schwörer, R. Von Bünau, M. Richter, A. Klein, R. K. Thauer, *Eur J Biochem* **1992**, *208*, 511-520.

[32] G. Huang, T. Wagner, M. D. Wodrich, K. Ataka, E. Bill, U. Ermler, X. Hu, S. Shima, *Nat. Catal.* **2019**, *2*, 537-543.

[33] Y. Nicolet, *Nat. Catal.* **2019**, *2*, 481-482.

[34] G. Huang, T. Wagner, M. D. Wodrich, K. Ataka, E. Bill, U. Ermler, X. Hu, S. Shima, *Nature Catalysis* **2019**, *2*, 537-543.

[35] T. Happe, J. D. Naber, *Eur. J. Biochem.* **1993**, *214*, 475.

[36] J. M. Kuchenreuther, C. S. Grady-Smith, A. S. Bingham, S. J. George, S. P. Cramer, J. R. Swartz, *PLoS One* **2010**, *5*, e15491.

[37] J. W. Peters, W. N. Lanzilotta, B. J. Lemon, L. C. Seefeldt, *Science* **1998**, *282*, 1853-1858.

[38] M. Demuez, L. Cournac, O. Guerrini, P. Soucaille, L. Girbal, *FEMS Microbiol. Lett.* **2007**, *275*, 113-121.

[39] W. Roseboom, A. L. de Lacey, V. M. Fernández, C. Hatchikian, S. P. J. Albracht, *J. Biol. Inorg. Chem.* **2006**, *11*, 102-118.

[40] J. A. Birrell, K. Wrede, K. Pawlak, P. Rodriguez-Maciá, O. Rüdiger, E. J. Reijerse, W. Lubitz, *Isr. J. Chem.* **2016**, *56*, 852-863.

[41] G. Hong, A. J. Cornish, E. L. Hegg, R. Pachter, *Biochim. Biophys. Acta Bioenerg.* **2011**, *1807*, 510-517.

[42] H. Long, P. W. King, C. H. Chang, *J. Phys. Chem. B* **2014**, *118*, 890-900.

[43] C. C. Moser, C. C. Page, R. Farid, P. L. Dutton, *J. Bioenerg. Biomembr.* **1995**, *27*, 263-274.

[44] A. S. Pandey, T. V. Harris, L. J. Giles, J. W. Peters, R. K. Szilagyi, *J. Am. Chem. Soc.* **2008**, *130*, 4533-4540.

[45] A. J. Cornish, K. Gärtner, H. Yang, J. W. Peters, E. L. Hegg, *J. Biol. Chem.* **2011**, *286*, 38341-38347.

[46] J. Duan, M. Senger, J. Esselborn, V. Engelbrecht, F. Wittkamp, U.-P. Apfel, E. Hofmann, S. T. Stripp, T. Happe, M. Winkler, *Nat. Commun.* **2018**, *9*, 4726.

[47] T. Lautier, P. Ezanno, C. Baffert, V. Fourmond, L. Cournac, J. C. Fontecilla-Camps, P. Soucaille, P. Bertrand, I. Meynial-Salles, C. Léger, *Faraday Discuss.* **2011**, *148*, 385-407.

References

[48] P. M. Vignais, B. Billoud, J. Meyer, *FEMS Microbiol. Rev.* **2001**, *25*, 455-501.

[49] W. G. M. B. R. Glick, and S. M. Martin, *Can. J. Microbiol.* **1980**, *26(10)*.

[50] G. Nakos, L. E. Mortenson, *Biochim. Biophys. Acta* **1971**, *227*, 576-583.

[51] J. D. Santangelo, P. Dürre, D. R. Woods, *J. Microbiol.* **1995**, *141*, 171-180.

[52] S. Morra, A. Giraudo, G. Di Nardo, P. W. King, G. Gilardi, F. Valetti, *PloS one* **2012**, *7*, e48400.

[53] M. Winkler, J. Esselborn, T. Happe, *Biochim. Biophys. Acta Bioenerg.* **2013**, *1827*, 974-985.

[54] S. Morra, *Front. Microbiol.* **2022**, *13*.

[55] M. F. J. M. Verhagen, T. O'Rourke, M. W. W. Adams, *Biochim. Biophys. Acta Bioenerg.* **1999**, *1412*, 212-229.

[56] S. Wang, H. Huang, J. Kahnt, R. K. Thauer, *J. Bacteriol.* **2013**, *195*, 1267-1275.

[57] N. Chongdar, K. Pawlak, O. Rüdiger, E. J. Reijerse, P. Rodríguez-Maciá, W. Lubitz, J. A. Birrell, H. Ogata, *J. Biol. Inorg. Chem.* **2020**, *25*, 135-149.

[58] N. Chongdar, J. A. Birrell, K. Pawlak, C. Sommer, E. J. Reijerse, O. Rüdiger, W. Lubitz, H. Ogata, *J. Am. Chem. Soc.* **2018**, *140*, 1057-1068.

[59] H. Land, A. Sekretareva, P. Huang, H. J. Redman, B. Németh, N. Polidori, L. S. Mészá ros, M. Senger, S. T. Stripp, G. Berggren, *Chemi. Sci.* **2020**, *11*, 12789-12801.

[60] D. W. Mulder, E. S. Boyd, R. Sarma, R. K. Lange, J. A. Endrizzi, J. B. Broderick, J. W. Peters, *Nature* **2010**, *465*, 248-252.

[61] P. Rodríguez-Maciá, L. M. Galle, R. Bjornsson, C. Lorent, I. Zebger, Y. Yoda, S. P. Cramer, S. DeBeer, I. Span, J. A. Birrell, *Angew. Chem. Int. Ed.* **2020**, *59*, 16786-16794.

[62] C. Greening, P. R. Cabotaje, L. E. Valentin Alvarado, P. M. Leung, H. Land, T. Rodrigues-Oliveira, R. I. Ponce-Toledo, M. Senger, M. A. Klamke, M. Milton, R. Lappan, S. Mullen, J. West-Roberts, J. Mao, J. Song, M. Schoelmerich, C. W. Stairs, C. Schleper, R. Grinter, A. Spang, J. F. Banfield, G. Berggren, *Cell* **2024**, *187*, 3357-3372.e3319.

[63] Y. Zhang, L. Tao, T. J. Woods, R. D. Britt, T. B. Rauchfuss, *J. Am. Chem. Soc.* **2022**, *144*, 1534-1538.

[64] R. D. Britt, T. B. Rauchfuss, G. Rao, *Acc. Chem. Res* **2024**, *57*, 1941-1950.

[65] G. Berggren, A. Adamska, C. Lambertz, T. R. Simmons, J. Esselborn, M. Atta, S. Gambarelli, J. M. Mouesca, E. Reijerse, W. Lubitz, T. Happe, V. Artero, M. Fontecave, *Nature* **2013**, *499*, 66-69.

[66] J. Esselborn, C. Lambertz, A. Adamska-Venkatesh, T. Simmons, G. Berggren, J. Noth, J. Siebel, A. Hemschemeier, V. Artero, E. Reijerse, M. Fontecave, W. Lubitz, T. Happe, *Nat. Chem. Biol.* **2013**, *9*, 607-609.

[67] V. Engelbrecht, P. Rodríguez-Maciá, J. Esselborn, A. Sawyer, A. Hemschemeier, O. Rüdiger, W. Lubitz, M. Winkler, T. Happe, *Biochim. Biophys. Acta Bioenerg.* **2017**, *1858*, 771-778.

[68] G. Caserta, A. Adamska-Venkatesh, L. Pecqueur, M. Atta, V. Artero, S. Roy, E. Reijerse, W. Lubitz, M. Fontecave, *Biochim. Biophys. Acta.* **2016**, *1857*, 1734-1740.

[69] J. F. Siebel, A. Adamska-Venkatesh, K. Weber, S. Rumpel, E. Reijerse, W. Lubitz, *Biochemistry* **2015**, *54*, 1474-1483.

[70] R. Gilbert-Wilson, J. F. Siebel, A. Adamska-Venkatesh, C. C. Pham, E. Reijerse, H. Wang, S. P. Cramer, W. Lubitz, T. B. Rauchfuss, *J. Am. Chem. Soc.* **2015**, *137*, 8998-9005.

References

[71] W. K. Myers, T. A. Stich, D. L. M. Suess, J. M. Kuchenreuther, J. R. Swartz, R. D. Britt, *J. Am. Chem. Soc.* **2014**, *136*, 12237-12240.

[72] J. A. Birrell, O. Rüdiger, E. J. Reijerse, W. Lubitz, *Joule* **2017**, *1*, 61-76.

[73] C. F. Megarity, J. Esselborn, S. V. Hexter, F. Wittkamp, U.-P. Apfel, T. Happe, F. A. Armstrong, *J. Am. Chem. Soc.* **2016**, *138*, 15227-15233.

[74] A. Silakov, C. Kamp, E. Reijerse, T. Happe, W. Lubitz, *Biochemistry* **2009**, *48*, 7780-7786.

[75] A. Adamska-Venkatesh, D. Krawietz, J. Siebel, K. Weber, T. Happe, E. Reijerse, W. Lubitz, *J. Am. Chem. Soc.* **2014**, *136*, 11339-11346.

[76] C. Kamp, A. Silakov, M. Winkler, E. J. Reijerse, W. Lubitz, T. Happe, *Biochim. Biophys. Acta.* **2008**, *1777*, 410-416.

[77] P. Rodríguez-Maciá, K. Pawlak, O. Rüdiger, E. J. Reijerse, W. Lubitz, J. A. Birrell, *J. Am. Chem. Soc.* **2017**.

[78] P. Rodríguez-Maciá, N. Breuer, S. DeBeer, J. A. Birrell, *ACS Catal.* **2020**, *10*, 13084-13095.

[79] S. Morra, J. Duan, M. Winkler, P. A. Ash, T. Happe, K. A. Vincent, *Dalton Trans.* **2021**, *50*, 12655-12663.

[80] A. Adamska, A. Silakov, C. Lambertz, O. Rüdiger, T. Happe, E. Reijerse, W. Lubitz, *Angew. Chem. Int. Ed.* **2012**, *51*, 11458-11462.

[81] D. W. Mulder, Y. Guo, M. W. Ratzloff, P. W. King, *J. Am. Chem. Soc.* **2017**, *139*, 83-86.

[82] E. J. Reijerse, C. C. Pham, V. Pelmenschikov, R. Gilbert-Wilson, A. Adamska-Venkatesh, J. F. Siebel, L. B. Gee, Y. Yoda, K. Tamasaku, W. Lubitz, T. B. Rauchfuss, S. P. Cramer, *J. Am. Chem. Soc.* **2017**, *139*, 4306-4309.

[83] D. W. Mulder, M. W. Ratzloff, M. Bruschi, C. Greco, E. Koonce, J. W. Peters, P. W. King, *J. Am. Chem. Soc.* **2014**, *136*, 15394-15402.

[84] C. Lorent, S. Katz, J. Duan, C. J. Kulka, G. Caserta, C. Teutloff, S. Yadav, U. P. Apfel, M. Winkler, T. Happe, M. Horch, I. Zebger, *J Am Chem Soc* **2020**, *142*, 5493-5497.

[85] J. A. Birrell, V. Pelmenschikov, N. Mishra, H. Wang, Y. Yoda, K. Tamasaku, T. B. Rauchfuss, S. P. Cramer, W. Lubitz, S. DeBeer, *J. Am. Chem. Soc.* **2020**, *142*, 222-232.

[86] Z. X. Cao, M. B. Hall, *J. Am. Chem. Soc.* **2001**, *123*, 3734-3742.

[87] Z. P. Liu, P. Hu, *J. Am. Chem. Soc.* **2002**, *124*, 5175-5182.

[88] P. Rodríguez-Maciá, E. J. Reijerse, M. van Gastel, S. DeBeer, W. Lubitz, O. Rüdiger, J. A. Birrell, *J. Am. Chem. Soc.* **2018**, *140*, 9346-9350.

[89] M. Winkler, J. Duan, A. Rutz, C. Felbek, L. Scholtysek, O. Lampret, J. Jaenecke, U.-P. Apfel, G. Gilardi, F. Valetti, V. Fourmond, E. Hofmann, C. Léger, T. Happe, *Nat. Commun.* **2021**, *12*, 756.

[90] S. Morra, M. Arizzi, F. Valetti, G. Gilardi, *Biochemistry* **2016**, *55*, 5897-5900.

[91] P. S. Corrigan, J. L. Tirsch, A. Silakov, *J. Am. Chem. Soc.* **2020**, *142*, 12409-12419.

[92] J. Duan, A. Hemschemeier, D. J. Burr, S. T. Stripp, E. Hofmann, T. Happe, *Angew. Chem. Int. Ed. Engl.* **2023**, *62*, e202216903.

[93] M. A. Martini, K. Bikbaev, Y. Pang, C. Lorent, C. Wiemann, N. Breuer, I. Zebger, S. DeBeer, I. Span, R. Bjornsson, J. A. Birrell, P. Rodríguez-Maciá, *Chem Sci* **2023**, *14*, 2826-2838.

[94] A. Parkin, C. Cavazza, J. C. Fontecilla-Camps, F. A. Armstrong, *J. Am. Chem. Soc.* **2006**, *128*, 16808-16815.

References

[95] J. A. Birrell, K. Wrede, K. Pawlak, P. Rodriguez-Maciá, O. Rüdiger, E. J. Reijerse, W. Lubitz, *Isr. J. Chem* **2016**, *56*, 852-863.

[96] P. W. King, M. C. Posewitz, M. L. Ghirardi, M. Seibert, *J. Bacteriol.* **2006**, *188*, 2163-2172.

[97] A. Kubas, C. Orain, D. De Sancho, L. Saujet, M. Sensi, C. Gauquelin, I. Meynial-Salles, P. Soucaille, H. Bottin, C. Baffert, V. Fourmond, R. B. Best, J. Blumberger, C. Léger, *Nat. Chem.* **2017**, *9*, 88-95.

[98] C. Orain, L. Saujet, C. Gauquelin, P. Soucaille, I. Meynial-Salles, C. Baffert, V. Fourmond, H. Bottin, C. Léger, *J. Am. Chem. Soc.* **2015**, *137*, 12580-12587.

[99] S. V. Hexter, F. Grey, T. Happe, V. Climent, F. A. Armstrong, *Proc. Nat. Acad. Sci. USA* **2012**, *109*, 11516-11521.

[100] S. Morra, S. Maurelli, M. Chiesa, D. W. Mulder, M. W. Ratzloff, E. Giamello, P. W. King, G. Gilardi, F. Valetti, *Biochim. Biophys. Acta Bioenerg.* **2016**, *1857*, 98-106.

[101] M. K. Akhtar, P. R. Jones, *Appl. Microbiol. Biotechnol.* **2008**, *78*, 853-862.

[102] A. Meunier, F. Cornet, M. Campos, *FEMS Microbiol Rev* **2021**, *45*.

[103] U. K. Laemmli, *Nature* **1970**, *227*, 680-685.

[104] J. Markwell, *Biochem. Mol. Biol. Educ.* **2009**, *37*, 317-318.

[105] M. M. Bradford, *Anal Biochem* **1976**, *72*, 248-254.

[106] A. J. Bard, L. R. Faulkner, *Electrochemical Methods: Fundamentals and Applications*, 2nd ed., John Wiley & Sons, Inc, New York, **2001**.

[107] P. V. Bernhardt, *Aust. J. Chem* **2006**, *59*, 233-256.

[108] C. Léger, P. Bertrand, *Chem. Rev.* **2008**, *108*, 2379-2438.

References

[109] J. L. Dempsey, B. S. Brunschwig, J. R. Winkler, H. B. Gray, *Acc. Chem. Res.* **2009**, *42 12*, 1995-2004.

[110] D. L. DuBois, R. M. Bullock, *Eur. J. Inorg. Chem.* **2011**, 1017-1027.

[111] T. Liu, D. L. DuBois, R. M. Bullock, *Nat. Chem.* **2013**, *5*, 228-233.

[112] O. Lampret, J. Duan, E. Hofmann, M. Winkler, F. A. Armstrong, T. Happe, *Proc. Nat. Acad. Sci.* **2020**, *117*, 20520-20529.

[113] O. Hammerich, and Ulstrup, J., *Bioinorganic Electrochemistry*, 2nd ed., Springer, **2007**.

[114] K. A. Vincent, A. Parkin, F. A. Armstrong, *Chem. Rev.* **2007**, *107*, 4366-4413.

[115] L. Gorton, A. Torstensson, H. Jaegfeldt, G. Johansson, *J. electroanal. chem. interfacial electrochem* **1984**, *161*, 103-120.

[116] F. A. Armstrong, J. Hirst, *Proc. Natl. Acad. Sci. USA.* **2011**, *108*, 14049-14054.

[117] K. Nakamoto, *Infrared and Raman Spectra of Inorganic and Coordination Compounds, Vol. 5th*, John wiley & Sons, Inc, New York, **1997**.

[118] P. A. Ash, S. E. T. Kendall-Price, K. A. Vincent, *Acc. Chem. Res* **2019**, *52*, 3120-3131.

[119] N. M. Atherton, *Principles of electron spin resonance*, Ellis Horwood PTR Prentice Hall, New York, **1993**.

[120] A. Silakov, E. J. Reijerse, S. P. J. Albracht, E. C. Hatchikian, W. Lubitz, *J. Am. Chem. Soc.* **2007**, *129*, 11447.

[121] V. Nasta, D. Suraci, S. Gourdoupis, S. Ciofi-Baffoni, L. Banci, *The FEBS Journal* **2020**, *287*, 2312-2327.

[122] G. Nakos, L. E. Mortenson, *Biochimica et Biophysica Acta* **1971**, *227*, 576-583.

[123] L. Girbal, G. von Abendroth, M. Winkler, P. M. C. Benton, I. Meynial-Salles, C. Croux, J. W. Peters, T. Happe, P. Soucaille, *Appl. Environ. Microbiol.* **2005**, *71*, 2777-2781.

[124] J. M. Kuchenreuther, C. S. Grady-Smith, A. S. Bingham, S. J. George, S. P. Cramer, J. R. Swartz, *Plos One* **2010**, *5*, e15491-e15491.

[125] J. Esselborn, C. Lambertz, A. Adamska-Venkatesh, T. Simmons, G. Berggren, J. Noth, J. Siebel, A. Hemschemeier, V. Artero, E. Reijerse, M. Fontecave, W. Lubitz, T. Happe, *Nat Chem Biol* **2013**, *9*, 607-609.

[126] M. C. Posewitz, P. W. King, S. L. Smolinski, L. P. Zhang, M. Seibert, M. L. Ghirardi, *J. Biol. Chem.* **2004**, *279*, 25711-25720.

[127] S. E. McGlynn, S. S. Ruebush, A. Naumov, L. E. Nagy, A. Dubini, P. W. King, J. B. Broderick, M. C. Posewitz, J. W. Peters, *J. Biol. Inorg. Chem.* **2007**, *12*, 443-447.

[128] D. W. Mulder, D. O. Ortillo, D. J. Gardenghi, A. V. Naumov, S. S. Ruebush, R. K. Szilagyi, B. H. Huynh, J. B. Broderick, J. W. Peters, *Biochemistry* **2009**, *48*, 6240-6248.

[129] J. M. Kuchenreuther, Y. Guo, H. Wang, W. K. Myers, S. J. George, C. A. Boyke, Y. Yoda, E. E. Alp, J. Zhao, R. D. Britt, J. R. Swartz, S. P. Cramer, *Biochemistry* **2013**, *52*, 818.

[130] R. C. Driesener, M. R. Challand, S. E. McGlynn, E. M. Shepard, E. S. Boyd, J. B. Broderick, J. W. Peters, P. L. Roach, *Angew. Chem., Int. Ed.* **2010**, *49*, 1687-1690.

[131] E. M. Shepard, B. R. Duffus, S. J. George, S. E. McGlynn, M. R. Challand, K. D. Swanson, P. L. Roach, S. P. Cramer, J. W. Peters, J. B. Broderick, *J. Am. Chem. Soc.* **2010**, *132*, 9247-9249.

[132] J. M. Kuchenreuther, W. K. Myers, D. L. M. Suess, T. A. Stich, V. Pelmenschikov, S. A. Shiigi, S. P. Cramer, J. R. Swartz, R. D. Britt, S. J. George, *Science* **2014**, *343*, 424-427.

References

[133] R. D. Britt, L. Tao, G. Rao, N. Chen, L.-P. Wang, *ACS Bio & Med Chem Au* **2022**, *2*, 11-21.

[134] G. Rao, S. A. Pattenaude, K. Alwan, N. J. Blackburn, R. D. Britt, T. B. Rauchfuss, *Proc Natl Acad Sci U S A* **2019**, *116*, 20850-20855.

[135] B. Németh, H. Land, A. Magnuson, A. Hofer, G. Berggren, *J. Biol. Chem.* **2020**, *295*, 11891-11901.

[136] T. Lai, W. K. Myers, S. B. Carr, A. R. Miguel, K. A. Vincent, S. Morra, P. Rodríguez-Maciá, *Nat. Catal.* **In preparation**.

[137] S. Morra, S. Maurelli, M. Chiesa, D. W. Mulder, M. W. Ratzloff, E. Giamello, P. W. King, G. Gilardi, F. Valetti, *Biochim. Biophys. Acta. Bioenerg.* **2016**, *1857*, 98-106.

[138] S. Stoll, A. Schweiger, *J. Magn. Reson.* **2006**, *178*, 42-55.

[139] H. Beinert, *J. Biol. Inorg. Chem.* **2000**, *5*, 2-15.

[140] Y. Lu, *Chem Rev*.

[141] D. W. Bak, S. J. Elliott, *Curr. Opin. Chem. Biol.* **2014**, *19*, 50-58.

[142] C. Greening, A. Biswas, C. R. Carere, C. J. Jackson, M. C. Taylor, M. B. Stott, G. M. Cook, S. E. Morales, *The ISME Journal* **2016**, *10*, 761-777.

[143] E. Siebert, Y. Rippers, S. Frielingsdorf, J. Fritsch, A. Schmidt, J. Kalms, S. Katz, O. Lenz, P. Scheerer, L. Paasche, V. Pelmenschikov, U. Kuhlmann, M. A. Mroginski, I. Zebger, P. Hildebrandt, *J. Phys. Chem. B* **2015**, *119*, 13785-13796.

[144] S. Frielingsdorf, J. Fritsch, A. Schmidt, M. Hammer, J. Löwenstein, E. Siebert, V. Pelmenschikov, T. Jaenicke, J. Kalms, Y. Rippers, F. Lendzian, I. Zebger, C. Teutloff, M. Kaupp, R. Bittl, P. Hildebrandt, B. Friedrich, O. Lenz, P. Scheerer, *Nat. Chem. Bio.* **2014**, *10*, 378-385.

[145] P. Wulff, C. C. Day, F. Sargent, F. A. Armstrong, *Proc. Natl. Acad. Sci. U.S.A.* **2014**, *111*, 6606-6611.

[146] P. Rodríguez-Maciá, L. Kertess, J. Burnik, J. A. Birrell, E. Hofmann, W. Lubitz, T. Happe, O. Rüdiger, *J. Am. Chem. Soc.* **2019**, *141*, 472-481.

[147] P. Rodríguez-Maciá, L. M. Galle, R. Bjornsson, C. Lorent, I. Zebger, Y. Yoda, S. P. Cramer, S. DeBeer, I. Span, J. A. Birrell, *Angew. Chem. Int. Ed. Engl.* **2020**, *59*, 16786-16794.

[148] J. Meyer, *Cell. Mol. Life Sci.* **2007**, *64*, 1063-1084.

[149] C. Gauquelin, C. Baffert, P. Richaud, E. Kamionka, E. Etienne, D. Guieysse, L. Girbal, V. Fourmond, I. André, B. Guigliarelli, C. Léger, P. Soucaille, I. Meynial-Salles, *Biochim. Biophys. Acta Bioenerg.* **2018**, *1859*, 69-77.

[150] G. Caserta, C. Papini, A. Adamska-Venkatesh, L. Pecqueur, C. Sommer, E. Reijerse, W. Lubitz, C. Gauquelin, I. Meynial-Salles, D. Pramanik, V. Artero, M. Atta, M. del Barrio, B. Faivre, V. Fourmond, C. Léger, M. Fontecave, *J. Am. Chem. Soc.* **2018**, *140*, 5516-5526.

[151] J. H. Artz, D. W. Mulder, M. W. Ratzloff, C. E. Lubner, O. A. Zadvornyy, A. X. LeVan, S. G. Williams, M. W. W. Adams, A. K. Jones, P. W. King, J. W. Peters, *J. Am. Chem. Soc.* **2017**, *139*, 9544-9550.

[152] C. E. Lubner, J. H. Artz, D. W. Mulder, A. Oza, R. J. Ward, S. G. Williams, A. K. Jones, J. W. Peters, I. I. Smalyukh, V. S. Bharadwaj, P. W. King, *Chem. Sci.* **2022**, *13*, 4581-4588.

[153] J. H. Artz, O. A. Zadvornyy, D. W. Mulder, S. M. Keable, A. E. Cohen, M. W. Ratzloff, S. G. Williams, B. Ginovska, N. Kumar, J. Song, S. E. McPhillips, C. M. Davidson, A. Y.

Lyubimov, N. Pence, G. J. Schut, A. K. Jones, S. M. Soltis, M. W. W. Adams, S. Raugei, P. W. King, J. W. Peters, *J. Am. Chem. Soc.* **2020**, *142*, 1227-1235.

[154] M. Yoo, G. Bestel-Corre, C. Croux, A. Riviere, I. Meynial-Salles, P. Soucaille, *mBio* **2015**, *6*, e01808-01815.

[155] O. Guerrini, B. Burlat, C. Léger, B. Guigliarelli, P. Soucaille, L. Girbal, *Curr. Microbiol.* **2008**, *56*, 261-267.

[156] M. W. Ratzloff, J. H. Artz, D. W. Mulder, R. T. Collins, T. E. Furtak, P. W. King, *J. Am. Chem. Soc.* **2018**, *140*, 7623-7628.

[157] C. Sommer, A. Adamska-Venkatesh, K. Pawlak, J. A. Birrell, O. Rüdiger, E. J. Reijerse, W. Lubitz, *J. Am. Chem. Soc.* **2017**, *139*, 1440-1443.

[158] J. A. Birrell, P. Rodríguez-Maciá, E. J. Reijerse, M. A. Martini, W. Lubitz, *Coord. Chem. Rev.* **2021**, *449*, 214191.

[159] J. W. Sidabras, S. T. Stripp, *J Biol Inorg Chem* **2023**, *28*, 355-378.

[160] M. Heghmanns, A. Rutz, Y. Kutin, V. Engelbrecht, M. Winkler, T. Happe, M. Kasanmascheff, *Chem. Sci.* **2022**, *13*, 7289-7294.

[161] P. S. Corrigan, S. H. Majer, A. Silakov, *J. Am. Chem. Soc.* **2023**.

[162] F. Leroux, S. Dementin, B. Burlat, L. Cournac, A. Volbeda, S. Champ, L. Martin, B. Guigliarelli, P. Bertrand, J. Fontecilla-Camps, M. Rousset, C. Léger, *Proc. Natl. Acad. Sci. USA* **2008**, *105*, 11188-11193.

[163] P.-P. Liebgott, F. Leroux, B. Burlat, S. Dementin, C. Baffert, T. Lautier, V. Fourmond, P. Ceccaldi, C. Cavazza, I. Meynial-Salles, P. Soucaille, J. C. Fontecilla-Camps, B. Guigliarelli, P. Bertrand, M. Rousset, C. Léger, *Nat. Chem. Biol.* **2010**, *6*, 63-70.

References

[164] A. Abou Hamdan, S. Dementin, P.-P. Liebgott, O. Gutierrez Sanz, P. Richaud, A. L. de Lacey, M. Roussett, P. Bertrand, L. Cournac, C. Léger, *J. Am. Chem. Soc.* **2012**, *134*, 8368-8371.

[165] M. W. Adams, *J. Biol. Inorg. Chem* **1987**, *262*, 15054-15061.

[166] C. Baffert, L. Bertini, T. Lautier, C. Greco, K. Sybirna, P. Ezanno, E. Etienne, P. Soucaille, P. Bertrand, H. Bottin, I. Meynial-Salles, L. De Gioia, C. Léger, *J. Am. Chem. Soc.* **2011**, *133*, 2096-2099.

[167] J. Cohen, K. Kim, P. King, M. Seibert, K. Schulten, *Structure* **2005**, *13*, 1321-1329.

[168] C. Baffert, M. Demuez, L. Cournac, B. Burlat, B. Guigliarelli, P. Bertrand, L. Girbal, C. L éger, *Angew. Chem. Int. Ed.* **2008**, *47*, 2052-2054.

[169] S. T. Stripp, G. Goldet, C. Brandmayr, O. Sanganas, K. A. Vincent, M. Haumann, F. A. Armstrong, T. Happe, *Proc. Nat. Acad. Sci. USA* **2009**, *106*, 17331-17336.

[170] M. T. Stiebritz, M. Reiher, *Inorg. Chem.* **2009**, *48*, 7127-7140.

[171] A. Kubas, D. De Sancho, R. B. Best, J. Blumberger, *Angew. Chem. Int. Ed.* **2014**, *53*, 4081-4084.

[172] J. Esselborn, L. Kertess, U.-P. Apfel, E. Hofmann, T. Happe, *J. Am. Chem. Soc.* **2019**, *141*, 17721-17728.

[173] C. Lambertz, N. Leidel, K. G. V. Havelius, J. Noth, P. Chernev, M. Winkler, T. Happe, M. Haumann, *J. Biol. Chem* **2011**, *286*, 40614-40623.

[174] V. Fourmond, N. Plumeré, C. Léger, *Nature Rev. Chem.* **2021**, *5*, 348-360.

[175] A. L. De Lacey, A. Pardo, V. M. Fernández, S. Dementin, G. Adryanczyk-Perrier, E. C. Hatchikian, M. Rousset, *J. Biol. Inorg. Chem* **2004**, *9*, 636-642.

[176] A. K. Jones, S. E. Lamle, H. R. Pershad, K. A. Vincent, S. P. J. Albracht, F. A. Armstrong, *J. Am. Chem. Soc.* **2003**, *125*, 8505-8514.

[177] S. E. Lamle, K. A. Vincent, L. M. Halliwell, S. P. J. Albracht, F. A. Armstrong, *Dalton Trans.* **2003**, 4152-4157.

[178] G. Goldet, C. Brandmayr, S. T. Stripp, T. Happe, C. Cavazza, J. C. Fontecilla-Camps, F. A. Armstrong, *J. Am. Chem. Soc.* **2009**, *131*, 14979-14989.

[179] M. del Barrio, M. Sensi, L. Fradale, M. Bruschi, C. Greco, L. de Gioia, L. Bertini, V. Fourmond, C. Léger, *J. Am. Chem. Soc.* **2018**, *140*, 5485-5492.

[180] M. del Barrio, M. Sensi, L. Fradale, M. Bruschi, C. Greco, L. de Gioia, L. Bertini, V. Fourmond, C. Léger, *J. Am. Chem. Soc.* **2018**.

[181] S. T. Stripp, G. Goldet, C. Brandmayr, O. Sanganas, K. A. Vincent, M. Haumann, F. A. Armstrong, T. Happe, *Proc. Natl. Aad. Sci. USA* **2009**, *106*, 17331-17336.

[182] K. D. Swanson, M. W. Ratzloff, D. W. Mulder, J. H. Artz, S. Ghose, A. Hoffman, S. White, O. A. Zadvornyy, J. B. Broderick, B. Bothner, P. W. King, J. W. Peters, *J. Am. Chem. Soc.* **2015**, *137*, 1809-1816.

[183] P. Rodriguez-Macia, J. A. Birrell, W. Lubitz, O. Rudiger, *Chempluschem* **2017**, *82*, 540-545.

[184] V. Fourmond, T. Lautier, C. Baffert, F. Leroux, P.-P. Liebgott, S. Dementin, M. Rousset, P. Arnoux, D. Pignol, I. Meynial-Salles, P. Soucaille, P. Bertrand, C. Léger, *Anal. Chem.* **2009**, *81*, 2962-2968.

[185] Y. Zu, M. M. J. Couture, D. R. J. Kolling, A. R. Crofts, L. D. Eltis, J. A. Fee, J. Hirst, *Biochemistry* **2003**, *42*, 12400-12408.

References

[186] C. M. Krest, A. Silakov, J. Rittle, T. H. Yosca, E. L. Onderko, J. C. Calixto, M. T. Green, *Nature Chem.* **2015**, *7*, 696-702.

[187] X. Wu, T. A. Rapoport, *Proc. Natl. Acad. Sci. U.S.A.* **2021**, *118*, e2115001118.

[188] S. Matsumoto, S. Ishida, M. Araki, T. Kato, K. Terayama, Y. Okuno, *Nat. Mach. Intell* **2021**, *3*, 153-160.